Amin Lopes Ismael

Structure and reactivity of novel tetrazole-saccharinates useful as multidentate nitrogen ligands

UNIVERSIDADE DO ALGARVE

FACULDADE DE CIÊNCIAS E TECNOLOGIA

Doutoramento em Química

2017

Amin Lopes Ismael

Structure and reactivity of novel tetrazole-saccharinates useful as multidentate nitrogen ligands

Tese de Doutoramento em Química

Especialidade em Espectroscopia Molecular

Trabalho efetuado sob a orientação de:

Prof.ª Doutora Maria de Lurdes dos Santos Cristiano
(Professora Associada com Agregação na Universidade do Algarve)

Prof. Doutor Rui Fausto Martins Ribeiro da Silva Lourenço
(Professor Catedrático na Universidade de Coimbra)

UNIVERSIDADE DO ALGARVE

FACULDADE DE CIÊNCIAS E TECNOLOGIA

2017

Structure and reactivity of novel tetrazole-saccharinates useful as multidentate nitrogen ligands

Doutoramento em Química

Especialidade em Espectroscopia Molecular

Declaração de Autoria do Trabalho

Declaro ser o autor deste trabalho, que é original e inédito. Autores e trabalhos consultados estão devidamente citados no texto e constam das listagens de referências incluídas.

Amin Lopes Ismael

…….

Direitos de cópia ou Copyright

Acknowledgments

I am deeply grateful to my supervisor Professor Maria de Lurdes Cristiano for all the support, experience and motivation expressed throughout all these years. Thank you for all your guidance and friendship.

To Professor Rui Fausto, my co-supervisor, I would like to express my gratitude for all the support and enthusiasm, and for the opportunity to carry out, part of this project at the Laboratory for Molecular Cryospectroscopy and Biospectroscopy (LMCB) at University of Coimbra.

Special thanks to my lab colleagues and friends, Lília Cabral and Pedro Horta. Thank you for all the great time we spent together.

Also, to the great people I meet in the Chemistry Department of the University of Coimbra.

Sincere thanks to Andrea Gómez-Zavaglia and Ana Borba for the precious advice regarding research work during a great part of the investigation and by the stimulating collaboration.

To Luís Frija, who took the first steps in this project, I would like to acknowledge for keeping the interest in these compounds and for all collaborations.

To Cátia Marques and Maria Rodrigues, I would like to acknowledge for conducting the biological assays to my compounds.

To Professor José António Paixão and Marta Henriques of the CFisUC (Department of Physics, University of Coimbra), for all collaboration and availability in X-ray facilities.

To Fundação para a Ciência e Tecnologia (FCT–Portugal) and Centro de Ciências do Mar (CCMAR) for generous financial support, especially for the FCT doctoral grant that allowed the accomplishment of this research (SFRH/BD/90435/2012).

To my mother and brother, Iolanda and Francisco, for unconditional support and understanding throughout the course of this dissertation. Thank you very much for everything.

Finally, I would like to offer my special thanks to Adriana Silva, without whose love, understanding and patience I would not have completed this work.

Abstract

Tetrazoles have attracted increasing attention in recent years in the fields of coordination and supramolecular chemistry, due to the excellent coordination ability of the four nitrogen atoms, acting either as multidentate ligands or as bridging building blocks in supramolecular assemblies. Moreover, the structure of the coordination complex can be tailored by employing functional tetrazoles in the assembly process. Likewise, several studies on saccharin have shown that its coordination chemistry is very interesting, acting either as a bidentate or as bridging ligand. Inspired by the versatility of those heterocycles, the research described within this thesis focus on the synthesis, structure and reactivity of a library of new tetrazole-saccharyl conjugates with applications as multidentate nitrogen ligands.

Ligands are the very body of coordination chemistry, therefore understanding the structural properties of these systems is crucial, in order to explore their properties and functions. As such, the structure of these new ligands has been investigated in detail, and their chelating capacity towards divalent cations of transition metals was evaluated.

In parallel, the photochemistry of these ligands, isolated in solid argon, was investigated by means of infrared spectroscopy and quantum chemical calculations. The plethora of applications of saccharin derivatives often rely on the photochemical stability of the saccharyl system. On the other hand, tetrazoles are known for their rich photochemistry. As such, the photochemical stability of these conjugates, introduced by the saccharyl system into the photolabile tetrazole, was evaluated. In the course of those studies, important mechanistic questions regarding the effects of the ring substitution pattern, on the photochemical pathways of disubstituted tetrazoles, were addressed.

Two novel copper(II) complexes based on selected tetrazole-saccharinates were prepared and their structural and spectroscopic properties investigated. Additionally, selected conjugates were tested as selective copper(II) chelators, and the complexes were evaluated for their *in vitro* cytotoxicity against human tumour cell lines.

Keywords: Benzisothiazole; Tetrazole; Multidentate nitrogen ligands; Structural analysis; Photoreactivity, Transition metal-based complexes.

Resumo

A maioria dos metais, na crosta terrestre, são encontrados em ambientes inorgânicos, como rochas ou solos, onde os metais formam agregados em elevadas concentrações, sob a forma de minerais metálicos ou metais nativos, obtidos na sequência de longos processos geológicos. Por esta razão talvez não seja surpreendente que, durante muitos anos, tenha existido uma divisão entre o "mundo dos metais" e o "mundo vivo". Efetivamente, os iões metálicos estão presentes por toda a parte, na natureza, desempenhando papéis essenciais nos seres vivos, inclusive no local ativo de enzimas. Na realidade, as biomoléculas contendo metais são surpreendentemente comuns e importantes. O ferro, o zinco e o cobre são os metais de transição mais comuns no corpo humano, desempenhando papéis importantes nos sítios ativos de diversas proteínas. Como exemplo de algumas biomoléculas bem conhecidas temos a clorofila, um complexo de Mg^{2+}; a hemoglobina, um complexo de Fe^{2+} e a vitamina B12, um complexo de Co^{3+}. Na verdade, estes são exemplos de complexos de coordenação naturais, e toda a vida depende deles. A natureza desenvolveu uma notável utilização de complexos de coordenação, sem qualquer intervenção humana. No entanto, a química de coordenação e os complexos de coordenação estão hoje em dia no cerne de uma série de importantes aplicações na indústria, por exemplo na extração de metais, na medicina e em diversos outros campos.

Durante muito tempo, a indústria farmacêutica revelou-se bastante resistente ao desenvolvimento de fármacos baseados em compostos de coordenação, talvez devido a preocupações com toxicidade, especificidade e acumulação de catiões metálicos em pacientes durante longos períodos de uso. Nas últimas décadas, o reconhecimento de que os compostos de coordenação podem ser sofisticadas alternativas aos convencionais fármacos orgânicos permitiu, juntamente com a atividade farmacológica, o acesso a propriedades nucleares, magnéticas e óticas, simplesmente não disponíveis com compostos orgânicos. De facto, os compostos de coordenação que mostraram capacidade para curar ou controlar doenças, têm crescido notavelmente em número e gama de aplicações nas últimas décadas.

Por outro lado, as propriedades luminescentes dos complexos permitiram o desenvolvimento de importantes aplicações em diversas outras áreas. Estas propriedades podem ser utilizadas no desenvolvimento de sondas para a deteção de iões metálicos específicos, ou pode mesmo ser possível utilizar a complexação como um sensor de outro processo ou espécie, conhecido como método "switch on". Devido à facilidade de manipulação ligada à elevada sensibilidade de deteção, as sondas fluorescentes são hoje largamente utilizadas em

microscopia de fluorescência, na análise de sequências de genes e em testes de imunofluorescência. Além disso, a fosforescência ou fluorescência de complexos na região visível resultou num mercado emergente de díodos óticos emissores de luz (OLEDs) ou díodos óticos emissores de luz fosforescentes (PHOLEDs).

A indústria química, tal como a conhecemos atualmente, seria marcadamente diferente sem compostos de coordenação, visto que estes desempenham papéis essenciais numa ampla gama de processos, enquanto catalisadores. Na atualidade, os catalisadores assumem uma grande importância económica nos processos industriais, estimando-se que 90% de todos os produtos químicos produzidos envolvam a utilização de um catalisador em alguma das suas etapas de produção. Naturalmente, com o aumento do desenvolvimento industrial, os solos contaminados com resíduos de metais pesados são um grave problema, muitas vezes tornando extensas parcelas de terra inadequadas para reutilização. Uma maneira óbvia de remediar este problema seria a extração dos metais contaminantes do solo, no entanto este procedimento, necessitaria ser feito sem a remoção dos iões de metais naturais benignos e dominantes no solo. Este processo pode ser alcançado através da utilização de moléculas com propriedades de ligação fortemente seletivas para o metal ou metais alvo, permitindo que outros permaneçam inalterados. De facto, a complexação seletiva é bastante utilizada, e já desenvolvida para a extração de metal a partir de minérios comerciais. A recuperação do ouro é um exemplo simples, onde a complexação seletiva desempenha um papel fundamental. Deste ponto de vista, o desenvolvimento de ligandos com capacidade de complexação seletiva para metais alvo é de extrema importância, permitindo que solos contaminados possam vir a ser "minerados" dos seus metais contaminantes indesejados.

A nanotecnologia é uma das novas fronteiras da química, visando o desenvolvimento de materiais com uma estrutura bem definida e com dimensões na gama de 1 a ~ 100 nm. Esta é uma área emergente na qual os complexos metálicos têm vindo a ser utilizados como ponto de partida, no que é geralmente designado como abordagem “bottom up” na síntese de nanomateriais. Estes materiais são obtidos através da combinação de ligandos especificamente moldados e capazes de atuar como grupos de ligação, com complexos simples, os quais se agregam em grandes produtos à nanoescala.

O número de moléculas conhecidas por atuar como ligandos ou serem potencialmente capazes de se ligar a metais é extremamente grande. De facto, a maioria das moléculas orgânicas pode atuar como ligandos, uma vez que a chave para um átomo ou molécula atuar como um ligando é a presença de pelo menos um par de eletrões não ligantes. Como regra geral, os heteroátomos (particularmente O, N, S e P) em moléculas orgânicas incluem um ou mais

pares de eletrões não ligantes, pelo que a presença destes átomos é um bom começo para identificar se uma molécula pode ou não atuar como um ligando. Naturalmente, a localização, o ambiente local, a estrutura tridimensional do composto e a orientação relativa dos potenciais dadores em moléculas grandes desempenham um papel fundamental no número de grupos dadores disponíveis que podem ligar-se a um único ião metálico, conhecidos como agentes quelantes ou, por outro lado, na expansão através de ligações com mais de um ião metálico, atuando como grupos de ligação (pontes) em estruturas polinucleares.

Os ligandos são o próprio corpo dos compostos de coordenação, e nos últimos anos evoluíram através de avanços em síntese até ao nível em que é praticamente possível produzir o ligando desejado para um propósito particular. No entanto, para antecipar o comportamento de moléculas enquanto ligandos é fundamental a compreensão das propriedades eletrónicas e estruturais dessas mesmas moléculas. Desta forma, embora a síntese esteja na base da preparação de novos compostos, tem-se verificado um crescente interesse nos estudos *in silico*. Ao longo das últimas décadas, os métodos computacionais desenvolveram-se até um ponto em que é possível determinar uma ampla gama de propriedades moleculares, *e.g.* estruturais, distribuição da densidade de carga, frequências vibracionais, transições eletrónicas, *etc*., fornecendo uma ajuda inestimável na interpretação de medições experimentais.

O trabalho descrito nesta tese está relacionado principalmente com a estrutura e reatividade de novas moléculas que incorporam derivados de duas classes importantes de compostos heterocíclicos, tetrazoles e benzisotiazoles (derivados de sacarina), acoplados por grupos que funcionam como ponte. Como objetivo final pretende-se avaliar a capacidade destas novas moléculas enquanto ligandos multidentados para coordenação com metais de transição e explorar as propriedades dos complexos formados.

Nos últimos anos, os tetrazoles têm atraído cada vez mais atenção na química de coordenação, devido à excelente capacidade de coordenação dos quatro átomos de azoto, conhecidos por atuar como ligandos multidentados e como grupos de ligação em montagens supramoleculares. Além disso podem ser prontamente introduzidas funcionalidades nas estruturas supramoleculares, utilizando tetrazoles funcionalizados no processo de montagem. Da mesma forma, vários estudos sobre a sacarina e alguns dos seus derivados mostraram que a química de coordenação do sistema benzisotiazolílico é bastante interessante, podendo agir como um ligando multidentado ou como um grupo de ligação em estruturas polinucleares.

No capítulo 1 desta tese é apresentada a descrição das aplicações mais importantes de tetrazoles e benzisotiazoles, que foram de alguma forma relevantes para a investigação desenvolvida no programa de doutoramento, a que a tese diz respeito. Uma das preocupações

importantes durante a conceção destes novos conjugados foi a capacidade de introduzir facilmente diversidade química, através de diferentes grupos ponte e também de diferentes substituintes no anel tetrazolílico. A fim de mostrar capacidade de funcionalização do anel tetrazolílico, é apresentada uma visão geral dos métodos considerados mais relevantes para a síntese de vários tetrazoles substituídos e também para a funcionalização de tetrazoles substituídos em posição 5. Adicionalmente, é feita uma revisão da reatividade fotoquímica observada em ambos os compostos heterocíclicos, quando isolados em matrizes sólidas inertes a baixa temperatura. Finalmente, são descritas algumas das técnicas teóricas e experimentais utilizadas.

No capítulo 2 são descritos os detalhes experimentais e computacionais dos estudos desenvolvidos durante este trabalho. Foram desenvolvidas e otimizadas metodologias sintéticas para a preparação de uma série de conjugados de tetrazole-benzisotiazolilo e avaliou-se o potencial de quelatação destes conjugados para uma gama de catiões divalentes. Os resultados revelaram claramente a capacidade destes conjugados para serem utilizados como ligandos multidentados em química de coordenação.

No capítulo 3 são apresentados e discutidos os resultados obtidos na sequência de uma detalhada investigação estrutural relativamente a preferências conformacionais e tautoméricas dos compostos, tanto na situação monomérica (molécula isolada) como na fase cristalina. A investigação estrutural na fase cristalina foi realizada com recurso a métodos espectroscópicos de infravermelho e Raman e cristalografia de raios-X. No caso dos monómeros, foi utilizada a técnica de isolamento em matriz de gás inerte a baixas temperaturas (~15 K), acoplada com espectroscopia de infravermelho. Esta técnica fornece diversas vantagens para a investigação, tanto estrutural como dos processos fotoquímicos, dos compostos no seu estado monomérico. As condições experimentais nas quais estas moléculas se encontram permitem a interpretação dos dados experimentais através de uma direta comparação com dados obtidos por métodos computacionais. As espécies tautoméricas preferidas pelos conjugados de tetrazole-benzisotiazolilo demonstraram ser especialmente determinadas pelo ambiente químico. Na fase cristalina, as redes resultantes de ligações por pontes de hidrogénio revelaram ser determinantes nas preferências estruturais dos conjugados. Por outro lado, na forma monomérica (molécula isolada em matrizes inertes) os conjugados demonstram existir preferencialmente na forma estrutural prevista por métodos computacionais como sendo a mais estável.

No capítulo 4 é apresentado e discutido o estudo fotoquímico de conjugados selecionados, em matrizes de árgon solidificado a baixas temperaturas. Quando se considera a aplicação dos conjugados tetrazole-benzisotiazolilo, a avaliação da sua estabilidade fotoquímica é sem dúvida

um aspeto relevante. Por outro lado, o conhecimento da reatividade característica destes conjugados é de grande importância para melhor compreensão da sua reatividade em campos cruciais da ciência e engenharia, como na medicina, em aplicações como materiais energéticos, na remediação ambiental ou na área de tecnologias de imagem. No decorrer destes estudos foram respondidas importantes questões mecanísticas sobre os efeitos do padrão de substituição dos anéis de tetrazoles di-substituídos, nas vias fotoquímicas.

No capítulo 5 são apresentados e discutidos resultados da investigação da estrutura e propriedades espectroscópicas de complexos de cobre (II), com os conjugados de tetrazole-benzisotiazolilo, bem como da avaliação da citotoxicidade dos complexos e dos ligandos correspondentes em diferentes linhas de células tumorais humanas (HepG2, HeLa, SH-SY5Y, U937 e THP1). Verificou-se que alguns dos ligandos testados atuam prontamente como quelantes seletivos de cobre (II), em relação ao ferro (II) e cálcio (II). Adicionalmente, estudos sobre a atividade citotóxica exibida por esses complexos de cobre (II) revelaram atividades para concentrações na gama micromolar baixa, em algumas das linhas de células tumorais (HepG2, HeLa e SH-SY5Y) o que, combinado com a seletividade observada desses ligandos para iões de cobre (II), pode oferecer perspetivas para novas metodologias e ferramentas para a terapia no tratamento de cancro.

No capítulo 6 é apresentada uma visão geral do trabalho desenvolvido durante este projeto de doutoramento, as conclusões finais e algumas perspetivas sobre o trabalho em desenvolvimento.

Palavras-chave: Benzisotiazole; Tetrazole; Quelantes; Análise estrutural; Fotoreatividade, Complexos baseados em metais de transição.

Publications

The work developed during this investigation project resulted in 8 publications in international scientific journals, from which the most recent (5 publications), resulted from research developed during the PhD period. By decision of the author, and in order to maintain the cohesion of the topics approached in this thesis, it was chosen not to include two of these publications (numbers **2**, and **7**).

Parts of this thesis have been adapted or excerpted from articles co-written by the author.

Publications issued from the project:

1 - Ismael, A.; Henriques, M. S. da C.; Marques, C. F. S.; Rodrigues, M. J.; Barreira, L. A.; Paixão, J. A.; Fausto, R.; Cristiano, M. L. S.; "Exploring saccharinate-tetrazoles as selective Cu (II) ligands: structure, magnetic properties and cytotoxicity of copper (II) complexes based on 5-(3-aminosaccharyl)-tetrazoles." *RSC Adv.* **2016**, 6 (75), 71628–71637.

2 - Frija, L. M. T.; Alegria, E. C. B. A.; Sutradhar, M.; Cristiano, M. L. S.; Ismael, A.; Kopylovich, M. N.; Pombeiro, A. J. L.; "Copper(II) and cobalt(II) tetrazole-saccharinate complexes as effective catalysts for oxidation of secondary alcohols." *J. Mol. Catal. A Chem.* **2016**, *425*, 283–290.

3 - Ismael, A.; Fausto, R.; Cristiano, M. L. S.; "Photochemistry of 1- and 2-Methyl-5-aminotetrazoles: Structural Effects on Reaction Pathways."; *J. Org. Chem.* **2016**, *81* (23), 11656–11663.

4 - Ismael, A.; Borba, A.; Henriques, M. S. C.; Paixão, J. A.; Fausto, R.; Cristiano, M. L. S.; "Structure and Photochemistry of a Saccharyl Thiotetrazole." *J. Org. Chem*. **2015**, 80(1); 392-400.

5 - Ismael, A.; Gómez-Zavaglia, A.; Borba, A.; Cristiano, M. de L. S.; Fausto, R.; "Amino→Imino Tautomerization upon *in Vacuo* Sublimation of 2-Methyltetrazole-Saccharinate as Probed by Matrix Isolation Infrared Spectroscopy." *J. Phys. Chem. A* **2013**, 117 (15); 3190-3197.

6 - Ismael, A.; Paixão, J. A.; Fausto, R.; Cristiano, M. L. S.; "Molecular structure of nitrogen-linked methyltetrazole-saccharinates."; *J. Mol. Struct*. **2012**, 1023; 128-142.

7 - Ismael, A.; Borba, A.; Duarte, L.; Giuliano, B. M.; Gómez-Zavaglia, A.; Cristiano, M. L. S.; "Structure and photochemistry of a novel tetrazole-saccharyl conjugate isolated in solid árgon."; *J. Mol. Struct.* **2012**, *1025*, 105-116.

8 - Gómez-Zavaglia, A.; Ismael, A.; Cabral, L. I. L.; Kaczor, A.; Paixão, J. A.; Fausto, R.; Cristiano, M. L. S.; "Structural investigation of nitrogen-linked saccharinate-tetrazole." *J. Mol. Struct*. **2011**; 1003; 103-110.

Other Publications:

9 - Ismael, A.; Gago, D. J. P.; Cabral, L. I. L.; Fausto, R.; Cristiano, M. L. S.; "Investigations into the Mechanism of Solvolysis of 3-aryloxybenzisothiazoles."; *Croat. Chem. Acta* **2014**, *87* (4), 363-373.

10 - Ismael, A.; Serpa, C.; Cristiano, M. L. S; "Photochemistry of 1-allyl-4-aryltetrazolones in solution; structural effects on photoproduct selectivity"; *Photochem. Photobiol. Sci.* **2012**, 12, 272–283.

11 - Frija, L. M. T.; Reva, I.; Ismael, A.; Coelho, D. V; Fausto, R.; Cristiano, M. L. S.; "Sigmatropic rearrangements in 5-allyloxytetrazoles."; *Org. Biomol. Chem.* **2011**, *9* (17), 6040-6054.

12 - Frija, L. M. T.; Ismael, A.; Cristiano, M. L. S.; "Photochemical Transformations of Tetrazole Derivatives: Applications in Organic Synthesis"; *Molecules* **2010**, *15* (5), 3757–3774.

13 - Ismael, A.; Cristiano, M. L. S.; Fausto, R.; Gómez-Zavaglia, A.; "Tautomer Selective Photochemistry in 1-(Tetrazol-5-yl)ethanol."; *J. Phys. Chem. A* **2010**, *114* (50), 13076-13085.

14 - Almeida, R.; Gómez-Zavaglia, A.; Kaczor, A.; Ismael, A.; Cristiano, M. L. S.; Fausto, R.; "Matrix-isolation FTIR, theoretical structural analysis and reactivity of amino-saccharins: *N*-(1,1-dioxo-1,2-benzisothiazol-3-yl)-*N*-methyl amine and -*N*,*N*-dimethyl amine."; *J. Mol. Struct.* **2009**, *938* (1–3), 198–206.

Table of Contents

General organization of the thesis

The work described in this thesis is mostly related with the structure and reactivity of novel molecules incorporating derivatives of two important classes of heterocyclic compounds: tetrazoles and benzisothiazoles, linked by a spacer group, and investigation on their ability to be used as multidentate nitrogen ligands for coordination with transition metals.

This PhD thesis includes six chapters.

Chapter 1 presents the description of the most important applications of tetrazoles and benzisothiazoles, which were somehow relevant for the present work. One of the important concerns during design of these novel conjugates, was the ability to easily introduce chemical diversity through different spacer-groups and substituents on the tetrazolyl ring. In order to show that ability, a general overview of the relevant published data on the synthesis of several substituted tetrazoles and functionalization of 5-substituted tetrazoles is presented. Additionally, the observed photoreactivity of both heterocycles, isolated on solid matrices is disclosed. Finally, some of the theoretical and experimental techniques used is also described.

Chapter 2 provides the experimental and computational details developed during this work. Synthetic methodologies were devised and optimized for the preparation of a series of tetrazole-saccharyl conjugates, and their ability to be used as multidentate nitrogen ligands for coordination with a range of divalent cations was investigated. The results clearly reveal the ability of these conjugates to be used as multidentate ligands in coordination chemistry.

In chapter 3, the work performed in order to obtain a deep understanding of the conformational and tautomeric preferences of the compounds in both the isolated molecule situation and in crystalline phase is presented. The structural investigation of these systems is instrumental for predicting and exploring their properties and functions.

Chapter 4 describes the photochemical studies of selected ligands isolated in solid argon. When considering applications of tetrazole-saccharyl conjugates, the assessment of their photochemical stability may be a relevant aspect. On the other hand, the knowledge of the characteristic reactivity of these tetrazole-saccharyl conjugates is of considerable value for a better understanding of their opportunities in crucial fields of science and engineering, such as medicine, energetic materials, environmental remediation and imaging technology. In the course of these studies, important mechanistic questions regarding the effects of the ring substitution pattern on the photochemical pathways of disubstituted tetrazoles were answered.

Chapter 5 reports the studies undertaken to prepare and characterize structurally and spectroscopically novel copper (II) complexes based on tetrazole-saccharinates, as well as the work aiming to evaluate their *in vitro* cytotoxicity. It was found that some of the nitrogen-linked conjugates tested act readily as selective copper (II) chelators. Moreover, studies on cytotoxic activity exhibited by those copper (II) complexes against different tumoral cells revealed their activity in the low micromolar values which, combined with the observed selectivity of the new ligands to copper ions, may offer perspectives for new leads in cancer chemotherapy.

Finally, chapter 6 presents an overview of the work developed during this PhD project, the final conclusions, and some perspectives about the ongoing work.

As a final note, it should be mentioned that the investigated conjugates have shown potential applications in catalysis and quite interesting luminescence properties. Although not included in these thesis, copper (II) and cobalt (II) tetrazole-saccharinate complexes were used as effective catalysts for oxidation of diverse secondary alcohols. The results were recently published in *J. Mol. Catal. A Chem.* 2016, 425, 283–290.

Chapter 1. Introduction

1.1. Tetrazoles

1.1.1. Tetrazoles - general information on properties, synthesis and applications

The chemistry of tetrazole and its derivatives has been under scrutiny for many decades and remains a topic of intense research. The perennial interest in this class of compounds is largely due to their potential and important applications in major areas. Tetrazoles find applications in medicine,[1,2] in gas-generating compositions,[3,4] in high energy materials,[5–7] in coordination chemistry,[8–11] in agriculture[12,13] and in imaging technology.[14–17]

In the recent years, relevant results were obtained in the design of new drug candidates containing the tetrazole moiety, aimed to be used as antibacterial,[18] antiallergic,[19,20] analgesic,[21,22] antihypertensive[23–26] or anti-inflammatory[27] agents. Also, tetrazole derivatives have been successfully used in several organic and bioorganic synthetic strategies, as reagents and catalysts.[28–45] Decomposition of the tetrazole ring results in the liberation of molecular nitrogen and a significant amount of energy.[46,47] Therefore, several tetrazole derivatives have been explored as propellant components for missiles[5–7] and as gas-generating compositions.[3,4] Furthermore tetrazole-based compounds exhibit good coordination properties and are able to form stable complexes with several metal ions.[9,10] This ability is successfully used in analytical chemistry, for the removal of heavy metal ions from liquids, and in chemical systems formulated for metal protection against corrosion.[48,49] In addition, tetrazoles play an important role in agriculture, as plant growth regulators,[13] herbicides and fungicides,[12] in imaging technology, as biosensors for medical imaging[14,15] and as stabilizers in photography and in photoimaging.[16]

Besides all these important applications, tetrazoles are also interesting molecules from a structural point of view. In fact, the wide application of tetrazoles became possible due to the constantly increasing research efforts devoted to the knowledge of structural and physicochemical properties of this heteroaromatic system and to the development of new and improved synthetic methods for the preparation of functionally substituted tetrazoles.

In nature, the tetrazole fragment is virtually absent, although its presence was reported in metabolic products of some protozoa.[50] The unsubstituted tetrazole (CN_4H_2) contains the maximum number of nitrogen atoms, among the stable unsubstituted heterocyclic systems, which is the reason why tetrazoles exhibit the extreme values of acidity, basicity, and complex formation constants.[51] Hydrogen atoms directly bound to the tetrazole ring are labile and may give rise to 1*H*- and 2*H*- tautomers (Figure 1.1, **1** and **2**, respectively), with their relative

populations depending on the chemical environment. Many physical, chemical and biological properties of unsubstituted tetrazoles are related to their ability to act as acids and bases, and also the possibility of prototropic annular tautomerism.[51–53]

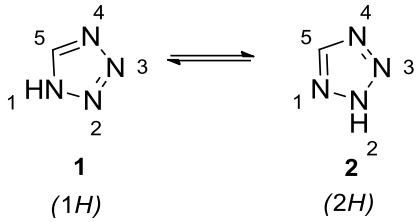

Figure 1.1 - 1*H*- and 2*H*- tautomers of tetrazole.

Unsubstituted tetrazole, was found to exist exclusively as the *1H*-tautomer in the crystalline phase,[54,55] whereas in solution and gas phase 1*H*- and 2*H*-tautomers coexist, with the population of the most polar 1*H*- form increasing with the polarity of the solvent.[56–61] According to the experimental findings, 2*H*-tetrazole was found to be the lowest energy tautomer in media with a dielectric constant smaller than about 7, while in media with a larger dielectric constant, a reversal of energy takes place and 1*H*-tetrazole becomes the tautomeric ground state.[62,63] The infrared spectrum of tetrazole (CN_4H_2) isolated in solid argon (T = 10 K) was investigated, showing essentially the expected signature of the 2*H*-tetrazole tautomer. The amount of the *1H*-tautomer in the matrix was found to be *ca.* 10% of the most abundant form.[56] This study has solved a long-term controversy regarding the existence of the 1*H*-tautomer of tetrazole in the gas phase.[59,64,65] In the case of substituted tetrazoles, tautomerism may also involve substituent groups, as was found in the case of 1-methyl-tetrazol-5-thione and 2-methyl-tetrazol-5-amine.[66,67]

1.1.2. Tetrazoles as bioisosteres

Bioisosteres are substituents or groups that impart similar biological properties to a chemical compound; for example, the bioisosteric replacement of a hydrogen atom with a fluorine atom within a drug molecule will generally have no influence on the drug's efficacy, but it may prolong the drug's half-life by inhibiting metabolic oxidation. Thus, the purpose of exchanging one bioisostere for another is to fine tune the pharmacokinetic or pharmacodynamic properties of a bioactive compound. Although the chemical and physical basis of equivalence for most classical bioisosteric substitutions is obvious (*e.g.*, hydrogen to fluorine, ester to amide, phenyl to thiophene), there are many nonclassical bioisosteric substitutions for which the physicochemical similarities between the two bioisosteres are not readily apparent.[68]

It has been long held that 5-substituted-tetrazoles **4** and **5** may serve as non-classical isosteres for the carboxylic acid moiety **3** in biologically active molecules.[50,69–72] Hence, tetrazoles have received a particular interest from medicinal chemists and they probably constitute the most commonly used bioisosteres of the carboxylic acid moiety.[1] 5-Substituted tetrazoles are also frequently referred to as tetrazolic acids, and can exist as 1*H*- and 2*H*-tautomeric forms (Figure 1.2, **4** and **5**, respectively).

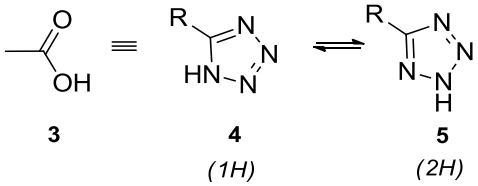

Figure 1.2 – Tetrazolic acids are bioisosteres of carboxylic acids.

In general, 5-substituted tetrazoles are relatively strong N–H acids due to the ability of the tetrazolyl moiety to stabilize a negative charge by electron delocalization, and are strongly influenced by the effect of substituents at the *C*5-position.[1,50] Like carboxylic acids **3**, tetrazoles are ionized at physiological pH and exhibit a planar structure. However, anionic tetrazoles are almost 10 times more lipophilic than the corresponding carboxylates while having similar acidity (pKa 4.5–4.9 *vs.* 4.2-4.4 respectively).[45,50,73] The increase in lipophilicity could account for the higher membrane permeability seen with tetrazole bioisosteres. This fact is an important factor for the pharmacokinetics of the tetrazole analogues of carboxylic acids. From the point of view of the pharmacodynamics, the effect of the replacement of a carboxylic acid by a 5-subtituted tetrazoles is more complex. The delocalization of the negative charge in the tetrazole ring can either enhance or reduce the interaction with an appropriate receptor, depending on the electron distribution in the receptor site.[74] The size of the tetrazole ring might decrease the affinity towards the receptor site relative to a carboxylate group as a result either of steric hindrance or of an inconvenient orientation of the functional groups of the active site.[75] The main advantage of 5-substuituted tetrazoles is their resistance to many biological metabolic degradation pathways. One of the first *in vivo* studies found that the tetrazole analogue of nicotinic acid was excreted unchanged, whereas nicotinic acid itself was quickly metabolized.[76] It is often seen that the resistance of tetrazolic drug substances to metabolism may result in a longer duration of action *versus* carboxylic acid analogues.[76,77] In fact, the tetrazole ring features as a fragment in a number of modern drugs with antibacterial, antiallergic, antihypertensive and anti-inflammatory activity,[18,23,24] and tetrazole derivatives are also used as anticonvulsants[78] and in cancer and AIDS treatments.[79,80]

The most important group of biologically active compounds based on 5-substituted tetrazoles are the selective antagonists of the receptor for angiotensin II. The first representative, Losartan **6** (Figure 1.3), has been in clinical use since 1994. Losartan is a good example of a drug in which the optimal ratio of antihypertensive activity and bioavailability was achieved. Carboxylic acid analogues of this drug, **7** and **8**, also have antihypertensive properties but are less active, even when they are administered intravenously. Other bioisosteric replacements of carboxylic acid were examined during the development of this drug, but none had better properties than the tetrazole derivatives.[81]

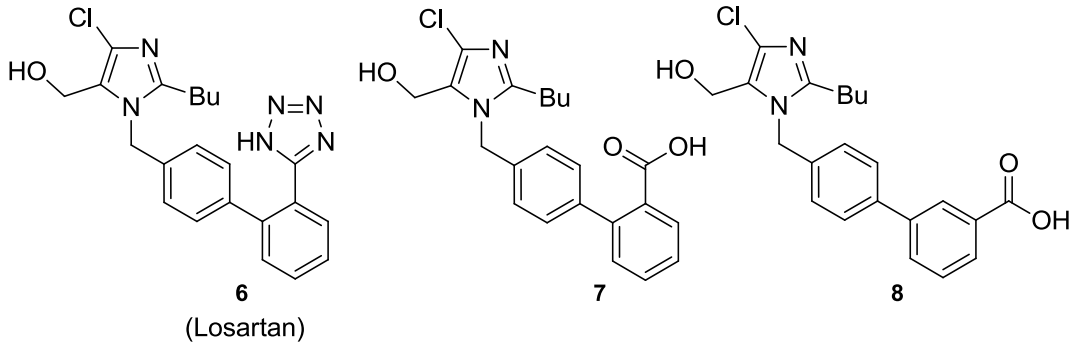

Figure 1.3 – Structures of Losartan and of 2- and 3-carboxybiphenyl analogues.

Other important compounds in which the 5-substituted tetrazole moiety plays a notable role are in leukotriene receptor antagonists.[82] Compound LY171883, later known as the drug Tomelukast **9** (Figure 1.4), is one example.[83] The replacement of a carboxylic acid group by a 5-substituted tetrazole moiety led to an increase in the *in vitro* activity by approximately thirty times, probably due to a better interaction between the delocalized negative charge on the tetrazole ring and the arginine residue in the active site of the cysLT$_1$ receptor for Leukotriene D4 (LTD$_4$).[84] In addition, *in vivo* activity after oral administration was increased, due to the higher lipophilicity of the tetrazole analogue.

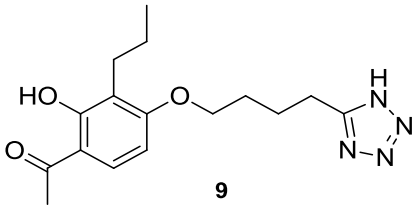

Figure 1.4 – Structure of Tomelukast.

Since the introduction of Losartan **6** into the clinic, a huge number of papers have been published related to potential analogues of this compound, as well as a variety of other tetrazolic acid structures, proposed for other clinical uses.[85,86] However, it is difficult to accurately predict

the pharmacodynamic response to the replacement of a carboxylic acid group by a 5-substituted tetrazole moiety. Various examples from the literature show that the pharmacodynamic effect can increase, decrease, or completely disappear.[1]

1.1.3. Synthesis of tetrazoles

The compounds derived from tetrazole can be classified into 1-, 2-, and 5-monosubstituted tetrazoles, 1,5- and 2,5-disubstituted tetrazoles, and trisubstituted tetrazolium salts. Other important tetrazole derivatives include 1,4-disubstituted: 1*H*-tetrazol-5(4*H*)-ones, 1*H*-tetrazol-5(4*H*)-thiones, or 1*H*-tetrazol-5(4*H*)-imines. Various methodologies for preparing compounds with a tetrazole ring system have been developed, mostly for the preparation of 5-substituted tetrazoles, whereas syntheses of 1- and 2-substituted derivatives were studied to a considerably lesser extent. However, in the most recent years these syntheses have received more attention due the increasing applications of 1- and 2-substituted tetrazoles in medicine[87] and in other relevant fields.[88] Nonetheless, 5-substituted tetrazoles remain the most common compounds containing tetrazole moieties, mainly due to the important applications found in medicinal chemistry. The first part of this sub-section briefly outlines strategies for the syntheses of 1- and 2-substituted tetrazoles. Among a variety of methods for the preparation of 1,5- and 2,5-disubstituted tetrazoles,[50,71,89–91] only those involving functionalization of 5-substituted tetrazoles, including alkylation, arylation, and vinylation, will be addressed in this thesis.

1.1.3.1. Preparation of 1-substituted tetrazoles

One of the most known methods of synthesis of 1-substituted tetrazoles **12** involves [2+3]-cycloaddition of isocyanides **10** with hydrazoic acid **11** (Scheme 1.1).[92,93] However, until recently the use of this procedure was restricted, obviously due to inconvenience in handling isocyanides and hydrazoic acid. The method was substantially improved via replacement of hydrazoic acid by a more effective and convenient reagent, trimethylsilyl azide **13** ($TMSN_3$).[94] Various isocyanides were reported to react with $TMSN_3$ in methanol, in the presence of a catalytic amount of hydrochloric acid, to afford 1-substituted tetrazoles **12** (Scheme 1.2) in good to excellent yields (58–92%).

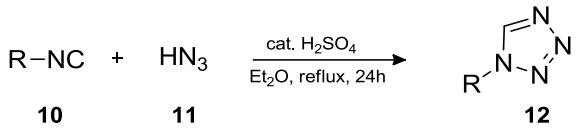

Scheme 1.1 – Representation of the synthesis of 1-substituted tetrazoles from [2+3] cycloaddition of isocyanides with hydrazoic acid, according to the methodology developed by Fallon and Herberst.[102]

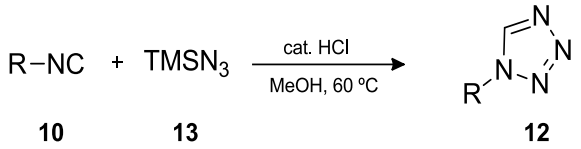

Scheme 1.2 – Representation of the synthesis of 1-substituted tetrazoles from [2+3] cycloaddition of isocyanides with, $TMSN_3$, according to the methodology developed by Jin and co-workers.[94]

One reaction frequently used for the synthesis of 1-substituted tetrazoles is alkylation or arylation of unsubstituted tetrazole.[45] The main disadvantage of this method is that mixtures of isomeric 1- and 2-substituted derivatives are always formed; in many cases, separation of the isomeric products involves strong experimental difficulties.

1.1.3.2. Preparation of 2-substituted tetrazoles

2-Substituted tetrazoles are usually synthesized by alkylation (or arylation) of unsubstituted tetrazole.[45,90] However, the reaction is characterized by low selectivity and poor yield of the alkylation products. Nonetheless, 2-substituted tetrazoles **14** were obtained as the only products when propan-2-ol, 2-methylpropan-2-ol, cyclohexanol, propene, or 2-methylpropene were used as alkylating agents in the presence of 96% sulfuric acid (Scheme 1.3).[95]

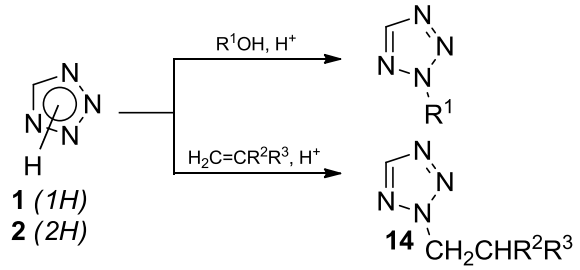

R^1 = *i*-Pr,*t*-Bu, cyclohexyl; R^2 = H; R^3 = Me; R^2 = R^3 = Me

Scheme 1.3 - Preparation of 2-Substituted tetrazoles by alkylation of unsubstituted tetrazole, according to the methodology developed by Koldobskii and co-workers.[95]

1.1.3.3. Preparation of 5-substituted tetrazoles

The first specific and widely used methods for the synthesis of 5-substituted tetrazoles consisted of the diazotization of polynitrogen compounds, especially hydrazidines (imidohydrazides) such as **15** (Scheme 1.4), which are prepared primarily from reaction of iminoethers (imidates) with hydrazine. It is generally assumed that the mechanism of this synthesis involves the preliminary formation of an imido-azide **16** which subsequently cyclizes to the target 5-substituted tetrazole **17**.[96]

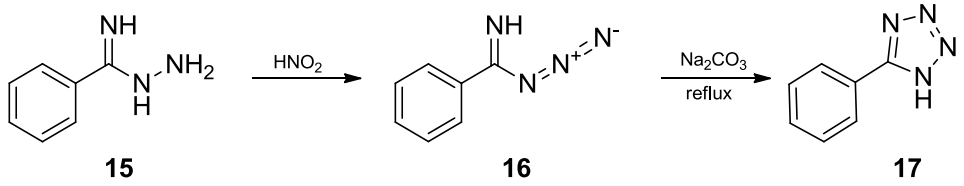

Scheme 1.4 – Representation of the synthesis of 5-phenyl-tetrazole from benzimido-hydrazide.[96]

The currently favoured approach to the synthesis of 5-substituted tetrazoles lies in the interaction of nitrile moieties with azide groups. A reaction of this type was successfully accomplished for the first time in 1901, when 5-amino-tetrazole was prepared from cyanamide and hydrazoic acid.[97] This process is generally thought to occur by a concerted 1,3-dipolar cycloaddition mechanism (Scheme 1.5), in which nitrile **18** acts as the dipolarophile, while the hydrogen bonded complex of the amine with hydrazoic acid serves as the 1,3-dipole.[91] Cycloaddition through **19** leads to the tautomeric tetrazolium anions **20** and **21**, which can simply be drawn as the delocalized resonance form **22**. Protonation of **22** upon workup provides the tetrazolic acid **4**.

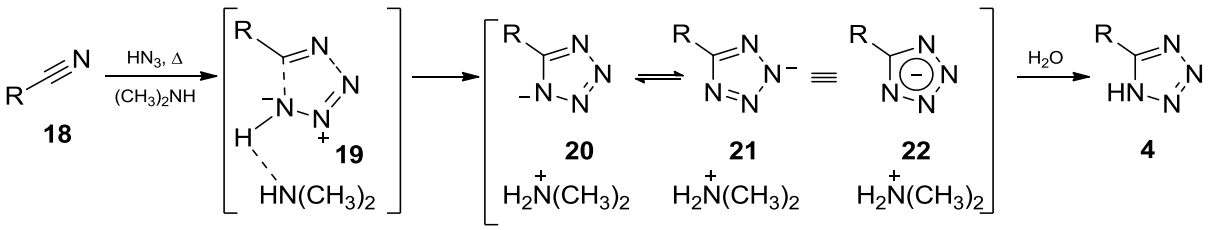

Scheme 1.5 – Representation of the synthesis of 5-susbtituted tetrazoles from a concerted 1,3-dipolar cycloaddition mechanism of substituted nitriles and hydrazoic acid.[91]

The parent 1*H*-tetrazole was synthesized in 1910 by a similar synthetic approach, which involved the cycloaddition of hydrazoic acid to hydrogen cyanide.[98] A great disadvantage of this procedure is that hydrazoic acid in organic solution is toxic and extremely explosive. Also,

not many organic solvents are stable at the high temperatures required for this cycloaddition (sometimes as high as 130 ºC), and for this reason *N*,*N*-dimethylformamide (DMF) is most commonly used for this purpose.[50,71,91] Nevertheless, hydrazoic acid, prepared either in advance or *in situ*, was used as a major reactant for the preparation of 5-substituted tetrazoles until the end of the 1950s.[96,99]

In 1958, Finnegan *et al.* published their fundamental work on the synthesis of 5-substituted tetrazoles using sodium azide and ammonium chloride in dimethylformamide (DMF) (Scheme 1.6).[100]

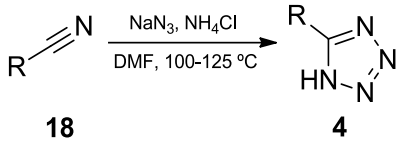

Scheme 1.6 – Representation of the Finnegan's method for the preparation of 5-substituted tetrazoles.[100]

Although hydrazoic acid could also be detected in the reaction mixture, Finnegan's method changed substantially the synthetic approaches to 5-substituted tetrazoles. A number of other amine salts were investigated, leading the researchers to conclude that reaction temperatures lower than 130 ºC, at atmospheric pressure, could be achieved when hydrazoic acid was generated from an ammonium azide. This 'gentle' acidic media (proton catalysed) procedure was more efficient than the older methods in which hydrazoic acid was used directly, where high-pressure equipment and/or heating from four to seven days were commonly required conditions to reach completion of the reaction.[100] Since then, the processes have become much safer, the reaction times have been significantly reduced, and the yields of 5-substituted tetrazoles have increased.[101]

With regard to the preferred mechanism of the reactions in acidic media (proton-catalyzed), three hypotheses have been discussed: 1) two-step [2+3] cycloaddition, 2) concerted dipolar [2+3] cycloaddition, and 3) activation of the nitrile by protons via an intermediate imidoyl azide.

Although Finnegan's group formulated the role of the acid catalyst in the preparation of 5-substituted tetrazoles, they proposed that the determining step of the reaction is the attack of the azide anion on the nitrile carbon, followed by ring closure in a two-step mechanism.[100] This was confirmed by Jursic and Zdravkovski in 1994,[102] in which a two-step [2+3] cycloaddition, involving nucleophilic attack of the azide ion **23** on the carbon of the nitrile group **18**, followed by tetrazole ring closure, was shown to be the preferred mechanism (Scheme 1.7). However,

intermediates **24** could be found only in the cases of nitriles with very strongly electron-withdrawing groups, such as F or CH_3SO_2.

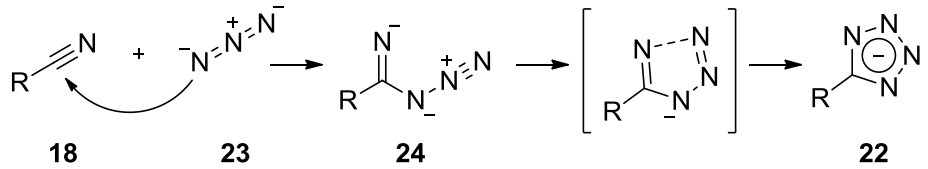

Scheme 1.7 – Representation of the mechanism of formation of 5-substituted tetrazoles through a two-step [2+3] cycloaddition of azide anion and substituted nitrile.[102]

On the other hand, data supporting the concerted dipolar [2+3] cycloaddition were presented by scientists from the St. Petersburg Technological Institute.[103,104] The authors suggest that hydrazoic acid (HN_3) and organic azides **25a** act as typical 1,3-dipoles in a dipolar cycloaddition reaction **26** (Scheme 1.8). Experimentally, the 1,5-disubstituted tetrazoles were exclusively formed.[103,104]

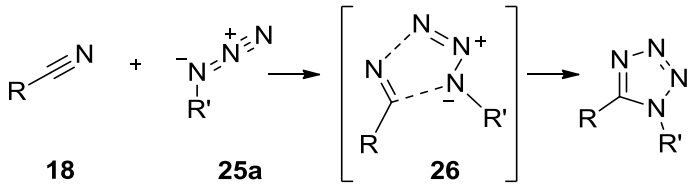

Scheme 1.8 – Representation of the mechanism of formation of 1,5-disubstituted tetrazoles through concerted dipolar [2+3] cycloadditions.[104]

In 2001, Demko and Sharpless have shown that organic azides **25a** react at elevated temperatures only with highly reactive nitriles **18**, through concerted dipolar [2+3] cycloadditions, whereas ammonium azides **25b** react readily with a wide range of nitriles under the same conditions.[105] Although the electronic structures of organic azides and ammonium azides are very similar, their reactivities are significantly different, suggesting different mechanisms of formation of 5-substituted tetrazoles. Actually, in 2002 it was confirmed that the preparation of a 5-substituted tetrazoles in an acidic medium proceeds preferentially through an imidoyl azide intermediate such as **24** (Scheme 1.9), which spontaneously cyclizes to the 5-substituted tetrazole **4** under the reaction conditions.[106] Protonation of the nitrile increases its reactivity and susceptibility to attack by azide anions **27**. The transition states associated to this process, **27**, have a significantly lower energy than those resulting from concerted or anionic two-step [2+3] cycloadditions.

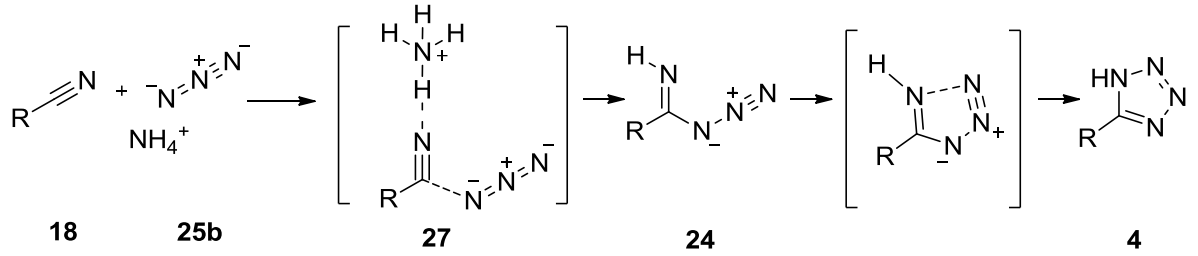

Scheme 1.9 – Representation of the mechanism of formation of 5-substituted tetrazoles *via* imidoyl azide intermediates **27**.[106]

Methods using acidic media are widely used, both in laboratory and industrial scales. The main drawbacks are the presence of the highly toxic and explosive hydrazoic acid in the reaction media and the use of the thermally unstable (generated *in situ*) ammonium azides, which readily sublimate from the reaction mixtures.

At the end of 2001 Demko and Sharpless published one of the most notable contemporary advances in tetrazolic acid synthesis, describing a method for the assembly of tetrazoles from nitriles, in water (Scheme 1.10).[107] They found that various nitriles smoothly react with sodium azide in water in the presence of Lewis acids, *e.g.*, $ZnCl_2$ or $ZnBr_2$. Under these conditions, 5-substituted tetrazoles are successfully formed from functionally substituted, heterocyclic and aromatic nitriles. The principle of this method for the preparation of 5-substituted tetrazoles is close to the previous one, because Lewis acids also coordinate nitriles and activate them towards attack by the azide anion, like in **27** (Scheme 1.9). The main disadvantage of all the reactions mentioned above lies in their water sensitivity. They should therefore be carried out under inert atmosphere. For this reason Shapless and Demko's work was a major breakthrough in this field. With electron poor aromatic nitriles the reaction reaches completion at reflux after a few days. However, when using electron-rich aromatic species and unactivated aliphatic nitriles the reaction requires higher temperatures and the use of a sealed glass pressure reactor. Nevertheless, this protocol minimizes the risk of liberating hydrazoic acid, and usually a simple acidification is all that is necessary to provide the pure tetrazole products.

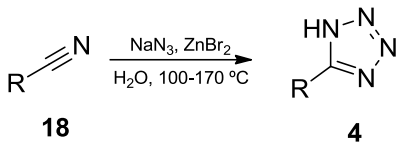

Scheme 1.10 – Representation of the Sharpless's method for preparation of 5-substituted tetrazoles.[107]

The general disadvantage in preparations of 5-substituted tetrazoles is long reaction times. In 2009, a series of 5-aryl-1*H*-tetrazoles was prepared using the Sharpless's methodology but in solvent free conditions. As a result of this modification, the reaction times were shortened, but larger amounts of sodium azide and zinc salts were used than in the original procedure.[108] Recently, a number of 5-substituted tetrazoles were synthesizes using microwave irradiation, and in many cases resulted in decreased reaction times, increased yields and/or improved selectivity of reactions.[109–112]

Since Finnegan's invention, several new methods and modifications of existing processes have appeared, using different Lewis acids, organometallic and organosilicon azides. Yet, the fundamental of all of these methods remains the reaction between nitrile and an azide moiety.

1.1.4. Functionalization of 5-substituted tetrazoles

Among tetrazolyl derivatives, 5-substituted tetrazoles assume a relevant role in synthesis, as they often act as valuable intermediate compounds or building blocks in the synthesis of several chemotypes. During these reactions, the tetrazole ring can be preserved, transformed into other cycles, or even completely eliminated. For instance, 5-substituted tetrazoles are commonly used as starting materials for the preparation of 1,5- and 2,5-disubstituted tetrazoles.[89,90]

The available methods for the synthesis of 1,5-disubstituted tetrazoles, reviewed recently,[89] include the use of nitriles, amides, thioamides, imidoyl chlorides, heterocumulenes, isocyanates, isothiocyanates, carbodiimides, ketenimines, ketones, amines, and alkenes as the starting materials. However, until very recently, the only known method for the preparation of 2,5-disubstituted tetrazoles was by functionalization of the corresponding 5-substituted tetrazoles.[113–117] In 2015, a new method for the synthesis of 2,5-disubstituted tetrazole from the reaction of aryldiazonium salts **28** with amidines **29**, followed by oxidative ring closure, was published (Scheme 1.11).[118]

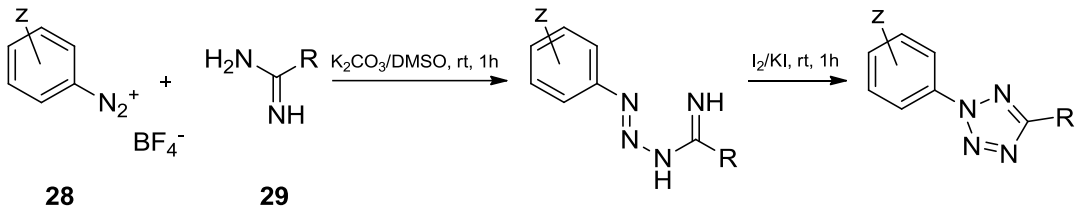

Scheme 1.11 – Representation of the synthesis of 2,5-disubstituted tetrazoles from aryldiazonium salts with amidines, according to the methodology developed by Ramanathan and co-workers.[118]

As a result of their π electron systems and also the presence of a lone pair on all nitrogen atoms of the heterocyclic system, tetrazoles react easily with a wide range of electrophiles. Reactions between 5-substituted tetrazoles and electrophiles have been widely investigated, with special attention paid to the underlying mechanisms. Functionalization of 5-substituted tetrazoles are usually carried out in aqueous or alcoholic alkaline solutions, in aprotic organic solutions in the presence of a base, or under phase-transfer catalysis conditions. Depending on the reaction conditions, 5-substituted tetrazoles can act as free tetrazolate anions, ion pairs, or hydrogen-bonded complexes with nitrogen bases.[45] The main problem with functionalization of 5-substituted tetrazoles lies in its low regioselectivity. Alkylation of 5-substituted tetrazoles often leads to a mixture of the 1,5- and 2,5-disubstituted tetrazoles regioisomers (Scheme 1.12, **31** and **32** respectively). Other functionalizations, such as arylation and acylation, proceed in the same manner.[89,90,95]

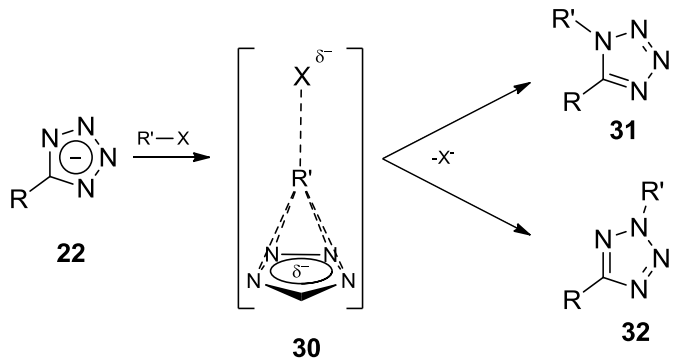

Scheme 1.12 – Representation of the bimolecular mechanism proposed for the reaction between a tetrazolate anion and an alkyl halide.

The ratio of isomers formed during the reaction depends on the reaction temperature and the properties of the substituent at the 5-position, in particular with regard to steric hindrance. Higher reaction temperatures lead to increased amounts of 1,5-isomers, whereas electron-

withdrawing properties of substituents at the 5-position increase the amounts of 2,5-isomers. Bulky substituents (either R or R' or their combination) direct the functionalization to the position 2 of the tetrazole ring. The mechanism of these reactions involves a bimolecular process leading to the formation of an unstable intermediate of type **30** in the first (rate-limiting) step. In the second step, isomeric products are formed. The reaction rate is influenced by the properties of substituent R, by the reactivity of the electrophile, R'-X, and by the reaction medium. Formation of the isomeric products is controlled by the properties of the reaction intermediate **30**.[45]

As previously mentioned, 2*H*-tautomers are thought to be more stable than 1*H*-tautomers. It was shown that 2*H*-tetrazole is more stable than 1*H*-tetrazole by *ca.* 6.95 kJ mol^{-1} in the gaseous phase, corresponding to a relative population of 10 : 1 at T = 363.15 K.[56] In the crystalline state, however, the majority of 5-substituted tetrazoles exist in the 1*H*-form, stabilized by hydrogen bonds to the neighbouring molecules, which results in the formation of dimers and larger agglomerates.[54,55] In media of high dielectric constant, 1*H*-tautomers are preferred due to their higher polarities.[62,63] A ^{15}N-NMR study of tetrazole in dimethyl sulfoxide (DMSO) revealed that 90–99% of the tetrazole exists in the 1*H*-form.[119] Nevertheless, there are several situations in which the relative proportion of 2*H*-tautomers strongly increases. This is seen especially in solvents with lower polarities, in which the less polar 2*H*-form is better solvated and both the 1*H*- and 2*H*-forms are predicted to exist in comparable amounts. Additionally, the presence of an electron-withdrawing substituent at the 5-position increases the polarity of the 2*H*-tautomer and also the relative proportion of the 2*H*-form in polar solvents. The presence of a bulky substituent on the tetrazole carbon can also increase the relative proportion of the 2*H*-form.[51]

Various reports on the alkylation of 5-substituted tetrazoles, disclosed in recent years, indicate that the treatment of 5-substituted tetrazoles with alkyl halides in the presence of a base provides the corresponding 1,5- and 2,5-disubtituted tetrazole derivatives as mixtures in which the 2,5-isomers are the major products.[50,95,101] Moreover, the alkylation of 5-substituted tetrazoles under microwave irradiation conditions proved to be successful. Significant advantages of this method are shorter reaction times and higher yields in comparison with conventional heating conditions.[120,121]

In conclusion, several approaches to the preparation of 5-substituted tetrazoles are described in the literature and the number is still increasing because this chemotype is relevant for many applications in various fields of science, for instance in medicinal chemistry, where the tetrazole moiety features as a metabolically stable surrogate for the carboxylic acid group.

The main problem with further functionalization of 5-substituted tetrazoles lies in the poor regioselectivity of this process. The search for highly regioselective procedures resulting in the formation of only one isomer, either a 1,5- or 2,5-disubstituted tetrazole, is therefore currently an intensely investigated research topic. This is especially true for 2,5-disubstituted tetrazoles, which can be prepared almost solely by these methods.

1.1.5. 5-Substituted tetrazoles as ligands in coordination chemistry

Tetrazoles have attracted increasing attention in recent years in coordination chemistry due to the excellent coordination ability of the four nitrogen atoms of the tetrazole group, which can act as either a multidentate or a bridging building block in supramolecular assemblies. The tetrazole unit exhibits 10 different coordination modes (Figure 1.5). Thus, neutral tetrazole (*Modes* I-IV) may function both as a dinucleating ligand ($\mu_{2,3}$-, $\mu_{2,4}$- and $\mu_{3,4}$- binding modes) and a trinucleating ligand ($\mu_{2,3,4}$-binding modes), whereas deprotonated tetrazolate (*Modes* V-X) can bridge two, three and up to four metal ions (dinucleating $\mu_{1,2}$-, $\mu_{2,3}$- and $\mu_{1,3}$-, trinucleating $\mu_{1,2,3}$- and $\mu_{1,2,4}$- and tetranucleating $\mu_{1,2,3,4}$- binding modes).

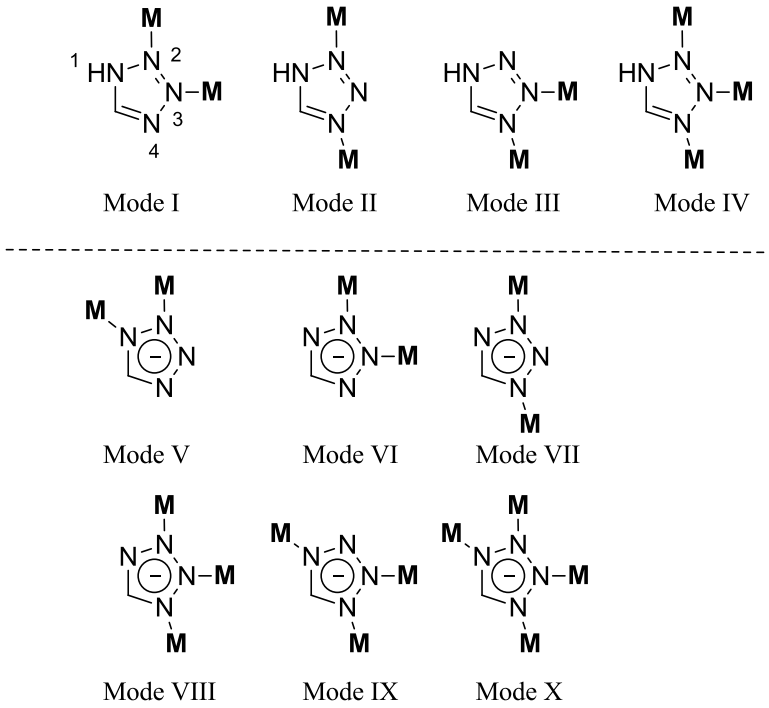

Figure 1.5 – Representation of the bridging coordination modes of neutral tetrazole (*Modes* I-IV) and of deprotonated tetrazolate (*Modes* V-X).

The metal ion (**M**) in metal-tetrazole derivatives can be bound to the heterocycle by a covalent, ionic or coordination bond. Due to the availability and good prospects for practical uses, derivatives of types **33-35** are the most studied (Figure 1.6).[122]

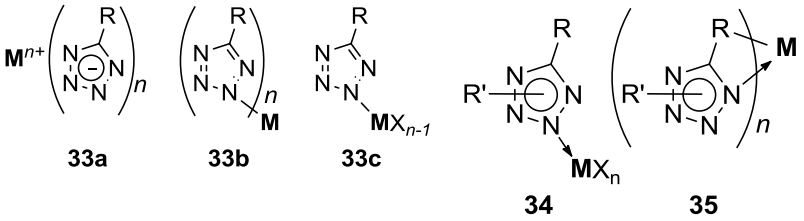

Figure 1.6 – Representation of common metal-tetrazole derivatives. X is an inorganic or organic ligand.

Compounds **33** are formed upon deprotonation of 5-substituted tetrazoles. In the case of alkali and alkaline earth metals, their nature is mainly ionic (**33a**), but for other metals a bond with some covalent character may be formed (type **33b**, or **33c** for mixed-ligand complexes). Compounds **34** are *N*-complexes in which neutral, mono- and disubstituted tetrazoles are present as ligands. A separate type of metal tetrazole derivatives is represented by chelates **35**, formed by *C*- and *N*-substituted tetrazoles in which substituents participate in the coordinate bond.

While the method of preparation of tetrazole-containing metal derivatives based on direct reaction of tetrazoles with metal bases or salts, has been known for over a half century,[123] in recent years, several studies were dedicated to the synthesis, structural features and properties of metal derivatives containing the 5-substituted tetrazole fragment.[122]

1.1.5.1. Reactions of 5-substituted *NH*-tetrazoles with metal bases and salts

Because 5-substituted *NH*-tetrazoles possess a high acidity and very low basicity,[51] the ability of these systems to act as *NH*-acids underlies the reactivity of these compounds towards various bases, resulting in formation of the corresponding salts, known as tetrazolates. As previously indicated, the reactions of 5-susbtituted *NH*-tetrazoles **4** with hydroxides, alcoholates and hydrides of alkali and alkaline-earth metals possess predominantly ionic character (**33a**; Scheme 1.13). Mainly, these reactions are carried out in aqueous medium, ethanol or acetonitrile.[122]

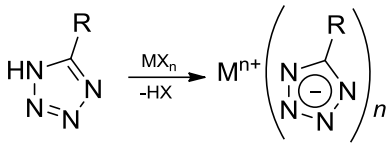

4 **33a**

M = alkali or alkaline-earth metal, n = 1, 2; X = H, OH, OAlk

Scheme 1.13 – Representation of the reaction of 5-susbtituted *NH*-tetrazoles with hydroxides, alchoholates and hydrides of alkali and alkaline-earth metals.

Numerous tetrazole-containing coordination compounds were prepared from reactions of 5-substituted *NH*-tetrazoles with various metal salts (chlorides, nitrates, sulphates, acetates, phosphates, perchlorates, *etc.*).[122] Generally, 5-substituted *NH*-tetrazoles enter into the composition of the arising complex in the deprotonated form (tetrazolate anion). Due to poor solubility, the target coordination compounds are formed on mixing aqueous or aqueous ethanolic solutions of the reactants at room temperature. Generally the products composition depends on the ratio of the initial reagents and exist as one-, two- or three-dimensional coordination polymers.[9]

For example, the Zn(II) cation reacts with 2,3-diethyl-5,6-di(1*H*-tetrazol-5-yl)pyrazine **36** by coordination to the nitrogen atoms of the tetrazole rings, forming the respective tetrazolate complex **37** (Scheme 1.14). As observed by X-ray analysis, complex **37** has a dinuclear structure in which Zn(II) is four-coordinated to furnish a distorted tetrahedral geometry and in the crystal structure the dinuclear units are further assembled to form a three-dimensional (3D) framework by hydrogen bonds.[124]

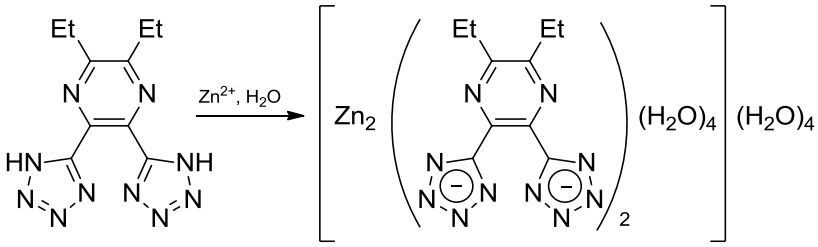

36 **37**

Scheme 1.14 – Representation of the formation of Zn(II) complexes from bis(tetrazolate) ligands.[124]

In few other studies, it was described the presence of a neutral form of 5-substituted *NH*-tetrazoles in the complexes.[124] In particular for palladium salts, palladium(II) chloride reacts with 5-vinyltetrazole, in water or chloroform, to give the molecular complex $Pd(CH_2{=}CH_7CN_4H)_2Cl_2$.[122]

1.1.5.2. Reactions of 1,5-disubstituted tetrazoles with metal salts

1,5-disubstituted tetrazoles lack the labile hydrogen atom in the ring (unlike the *NH*-unsubstituted tetrazoles) and therefore do not exhibit acidic properties, being only weak bases.[51] As such, 1,5-disubstituted tetrazoles, like compound **38**, generally lead to exclusive formation of metal derivatives in the neutral form (**39**; Scheme 1.15). It should be noted that in N(1)-substituted tetrazoles the highest basicity is at the N(4) atom; therefore, in most cases 1,5-disubstituted tetrazoles act as monodentate ligands, with the complex formation involving the N(4) atom. In the complex presented in Figure 1.7 we can see that the molecule **38** is coordinated to the metal atom through the N(4) atom of the tetrazole ring and through the 5-substituent. In this case, the lone pair of the nitrogen is not conjugated with the pi-system of the ring, and is therefore available for metal binding.[125] As a rule, complex formation involving 1,5-disubstituted tetrazoles as ligands proceeds easily at room temperature, in weakly coordinating solvents (alcohols, acetone, diethyl ether, acetonitrile, *etc.*), affording solid coordination compounds.[122]

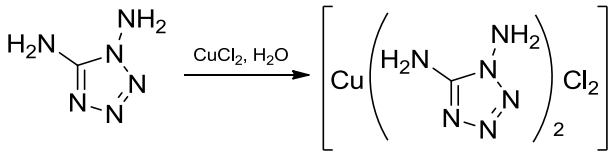

38 **39**

Scheme 1.15 - Formation of a Cu(II) coordination complex with 1,5-diaminotetrazole.

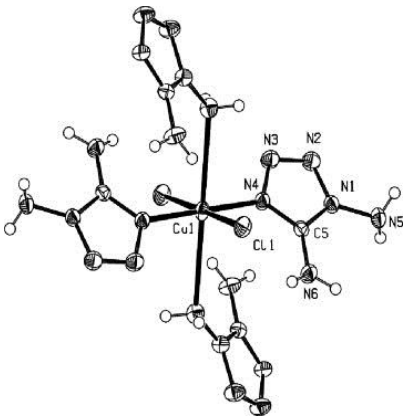

Figure 1.7 – ORTEP plot of the complex bis(1,5-diaminotetrazole)dichloro copper(II).[125]

1.1.5.3. Reactions of 2,5-disubstituted tetrazoles with metal salts

2,5-disubstituted tetrazoles are more sensitive to the conditions for complexation reaction, in particular to the presence of water in the reaction mixture. Besides, the formation of solid

coordinated N(2)-substituted tetrazoles is often hampered by their good solubility. Therefore the synthesis of such complexes requires the use of high concentration of reagents and dry solvents; in some cases the reaction mixture should be heated and subsequently concentrated.[51] The basicity of the N(2)-substituted tetrazoles is somewhat lower than that of the corresponding N(1)-isomers, and the nitrogen in position 4 is also the most basic atom in the tetrazole ring; therefore, like in N(1)-substituted tetrazoles, complex formation generally involves the N(4) atom.[122]

1.1.5.4. Some applications of tetrazole-based coordination complexes

Coordination complexes containing tetrazoles have received wide attention, due to their suitability for various functional applications. Many valuable properties were uncovered, demonstrating good prospects for their use in various fields of science and engineering. In this sub-section we will summarise some of these applications.

i. Tetrazole-based coordination complexes as biologically active compounds

One of the key applications of tetrazole-based coordination complexes, is the introduction of tetrazolyl groups in complex biologically active compounds. Cephazolin, a widely used antibacterial agent, has shown higher *in vitro* antibacterial activity when complexed with metal(II) chlorides, as ML_2Cl_2 or MLCl **40** (Figure 1.8), (L is the deprotonated cephazolin).[126,127] A similar activity should be expected for complexes of another tetrazole-containing antibiotic, cefamandole, with copper,[128] cadmium[129] and zinc[130] salts.

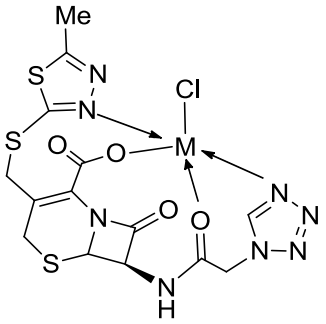

M = Cu, Co, Ni, Zn

40

Figure 1.8 – Representation of coordination complexes prepared from deprotonated cephazolin and M(II) chlorides.

Platinum(II) complexes of tetrazole[1,5-a]quinolines (**41**, Figure 1.9) have demonstrated cytotoxic activity towards malignant cells; for instance, compounds **41d,e** exhibited similar cytotoxicity to cisplatin, when tested against the same cellular lines, while complexes **41a-c** demonstrated a higher activity.[131]

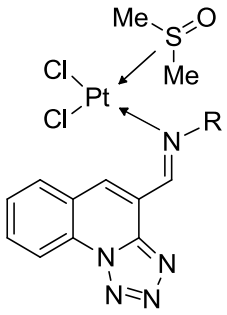

R = Ph(**a**), 4-MeC_6H_4(**b**), 4-ClC_6H_4(**c**), NHPh (**d**), NHMe (**e**)

41a-e

Figure 1.9 – Representation of platinum(II)-tetrazole[1,5-a]quinolones coordination complexes.[131]

ii. Tetrazole-based coordination complexes as catalysts

Numerous tetrazolyl ligands have been coordinated with different metal centres and tested as catalysts for organic reactions. For example, iron(III) complexes **42** (Figure 1.10) demonstrated high efficiency as oxidation catalysts in the epoxidation of olefins **43** (Scheme 1.16) . The epoxides **44** were generated in excellent yields.[132]

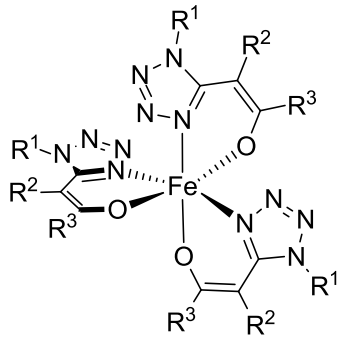

R^1 = Bu^i, R^2 = CN, R^3 = OMe (**a**); R^1= Bu^t, R^2 = H, R^3 = Ph (**b**)

42a,b

Figure 1.10 – Representation of Fe(III) complexes of tetrazolyl enol derivatives (FeL_3).[132]

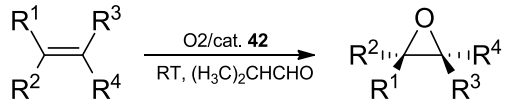

43 **44**

Scheme 1.16 – Representation of the [FeL_3]-catalyzed aerobic epoxidation of olefins. Structure of FeL_3 represented in Figure 1.10.

Palladium(II) acetate complexes with 1,3-phenylene-bis-(1*H)*-tetrazole **45**[38] and 1-(2-iodo-phenyl)tetrazole **46**,[37] proved to be good catalysts in the Suzuki and Heck coupling reactions, respectively (Figure 1.11).

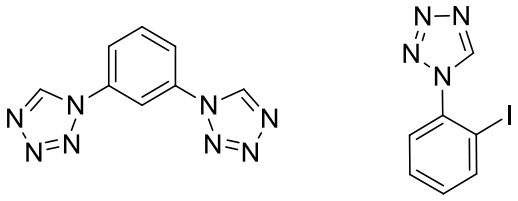

45 **46**

Figure 1.11 – Representation of tetrazole derivatives used as ligands in Suzuki (**45**)[38] and Heck (**46**)[37] coupling reactions.

Ligand **45** has shown to be an effective catalyst for Suzuki cross-coupling reactions of various aryl halides **47** with aryl boronic acids **48**. Cross-coupled biphenyl compounds **49** were obtained in good to excellent yields (Scheme 1.17).[38]

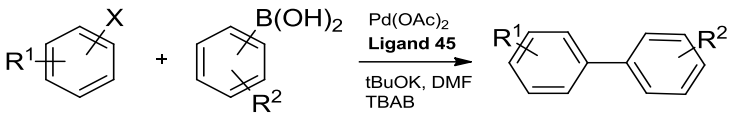

47 **48** **49**

Scheme 1.17 – Representation of the Suzuki methodology for cross-coupling of aryl halides with aryl boronic acids, catalyzed by tetrazolyl-Pd complexes (structure of ligand **45** as in Figure 1.11).[38]

The activity of ligand **46** in the Heck methodology was assessed using combinations of 4-iodotoluene **50** with various *α,β*-unsaturated carbonyl compounds **51**. Heck reactions catalyzed by the tetrazolyl–Pd complex afforded the products **52** stereoselectively, in excellent yields (Scheme 1.18).[37]

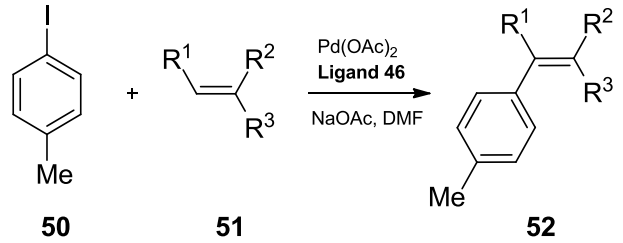

50 **51** **52**

Scheme 1.18 – Representation of the Heck methodology for cross-coupling of 4-iodotoluene with various *α*,*β*-unsaturated carbonyl compounds, catalyzed by tetrazolyl-Pd complexes (structure of ligand **46** as in Figure 1.11).[37]

iii. Tetrazole-based coordination complexes as energetic materials

Many energetic metal tetrazole derivatives are able to pass from the combustion mode to detonation and are thus promising as initiating explosives, although for safe initiating means, including those operating from low-voltage current sources or on exposure to laser radiation.[133] An extremely high susceptibility to laser pulse was found for the complexes of 5-hydrazinotetrazole with mercury(II) perchlorate. This complex has found use for the production of film light-sensitive charges employed for the formation of shaped shock waves and blast hardening of steels. Additionally, the metal tetrazole derivatives have shown to be highly relevant as gas generating agents. 5-Aminotetrazole, 5-nitramino-tetrazole and corresponding salts from alkali, alkaline earth and transition metal cations [copper(II), zinc(II), cobalt(II), iron(III)] were patented for applications in gas-generation systems.[134–139]

iv. Tetrazole-based coordination complexes as tools for corrosion control

The ability of tetrazoles to form stable complexes with various metal ions is widely used in photoprocesses and for protection of metals from corrosion.[140–143] Some 5-substituted tetrazoles, namely 5-mercapto-1-phenyltetrazole and its derivatives, and their salts, are used as light-sensitive materials and reagents that improve sharpness, enhance the mechanical and thermal stability of the image and prevent bleaching.[144] 5-Mercapto-1-phenyltetrazole is the most effective metal corrosion inhibitor in the series of heterocyclic compounds. On a metal surface, this compound forms inert, insoluble and stable complexes with metal ions, which prevent the material from destruction.[145,146] The film of these complexes inhibits corrosion of copper,[147–150] nickel, iron,[151] steel,[152] and bronze,[148] in acidic media. In addition, tetrazoles inhibit not only electrochemical but also microbiological corrosion of metals.[153]

v. Spectrophotometric properties of tetrazole-based coordination complexes

The formation of coloured metal complexes of azotetrazoles **53** and **54** that are stable in solution is used for spectrophotometric determination of traces of iron(III), bismuth(III) and palladium(II) in various mixtures (Figure 1.12).[154]

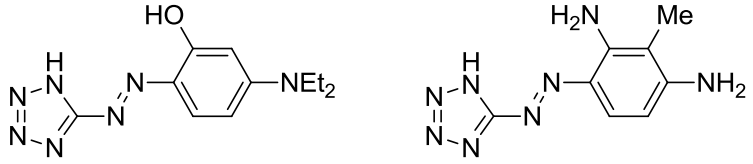

53 **54**

Figure 1.12 – Representation of tetrazoles used as dyes for spectrophotometric determination of iron(III), bismuth(III) and palladium(II).[154]

Recently a new tetrazole based turn-on fluorescent chemosensor for Zn(II) was synthesized **55**. This fluorescent probe is known to coordinate with Zn(II) ions via a 1:1 binding mode **56**, and showed high sensitivity and selectivity for Zn(II) ions (Scheme 1.19). The chemosensor **55** can be employed for fluorescent imaging of Zn(II) ions in living cells.[11]

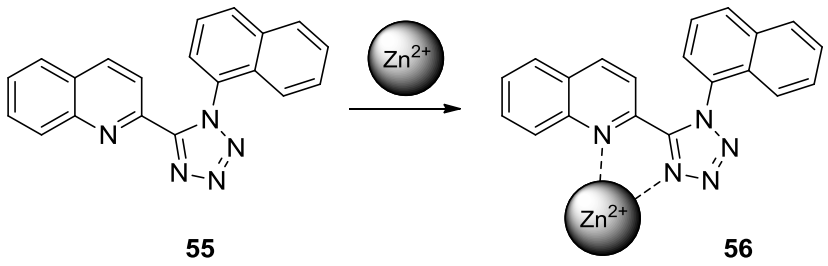

55 **56**

Non-fluorescence Fluorescence

Scheme 1.19 – Representation of a tetrazole based turn-on fluorescent chemosensor for Zn(II).[11]

In conclusion, the tetrazole moiety bears a wide range of potential applications in coordination chemistry. Chemical diversity can be readily introduced onto the coordination complex structure by employing functionalized tetrazoles in the assembly process, enabling structure-based design and optimization of properties. Moreover tetrazole-based coordination complexes are generally more sensitive and responsive to electro- and photochemical stimuli than the corresponding metal-free tetrazole molecules and demonstrated good prospects for applications that rely on photo- and thermochromism, ferromagnetism, luminescence and nonlinear optical properties[9,10]

Tetrazole derivatives can be tuned to exhibit a wealth of properties, enabling a wide range of applications. A deep understanding of the reactivity of tetrazoles, as well as the fine-tuning of properties and applications of the class, require a deep knowledge of the structure prior to its adjustment and control. As such, the detailed investigation of the structure of representative tetrazoles, in the condensed phase, in solution and also as isolated species, has played a major part in most studies.

1.1.6. Matrix isolation

The matrix isolation technique, was originally invented to study free radicals and other short-lived chemical reaction intermediates. This experimental technique requires that the material to be analysed is trapped within an unreactive matrix, usually solidified inert gases at temperatures close to absolute zero. The combination of this trapping technique with spectroscopic detection methods resulted in a powerful research tool for studying the structure, reactivity and possible interactions of small molecules.

The term matrix isolation was first introduced by Pimentel and co-workers in 1954, to describe a method whereby a substrate (guest) is mixed with a large excess of an host gas and is condensed on a surface that is sufficiently cold to assure rapid solidification of the material.[155] Ideally each substrate molecule is immobilized in a cavity surrounded by one or more layers of solid material (often solidified noble gases such as Ar, Kr, Xe, or cryogenic solids *e.g.*, N_2, O_2, CO, CH_4) and is thus ‘‘isolated’’ from the other substrate molecules in a ‘‘matrix’’ of the host gas. Because the species are embedded in a host material, the diffusion process is prevented and bimolecular reactions cannot take place, except with the host material. Also intramolecular rearrangements are inhibited for any process with an activation barrier larger than a few kJ mol^{-1}. The usual host materials which are known to have only minor interactions with the trapped guest species are solid noble gases (Ne, Ar, Kr, and Xe) and offer three main advantages: they form clear glasses, show transparency through the IR, Vis, and UV ($\lambda > 200$ nm) regions of the spectrum and are, for most guests, chemically inert.[156–159]

1.1.6.1. Matrix isolation associated to spectroscopic techniques

A variety of spectroscopic methods can then be used for the detection and characterization of the trapped species, *e.g.*, infrared, ultraviolet/visible, nuclear magnetic resonance (NMR), electronic spin resonance (ESR) and Raman spectroscopies. Among these methods, infrared spectroscopy is one of the most effective techniques to determine the

structure of molecules and other intermediate species isolated in low-temperature matrices. The isolation of monomeric solute molecules in an inert environment reduces intermolecular interactions, resulting in a sharpening of the solute absorptions compared with other condensed phases, the effect being particularly dramatic for substances that may form intermolecular hydrogen bonds. The rotational structure is, with few exceptions, quenched, thus giving much narrower bands than are obtained in the vapour phase. Also, the low temperature itself results in small band widths. Consequently, infrared absorptions are typically sharp in these matrices, with half band widths between 0.1 cm^{-1} and 1 cm^{-1}. Bands due to different vibration modes, which overlap completely in the vapour phase or in dilute solution at room temperature, may often be resolved in matrix spectra, enabling vibrational assignments to be made with greater confidence and the frequencies to be obtained more accurately. However, care should still be taken in the band assignment since, for example, it is frequent that in matrix isolation spectral bands show splittings caused by matrix anisotropy (sites). The site effects result from the fact that a rigid host material may accommodate a guest molecule in different local environments (sites) where these molecules may experience slightly different external fields or geometrical constraints. Thus, the nature of the observed splittings can be due to different chemical species (different conformers) or to the same species in different trapping sites. Moreover, pairs of lines of different intensity that occur in a region where only a single one is expected are often indicative of *Fermi-resonances*, that is, a (near) coincidence of an IR active fundamental with an overtone or a combination mode of the same symmetry that ‘‘borrows’’ intensity from the former.[156,158]

In matrix isolation studies, the assignment of bands in IR spectra of intermediates was based primarily on the registry of the characteristic absorption bands, whenever possible with use of the isotopic substitution. Nowadays, the interpretation of experimental IR spectra is greatly simplified due to the development of accurate theoretical methods for their calculation.

1.1.6.2. Matrix studies

A matrix isolated sample can be prepared by deposition of a pre-mixed gaseous mixture or by co-deposition of the species to be studied (or a suitable precursor) and the host gas. In both situations, the gas mixture is directed towards a cold window kept typically in the 4-20 K temperature range and at very low pressure (10^{-8} - 10^{-10} atm) inside a cryostat (Figure 1.13). Rapid cooling of the sample mixed with the inert matrix allows an efficient trapping of the populations of the different conformational species, in cases where the energy barriers

separating them are large enough. Hence, the method is particularly suitable in the study of conformational isomerism. Assuming that no isomerization occurs during deposition, it is possible to determine the relative population of the conformers, which should correspond to the equilibrium existing in the gas phase prior to deposition. However, for systems with low energy barriers (~1-2 kJ mol^{-1}) conversion of higher energy forms into lower energy forms can take place during deposition of the matrix, and thus, the population distribution may differ considerably from that of the equilibrium gas phase due to *conformational cooling*.[160–162]

i. Annealing

Temperature variation studies, known as *annealing* of the matrices to higher temperatures (in general up to 35, 45 and 60 K, for argon, krypton and xenon matrices, respectively), may result in the conversion of higher energy forms into more stable forms, depending on the energy required to overcome the barriers to conversion.[163] Thus, the knowledge of the energy barriers for interconversion between the conformers is of extreme importance in the interpretation of the experimental results.

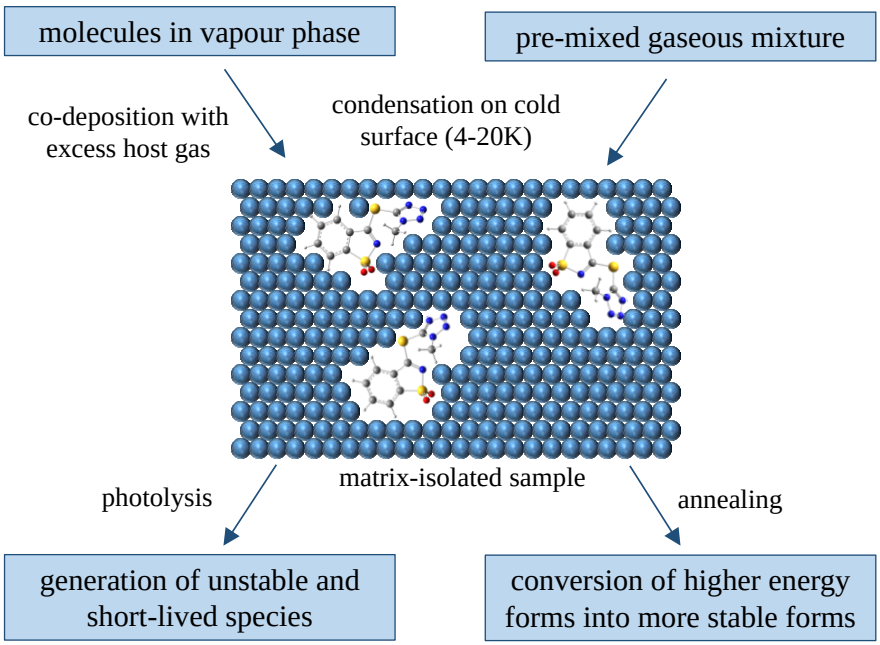

Figure 1.13 – General representation of a matrix isolation preparation and principal studies

ii. Photochemistry of matrix isolated species

One of the most important advantages of matrix isolation coupled to a suitable spectroscopic technique is the possibility to follow photochemical reactions of the matrix

isolated monomeric species. Irradiation *in situ* of the matrix with ultraviolet light allows the observation of processes with high energy barriers, since it may provide the molecule under study with a large amount of energy. Thus, a wide range of intramolecular changes, including decomposition of molecules with formation of new entities, can be studied. Besides, the photochemical processes are cage-confined, precluding subsequent cross-reactions involving species resulting from photolysis of different reactant molecules. Therefore, the number of possible photochemical reaction pathways leading to different products can be strongly reduced in comparison with gas phase or solution. Another great advantage of low temperature matrix isolation is the increase in the lifetime of unstable or usually short-lived species, which can be easily generated photochemically, allowing for detailed structural investigations of novel and/or highly reactive molecules[156]

A description of the matrix isolation setup coupled with infrared spectroscopy, used in the course of our studies, will be presented in chapter 2 of this thesis.

1.1.7. Photochemistry of tetrazoles

Tetrazoles are known to have a very rich photochemistry. The photoreactivity of a representative range of tetrazole derivatives has been widely investigated, in solution and in the rigid environment of solid matrices, resulting in a wealth of information that unrevealed the potential of tetrazoles as precursors of a wide variety of new scaffolds through photolysis.[66,164–198]

An important contribution to the available data on the photochemistry of tetrazole derivatives in solution came from the work led by Quast and co-workers during the 1980s.[190–196] Since then, other important contribution were added to the field, and several photochemical transformation of tetrazole derivatives in solution were reported.[175,177,179,180,184,187] It is known nowadays that, through a careful selection of solvent and other reaction conditions, the photofragmentation process may be tuned to grant selectivity, affording stable and synthetically useful photoproducts such as 9*H*-pyrimido(4,5-b) indoles, diaziridinones, iminoaziridines, iminodiaziridines, carbodiimides, benzimidazolones, pyrimidinones and oxazines that may be isolated and stored, or trapped in the reaction media. Photolysis of tetrazole derivatives in solution may thus be an attractive synthetic methodology for the preparation of other compounds. Nevertheless, due to the diversity in photodegradation pathways and putative photoproducts, tetrazoles remain a challenge to photochemists.

1.1.7.1. Photochemistry of matrix-isolated tetrazole and derivatives

The photochemistry of monomeric tetrazoles has been extensively investigated, since an understanding of the photoreactivity of tetrazoles as isolated species is relevant for evaluation of their inherent photostability. As mentioned, the use of matrix isolation technique coupled to a suitable probing method, such as FTIR spectroscopy, represents an accurate strategy to understand the mechanisms involved in photochemical reactions of monomeric species. Photolysis of tetrazoles trapped in a rigid environment of solidified noble gases at cryogenic temperatures (usually argon at 10–15 K) results in photofragmentation of the monomeric species, generally through more than one exit channel. Since the obtained fragments are generally confined to the matrix cage where they are formed, no subsequent cross-reactions involving species resulting from photolysis can occur, strongly reducing the number of possible photoproducts in comparison with gas phase or solution studies. These conditions enable spectroscopic characterization of novel and/or highly reactive molecules like antiaromatic diazirines, diaziridines, carbodiimides, nitriles, reactive isocyanates and azides.

The photochemistry of matrix-isolated unsubstituted tetrazole **2**, which was found to exist essentially as the 2*H*-tautomer when isolated in solid argon,[56] was studied for the first time by Maier and co-workers.[188] Upon photolysis with the 193 nm emission line of an ArF laser, rapid photocleavage of tetrazole was observed, leading to extrusion of N_2 and formation of several different photoproducts, including nitrilimine **57**, an HCN···NH complex **58**, diazomethane **59**, carbodiimide **60** and cyanamide **61** (Scheme 1.20). By use of different excitation wavelengths, cyanamide and carbodiimide could be accumulated as final products. This investigation also revealed, for the first time, the vibrational signature of matrix-isolated nitrilimine **57**.

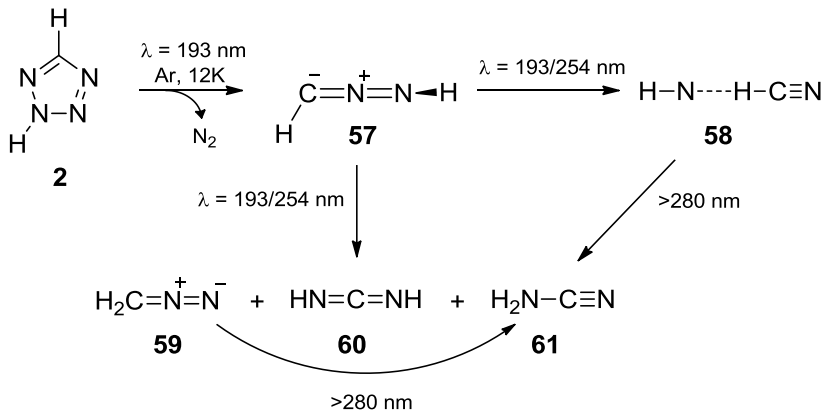

Scheme 1.20 –Representation of the photodecomposition of matrix-isolated unsubstituted tetrazole.[188]

The photochemistry of the tetrazole chemotypes **62** and **63** (Figure 1.14) isolated in solid argon has been addressed and is described in the literature. Results show that, for 1,5-disubstituted tetrazoles **62** with three formally single bonds, two photofragmentation channels are generally active, with that corresponding to direct N_2 elimination always playing the most important role.[164,165,172,173,182,183] In the case of 2,5-disubstituted tetrazoles **63**, N_2 elimination seems to be the sole primary photofragmentation route observed.[166,167,169,170,172,174,188] The photochemistry of several tetrazole derivatives bearing four single bonds in the tetrazole ring, like tetrazolones or tetrazole-thiones **64**, was also studied in a rigid environment of solid matrices and the results have shown that the number of available reaction channels correlates with the number of formally single bonds in the tetrazole ring.[66,181,185] In fact, when four single bonds are present, like in **64**, an additional photofragmentation channel can take place, and sometimes also a fourth reaction corresponding to cleavage through the N_1-C_5 and N_4-C_5 bonds.[66,181,185]

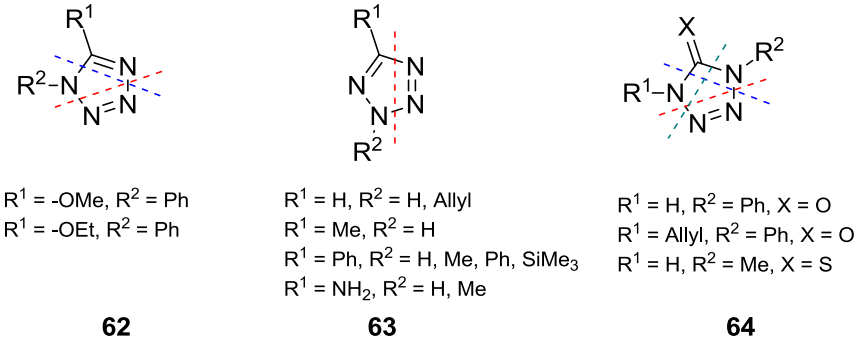

Figure 1.14 – Schematic representation of the photodecomposition patterns observed for representative tetrazole derivatives isolated in cryogenic matrices.

Generally, results show that the photochemistry of matrix-isolated tetrazoles always involves cleavage of the tetrazolyl ring, leading to a variety of photoproducts. The major factor contributing to the observed range and versatility in photochemical pathways for tetrazoles is the possibility of tautomerism. In general, the presence of labile hydrogen atoms (either directly linked to the tetrazole ring or belonging to the tetrazole substituents) is a source of complexity in photochemical reactions, generally opening additional primary channels or enabling secondary photochemical reactions. When substituents are linked to the tetrazole ring, the photochemistry of the molecule can also be influenced by their nature and conformational flexibility, which may favour or exclude certain reaction channels, determining the nature and relative amount of the final photoproducts. Specific examples are provided below.

1.1.7.2. 1-(Tetrazol-5-yl)ethanol

Recently, 1-(tetrazol-5-yl)ethanol **65** has assumed an important role in the synthesis of tetrazole-saccharinates useful as nitrogen ligands.[173,199] As such, its structure and photochemistry were studied in detail. Matrix isolation of **65** allowed a detailed investigation of its monomeric structure.[178] Results have shown that 1-(tetrazol-5-yl)ethanol presents two different tautomeric forms, which are stabilized by different types of intramolecular hydrogen bonds NH···O **65a** or OH···N **65b** (Scheme 1.21). Remarkably, these non-covalent interactions were found to determine the photochemical behaviour of the tautomers in an argon matrix.

Deposition of the matrix at 30 K led to simplification of the conformational mixture, with only one conformer of each tautomer of **65** surviving. These conformers correspond to the most stable forms of each tautomer 1*H* and 2*H* (**65a** and **65b**, respectively). Upon irradiating with UV light (λ > 200 nm), an unprecedented tautomer selective photochemistry was observed, with the 2*H*-tautomeric form undergoing unimolecular decomposition to azide **66** and 2-hydroxypropanenitrile **67** while the 1*H*-tautomer remained photostable (Scheme 1.21). For the 1*H*-tautomer **65a**, photo-induced ring-cleavage requires simultaneous cleavage of the intramolecular *H*-bond connecting the tetrazole hydrogen to the oxygen atom of the substituent, which appears to preclude the reaction. In the case of the 2*H*-tautomer there are low energy conformers **65c**, that can be easily accessed from the lowest energy conformer **65b**, in which cleavage of the intramolecular H-bond is not required during the ring-opening reaction. In this case, the ring-opening reaction is then much easier, since the two molecular fragments resulting primarily from the reaction are not linked by any H-bond.

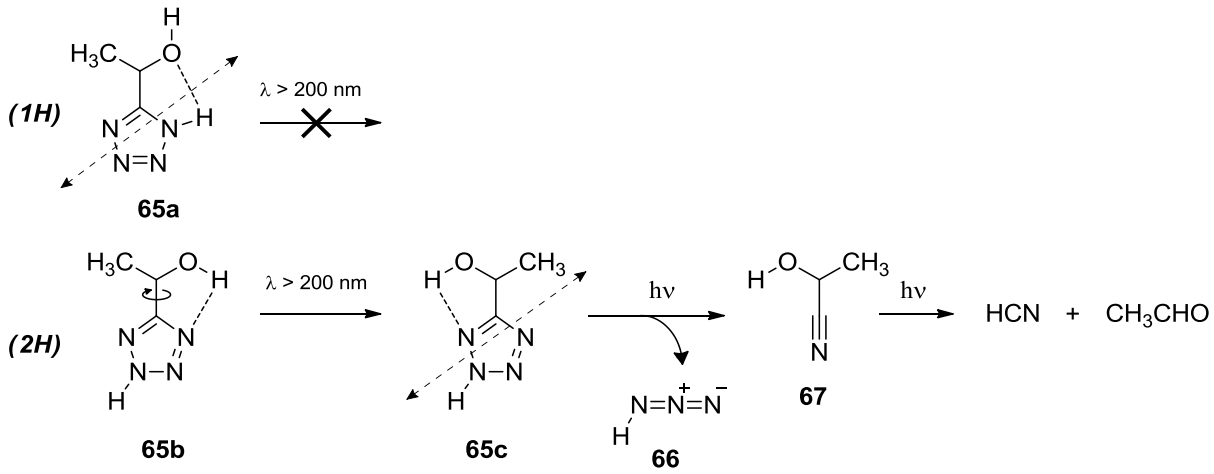

Scheme 1.21 – Representation of the photochemical reaction observed for 1-(2*H*-tetrazol-5-yl)ethanol isolated in solid argon upon irradiation with UV light (λ > 200 nm).[178]

1.1.7.3. 5-alkoxy-1-phenyl-1*H*-tetrazoles

The photochemistry of monomeric 5-alkoxy tetrazoles was also investigated.[182,183] Upon UV irradiation (λ > 235 nm), 5-alkoxy-1-phenyl-1*H*-tetrazole **68** (R = Me; Et) was found to react through two fragmentation pathways (Scheme 1.22): (a) N_2 elimination, with production of the antiaromatic 3-alkoxy-1-phenyl-1*H*-diazirine **69**; (b) ring-opening, leading to phenylazide **70** and alkylcyanate **71**. The latter compound was found to quickly convert to its more stable isomer alkyl-isocyanate **72**. Phenylazide **70** further eliminated molecular nitrogen to give phenylnitrene **73** that underwent subsequent ring expansion to form the seven-membered ring 1-aza-1,2,4,6-cycloheptatetraene **74**.

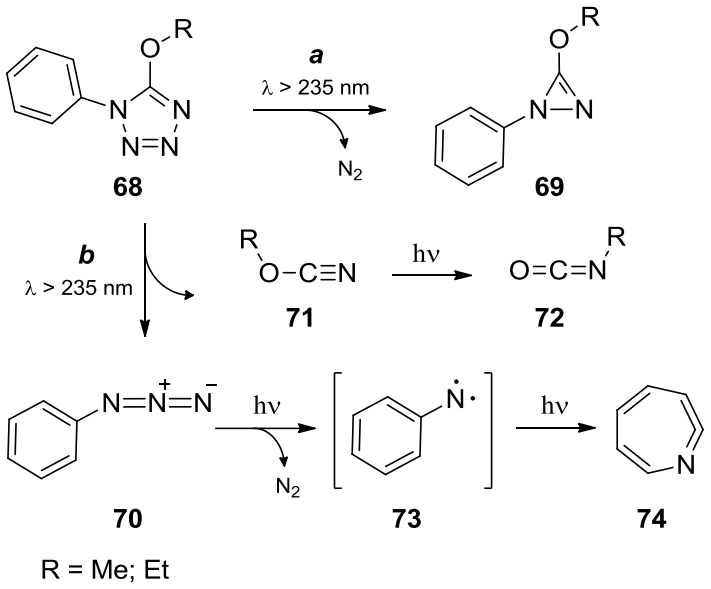

Scheme 1.22 – Representation of the photochemical reactions observed for 5-alkoxy-1-phenyl-1*H*-tetrazoles isolated in solid argon, upon irradiation with UV light (λ > 235 nm).[182,183]

1.1.7.4. 2-Methyl-2*H*-tetrazol-5-amine

The research described in this thesis was mostly dedicated to the synthesis and study of tetrazole saccharinates useful as nitrogen ligands.[200] For the synthesis of these conjugates 2-methyl-2*H*-tetrazol-5-amine **75** played an important role, as it served as one of the tetrazole building blocks used.

2-Methyl-2*H*-tetrazol-5-amine is an interesting compound because it may exist in different tautomeric forms (**75a-d**; Figure 1.15). The possibility of hydrogen shift from the amino group to three different positions of the tetrazole ring leads to three possible pairs of tautomers bearing an imine (or aminide) *NH*-substituent at the position 5.[186] The hydrogen

involved in the tautomeric rearrangement can occupy positions 1, 3 and 4 of the ring. In the first case, tautomerism leads to the imine species, 2-methyl-1,2-dihydro-5*H*-tetrazol-5-imine **75c** (Figure 1.15), which can exist in two different conformations, depending on the orientation of the hydrogen atom in the imino group at position 5. The remaining two cases lead to mesoionic-type structures, 2-methyl-3*H*-tetrazol-2-ium-5-aminide **75d** and 3-methyl-1*H*-tetrazol-3-ium-5-aminide **75b**, that may also exist in two different stable conformations.

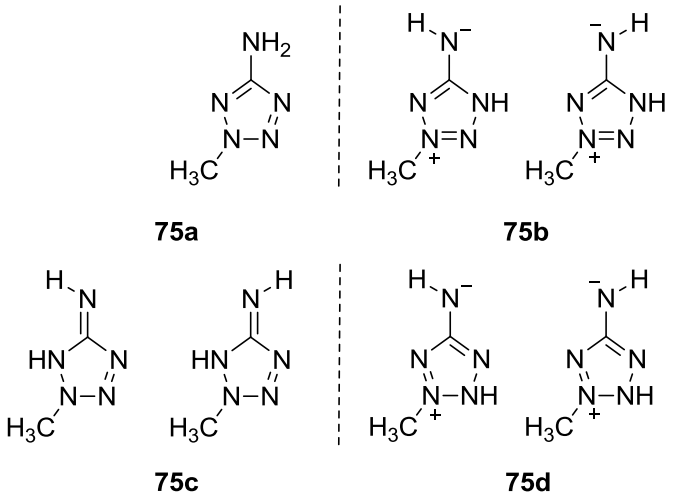

Figure 1.15 – Representation of tautomeric forms of 2-methyl-2*H*-tetrazol-5-amine.[186]

The experimental spectrum of **75** isolated in an argon matrix fits well the spectrum of tautomer **75a** calculated at the DFT(B3LYP)/6-311++G(d,p) level of theory and no evidence of presence of any of the imine (aminide) tautomers was found.

Photochemical studies in solid argon[186] revealed the involvement of three different primary photochemical pathways: two of them correspond to the prototype reactions found for other tetrazoles (Scheme 1.23): (a) N_2 elimination, with production of 1-methyl-1*H*-diazirine-3-amine **77**; and (b) ring cleavage leading to production of methyl azide **78** and cyanamide **64**. The third observed reaction, pathway (c), was tautomerization of **75a** to mesoionic 3-methyl-1*H*-tetrazol-3-ium-5-aminide **75b** via [1,3]-hydrogen shift. Additionally, secondary reactions were observed, leading to spectroscopic observation of methylenimine **79** and hydrogen isocyanide **80**. In this first experiment, the photolysis of **75a** was conducted at $\lambda > 235$ nm. Under this conditions, the entire set of products was formed immediately, and nitrile imine **76** was not identified. Later Baskir *el al.*,[168] reported a successful observation of this nitrile imine, using a low-pressure lamp ($\lambda = 254$ nm) to induce a stepwise photolysis of the matrix isolated **75a**. Prolonged photolysis ($\lambda > 254$ nm) for 70 min led to the complete disappearance of the initial photoproduct, nitrile imine **76**, with generation of diazirine **77**. Additional photolysis

with light within 280 < λ < 350 nm resulted in the decrease of bands corresponding to diazirine **77** and in the growth of bands from several other products observed earlier (**79**, **64** and **80**). The authors claimed that, unlike other nitrile imines with other substituents which isomerized into carbodiimide **81** as final photoproduct,[166,167,169,170,172,174] this isomerization was precluded in the case of amino-substituted nitrile imines.

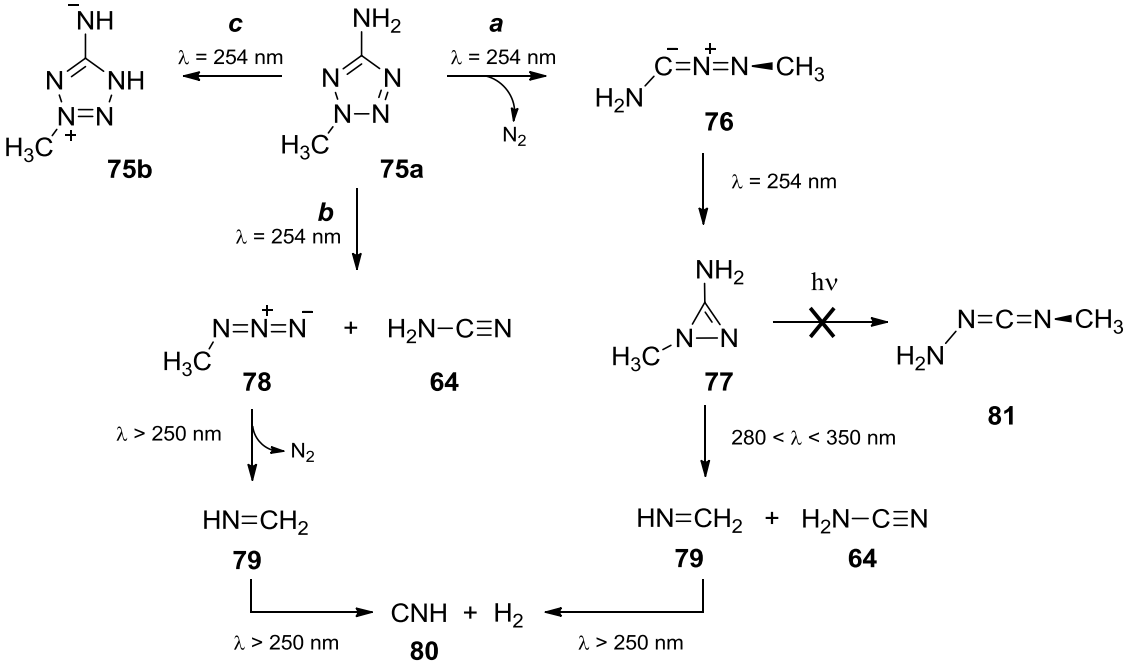

Scheme 1.23 – Representation of the photochemical reaction observed for 2-methyl-*2H*-tetrazol-5-amine isolated in solid argon upon irradiation with UV light (λ = 254 nm, 280 < λ <350 nm and λ > 250 nm).

As mentioned above, 2-methyl-2*H*-tetrazol-5-amine **75** has assumed an important role in the synthesis of tetrazole-saccharinate type nitrogen ligands.[200] The work proposed in this PhD project also included the investigation of the reactivity of the tetrazole-saccharinates prepared, including the study of their photochemistry. We observed that the photochemistry of the tetrazole-saccharinates could only be duly interpreted after analysis of the photodegradation pathways exhibited by the tetrazolyl building block used as precursor in the synthesis of our conjugate. A detailed discussion on this subject will be presented in chapter 4 of this thesis.

1.1.7.5. 1-Allyltetrazole and 2-allyltetrazole

The photochemistry of 1-allyltetrazole **82** and 2-allyltetrazole **83** has been studied isolated in solid argon.[172] The results of these investigations have shown that UV irradiation (λ > 280 nm) of both compounds, **82** and **83**, in argon matrices led to the same photoproducts,

suggesting a common intermediate, 1-allyl-1*H*-diazirine **84** (Scheme 1.24).[172] The main photolysis pathway proceeded through tetrazole ring cleavage, N_2 elimination and formation of *N*-allylcarbodiimide **85** as the main product. Two other species, allylcyanamide **86** and allylnitrilimine **87** were also detected in the irradiated matrices (Scheme 1.24).

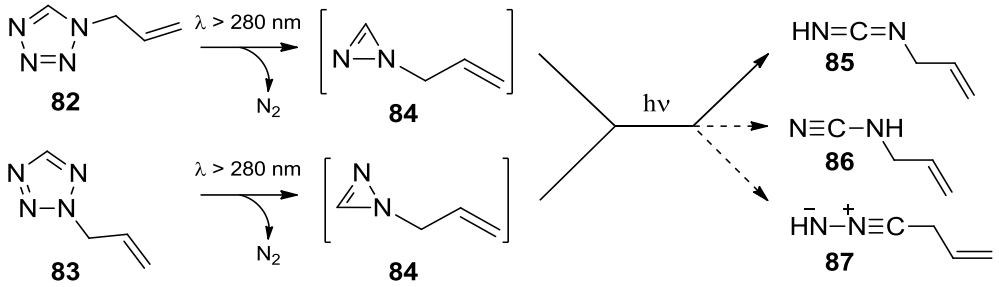

Scheme 1.24 – Representation of the photochemical reaction observed for 1-allyltetrazole and 2-allyltetrazole isolated in solid argon, upon irradiation with UV light (λ > 280 nm).[172]

1.1.7.6. Tetrazole coupled with another heterocycle

Heterocycles find wide applications in coordination chemistry as ligands and, among them, tetrazoles are known to play an important role. Especially relevant in this context are bis-tetrazoles or conjugates where the tetrazole ring is linked to other heterocycles.[2,9,10,122,201] In all these systems, a detailed investigation of the structure, including tautomeric and conformational preferences of the molecules, and of their thermal and photochemical stability, is of crucial relevance to define properties and function. Tetrazolyl-triazole, tetrazolyl-pyridine and tetrazolyl-benzisothiazole conjugates were studied recently, with the aim of exploring their potential as multidentate nitrogen ligands. Some of the molecules prepared were deeply investigated regarding their structure and/or their photochemical stability.[164,173,200,202–205]

i. 5-(1*H*-tetrazol-1-yl)-1,2,4-triazole

The 5-(1*H*-tetrazol-1-yl)-1,2,4-triazole molecule **88** may exist in five tautomeric forms, differing by the position of the *H*-atom in the triazole ring.[204] Bands due to both tautomers **88a** and **88b** (Scheme 1.25) were identified in the experimental spectrum of a freshly deposited sample. Moreover, trapping **88** in xenon matrices at 15 K, and subsequent heating of the sample to temperatures to ~30 K (annealing), permitted to induce conformational transformations and enabled to establish the experimental conditions to use during the photochemical studies, where the conformational composition of the molecule was reduced to only two structures (the most stable conformers of **88a** and **88b**).

The most noteworthy behaviour of matrix isolated tetrazolyltriazole is its tautomer-selective photochemistry (a similar feature was observed, and discussed above, for 1-(tetrazol-5-yl)ethanol **65** isolated in solid argon).[178] UV irradiation (λ > 288 nm) of the compound in a xenon matrix led to fast consumption of tautomer **88a**, while **88b** remained intact. Simultaneously, new bands appeared in the spectrum of the irradiated sample, which are due to the photoproduct **91**. Upon subsequent irradiation of the matrix with UV-light of shorter wavelengths (λ > 234 nm), the bands due to the **88b** tautomer strongly decreased, due to photolysis. At the same time, a set of bands showed up in the spectra, which are due to a second photoproduct **92**. Both **88a** and **88b** tautomers photolyze according to the same pathway, through N_2 elimination, yielding analogous products, differing solely in the position of the *H*-atom attached to the triazole ring: 1*H*-1,2,4-triazol-5-yl carbodiimide **91** and 1*H*-1,2,4-triazol-3-yl carbodiimide **92**. The formation of products **91** and **92** proceeds most probably through the 1-(1*H*-1,2,4-triazol-5-yl)diaziridine **89** and 1-(2*H*-1,2,4-triazol-3-yl)diaziridine **90** intermediates, respectively. However, these species were not detected experimentally.

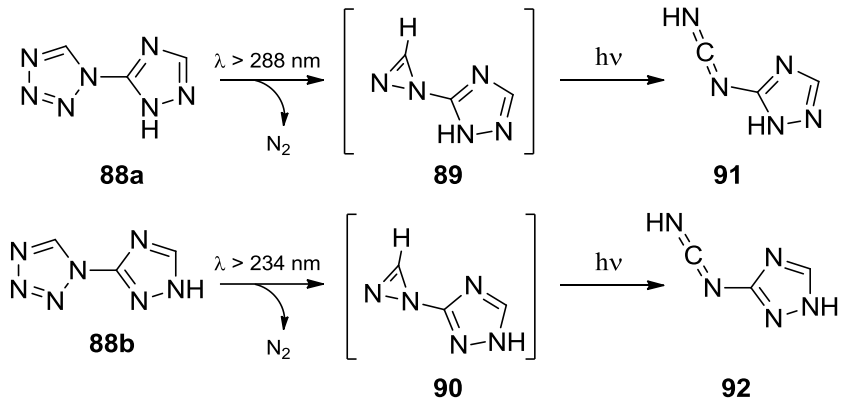

Scheme 1.25 – Representation of the photochemical reactions observed for tautomers of 5-(1*H*-tetrazol-1-yl)-1,2,4-triazole, isolated in xenon, upon irradiation with UV light (λ > 288 nm and λ > 234 nm).[204]

ii. 2-[1-(1*H*-tetrazol-5-yl)ethyl]-1,2-benzisothiazol-3(2*H*)-one-1,1 dioxide

Based on the known versatility of tetrazole[9,10] and benzisothiazole (saccharin) derivatives[206] as coordinating ligand, novel tetrazole-saccharyl conjugates were designed recently in our group. One of the conjugates prepared is 2-[1-(1*H*-tetrazol-5-yl)ethyl]-1,2-benzisothiazol-3(2*H*)-one 1,1-dioxide **93** (Figure 1.16). The structure and matrix photochemistry of **93** were investigated using vibrational spectroscopy and quantum chemical calculations.[173]

The tetrazole-saccharyl conjugate **93** has a chiral centre, the two enantiomers (R and S forms) being spectroscopically equivalent. The compound may exist in two tautomeric forms, **93a** and **93b** (Figure 1.16), both having two conformationally relevant internal degrees of rotation, which are defined by the bridging N-C and C-C bonds. According to calculations, conformers belonging to the 1*H*-tautomer were found to be the most stable forms. The stabilization of these forms results from the presence of an intramolecular hydrogen bond-like interaction (NH···O=X, where X = S, C) that is absent in all the 2*H*-conformers. In the experimental spectrum of a freshly deposited sample, only the bands due to the most stable conformer of 1*H*-tautomer **93a** could be identified.

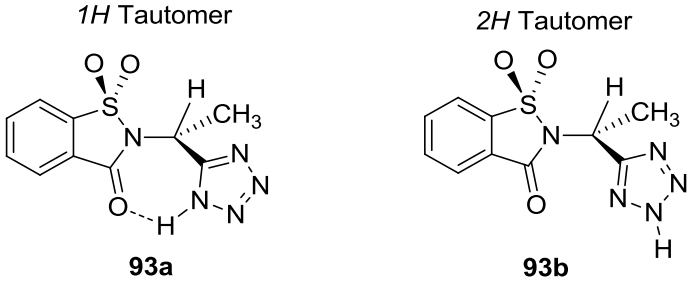

Figure 1.16 - Representation of the tautomeric forms of 2-[1-(1*H*-tetrazol-5-yl)ethyl]-1,2-benzisothiazol-3(2*H*)-one 1,1 dioxide.[173]

UV irradiation (λ = 275 nm) of **93a** in solid argon led to different photodegradation pathways: (a) photocleavage of the tetrazole ring with extrusion of N_2 leading to formation of 2-[1-(1*H*-diazirin-3-yl)ethyl]-1,2-benzisothiazol-3(2*H*)-one 1,1-dioxide **94**; (b) photo-cleavage of the tetrazole ring leading to formation of azide **66** and 2-(1,1-dioxide-3-oxo-1,2-benzisothiazol-2(3*H*)-yl)propanenitrile **95**; (c) photocleavage of the saccharyl ring (decarbonylation) and of the tetrazole ring, with formation of azide **66**, 7-thia-8-azabicyclo[4.2.0] octa-1,3,5-triene 7,7-dioxide **96** and propene-nitrile **97**.

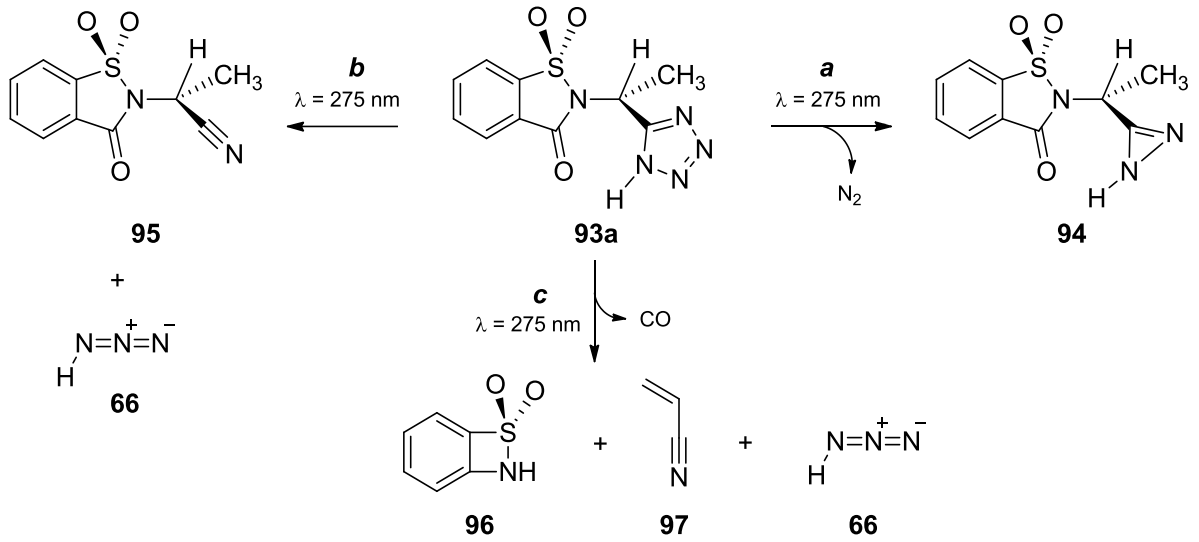

Scheme 1.26 – Representation of the photochemical reactions observed for 2-[1-(1*H*-tetrazol-5-yl)ethyl]-1,2-benzisothiazol-3(2*H*)-one 1,1-dioxide isolated in solid argon, upon irradiation with UV light (λ = 275 nm).[173]

Although with low efficiency, these experiments provided the first observation of photocleavage of the benzisothiazole ring upon irradiation in rare gas matrices. More recently, the UV induced photoisomerization of saccharin in solid argon has been studied, revealing the formation of a new compound, isosaccharin (this will be explained below in section 1.2).[207]

1.1.7.7. Recent developments in tetrazole-based photoclick chemistry

In the last few years, photolysis of several 2,5-disubstituted tetrazoles was used for *in situ* generation of highly reactive nitrile imine dipolar species, which readily undergo 1,3-dipolar cycloaddition with alkenes present in a biological system. This powerful method of biological tagging has been applied for proteome profiling in living cells.[208–210] The utility of this photoinduced cycloaddition reaction for selective labelling of proteins *in vivo* was first demonstrated in *Escherichia coli*, known to overexpress an alkene-containing protein (Scheme 1.27).[211]

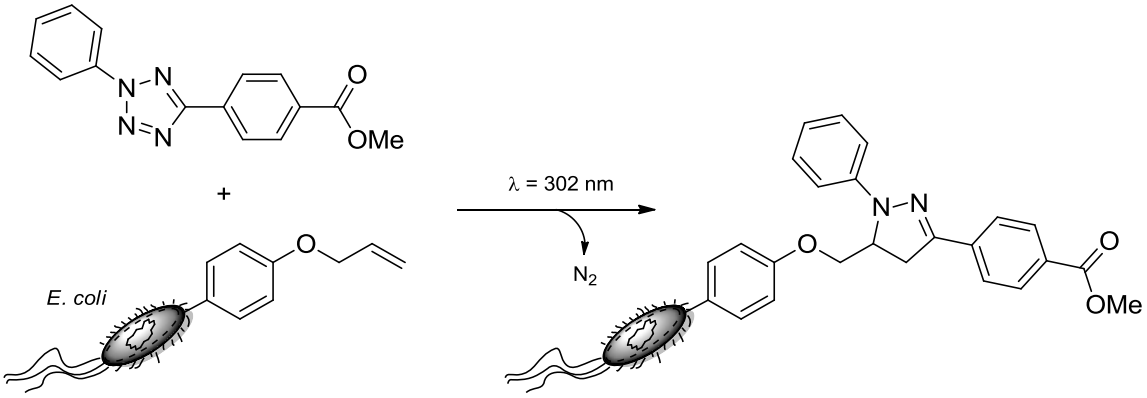

Scheme 1.27 – Representation of the 1,3-dipolar cycloaddition reaction between a nitrile imine dipole, photogenerated *in situ* from a 2,5- disubstitited tetrazole, and an alkene moiety, linked to a protein of *E. coli*.[211]

In order to adjust and optimize this promising tagging methodology, a deep understanding of the light-induced processes involved in the generation of the reactive nitrile imines is required. As such, several studies were recently conducted on the photolysis of 2,5-disubstituted tetrazoles under low-temperature matrix-isolation conditions, which seems to be an efficient way to generate, capture and characterize unstable nitrile imines.[166–170,172,174] The results have shown that the substituents play a major role on the structural characteristics of nitrile imines, this being particularly noticeable by the υCNN anti-symmetric stretching infrared absorption of the nitrile imine moiety, which appears over a wide range of frequencies (2000-2250 cm^{-1}). Given the relevance of nitriles imines, a brief analysis of the structure of these reactive intermediates is provided in this section.

i. Nitrile imines may assume 6 canonical forms

Six canonical structures with different weights have been considered for the description of nitrile imines (Figure 1.17). Characterization of the electronic structure of nitrile imines with combination of density-functional theory (DFT) and natural resonance theory (NRT) has shown that a complete description of nitrile imines requires a combination of four major resonance structures: allenic, propargylic, 1,3-dipolar and carbenic (Figure 1.17).[212] It was proposed that nitrile imines with IR absorptions above 2200 cm^{-1} have essentially propargylic character, possessing a CN triple bond, while those with IR absorptions below *ca.* 2200 cm^{-1} are more likely to be of allenic character.[174] Furthermore theoretical studies have indicated that substituents bearing a lone-electron pair should increase the importance of the carbenic resonance structure of nitrile imines.[212–214] These postulated carbenic nitrile imines were predicted to lack the intense IR absorption in the 2000–2250 cm^{-1} region that characterizes other nitrile imines. Instead, moderate IR intensities below 2000 cm^{-1} are expected for carbenic nitrile imines.[213]

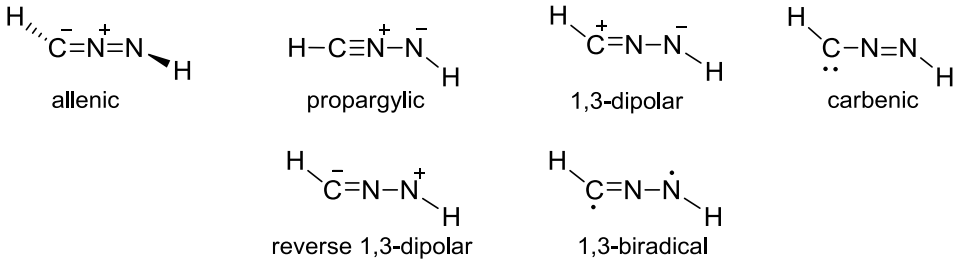

Figure 1.17 – Representation of six different structures of parent nitrile imine.[212]

ii. Co-existence of allenic and propargylic forms of nitrile imine (the case of 5-phenyl-2*H*-tetrazole)

Photolysis of matrix-isolated 5-phenyl-2*H*-tetrazole **98** (Scheme 1.28) generated two forms of *C*-phenylnitrile imine co-existing in two different structures: allenic **99** and propargylic **100**.[167] Spectroscopic results demonstrated that **99** and **100** are distinct species and allowed to obtain their individual IR signatures. For the allenic form **99**, the a band was observed at ~2070 cm^{-1}, corresponding to the antisymmetric stretching of the CNN moiety, while for the propargylic form **100**, a band was observed at ~2239 cm^{-1}, corresponding to the υC≡N stretching mode, in agreement with the postulated range of frequency for each form of nitrile imine (allenic < 2200 cm^{-1} < propargylic). Calculations at several levels of theory confirmed that the generated forms are not resonance structures but correspond to two distinct

energy minima, representing bond-shift isomers.[167] Upon further photolysis both of them convert into 3-phenyl-1*H*-diazirine **101** at different rates. The diazirine undergo subsequent photoconversion into *N*-phenylcarbodiimide **102**. Also a small amount of *N*-phenylcyanamide **103** was observed due to tautomerization of **102** (Scheme 1.28).[167,174]

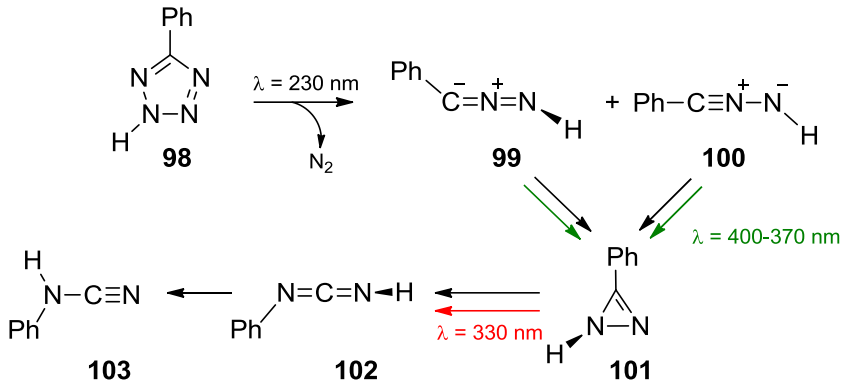

Scheme 1.28 – Representation of allenic and propargylic phenylnitrile imines captured during photolysis of 5-phenyl-2*H*-tetrazole isolated in solid argon and krypton upon irradiation with UV light (λ = 230 nm, λ = 330 and λ = 400-370 nm).[167]

iii. Carbenic form of nitrile imine (the case of 5-aminotetrazole)

Photolysis of 5-aminotetrazole **104** in an argon matrix allowed to capture the *C*-amino nitrile imine **105** as the primary photoproduct (Scheme 1.29).[166] The experimental frequency of the υCNN mode was observed at 1998 cm^{-1}. In agreement with the postulated range of frequency for each form of nitrile imine (allenic < 2200 cm^{-1} < propargylic and carbenic < 2000 cm^{-1}), these spectroscopic results suggests a significant carbenic character of the *C*-amino nitrile imine **105**. Accordingly, the analysis of the electronic structure using natural resonance theory (NRT), showed a contribution of around 20% of the carbenic resonance hybrid.[166]

These experiments also revealed two different pathways for the photochemistry of this nitrile imine **105**; the usual isomerization route to 1*H*-diazirine **106** and subsequent rearrangement to carbodiimide **107**, and a new route to methylenimine **79**, ascribed as a result of the carbenic character of the *C*-amino nitrile imine **105**.[166]

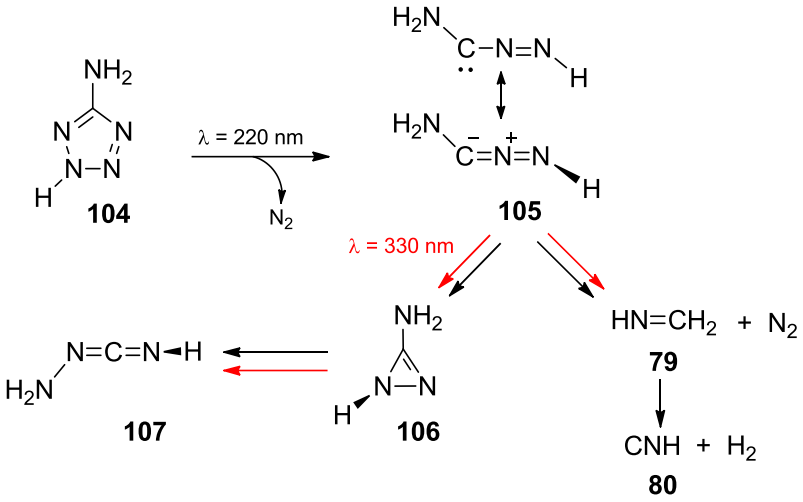

Scheme 1.29 – Representation of the photochemical reactions observed for 5-aminotetrazole isolated in solid argon upon irradiation with UV light (λ = 220 nm and λ = 330 nm).[166]

iv. 1*H*-diazirines (the case of 5-methyl-tetrazole)

In the photochemical study of the parent tetrazole **2** (Scheme 1.20), Maier *et al.* have identified four CH_2N_2 isomers after photolysis of the matrix-isolated compound: the nitrile imine **60**, carbodiimide **63**, cyanamide **64**, and diazomethane **62**.[188] More than a decade later, Bégué *et al.* investigated the thermolysis and photolysis of several 2-substituted-5-phenyltetrazoles (**108**; R^1 = Ph; R^2 = H, Me, Ph, $SiMe_3$) and postulated a general photofragmentation pattern (Scheme 1.30), with generation of short-lived nitrile imines **109** by extrusion of N_2, which rearrange to carbodiimides **112**. A 4π-electron three-membered-ring, the 1*H*-diazirine **110**, have been postulated to play a key role in the photolysis of tetrazoles, allowing the rearrangement of the initial formed nitrile imine **109** to the final carbodiimide **112**.[174] However only very recently, in a detailed study on the photochemistry of 5-methyl tetrazoles (**108**; R^1 = Me, R^2 = H), under low-temperature matrix isolation conditions, Claudio *et al.*[169] clearly proved that the elusive 1*H*-diazirine **110** can be generated photochemically from nitrile imines **109** and undergo subsequent photoconversion into carbodiimides **112**. It was also shown that 1*H*-diazirines **110** exhibit a close structural relation to imidoylnitrenes **111**, a postulated intermediate in this reaction. As a general case, all nitrile imines where reported to isomerize to the corresponding carbodiimides, both thermally and photochemically.

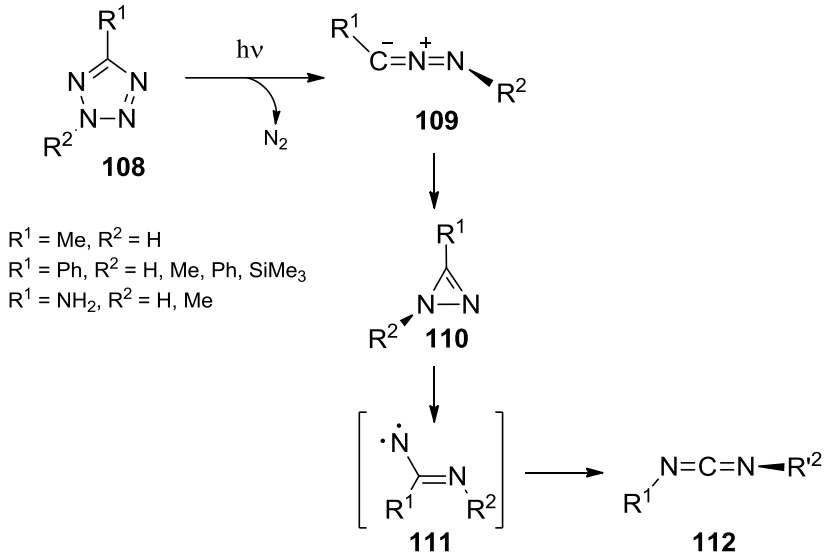

Scheme 1.30 – Representation of the general photochemical reactions observed for 2,5-disubstituted tetrazoles in solid argon upon irradiation with UV light.[174]

Most studies directed to the use of tetrazoles as photoprecursors of reactive intermediates and unusual molecules are based on 2,5-disubstituted tetrazoles,[166–170,172,174,188] Even in 5-substituted tetrazoles, where the tetrazole ring bears a labile hydrogen as substituent, it was observed that the 2*H*-tautomer **108** was the predominant form isolated in the matrix,[166,169,174] in keeping with the behaviour observed for the parent tetrazole.[188] Thus, the matrix photochemistry of 1,5-disubstituted tetrazoles remains mostly unexplored, apart from the work by Begué *et al.* on the photolysis of 1-methyl-5-phenyltetrazole **113** (Scheme 1.31), where the formation of a carbodiimide **115** as the final photoproduct was demonstrated but no intermediates were detected, although imidoylnitrene **114** was assumed to be an intermediate of the reaction.[174]

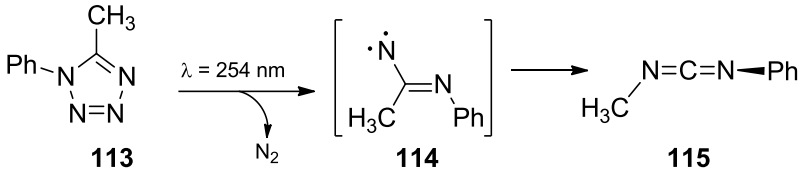

Scheme 1.31 – Representation of the photochemical reaction observed for 1-methyl-5-phenyltetrazole in solid argon upon irradiation with UV light (λ = 254 nm).[174]

In chapter 4 of this thesis we will address this topic, presenting for the first time the intermediates generated from the photolysis of a 1,5-disubstituted tetrazole in solid argon.

1.2. Benzisothiazoles (saccharin derivatives)

1.2.1. Saccharin; general information

1,2-Benzisothiazol-3(2*H*)-one-1,1-dioxide, also known as saccharin, **116** (Figure 1.18), was discovered accidentally by Fahlberg in 1878 during investigations on the oxidation of *o*-toluenesulfonamide.[215–217]

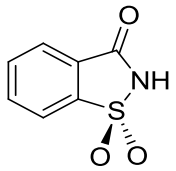

116

Figure 1.18 – Representation of structure of 1,2-benzisothiazol-3(2*H*)-one-1,1-dioxide (saccharin)

Shortly after its discovery and the acknowledgement of its potential as an artificial sweetener, saccharin was produced on an industrial scale (1887) as the first sweetening agent which was not a carbohydrate.[216] Saccharin has been commonly used as a non-caloric artificial sweetener, normally in the form of the sodium or calcium salt, being the principal sweetening component of diabetic diets.[218] In the 1970s there was some basis of concern regarding saccharin when a study showed that rats given high doses developed bladder cancer.[219] In following years, discussions on the health risks of saccharin were present in both the scientific reports and the informative media. In 2000 the US National Toxicology Program removed saccharin from the list of carcinogens and, finally, in 2010 the EPA (United States Environmental Protection Agency) stated that saccharin is no longer considered a potential hazard to human health.[220]

Investigations on the interaction of saccharin with different biologically relevant cations attracted great interest due to the suspected carcinogenicity of this compound.[221,222] These studies have shown that the coordination chemistry of saccharin is very interesting and versatile, since the saccharinate anion, obtained by deprotonation of the *NH*-group, offers different coordination sites to metallic centres, *i.e.* one *N*, one *O* (carbonylic) and two *O* (sulfonic) atoms. As a polyfunctional ligand, deprotonated saccharin (sac) can exist as an ion or it can be incorporated into a complex as a ligand. Is has also been found that in some compounds the saccharinate anion can be present both as ligand, in the coordination complex, and as a counter-ion, outside the coordination sphere.[206]

1.2.2. Complexes based on saccharin

1.2.2.1. Saccharin-based monodentate *N*-coordinated metal complexes

The reaction of sodium saccharinate with the first row divalent metal ions, from V(II) to Zn(II), results in isomorphous coordination compounds with the formula $[M(sac)_2(H_2O)_4]\cdot 2H_2O$.[206] All these divalent metal cations show a clear preference to interact with the saccharinate anion, through its deprotonated and negatively charged *N*-atom. The crystal structures of these $[M(sac)_2(H_2O)_4]\cdot 2H_2O$ species were investigated and fit in with the general structure represented in Figure 1.19, showing that these octahedral complexes contain two *N*-bonded saccharinate ligands in trans positions.

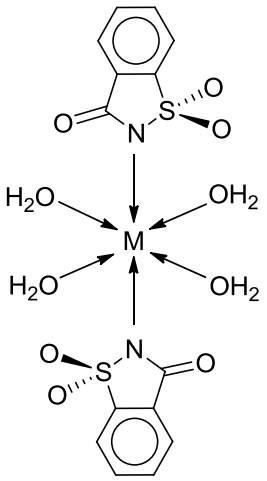

Figure 1.19 – Representation of the structure of the $[M(sac)_2(H_2O)_4]\cdot 2H_2O$ complexes (M^{II} = V, Cr, Fe, Co, Ni, Cu and Zn).

1.2.2.2. Saccharin-based monodentate *O*-coordinated metal complexes

As a ligand, the saccharinate anion offers two different donor *O*-atoms, from the carbonyl and sulfonyl groups. The latter is less basic and is rarely involved in bonding but the former often participates in coordination, with the anion acting as a chelating or bridging ligand. Monodentate coordination of the carbonyl *O*-atom is rather unusual and is found when branched or bulky co-ligands are present. This type of coordination was first observed in vanadium(II) complexes $[V(sac)_2(py)_4]\cdot 2py$. The general structure of this type of vanadium(II) and nickel(II) complexes, represented in Figure 1.20, shows that the saccharinate (sac) ligands are forced to bind via the carbonyl group when the equatorial plane of the octahedron is occupied by four planar pyridine rings (py).[223]

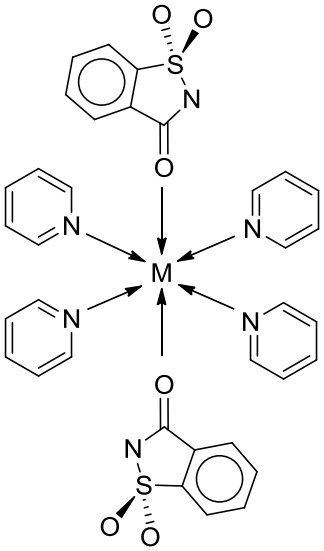

Figure 1.20 – Representation of the structure of the mixed ligand $[M(sac)_2(py)_4]$ complexes (M^{II} = V and Ni)

1.2.2.3. Saccharin-based multidentate *N, O*-coordinated metal complexes

Another possibility is the simultaneous coordination of various donor sites of saccharinate where the ligand can act either as a bidentate ligand for only one metal centre or as a bridging ligand between two or more metal ions (*Modes* III-IX, Figure 1.21).[206]

Since the saccharinate anion acts as a polyfunctional ligand it is capable not only to interact with metal centres in different ways, but also to generate relatively strong interactions in the crystalline environments, mostly through hydrogen bonding. Diverse forms of ligand-to-metal interactions of saccharinate anion **117** are summarized in Figure 1.21.

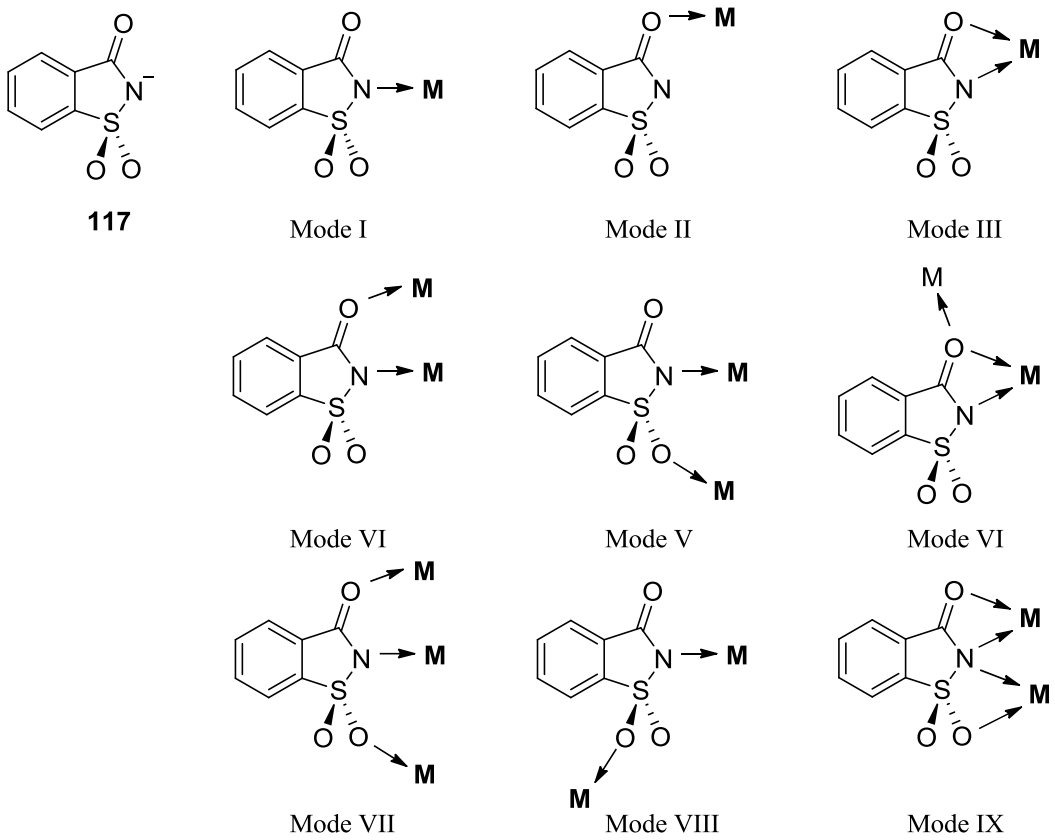

Figure 1.21 – Representation of bridging coordination modes of saccharinate ligands

1.2.2.4. Biological effects of saccharinate complexes

Besides their properties as sweetener, saccharin and saccharin-based complexes exhibit activity towards biological targets. One example is carbonic anhydrase IX (CA IX), a key modulator of aggressive tumour behaviour and a prognostic marker and target for several cancers. This metalloenzyme, similar to other isoforms, catalyses the interconversion of carbon dioxide and water to bicarbonate and a proton, essential for pH regulation.[224] Inhibition of CA IX activity has shown to reduce tumour growth and proliferation, and also enhance common chemo- and radiation therapies.[225] The complexes $[Zn(sac)_2(H_2O)_4]\cdot 2H_2O$ and $[Cu(sac)_2(H_2O)_4]\cdot 2H_2O$ showed inhibitory effect, *in vitro*, over carbonic anhydrase.[226] More recently it has been shown that saccharin selectively binds to CA IX at nanomolar concentrations, acting as an efficient inhibitor of the carbonic anhydrase IX.[227] It was postulated that saccharin coordinates as the saccharinate anion, through its nitrogen atom, to the catalytically active zinc ion present in the binding pocket of the metalloenzyme (Figure 1.22).

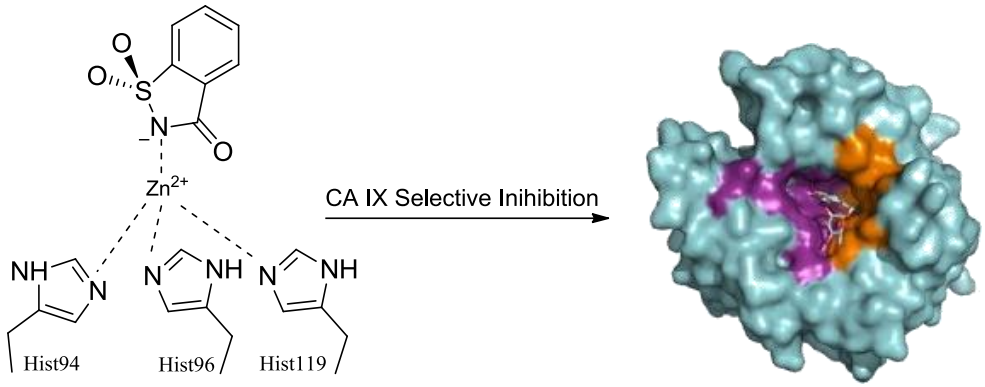

Figure 1.22 – Representation of the coordination of saccharinate with the catalytically active zinc ion present in the biding pocket of the carbonic anhydrase IX.

The superoxide dismutase-like activity of a series of divalent metal aqua-saccharinato complexes of the type $[M(sac)_2(H_2O)_4]\cdot 2H_2O$ (with M^{II} = Mn, Fe, Co, Ni, Cu and Zn) has been investigated. The results show that all these complexes, can mimic the metalloenzyme superoxide dismutase (SOD), with the ability to dismutate the superoxide O_2^{-}.[228]

It was also suggested that saccharin may be potentially useful as an antidote for metal poisoning. Although this property has not been explored in detail, it becomes apparent that the stability of certain polymeric saccharinato complexes, for example, those of Pb(II), Tl(I) or Ag(I) generates very good perspectives in this context, suggesting the potential uses of saccharinate as ligand for chelation therapies.[229,230]

1.2.3. Photochemistry of benzisothiazoles

In general, benzisothiazoles (saccharins) are known to be photostable, especially if compared, for instance, with tetrazoles. As such, the number of reports on the photochemistry of benzisothiazoles, is restricted to only a few papers. Early works on the photochemistry of *N*-alkylsaccharins **118** suggested that photolysis (λ = 254 nm) of these compounds in ethanol, leads to cleavage of the *S*-*N* bond followed by elimination of sulphur dioxide, resulting in formation of *N*-alkylbenzamide **120** (Scheme 1.32).[231,232] Later, the photochemistry of 3,3-disubstituted-2,3-dihydro-1,2-benzisothiazole-1,1-dioxides **121** was investigated, (λ = 254 nm) in methanol (Scheme 1.33). Results suggested two different photochemical pathways, both generating cyclic *N*-hydroxysulfinamides **124** as final product: (a) in most cases the light induced reactions appeared to be initiated by *S*-*N* homolysis, through formation of intermediate biradical **122**, which seems to be vital for these processes; (b) a different photochemical process was proposed, involving a formal oxygen shift from *S* to *N via* the zwitterionic intermediate **123**.[233,234]

More recently, an investigation of the photochemistry of *N*-[(trimethylsilyl)alkyl]saccharins (**118**, R = $CH_2CH_2SiMe_3$) in solution showed that, upon excitation, the photoreactivity of these compounds can take place either *via* single electron transfer (SET) promoted *C*-to-*O* silyl transfer pathway or by a route involving *S*-*N* homolysis, the relative contribution of each pathway being governed by the polarity of the medium and the nature (*e.g.* protic nature) of the solvent.[235]

As a whole, the studies mentioned indicate that the photochemistry of saccharyl derivatives in solution is determined by the structure of the saccharyl ring, the nature of the substituents, and the reaction media.

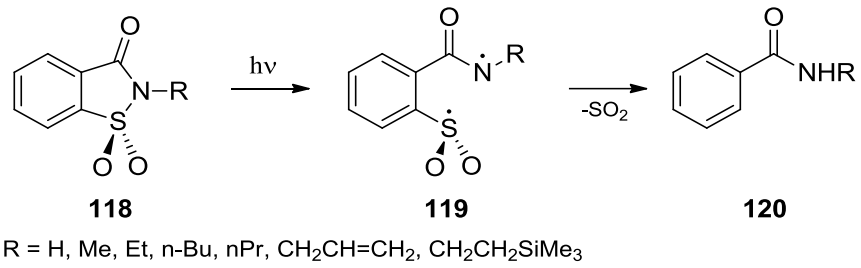

Scheme 1.32 – Representation of the photocleavage reactions observed for *N*-alkylsaccharins (λ = 254 nm).[231]

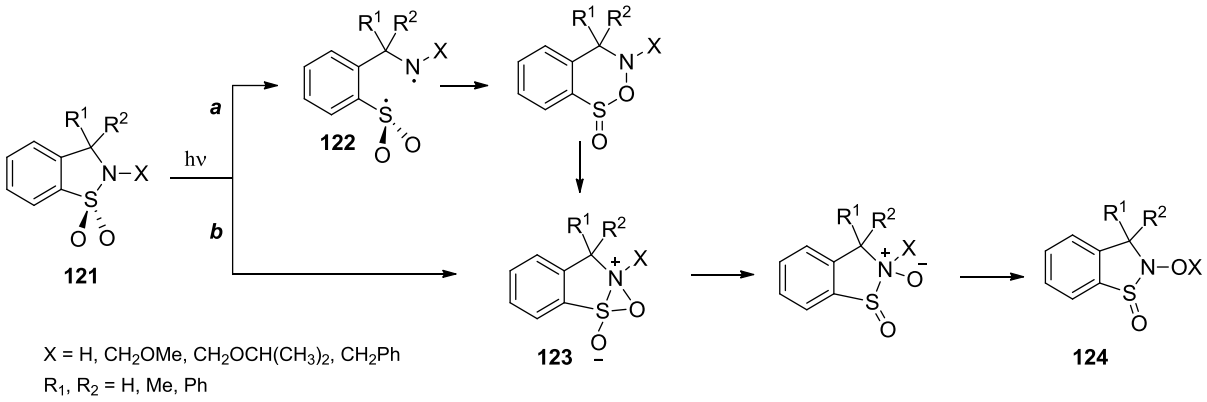

Scheme 1.33 – Representation of the photochemical isomerisations observed for 3,3-disubstituted-2,3-dihydro-1,2-benzisothiazole-1,1-dioxides upon UV-induced irradiation (λ = 254 nm).[233]

The photocleavage of the benzisothiazole ring in the rigid environment of an argon matrix was observed for the first time for the monomeric tetrazole-saccharyl conjugate **93** (Scheme 1.26).[173] The results, discussed in section 1.1.7.6, *ii*, have shown that the photoreactivity of compound **93** is mostly determined by the photolability of the tetrazole ring but also proved the presence of a photodegradation channel, involving the saccharyl moiety, that resulted in 7-thia-8-azabicyclo[4.2.0] octa-1,3,5-triene 7,7-dioxide **96**.

More recently, the photochemistry of monomeric saccharin isolated in solid argon was investigated.[207] Upon UV irradiation at λ= 290 nm, saccharin **116** isomerised to a new compound, iso-saccharin **125** (Scheme 1.34). The structures of the isomers, saccharin and iso-saccharin, where investigated theoretically. Because both isomers bear labile hydrogen atoms, the conjugate bases of saccharin and iso-saccharin were also theoretically investigated. Their free energies and dipole moments suggest that both anions may play a relevant part in systems where saccharin participates, as is the case of the recently proposed saccharin-based ionic liquids.[207]

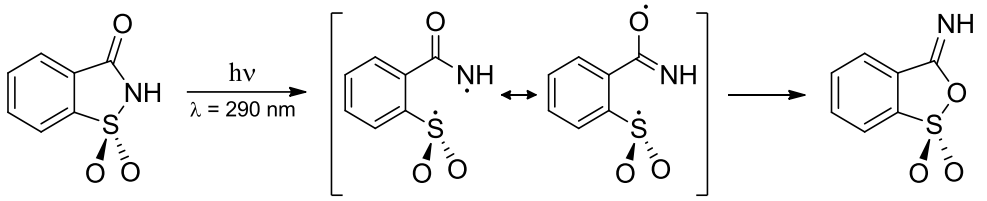

116 **125**

Scheme 1.34 – Representation of the UV-induced photoisomerization reaction observed for saccharin (λ= 290 nm).[207]

Although the saccharyl system appears to be relatively photostable, the results described above set some boundaries to the use of saccharins. Nevertheless, a deeper knowledge of the photoreactivity of saccharin-based systems would be welcome, since most known applications of saccharin and saccharyl derivatives rely on the thermal and photochemical stability of the saccharyl system, and a better insight on the structure and chemical reactivity of saccharin-based systems will help to improve the sustainability and reliability, in present and potentially new applications.

1.3. Computational Chemistry

Computational chemistry is a branch of chemistry that uses computer simulations to assist in solving chemical problems. The use of computational methods can simplify significantly the interpretation of results obtained from experimental studies. It is in general possible nowadays to find a suitable method with a level of calculation adequate to the study of the desired systems or properties. Examples of such properties are structure, absolute and relative energies, transition states, electronic charge density distributions, reaction pathways, kinetics and mechanisms, dipole moments, vibrational frequencies, electronic transitions and other spectroscopic quantities.[236]

The most accurate molecular models use *ab initio* electronic structure methods, based entirely on quantum mechanics and basic physical constants. However, these are usually feasible only for small systems and are generally very computer-intensive. Other methods, called semi-empirical, use additional parameters obtained from empirical data in order to simplify the calculation and achieve a faster solution, therefore using much less computational resources than *ab initio* calculations. Molecular mechanics methods are also applied in cases where details of electronic structure are less important than the long-time phase space behaviour of molecules. These molecular mechanics methods use classical approximations to the potential energy surface, which are computationally less intensive than electronic calculations, and enable longer simulations of molecular dynamics, as is the case of approach and interaction studies (docking) of proteins and potential drug molecules.[237,238]

***Ab initio* calculations**

Methods that do not include any empirical or semi-empirical parameters in their equations, being derived directly from theoretical principles, are called *ab initio* methods. In principle, *ab initio* methods eventually converge to the exact solution of the underlying equations as the number of approximations is reduced. In practice, however, it is impossible to eliminate all approximations, and residual errors inevitably remain.

The general objective of quantum chemical methods is the solution of the time-independent Schrödinger equation (1.1).[239] In this equation, $\hat{H}$ is the Hamiltonian operator, Ψ is the molecular wave function for all electrons and nuclei in the molecule, and E is the total energy associated to this wave function.

$$\hat{H}\Psi = E\Psi \qquad (1.1)$$

Solutions of the time-independent Schrödinger equation represent various stationary states of the molecule (corresponding to stable or meta-stable electronic configurations). The set of wave functions Ψ which satisfy equation (1.1) are its eigenfunctions, and the energies of the molecule, E, in each stationary state are its eigenvalues. The stationary state with the lowest energy is called the 'ground state'.

The major difficulty in solving equation (1.1) is the interaction between electrons. Since the motion of the electrons is correlated one should know the instantaneous coordinates of each electron, which essentially requires the treatment of 3^n variables for an n-electron system.

Despite the almost intractable nature of these interactions, many approximate methods have been developed to solve the Schrödinger-like equation by mapping the *n* electrons into an effective one-electron Schrödinger-like equation, which are easier to approach. The different approximate methods, can be divided in to two major categories: (i) the wave function based methods, where the *n*-electron wave function is the key (*e.g.* Hartree-Fock (HF) and post-Hartree-Fock methods); and (ii) density-functional theory (DFT), in which electron density is the central quantity.

Born-Oppenheimer Approximation

The very essence of the Born-Oppenheimer approximation comes from the fact that the nuclei are much heavier than the electrons. Even for the lightest nucleus, a proton, its mass is approximately 2000 times larger than that of the electron. So, in most cases the timescale of the response of the electrons is a few orders of magnitude faster than that of the nuclei, which allows the dynamics of the electrons and nuclei to be decoupled. Through this simple approximation, nuclei can be treated as classical particles and can be considered as static with respect to quantum particle electrons. Then, for any given nuclear configurations, the electrons are assumed to remain in their instantaneous ground state.[240]

1.3.1. Hartree-Fock method

The Hartree-Fock (HF) method is typically used to solve the time-independent Schrödinger equation for a multi-electron atom or molecule as described in the Born-Oppenheimer approximation. This approximation was introduced to separate the nuclear and the electronic motion.[240] One can consider the electrons in a molecule to be moving in the field of fixed nuclei. Consequently, the kinetic energy of the nuclei can be neglected and the repulsion between the nuclei E_{NN} can be considered to be constant.

In Hartree-Fock (HF) theory the energy of a system is given as a sum of five components:

$$E_{HF} = E_{NN} + E_T + E_V + E_{coul} + E_{exch} \qquad (1.2)$$

The nuclear-nuclear electrostatic repulsion E_{NN}, the kinetic energy of electrons (motion of electrons) E_T, the attraction of electrons to nuclei E_V, the classical electron-electron Coulomb repulsion E_{coul} and the non-classical electron-electron exchange energy E_{exch}. The particular approximation made in HF theory, for *n* electrons systems, is that each electron feels the other electrons only as an average charge cloud, and not as individual electrons. The wave function

is than taken as a single product of *n* one-electron wave functions called "orbitals", which is known as a Hartree product:

$$\Psi(r) = \Phi_1(r_1)\,\Phi_2(r_2)\ldots\,\Phi_n(r_n) \qquad (1.3)$$

In order to fulfill the Pauli exclusion principle, the wave function must be antisymmetric with respect to the exchange of the positions (and spin) of any two electrons, a Hartree-Fock wavefunction is constructed by assigning electrons to molecular orbitals $\Phi(r)$ in pairs of opposite spin, and then forming a determinant using two spin functions α and β, where:

$$\begin{aligned} \alpha(\uparrow)&=1 \qquad & \alpha(\downarrow)&=0 \\ \beta(\uparrow)&=0 \qquad & \beta(\downarrow)&=1 \end{aligned} \qquad (1.4)$$

Slater determinant

In the HF approach the wave function of interacting *n*-electrons, $\Psi(r)$ can be approximately described with a single Slater determinant. A Slater determinant is a linear combination of the product of independent electron wave functions (also known as spin orbitals) with all possible combinations of the permutations of their coordinates. For a molecule containing *n* electrons, the wavefunction takes the form:

$$\Psi(r) = \frac{1}{\sqrt{n!}} \begin{vmatrix} \Phi_1(r_1)\alpha(1) & \Phi_1(r_1)\beta(1) & \ldots & \Phi_{\frac{n}{2}}(r_1)\alpha(1) & \Phi_{\frac{n}{2}}(r_1)\beta(1) \\ \Phi_1(r_2)\alpha(2) & \Phi_1(r_2)\beta(2) & \ldots & \Phi_{\frac{n}{2}}(r_2)\alpha(2) & \Phi_{\frac{n}{2}}(r_2)\beta(2) \\ \vdots & \vdots & & \vdots & \vdots \\ \Phi_1(r_n)\alpha(n) & \Phi_1(r_n)\beta(n) & \ldots & \Phi_{\frac{n}{2}}(r_n)\alpha(n) & \Phi_{\frac{n}{2}}(r_n)\beta(n) \end{vmatrix} \qquad (1.5)$$

The best possible one-electron wavefunctions, by definition, will give the lowest possible total energy for a multi-electron system when combined into a Slater determinant and used with the complete multi-electron Hamiltonian to calculate the expectation value for the total energy of the system. These wavefunctions are called the Hartree-Fock wavefunctions and the calculated total energy is the Hartree-Fock energy of the system. Application of the variational method to the problem of minimizing the total energy leads to Schrödinger-like equations called Hartree-Fock equations:

$$\hat{f}\Phi_i = \varepsilon_i \Phi_i \qquad (1.6)$$

where $\hat{f}$ is called Fock operator, ε is the energy of orbital *i*, and Φ represents the molecular orbital. Each molecular orbital (holding one electron) can then be expressed as a linear combination of atomic orbitals (LCAO) called *basis sets*:

$$\Phi_i = \sum c_{\mu i}\chi_\mu \qquad (1.7)$$

The molecular orbital coefficients $c_{\mu i}$ describe the contribution of each of the basis functions χ_μ to a given molecular orbital Φ_i.

Self-Consistent Field (SCF)

The problem to obtain the molecular orbitals Φ_i is that the Fock operator $\hat{f}$ depends on the orbitals. In other words, we need to know the solution to this equation in order to solve the equation. A procedure to overcome this situation, is to make a guess at the initial orbitals. Then these orbitals are used to construct the Fock operator that is used to solve for new orbitals. The new orbitals then are used to construct a new Fock operator, and the process is repeated until no significant change in the orbital energies ε_i or functions occurs. The solution is then self-consistent, and therefore the method is called the *self-consistent field* (SCF).

Roothaan-Hall developed a procedure, based on the matrix form, to solve the Hartree-Fock equations:

$$FC = SC\varepsilon \qquad (1.8)$$

where *F* is the so-called Fock matrix, *C* is a matrix of coefficients, *S* is the overlap matrix of the basis functions, and ε is the matrix of orbital energies.[241]

With the increase flexibility of the wavefunctions by introducing additional parameters to the orbitals used in Hartree-Fock calculations, we can expect better and better energies. The variational principle says that any approximate energy calculated using the exact Hamiltonian is an upper bound to the exact energy of a system, so the lowest energy that we calculate using the Hartree-Fock method will be the most accurate. At some point, the improvements in the energy will be very slight. This limiting energy is the lowest that can be obtained with a single

Slater determinant wavefunction, and is called the Hartree-Fock limit. The energy is the Hartree-Fock energy, the orbitals producing this limit are by definition the best single-electron orbitals that can be constructed and are called Hartree-Fock orbitals, and the Slater determinant is the Hartree-Fock wavefunction.

1.3.2. Basis sets

Basis set is a mathematical description of the atomic orbitals (AOs) within a system, expanded as linear combinations used to approximate the electronic wave function. These atomic orbitals are well described with "Slater Type Orbitals" (STOs), however the two-electron integrals require excessive computer time. Nowadays, "Gaussian Type Orbitals" (GTOs) are often used as basis functions to simulate the STO functions, because it is easier to calculate, leading to huge computational savings. However, the price we pay is loss of accuracy. To compensate for this loss, larger basis set can be used, approximating more accurately the orbitals by imposing fewer restrictions on the locations of the electrons in space.

Standard basis sets use linear combinations of basis functions (also called "contracted Gaussian functions") to form the orbitals. These basis functions are themselves composed of a linear combination of Gaussian functions referred as "primitives".[237,242]

The smallest of these basis sets are called "minimal basis sets", and they are typically composed of the minimum number of basis functions required to represent all of the electrons on each atom. All basis set equations in the form STO-NG (where N represents the number of GTOs combined to approximate the STO) are considered to be minimal basis sets. For instance, STO-3G is a minimal basis set which combines three Gaussian primitive functions for each basis function.[243]

The "extended basis sets", then, are the ones that consider the higher orbitals of the molecule and account for size and shape of molecular charge distributions. The largest of these can contain dozens to hundreds of basis functions on each atom. With the minimal basis sets, all orbitals are approximated to be of the same shape. Therefore, to have a more accurate representation of each orbital, the double zeta (DZ, *double*-ζ) and triple zeta (TZ, *triple*-ζ) type basis are included, which uses two and three sets of basis functions for each atomic orbital (AO). These type of bases are usually calculated for the valence orbitals. Since the inner-shell electrons aren't as vital to the calculation, they are described with a single basis function. This method is called a "split valence basis set". A few examples of common split valence basis sets are 3-21G, 4-31G, 6-31G and 6-311G. For example using a 3-21G basis set (*double*-ζ) to

calculate a carbon atom, this means we are summing 3 gaussians (Gaussian primitive functions) for the inner shell orbital (1s), 2 gaussians for each of the 4 first basis functions (2s,2px,2py,2pz) of the valence shell and 1 additional gaussian for each of the 4 second basis functions (2s',2px',2py',2pz'), in a total of 9 basis functions (constructed of 15 primitive Gaussian functions).

Split valence basis sets can be improved by adding polarization functions, *e.g.*, 6-31G(d) or 6-31G* which, for elements of the first and second row, include d-type orbitals to describe the heavy atoms, while 6-31G(d,p) or 6-31G** also include p-type orbitals to describe the hydrogen atoms in addition to the d-type orbitals to describe the heavy atoms. Polarized basis sets add orbitals with angular momentum going beyond of requirement for the proper description of the ground state of each atom, taking account the fact that sometimes orbitals share of 's' and 'p' orbitals or 'p' and 'd', *etc*., and not necessarily have characteristics of only one or the other. As atoms are brought close together, their charge distribution causes a polarization effect which distorts the shape of the atomic orbitals. In addition, diffuse functions can also be added, denoted by + or ++, that consist of s-type and p-type orbitals to describe the heavy atoms and the hydrogen atoms. Diffuse functions are necessary for correct description of anions and weak bonds, and are frequently used for calculations of properties such as dipole moments, polarizabilities, hydrogen bonds, *etc.*[237,242]

1.3.3. Correlated methods; beyond Hartree-Fock

1.3.3.1. Electronic correlation methods

The energies extracted from the Hartree-Fock method have always an associated error, because the instantaneous correlation of the motions of electrons is neglected, and the method only treats it as an average. The neglect of electronic correlation has been blamed for systematic HF errors such as underestimated bond lengths and overestimated vibrational frequencies. Calculations added to HF-SCF theory to remedy these errors are termed 'electronic correlation' or 'post-HF' methods. Most of these methods require more flexible wave functions than that of a single determinant HF and usually this is obtained by means of excitations of electrons from occupied to virtual orbitals.

These methods include configuration interaction (CI), Møller-Plesset (MP) perturbation theory, and coupled cluster (CC). For CI methods, a linear combination of ground-state and excited state Slater determinants is used rather than one single Slater determinant as in HF to approximate the wave function. Møller-Plesset perturbation theory, as the name suggests, treats

electron correlation in a perturbative manner. And in the coupled cluster method, the electron correlation is handled through use of a so-called cluster operator. These methods were not used in this thesis, thus they will not be further discussed.

1.3.3.2. Density Functional Theory

Density functional theory (DFT) methods are nowadays the most widespread methods used in computational science and solid state physics, due to their high computational efficiency and very good accuracy compared to HF or MP methods.[236,237,242]

DFT differs from the, previous discussed, wave function based methods by using the electron density $\rho(\vec{r})$ as the central quantity. An important advantage of using the electron density over the wave function is the much reduced dimensionality. Regardless of how many electrons one has in the system, the density is always 3 dimensional. This enables DFT to readily be applied to much larger systems, hundreds or even thousands of atoms become possible.

Hohenberg-Kohn Theorems

The Hohenberg-Kohn theorems were able to relate the energy and other properties of the system with the electron density. The first theorem (*Existence Theorem*) demonstrates that all the properties of a molecule in the ground electronic state are uniquely defined by its electron density. Although, the first theorem confirms the existence of a functional relating the electron density and the energy of a system, it does not tell us the form of such functional. The second theorem (*Variational Theorem*) states that the functional that delivers the ground state energy of the system delivers the lowest energy if and only if the input density is the true ground state density.[244]

Kohn and Sham approach

Nowadays, DFT calculations are based on the Kohn and Sham approach, which allowed to overcome the difficulty related to the kinetic energy functional of the system. The basic idea in the Kohn and Sham formalism is splitting the kinetic energy functional into two parts, one part that can be calculated exactly, which considers non-interacting electrons, and a small correction term accounting for electron-electron interaction.[245]

The main advantage of DFT is that the energy of an electronic system can be defined in terms of its electronic probability density. For a system with n electrons, $\rho(\vec{r})$ represents the total electron density at a particular point in space. The electronic energy E is regarded as a

functional of the electron density, $E[\rho]$. In density functional theory (DFT) the energy of a system, regarded as a functional of the electron density $E[\rho]$, is given as a sum of six terms:

$$E(\rho) = E_{NN}(\rho) + E_T(\rho) + E_V(\rho) + E_{coul}(\rho) + E_{exch}(\rho) + E_{corr}(\rho) \qquad (1.9)$$

The definitions for the nuclear-nuclear repulsion E_{NN}, the nuclear-electron attraction E_V, and the classical electron-electron Coulomb repulsion E_{coul} energies are the same as those used in Hartree-Fock theory. The kinetic energy of the electrons E_T as well as the non-classical electron-electron exchange energies E_{exch} are, however, different from those used in Hartree-Fock theory. The last term E_{corr} describes the correlated movement of electrons of different spin and is not accounted for in Hartree-Fock theory. Due to these differences, the exchange energies calculated exactly in Hartree-Fock theory cannot be used in density functional theory.

Exchange-Correlation Functionals

Various approaches exist to calculate the exchange and correlation energy terms in DFT methods. These approaches differ in using either only the electron density (local density approximation, LDA) or the electron density as well as its gradients (generalized gradient approximation, GGA). Aside from these "pure" DFT methods, another group of hybrid functionals exists, in which mixtures of DFT and Hartree-Fock exchange energies are used.[246]

For example, the gradient-corrected density functional method BLYP (combines Becke's gradient-corrected exchange functional with the gradient-corrected correlation functional of Lee, Yang and Parr.[247] However, the generalised gradient approximation severely underestimates activation barriers for some reactions due to neglect of Coulomb 'self-interaction' of the electrons.[248] This problem is solved with hybrid methods that combine Hartree-Fock self-interaction corrections with density functional exchange and correlation, *e.g.*, B3LYP, where B3 denotes Becke's three-parameter hybrid functional,[249] while 'LYP' is the gradient-corrected correlation functionals of Lee, Yang and Parr.[247] The B3LYP method is undoubtedly one of the most widely used methods in computational chemistry. Generally, it provides very good results for organic molecules, namely in the estimation of geometries, relative energies and vibrational spectra.[250]

The aim of the research described in this thesis is the design, synthesis and investigation of the chemical properties and applications of tetrazole-saccharyl conjugates. During the course of the work, we synthesized tetrazole saccharinates through a convergent approach, by coupling tetrazole and saccharyl building blocks, previously prepared (Chapter 2). Then we investigated in detail their structure (Chapter 3) and photochemistry (Chapter 4). As will be shown, irradiation of the conjugates always led to photocleavage of the tetrazole moiety while the saccharyl system was kept untouched. We studied the photochemistry of the tetrazole building blocks and found that the conjugates are photochemically more stable than the corresponding tetrazoles, indicating that the saccharyl system brings photostability to the system. Finally, we investigated the applications of the prepared conjugates (Chapter 5).

1.4. References

(1) Herr, R. J. *Bioorganic Med. Chem.* **2002**, *10* (11), 3379–3393.
(2) Malik, M. A.; Wani, M. Y.; Al-Thabaiti, S. A.; Shiekh, R. A. *J. Incl. Phenom. Macrocycl. Chem.* **2014**, *78* (1), 15–37.
(3) Miyata, Y.; Date, S.; Hasue, K. *Propellants, Explos. Pyrotech.* **2004**, *29* (4), 247–252.
(4) Burns, S. P.; Khandhadia, P. S. Nonazide gas generant compositions. United States Patent US5872329, 1999.
(5) Stierstorfer, J.; Tarantik, K. R.; Klapötke, T. M. *Chemistry* **2009**, *15* (23), 5775–5792.
(6) Klapötke, T. M.; Mayer, P.; Schulz, A.; Weigand, J. J. *J. Am. Chem. Soc.* **2005**, *127* (7), 2032–2033.
(7) Xue, H.; Gao, Y.; Twamley, B.; Shreeve, J. M. *Chem. Mater.* **2005**, *17* (1), 191–198.
(8) Popova, E. a.; Trifonov, R. E.; Ostrovskii, V. a. *Arkivoc* **2012**, *2012* (1), 45–65.
(9) Aromí, G.; Barrios, L. a.; Roubeau, O.; Gamez, P. *Coord. Chem. Rev.* **2011**, *255* (5–6), 485–546.
(10) Zhao, H.; Qu, Z.-R. R.; Ye, H.-Y. Y.; Xiong, R.-G. G. *Chem. Soc. Rev.* **2008**, *37* (1), 84–100.
(11) Ponnuvel, K.; Padmini, V.; Sribalan, R. *Sensors Actuators, B Chem.* **2016**, *222*, 605–611.
(12) Sandmann, G.; Schneider, C.; Boger, P. *Zeitschrift fur Naturforsch. Sect. C - J. Biosci.* **1996**, *51* (7–8), 534–538.
(13) Bačkor, M.; Fahselt, D. *Environ. Exp. Bot.* **2005**, *53* (2), 125–133.
(14) Li, Z.; Qian, L.; Li, L.; Bernhammer, J. C.; Huynh, H. V.; Lee, J. S.; Yao, S. Q. *Angew. Chemie - Int. Ed.* **2016**, *55* (6), 2002–2006.
(15) An, P.; Yu, Z.; Lin, Q. *Org. Lett.* **2013**, *15* (21), 5496–5499.
(16) Ishikawa, W.; Fujiwhara, M.; Kojima, T.; Endo, T.; Kato, K. Method of forming dye image. United States Patent no. 4289847, 1980.
(17) Chermahini, Z. J.; Chermahini, A. N.; Dabbagh, H. A.; Teimouri, A. *J. Energy Chem.* **2015**, *24* (6), 770–778.
(18) Toney, J. H.; Fitzgerald, P. M.; Grover-Sharma, N.; Olson, S. H.; May, W. J.; Sundelof, J. G.; Vanderwall, D. E.; Cleary, K. a; Grant, S. K.; Wu, J. K.; Kozarich, J. W.; Pompliano, D. L.; Hammond, G. G. *Chem. Biol.* **1998**, *5* (4), 185–196.
(19) Honma, Y.; Hashiyama, T.; Hanamoto, K.; Ishida, A.; Ono, Y.; Tsuzuraharat, K. *J. Med. Chem.* **1983**, *26* (10), 1499–1504.
(20) Honma, Y.; Sekine, Y.; One, Y.; Tsuzuraharat, K. *J. Med. Chem.* **1984**, *27* (2), 125–128.

(21) Rajasekaran, A.; Thampi, P. P. *Eur. J. Med. Chem.* **2004**, *39* (3), 273–279.
(22) Kozikowski, A. P.; Zhang, J.; Nan, F.; Petukhov, P. A.; Grajkowska, E.; Wroblewski, J. T.; Yamamoto, T.; Bzdega, T.; Wroblewska, B.; Neale, J. H. *J. Med. Chem.* **2004**, *47* (7), 1729–1738.
(23) Mavromoustakos, T.; Kolocouris, A.; Zervou, M.; Roumelioti, P.; Matsoukas, J.; Weisemann, R. *J. Med. Chem.* **1999**, *42* (10), 1714–1722.
(24) Hashimoto, Y.; Ohashi, R.; Kurosawa, Y.; Minami, K.; Kaji, H.; Hayashida, K.; Narita, H.; Murata, S. *J. Cardiovasc. Pharmacol.* **1998**, *31* (4), 568–575.
(25) Schmidt, B.; Schieffer, B. *J. Med. Chem.* **2003**, *46* (12), 2261–2270.
(26) Wexler, R. R.; Greenlee, W. J.; Irvin, J. D.; Goldberg, M. R.; Prendergast, K.; Smith, R. D.; Timmermans, P. B. *J. Med. Chem.* **1996**, *39* (3), 625–656.
(27) Bekhit, A. A.; El-Sayed, O. A.; Aboulmagd, E.; Park, J. Y. *Eur. J. Med. Chem.* **2004**, *39* (3), 249–255.
(28) Luo, K.; Meng, L.; Zhang, Y.; Zhang, X.; Wang, L. *Adv. Synth. Catal.* **2013**, *355* (4), 765–780.
(29) Shaabani, A.; Hezarkhani, Z.; Mofakham, H.; Ng, S. *Synlett* **2013**, *24* (12), 1485–1492.
(30) Chattopadhyay, B.; Vera, C. I. R.; Chuprakov, S.; Gevorgyan, V. *Org. Lett.* **2010**, *12* (9), 2166–2169.
(31) Aïssa, C. *European J. Org. Chem.* **2009**, *2009* (12), 1831–1844.
(32) Khodaei, M. M.; Alizadeh, A.; Pakravan, N. *J. Org. Chem.* **2008**, *73* (7), 2527–2532.
(33) Jin, T.; Kitahara, F.; Kamijo, S.; Yamamoto, Y. *Tetrahedron Lett.* **2008**, *49* (17), 2824–2827.
(34) Aïssa, C. *J. Org. Chem.* **2006**, *71* (1), 360–363.
(35) Nikulin, V. V.; Artamonova, T. V.; Koldobskii, G. I. *Russ. J. Org. Chem.* **2005**, *41* (3), 444–449.
(36) Mitchell, C. E. T.; Cobb, A. J. A.; Ley, S. V. *Synlett* **2005**, No. 4, 611–614.
(37) Gupta, A. K.; Song, C. H.; Oh, C. H. *Tetrahedron Lett.* **2004**, *45* (21), 4113–4116.
(38) Gupta, A. K.; Rim, C. Y.; Oh, C. H. *Synlett* **2004**, No. 12, 2227–2229.
(39) Cobb, A. J.; Shaw, D. M.; Ley, S. V. *Synlett* **2004**, No. 3, 558–560.
(40) Yamamoto, Y.; Momiyama, N.; Yamamoto, H. *J. Am. Chem. Soc.* **2004**, *126* (19), 5962–5963.
(41) Torii, H.; Nakadai, M.; Ishihara, K.; Saito, S.; Yamamoto, H. *Angew. Chem. Int. Ed. Engl.* **2004**, *43* (15), 1983–1986.
(42) Dabbagh, H. A.; Noroozi-Pesyan, N.; Patrick, B. O.; James, B. R. *Can. J. Chem.* **2004**, *82* (7), 1179–1185.
(43) Jankowski, P.; Pleśniak, K.; Wicha, J. *Org. Lett.* **2003**, *5* (16), 2789–2792.
(44) Voitekhovich, S. V; Gaponik, P. N.; Ivashkevich, O. A. *Russ. Chem. Rev.* **2002**, *71* (9), 721–739.
(45) Ostrovskii, V. A.; Koren, A. O. *Heterocycles* **2000**, *53* (6), 1421–1448.
(46) Zhaoxu, C.; Heming, X. *Propellants, Explos. Pyrotech.* **1999**, *24* (5), 319–324.
(47) Akutsu, Y.; Tamura, M. *J. Energ. Mater.* **2006**, *11* (3), 205–217.
(48) Dhayabaran, V. V.; Lydia, I. S.; Merlin, J. P.; Srirenganayaki, P. *Ionics (Kiel).* **2004**, *10* (1–2), 123–125.
(49) Antonijevic, M. M.; Petrovic, M. B. *Int. J. Electrochem. Sci.* **2008**, *3* (1), 1–28.
(50) Butler, R. N. *Comprehensive Heterocyclic Chemistry II*; Elsevier: Pergamon, 1996; Vol. 4.
(51) Trifonov, R. E.; Ostrovskii, V. A. *Russ. J. Org. Chem.* **2006**, *42* (11), 1585–1605.
(52) Catalan, J.; Elguero, J. *Adv. Heterocycl. Chem.* **1987**, *41*, 187–274.
(53) Koldobskii, G. I.; Ostrovskii, V. A.; Gidaspov, B. V. *Chem. Heterocycl. Compd.* **1980**, *16* (7), 665–674.

(54) Goddard, R.; Heinemann, O.; Krüger, C. *Acta Crystallogr. Sect. C Cryst. Struct. Commun.* **1997**, *53* (5), 590–592.
(55) McCrone, W. C.; Grabar, D.; Lieber, E. *Anal. Chem.* **1951**, *23* (3), 543–543.
(56) Bugalho, S. C. S.; Maçôas, E. M. S.; Cristiano, M. L. S.; Fausto, R. *Phys. Chem. Chem. Phys.* **2001**, *3* (17), 3541–3547.
(57) Zhaoxu, C.; Heming, X. *J. Mol. Struct. THEOCHEM* **1998**, *453* (1–3), 65–70.
(58) Butler, R. N.; Garvin, V. C.; Lumbroso, H.; Liegeois, C.; Gbnbrale, L. D. C.; Pierre, U.; Jussieu, P.; Cedex, P. *J. Chem. Soc., Perkin Trans. 2* **1984**, 721–725.
(59) Krugh, W. D.; Gold, L. P. *J. Mol. Spectrosc.* **1974**, *49* (3), 423–431.
(60) Wong, M. W.; Leung-Toung, R.; Wentrup, C. *J. Am. Chem. Soc.* **1993**, *115* (6), 2465–2472.
(61) Fabian, W. M. F. *Zeitschrift für Naturforsch. A* **1990**, *45* (11–12), 1328–1334.
(62) Mazurek, A. .; Sadlej-Sosnowska, N. *Chem. Phys. Lett.* **2000**, *330* (1–2), 212–218.
(63) Sadlej-Sosnowska, N. *J. Org. Chem.* **2001**, *66* (26), 8737–8743.
(64) Rażyńska, A.; Tempczyk, A.; Maliński, E.; Szafranek, J.; Grzonka, Z.; Hermann, P. *J. Chem. Soc., Perkin Trans. 2* **1983**, No. 3, 379–383.
(65) Palmer, M. H.; Simpson, I.; Wheeler, J. R. *Zeitschrift für Naturforsch. A* **1981**, *36* (11), 1246–1252.
(66) Gómez-Zavaglia, A.; Reva, I.; Frija, L.; Cristiano, M.; Fausto, R. *J. Mol. Struct.* **2006**, *786* (2–3), 182–192.
(67) Gómez-Zavaglia, a; Reva, I. D.; Frija, L.; Cristiano, M. L.; Fausto, R. *J. Phys. Chem. A* **2005**, *109* (35), 7967–7976.
(68) Brown, N. Bioisosteres in medicinal chemistry; Wiley-VCH, 2012.
(69) Thornber, C. W. *Chem. Soc. Rev.* **1979**, *8* (4), 563–580.
(70) Butler, R. N. *Adv. Heterocycl. Chem.* **1977**, *21* (C), 323–435.
(71) Wittenberger, S. J. *Org. Prep. Proced. Int. New J. Org. Synth.* **1994**, *26* (5), 499–531.
(72) Lipinski, C. A. *Annu. Rep. Med. Chem.* **1986**, *21*, 283–291.
(73) Boraei, A. A. A. *J. Chem. Eng. Data* **2001**, *46* (4), 939–943.
(74) Kraus, J. L. *Pharmacol. Res. Commun.* **1983**, *15* (2), 183–189.
(75) Kraus, J. L.; Faury, P.; Charvet, A. S.; Camplo, M. *Res. Commun. Chem. Pathol. Pharmacol.* **1994**, *83* (2), 209–222.
(76) Holland, G. F.; Pereira, J. N. *J. Med. Chem.* **1967**, *10* (2), 149–154.
(77) Figdor, S. K.; von Wittenau, M. S. *J. Med. Chem.* **1967**, *10* (6), 1158–1159.
(78) Sarro, A. D. E.; Ammendola, D.; Zappala, M.; Grasso, S. **1995**, *39* (1), 232–237.
(79) Tamura, Y.; Watanabe, F.; Nakatani, T.; Yasui, K.; Fuji, M.; Komurasaki, T.; Tsuzuki, H.; Maekawa, R.; Yoshioka, T.; Kawada, K.; Sugita, K.; Ohtani, M. *J. Med. Chem.* **1998**, *41* (4), 640–649.
(80) Abell, A. D.; Foulds, G. J. *J. Chem. Soc. Perkin Trans. 1* **1997**, 2475–2482.
(81) Carini, D. J.; Duncia, J. V.; Aldrich, P. E.; Chiu, A. T.; Johnson, A. L.; Pierce, M. E.; Price, W. A.; Santella, J. B.; Wells, G. J. *J. Med. Chem.* **1991**, *34* (8), 2525–2547.
(82) Galemmo, R. A.; Johnson, W. H.; Learn, K. S.; Lee, T. D. Y.; Huang, F. C.; Campbell, H. F.; Youssefyeh, R.; O'Rourke, S. V.; Schuessler, G. *J. Med. Chem.* **1990**, *33* (10), 2828–2841.
(83) Marshall, W. S.; Goodson, T.; Cullinan, G. J.; Swanson-Bean, D.; Haisch, K. D.; Rinkema, L. E.; Fleisch, J. H. *J. Med. Chem.* **1987**, *30* (4), 682–689.
(84) Zhang, M.-Q.; Zwaagstra, M. E.; Nederkoorn, P. H. .; Timmerman, H. *Bioorg. Med. Chem. Lett.* **1997**, *7* (10), 1331–1336.
(85) Greenlee, W. J.; Mantlo, N. B. *Bioorg. Med. Chem. Lett.* **1994**, *4* (1), 1–222.
(86) Wexler, R. R.; Greenlee, W. J.; Irvin, J. D.; Goldberg, M. R.; Prendergast, K.; Smith, R. D.; Timmermans, P. B. M. W. M. *J. Med. Chem.* **1996**, *39* (3), 625–656.

(87) Young, M. B.; Barrow, J. C.; Glass, K. L.; Lundell, G. F.; Newton, C. L.; Pellicore, J. M.; Rittle, K. E.; Selnick, H. G.; Stauffer, K. J.; Vacca, J. P.; Williams, P. D.; Bohn, D.; Clayton, F. C.; Cook, J. J.; Krueger, J. A.; Kuo, L. C.; Lewis, S. D.; Lucas, B. J.; McMasters, D. R.; Miller-Stein, C.; Pietrak, B. L.; Wallace, A. A.; White, R. B.; Wong, B.; Yan, Y.; Nantermet, P. G. *J. Med. Chem.* **2004**, *47* (12), 2995–3008.
(88) Stassen, A. F.; Grunert, M.; Dova, E.; Muller, M.; Weinberger, P.; Wiesinger, G.; Schenk, H.; Linert, W.; Haasnoot, J. G.; Reedijk, J. *Eur. J. Inorg. Chem.* **2003**, No. 12, 2273–2282.
(89) Sarvary, A.; Maleki, A. *Mol. Divers.* **2015**, *19* (1), 189–212.
(90) Koldobskii, G. I.; Kharbash, R. B. *Russ. J. Org. Chem.* **2003**, *39* (4), 453–470.
(91) Koldobskii, G. I.; Ostrovskii, V. A. *Russ. Chem. Rev.* **1994**, *63* (10), 797.
(92) Zimmerman, D. M.; Olofson, R. A. *Tetrahedron Lett.* **1969**, *58*, 5081–5084.
(93) Fallon, F. G.; Herbst, R. M. *J. Org. Chem.* **1957**, *22* (8), 933–936.
(94) Jin, T.; Kamijo, S.; Yamamoto, Y. *Tetrahedron Lett.* **2004**, *45* (51), 9435–9437.
(95) Koldobskii, G. I. *Russ. J. Org. Chem.* **2006**, *42* (4), 469–486.
(96) Benson, F. R. *Chem. Rev.* **1947**, *41* (1), 1–61.
(97) Hantzsch, A.; Vagt, A. *Justus Liebig's Ann. der Chemie* **1901**, *314* (3), 339–369.
(98) Dimroth, O.; Merzbacher, S. *Berichte der Dtsch. Chem. Gesellschaft* **1910**, *43* (3), 2899–2904.
(99) Mihina, J. S.; Herbst, R. M. *J. Org. Chem.* **1950**, *15* (5), 1082–1092.
(100) Finnegan, W. G.; Henry, R. A.; Lofquist, R. *J. Am. Chem. Soc.* **1958**, *80* (15), 3908–3911.
(101) Roh, J.; Vávrová, K.; Hrabálek, A. *European J. Org. Chem.* **2012**, *2012* (31), 6101–6118.
(102) Jursic, B. S.; Zdravkovski, Z. *J. Mol. Struct. THEOCHEM* **1994**, *312* (1), 11–22.
(103) Ostrovskii, V. A.; Poplavskii, V. S.; Koldobskii, G. I.; Erusalimskii, G. B. *Chem. Heterocycl. Compd.* **1992**, *28* (9), 1027–1030.
(104) Titova, I. E.; Poplavskii, V. S.; Koldobskii, G. I.; Ostrovskii, V. A.; Nikolaev, V. D.; Erusalimskii, G. B. *Chem. Heterocycl. Compd.* **1986**, *22* (8), 880–883.
(105) Demko, Z. P.; Sharpless, K. B. *Org. Lett.* **2001**, *3* (25), 4091–4094.
(106) Himo, F.; Demko, Z. P.; Noodleman, L.; Sharpless, B. K. *J. Am. Chem. Soc.* **2002**, *124* (41), 12210–12216.
(107) Demko, Z. P.; Sharpless, K. B. *J. Org. Chem.* **2001**, *66* (24), 7945–7950.
(108) Rostamizadeh, S.; Ghaieni, H.; Aryan, R.; Amani, A. *Chinese Chem. Lett.* **2009**, *20* (11), 1311–1314.
(109) Cantillo, D.; Gutmann, B.; Kappe, C. O. *J. Am. Chem. Soc.* **2011**, *133* (12), 4465–4475.
(110) Yoneyama, H.; Usami, Y.; Komeda, S.; Harusawa, S. *Synthesis (Stuttg).* **2013**, *45* (8), 1051–1059.
(111) Roh, J.; Artamonova, T.; Vávrová, K.; Koldobskii, G.; Hrabálek, A. *Synthesis (Stuttg).* **2009**, *2009* (13), 2175–2178.
(112) Shie, J.-J.; Fang, J.-M. *J. Org. Chem.* **2007**, *72* (8), 3141–3144.
(113) Onaka, T.; Umemoto, H.; Miki, Y.; Nakamura, A.; Maegawa, T. *J. Org. Chem.* **2014**, *79* (14), 6703–6707.
(114) Liu, C.-Y.; Li, Y.; Ding, J.-Y.; Dong, D.-W.; Han, F.-S. *Chem. - A Eur. J.* **2014**, *20* (8), 2373–2381.
(115) Li, Y.; Gao, L.-X.; Han, F.-S. *Chem. Commun.* **2012**, *48* (21), 2719.
(116) Davydov, D. V.; Beletskaya, I. P.; Semenov, B. B.; Smushkevich, Y. I. *Tetrahedron Lett.* **2002**, *43* (35), 6217–6219.
(117) Beletskaya, I. P.; Davydov, D. V.; Gorovoy, M. S. *Tetrahedron Lett.* **2002**, *43* (35), 6221–6223.

(118) Ramanathan, M.; Wang, Y.-H.; Liu, S.-T. *Org. Lett.* **2015**, *17* (23), 5886–5889.
(119) Wofford, D. S.; Forkey, D. M.; Russell, J. G. *J. Org. Chem.* **1982**, *47* (26), 5132–5137.
(120) Efimova, J. A.; Mashkova, E. A.; Artamonova, T. V.; Koldobskii, G. I. *Chem. Heterocycl. Compd.* **2008**, *44* (4), 498–499.
(121) Couri, M. R.; Luduvico, I.; Santos, L.; Alves, R.; Prado, M. A.; Gil, R. F. *Carbohydr. Res.* **2007**, *342* (8), 1096–1100.
(122) Gaponik, P. N.; Voitekhovich, S. V; Ivashkevich, O. A. *Russ. Chem. Rev.* **2006**, *75* (6), 507–539.
(123) Popov, A. I. *Coord. Chem. Rev.* **1969**, *4* (4), 463–474.
(124) Tao, Y.; Li, J.-R.; Chang, Z.; Bu, X.-H. *Cryst. Growth Des.* **2010**, *10* (2), 564–574.
(125) Gaponik, P. N.; Voitekhovich, S. V.; Lyakhov, A. S.; Matulis, V. E.; Ivashkevich, O. A.; Quesada, M.; Reedijk, J. *Inorganica Chim. Acta* **2005**, *358* (8), 2549–2557.
(126) Chohan, Z. H.; Supuran, C. T.; Scozzafava, A. *J. Enzyme Inhib. Med. Chem.* **2004**, *19* (1), 79–84.
(127) Anacona, J. R.; Alvarez, P. *Transit. Met. Chem.* **2002**, *27* (8), 856–860.
(128) Osman, A.; Aly, A.; El-Maali, N. A.; Al-Hazmi, G. *Synth. React. Inorganic, Met. Nano-Metal Chem.* **2002**, *32* (7), 1289–1300.
(129) Osman, A. H.; El-Maali, N. A.; Aly, A. A. M.; Al-Hazmi, G. A. *Synth. React. Inorg. Met. Chem.* **2002**, *32* (4), 763–781.
(130) Aly, A. A. M.; Osman, A. H.; El-Maali, N. A.; Al-Hazmi, G. A. A. *J. Therm. Anal. Calorim.* **2004**, *75* (1), 159–168.
(131) Bekhit, A. A.; El-Sayed, O. A.; Al-Allaf, T. A. .; Aboul-Enein, H. Y.; Kunhi, M.; Pulicat, S. M.; Al-Hussain, K.; Al-Khodairy, F.; Arif, J. *Eur. J. Med. Chem.* **2004**, *39* (6), 499–505.
(132) Saalfrank, R. W.; Reihs, S.; Hug, M. *Tetrahedron Lett.* **1993**, *34* (38), 6033–6036.
(133) Tappan, B. C.; Incarvito, C. D.; Rheingold, A. L.; Brill, T. B. *Thermochim. Acta* **2002**, *384* (1), 113–120.
(134) Hermann, S. H.; Ruediger, H. S. A. Solid 5-aminotetrazole nitrate gas generating propellant with block copolymer binder. US3898112 A, 1970.
(135) Bernard, J. D.; Jean, P. T. Pyrotechnic compositions for gas generation. US3912561 A, 1973.
(136) Prior, J.; Siegelin, W. Pressurizing-gas-producing charges containing an aminoguanidine tetrazole and an oxygen-liberating or gas-evolving additive. US3719604 A, 1971.
(137) Gary K. Lund, R. J. B. Preparation of anhydrous tetrazole gas generant compositions. US5501823 A, 1993.
(138) Mackenzie, G.; B Moy, F. P. Gas generating solid propellant containing 5-aminotetrazole nitrate. US3734789 A, 1969.
(139) Hans, S.; Kurt, B.; Heinz, G. Gas-generating pyrotechnic composition consisting essentially of ammonium nitrate and aminotetrazole. US3348985 A, 1966.
(140) Pergolese, B.; Bigotto, A. *J. Raman Spectrosc.* **2002**, *33* (8), 646–651.
(141) Sägmüller, B.; Freunscht, P.; Schneider, S. *J. Mol. Struct.* **1999**, *482*, 231–235.
(142) Smith, T. A.; DeWitt, J. G.; Hedman, B.; Hodgson, K. O. *J. Am. Chem. Soc.* **1994**, *116* (9), 3836–3847.
(143) Brandt, E. S. *Appl. Spectrosc.* **1993**, *47* (1), 85–93.
(144) Isaac, W. H.; Wollman, E. W. Mercaptotetrazole transition metal salts for control of cyan stain. US 5543281 A, 1995.
(145) Szőcs, E.; Bakó, I.; Kosztolányi, T.; Bertóti, I.; Kálmán, E. *Electrochim. Acta* **2004**, *49* (9), 1371–1378.
(146) Ye, X. .; Xin, X. .; Zhu, J. .; Xue, Z. . *Appl. Surf. Sci.* **1998**, *135* (1), 307–317.

(147) Szőcs, E.; Vastag, G.; Shaban, A.; Kálmán, E. *Corros. Sci.* **2005**, *47* (4), 893–908.
(148) Brunoro, G.; Frignani, A.; Colledan, A.; Chiavari, C. *Corros. Sci.* **2003**, *45* (10), 2219–2231.
(149) Szocs, E.; Vastag, G.; Shaban, A.; Konczos, G.; Kálmán, E. *J. Appl. Electrochem.* **1999**, *29* (11), 1339–1345.
(150) YE, X. R.; XIN, X. Q.; XIN, F. B. *J. Appl. Electrochem.* **1997**, *27* (6), 659–666.
(151) Kertit, S.; Hammouti, B. *Appl. Surf. Sci.* **1996**, *93* (1), 59–66.
(152) Bensajjay, F.; Alehyen, S.; El Achouri, M.; Kertit, S. *Anti-Corrosion Methods Mater.* **2003**, *50* (6), 402–409.
(153) Tsarenko, I. V.; Makarevich, A. V.; Orekhov, D. A. *Bioprocess Eng.* **1998**, *19* (6), 469.
(154) Hernández, O.; Jiménez, A. I.; Jiménez, F.; Arias, J. J.; Havel, J. *Talanta* **1994**, *41* (5), 775–782.
(155) Whittle, E.; Dows, D. A.; Pimentel, G. C. *J. Chem. Phys.* **1954**, *22* (11), 1943.
(156) Bally, T. *Matrix Isolation*; John Wiley & Sons, Inc.: Hoboken, NJ, USA, 2004.
(157) Fausto, R. *Low Temperature Molecular Spectroscopy*; Fausto, R., Ed.; Springer Netherlands: Dordrecht, 1996.
(158) Dunkin, I. R. *Matrix-Isolation Techniques : A Practical Approach*; Oxford University Press: New York, 1998.
(159) Dunkin, I. R. *Chem. Soc. Rev.* **1980**, *9* (1), 1–23.
(160) Reva, I. .; Stepanian, S. .; Adamowicz, L.; Fausto, R. *Chem. Phys. Lett.* **2003**, *374* (5), 631–638.
(161) Reva, I. D.; Lopes Jesus, A. J.; Rosado, M. T. S.; Fausto, R.; Ermelinda Eusébio, M.; Redinha, J. S. *Phys. Chem. Chem. Phys.* **2006**, *8* (45), 5339–5349.
(162) Rosado, M. T. S.; Lopes Jesus, A. J.; Reva, I. D.; Fausto, R.; Redinha, J. S. *J. Phys. Chem. A* **2009**, *113* (26), 7499–7507.
(163) Barnes, A. J. *J. Mol. Struct.* **1984**, *113*, 161–174.
(164) Ismael, A.; Borba, A.; Henriques, M. S. C.; Paixão, J. A.; Fausto, R.; Cristiano, M. L. S. *J. Org. Chem.* **2015**, *80* (1), 392–400.
(165) Borba, A.; Cabral, L. I. L.; Fausto, R.; Cristiano, M. L. S. *Can. J. Chem.* **2015**, *10* (April), 150421143716005.
(166) Nunes, C. M.; Reva, I.; Rosado, M. T. S.; Fausto, R. *European J. Org. Chem.* **2015**, No. 34, 7484–7493.
(167) Nunes, C. M.; Reva, I.; Fausto, R.; Bégué, D.; Wentrup, C. *Chem. Commun.* **2015**, *51*, 14712–14715.
(168) Baskir, E. G.; Platonov, D. N.; Tomilov, Y. V.; Nefedov, O. M. *Mendeleev Commun.* **2014**, *24* (4), 197–200.
(169) Nunes, C. M.; Araujo-Andrade, C.; Fausto, R.; Reva, I. *J. Org. Chem.* **2014**, *79* (8), 3641–3646.
(170) Pagacz-Kostrzewa, M.; Krupa, J.; Wierzejewska, M. *J. Photochem. Photobiol. A Chem.* **2014**, *277*, 37–44.
(171) Frija, L. M. T.; Cristiano, M. L. S.; Gómez-Zavaglia, A.; Reva, I.; Fausto, R. *J. Photochem. Photobiol. C Photochem. Rev.* **2014**, *18*, 71–90.
(172) Pagacz-Kostrzewa, M.; Mucha, M.; Weselski, M.; Wierzejewska, M. *J. Photochem. Photobiol. A Chem.* **2013**, *251*, 118–127.
(173) Ismael, A.; Borba, A.; Duarte, L.; Giuliano, B. M.; Gómez-Zavaglia, A.; Cristiano, M. L. S. *J. Mol. Struct.* **2012**, *1025*, 105–116.
(174) Bégué, D.; Qiao, G. G.; Wentrup, C. *J. Am. Chem. Soc.* **2012**, *134* (11), 5339–5350.
(175) Ismael, A.; Serpa, C.; Cristiano, M. L. S. *Photochem. Photobiol. Sci.* **2012**, *12* (2), 272–283.
(176) Alawode, O. E.; Robinson, C.; Rayat, S. *J. Org. Chem.* **2011**, *76* (1), 216–222.

(177) Frija, L. M. T.; Ismael, A.; Cristiano, M. L. S. *Molecules* **2010**, *15* (5), 3757–3774.
(178) Ismael, A.; Cristiano, M. L. S.; Fausto, R.; Gómez-Zavaglia, A. *J. Phys. Chem. A* **2010**, *114* (50), 13076–13085.
(179) Frija, L. M. T.; Khmelinskii, I. V; Serpa, C.; Reva, I. D.; Fausto, R.; Cristiano, M. L. S. *Org. Biomol. Chem.* **2008**, *6* (6), 1046–1055.
(180) Quast, H.; Bieber, L. W. *J. Org. Chem.* **2008**, *73* (10), 3738–3744.
(181) Frija, L. M. T.; Reva, I. D.; Gómez-Zavaglia, A.; Cristiano, M. L. S.; Fausto, R. *Photochem. Photobiol. Sci.* **2007**, *6* (11), 1170–1176.
(182) Frija, L. M. T.; Reva, I. D.; Gómez-Zavaglia, A.; Cristiano, M. L. S.; Fausto, R. *J. Phys. Chem. A* **2007**, *111* (15), 2879–2888.
(183) Gómez-Zavaglia, A.; Reva, I. D.; Frija, L.; Cristiano, M. L. S.; Fausto, R. *J. Photochem. Photobiol. A Chem.* **2006**, *180* (1–2), 175–183.
(184) Frija, L. M. T.; Khmelinskii, I. V; Cristiano, M. L. S. *J. Org. Chem.* **2006**, *71* (9), 3583–3591.
(185) Gómez-Zavaglia, A.; Reva, I. D.; Frija, L.; Cristiano, M. L.; Fausto, R. *J. Photochem. Photobiol. A-Chemistry* **2006**, *179* (3), 243–255.
(186) Gómez-Zavaglia, A.; Reva, I. D.; Frija, L.; Cristiano, M. L.; Fausto, R. *J. Phys. Chem. A* **2005**, *109* (35), 7967–7976.
(187) Frija, L. M. T.; Khmelinskii, I. V; Cristiano, M. L. S. *Tetrahedron Lett.* **2005**, *46* (39), 6757–6760.
(188) Maier, G. G.; Eckwert, J. J.; Bothur, A.; Reisenauer, H. P.; Schmidt, C. *Liebigs Ann.* **1996**, No. 7, 1041–1053.
(189) Bertrand, G.; Wentrup, C. *Angew. Chemie Int. Ed. English* **1994**, *33*, 527–545.
(190) Dunkin, I. R.; Shields, C. J.; Quast, H. *Tetrahedron* **1989**, *45* (1), 259–268.
(191) Quast, H.; Nahr, U. *Chem. Berichte-Recueil* **1985**, *118* (2), 526–540.
(192) Quast, H.; Fuss, A.; Nahr, U. *Chem. Berichte-Recueil* **1985**, *118* (6), 2164–2185.
(193) Quast, H.; Nahr, U. *Chem. Berichte-Recueil* **1983**, *116* (10), 3427–3437.
(194) Quast, H.; Bieber, L. *Chem. Berichte-Recueil* **1981**, *114* (10), 3253–3272.
(195) Quast, H. *Heterocycles* **1980**, *14* (10), 1677–1702.
(196) Quast, H.; Bieber, L. *Angew. Chemie-International Ed. English* **1975**, *14* (6), 428–429.
(197) Hyatt, J. A.; Swenton, J. S. *J. Org. Chem.* **1972**, *37* (21), 3216–3220.
(198) Awadallah, A.; Kowski, K.; Rademacher, P. *J. Heterocycl. Chem.* **1997**, *34* (1), 113–122.
(199) Frija, L. M. T. T.; Fausto, R.; Loureiro, R. M. S. S.; Cristiano, M. L. S. *J. Mol. Catal. A-Chemical* **2009**, *305* (1–2), 142–146.
(200) Ismael, A.; Paixão, J. A.; Fausto, R.; Cristiano, M. L. S. *J. Mol. Struct.* **2012**, *1023*, 128–142.
(201) Ostrovskii, V. A.; Koldobskii, G. I.; Trifonov, R. E. In *Comprehensive Heterocyclic Chemistry III*; 2008; pp 257–423.
(202) Ismael, A.; Gómez-Zavaglia, A.; Borba, A.; Cristiano, M. de L. S.; Fausto, R. *J. Phys. Chem. A* **2013**, *117* (15), 3190–3197.
(203) Gómez-Zavaglia, A.; Ismael, A.; Cabral, L. I. L.; Kaczor, A.; Paixão, J. A.; Fausto, R.; Cristiano, M. L. S. *J. Mol. Struct.* **2011**, *1003*, 103–110.
(204) Pagacz-Kostrzewa, M.; Reva, I. D.; Bronisz, R.; Giuliano, B. M.; Fausto, R.; Wierzejewska, M. *J. Phys. Chem. A* **2011**, *115* (22), 5693–5707.
(205) Pagacz-Kostrzewa, M.; Krupa, J.; Olbert-Majkut, A.; Podruczna, M.; Bronisz, R.; Wierzejewska, M. *Tetrahedron* **2011**, *67* (44), 8572–8582.
(206) Baran, E. J.; Yilmaz, V. T. *Coord. Chem. Rev.* **2006**, *250* (15–16), 1980–1999.
(207) Duarte, L.; Reva, I.; Cristiano, M. de L. S.; Fausto, R. *J. Org. Chem.* **2013**, *78* (7), 3271–3275.

(208) Yu, Z.; Ohulchanskyy, T. Y.; An, P.; Prasad, P. N.; Lin, Q. *J. Am. Chem. Soc.* **2013**, *135* (45), 16766–16769.
(209) Shi, H.; Zhang, C. J.; Chen, G. Y. J.; Yao, S. Q. *J. Am. Chem. Soc.* **2012**, *134* (6), 3001–3014.
(210) Lim, R. K. V; Lin, Q. *Acc. Chem. Res.* **2011**, *44* (9), 828–830.
(211) Song, W.; Wang, Y.; Qu, J.; Lin, Q. *J. Am. Chem. Soc.* **2008**, *130* (30), 9654–9655.
(212) Mawhinney, R. C.; Muchall, H. M.; Peslherbe, G. H. *Chem. Commun.* **2004**, *2* (16), 1862.
(213) Bégué, D.; Wentrup, C. *J. Org. Chem.* **2014**, *79* (3), 1418–1426.
(214) Muchall, H. M. *J. Phys. Chem. A* **2011**, *115* (46), 13694–13705.
(215) Schulze, B.; Illgen, K. *J. für Prakt. Chemie/Chemiker-Zeitung* **1997**, *339* (1), 1–14.
(216) Ellis, J. W. *J. Chem. Educ.* **1995**, *72* (8), 671.
(217) Remsen, I.; Fahlberg, C. *J. Am. Chem. Soc., 1* **1880**, *1*, 426.
(218) Tandel, K. R. *J. Pharmacol. Pharmacother.* **2011**, *2* (4), 236–243.
(219) Price, J. M.; Biava, C. G.; Oser, B. L.; Vogin, E. E.; Steinfeld, J.; Ley, H. L. *Science (80-.).* **1970**, *167* (3921).
(220) EPA, U. Consolidated List of Chemicals Subject to the Emergency Planning and Community Right- To-Know Act (EPCRA), Comprehensive Environmental Response , Compensation and Liability Act (CERCLA) and Section 112 (r) of the Clean Air Act; 2015; Vol. 112.
(221) Suzuki, N.; Suzuki, H. *Cancer Res.* **1995**, *55* (19).
(222) Zurlo, J.; Squire, R. A. *J. Natl. Cancer Inst.* **1998**, *90* (1), 2–3.
(223) Cotton, F. A.; Falvello, L. R.; Llusar, R.; Libby, E.; Murillo, C. A.; Schwotzer, W. *Inorg. Chem.* **1986**, *25* (19), 3423–3428.
(224) Lindskog, S.; Silverman, D. N. In *The Carbonic Anhydrases*; Birkhäuser Basel: Basel, 2000; pp 175–195.
(225) McDonald, P. C.; Winum, J.-Y.; Supuran, C. T.; Dedhar, S. *Oncotarget* **2012**, *3* (1), 84–97.
(226) Supuran, C. T.; Scozzafava, A.; Briganti, F.; Ilies, M. A.; Jitianu, A.; Chimica, D.; Inorganica, C. *Rev. Roum. Chim.* **1998**, *5* (2), 103–114.
(227) Köhler, K.; Hillebrecht, A.; Schulze Wischeler, J.; Innocenti, A.; Heine, A.; Supuran, C. T.; Klebe, G. *Angew. Chemie - Int. Ed.* **2007**, *46* (40), 7697–7699.
(228) Apella, M. C.; Totaro, R.; Baran, E. J. *Biol. Trace Elem. Res.* **1993**, *37* (2–3), 293–299.
(229) Williams, D. R.; Taylor, D. M.; Taylor, D. M. *Trace Elements Medicine and Chelation Therapy*; RSC Paperbacks; Royal Society of Chemistry: Cambridge, 1995.
(230) Andersen, O. *Mini Rev. Med. Chem.* **2004**, *4* (1), 11–21.
(231) Ono, I.; Sato, S.; Fukuda, K.; Inayoshi, T. *Bull. Chem. Soc. Jpn.* **1997**, *70* (9), 2051–2055.
(232) Kamigata, N.; Saegusa, T.; Fujie, S.; Kobayashi, M. *Chem. Lett.* **1979**, No. 1, 9–12.
(233) Döpp, D.; Lauterfeld, P.; Schneider, M.; Schneider, D.; Henkel, G.; Abd el Sayed Issac, Y.; Elghamry, I. *Synthesis (Stuttg).* **2001**, *112* (8), 1228–1235.
(234) Döpp, D. *Int. J. Photoenergy* **2001**, *3* (1), 41–48.
(235) Cho, D. W.; Oh, S. W.; Kim, D. U.; Park, H. J.; Xue, J. Y.; Yoon, U. C.; Mariano, P. S. *Bull. Korean Chem. Soc.* **2010**, *31* (9), 2453–2458.
(236) Foresman, J. B.; Frisch, A. *Exploring Chemistry With Electronic Structure Methods.pdf*, 2nd Ed.; Gaussian Inc.: Pittsburg, PA, 1996.
(237) Lewars, E. G. Computational Chemistry - Introduction to the Theory and Applications of Molecular and Quantum Mechanics, 2nd Ed.; Springer Netherlands: Dordrecht, 2011.
(238) Rubenstein, L. A.; Zauhar, R. J.; Lanzara, R. G. *J. Mol. Graph. Model.* **2006**, *25* (4), 396–409.

(239) Schrödinger, E. *Ann. Phys.* **1926**, *384* (4), 361–376.
(240) Born, M.; Oppenheimer, R. *Ann. Phys.* **1927**, *389* (20), 457–484.
(241) Atkins, P. W.; Friedman, R. S. *Molecular Quantum Mechanics*, 5th Ed.; Oxford University Press: Oxford, 2010.
(242) Bachrach, S. M. *Computational Organic Chemistry*, 1st Ed.; John Wiley & Sons, Inc.: Hoboken, NJ, USA, 2007.
(243) Hehre, W. J.; Stewart, R. F.; Pople, J. A. *J. Chem. Phys.* **1969**, *51* (6), 2657.
(244) Hohenberg, P.; Kohn, W. *Phys. Rev.* **1964**, *136* (3B), 864–871.
(245) Kohn, W.; Sham, L. J. *Phys. Rev.* **1965**, *140* (4A), 1133–1138.
(246) W. Kohn, *; A. D. Becke, † and; Parr‡, R. G. **1996**.
(247) Lee, C. T.; Yang, W. T.; Parr, R. G. *Phys. Rev. B* **1988**, *37* (2), 785–789.
(248) Durant, J. L. *Chem. Phys. Lett.* **1996**, *256* (6), 595–602.
(249) Becke, A. D. *J. Chem. Phys.* **1993**, *98* (7), 5648.
(250) Sousa, S. F.; Fernandes, P. A.; Ramos, M. J. *J. Phys. Chem. A* **2007**, *111* (42), 10439–10452.

Chapter 2. Experimental and computational details

2.1. General synthetic approach to saccharyl-tetrazole ligands and corresponding coordination complexes

In this chapter the synthesis of the multidentate nitrogen ligands and of the corresponding coordination complexes is described and discussed. The ligands were prepared using a convergent synthetic strategy whereby the two building blocks containing the heterocycles (**1** and **2**; Scheme 2.1) were separately synthesised and then coupled to afford the target conjugates **3**. The prepared conjugates were than evaluated on their ability to bind divalent cations, (Cu, Pb, Ni, Co, Fe, Zn, Ca and Mn), and form the corresponding complexes (**4** and **5**). The general synthetic approach to prepare these compounds is presented in Scheme 2.1.

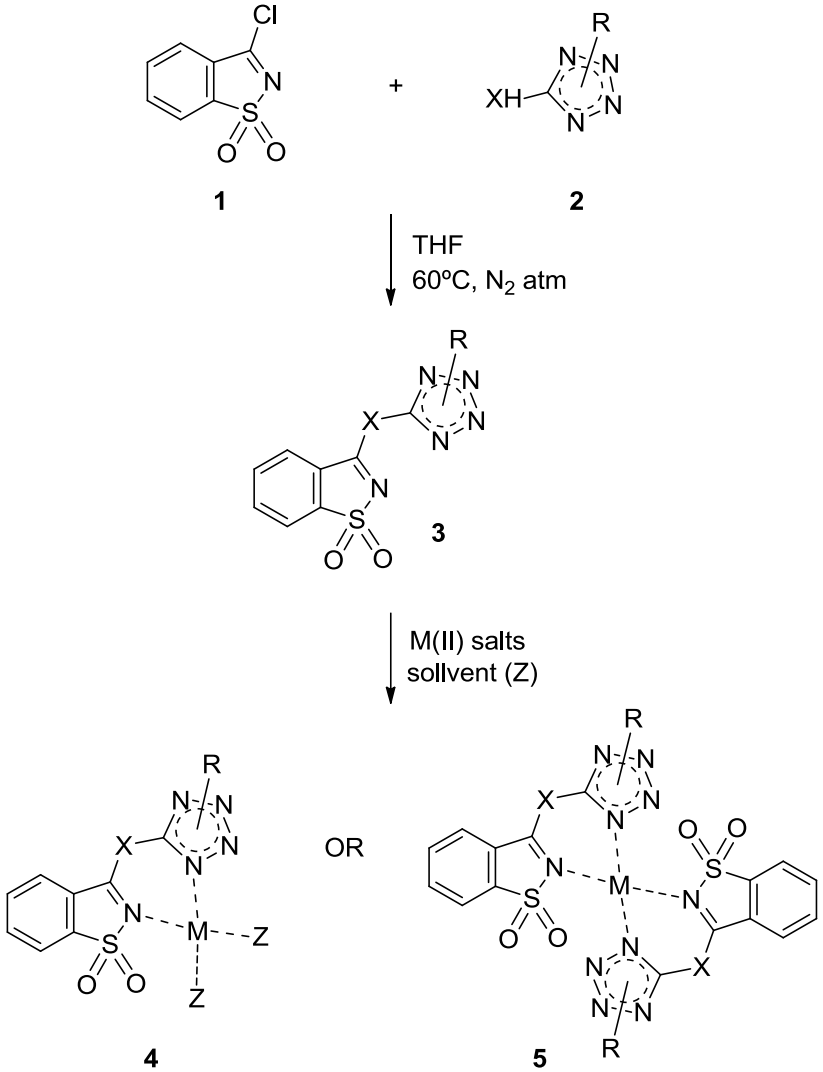

Scheme 2.1 – Representation of the general synthetic approach to tetrazole-saccharyl conjugates **3** and to complexes containing these conjugates as ligands. The complexes **4** and **5** are a general representation of types 1:1 and 1:2 metal-ligand complexes.

2.1.1. Preparation of the saccharyl building block

The saccharyl building block, 3-chloro-1,2-benzisothiazole 1,1-dioxide (*pseudo*-saccharyl chloride) **1**, was synthesised from commercially available saccharin **6**, through halogenation using PCl_5, at 220 ºC (Scheme 2.2). This reaction yields the sulfonyl chloride **7** as intermediate compound, which cyclises to the desired product **1**. The process involves attack of a chlorine anion on the carbon atom of the cyano group, which has a low nucleophilic susceptibility. Therefore, it was necessary to use higher temperatures, (from 180 up to 220 ºC), and/or longer reaction times (3 hours) to improve the yield of saccharine chlorination.[1] The reaction produces HCl and phosphorus oxychloride ($POCl_3$) as byproducts, which are removed from the reaction media by distillation. After filtration under pressure and recrystallization of the product from a mixture of toluene and trichloromethane (1:1) the desired product is recovered as colourless needles.

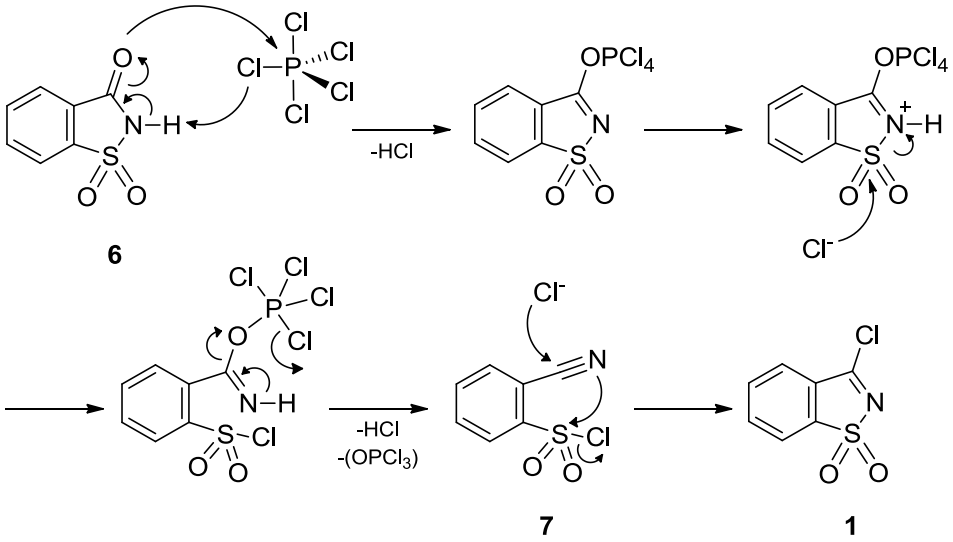

Scheme 2.2 – Schematic representation of the mechanism proposed for the synthesis of *pseudo*-saccharyl chloride **1**.[1]

2.1.2. Preparation of the tetrazole-based building blocks

Anhydrous 5-mercapto-1-methyltetrazole (**2**, X = SH, R = CH_3) and 5-aminotetrazole monohydrate (**2**, X = NH_2, R = H) were used as purchased. However 1- and 2-methyl-5-aminotetrazole, **11** and **12** respectively, were prepared from 5-aminotetrazole monohydrate (Scheme 2.3). The procedure for the mono-methylation of 5-aminotetrazole in a basic aqueous medium has been optimized to yield around 51% for **11** and 25% for **12**.

Substitutions of 5-substituted tetrazoles are usually carried out in alkaline solutions, where 5-substituted tetrazoles can act as free tetrazolate anions.[2–6] Dimethyl sulfate (DMS), used as methylating agent, was added to **9** in an alkaline medium and the mixture was refluxed for 1h. The mechanism proposed is depicted in Scheme 2.3.

As described in chapter 1 (section 1.1.4), the main problem of 5-substituted tetrazoles substitution lies in its low regioselectivity. The mechanism of these reactions involves a bimolecular process leading to the formation of an unstable intermediate of type **10** in the rate-limiting step. Therefore, formation of the isomeric products is controlled by the properties of the reaction intermediate **10**.[2,5] The ratio of isomers formed during the reaction is influenced by reaction temperature, the reactivity of the electrophile and the properties of the substituent at the 5-position, in particular with regard to steric hindrance. Higher reaction temperatures lead to increased amounts of 1-substituted isomers, whereas electron-withdrawing properties of substituents at the 5-position and bulky substituents increase the amounts of 2-substituted isomers. In agreement with these evidence, the methylation of **8** under the conditions used is expected to occur preferably at position 1, affording isomer **11**. However, 2-methylated isomer **12** could also be recovered, although in less amount. The two products obtained from methylation of 5-aminotetrazole **8** can be distinguished by mass spectrometry, through analysis of their fragmentation patterns (see Appendix; Figure S2). Moreover, the isomers have different solubility and can be separated during work-up.

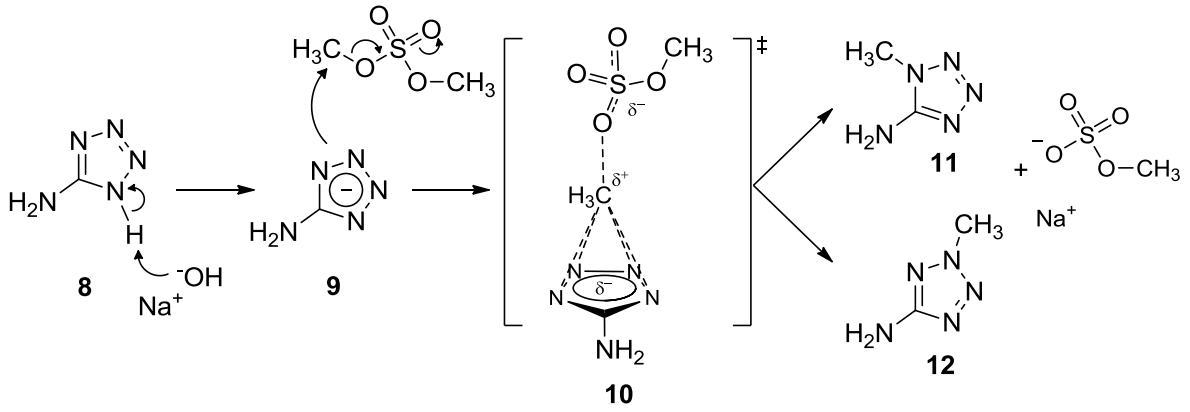

Scheme 2.3 – Schematic representation of the mechanism proposed for the mono-methylation of 5-aminotetrazole **8** to afford 1- and 2-methyl-5-aminotetrazoles, **11** and **12**.

2.1.3. Preparation of tetrazole-saccharyl conjugates

The synthetic approach to the preparation of tetrazole-saccharinates, depicted in Scheme 2.4, was developed based on the long experience of our group regarding synthesis and reactivity of tetrazole and benzisothiazole based compounds, especially for the large range of nucleophilic substitution reactions using *pseudo*-saccharyl chloride as substrate, involving different alcohols.[7,8]

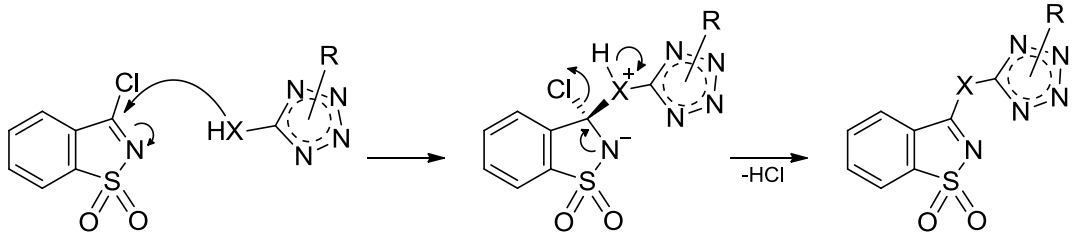

1 **2** **13** **3**

Scheme 2.4 - Schematic representation of the mechanism proposed for the synthesis of tetrazole saccharinates **3**.

In keeping with results obtained for the mechanism of solvolysis of 3-aryloxybenzisothiazoles, the nucleophilic substitution is believed to occur through an addition-elimination mechanism, with initial addition of the nucleophile **2** to the sp2 carbon of *pseudo*-saccharyl chloride **1**.[9,10] The proposed associative mechanism, that may involve a short-lived tetrahedral zwitterionic intermediate **13**, in the rate-determining step, is followed by elimination of the chloride ion, with the overall process yielding the target conjugate **3**.

2.1.4. Synthesis of complexes from tetrazole-saccharyl conjugates

The experimental investigation on the ability of tetrazole saccharinates to bind cations of transition metals was primarily assessed by typical titration experiments, through addition of freshly made solutions of metal ions to a solution of the ligand under investigation, following the reactions by UV/Vis spectroscopy. Titrations were conducted with several salts of divalent cations: Cu(II), Pb(II), Ni(II), Co(II), Fe(II), Zn(II), Ca(II) and Mn(II) (see Table S21 in Appendix). A more detailed spectroscopic study was conducted for copper(II) ions, due to its relevance as a promising selective cytotoxic agent against tumoral cells. Results of this study are presented in chapter 5 (see section 5.1.5 for details).

Preliminary complexation reactions involving conjugates **TS** and **2MTS** as potential multidentate nitrogen ligand, with cobalt(II), nickel(II) and copper(II) complexes, were also carried out.

The general procedure adopted involved the reaction of ligands, **TS** and **2MTS**, with a solution of $M(ClO_4)_2 \cdot 6H_2O$ [M = Co(II), Ni(II), Cu(II)] in an overall ligand-to-metal molar ratio of 1:1, in ethanol, methanol, acetone or a mixture of solvents. The reaction was conducted under vigorous stirring, at room temperature, during a period ranging from 3 to 24h. Slow evaporation of the solvent at room temperature normally affords a coloured powder. Using this approach, all attempts to synthesise crystalline complexes of cobalt(II), nickel(II) and copper(II) were unsuccessful. Then, by carefully layering each solution of ligand with a solution of $M(ClO_4)_2 \cdot 6H_2O$ at low concentrations (*ca.* 0.05 mM), in an overall ligand-to-metal molar ratio of 1:1, crystalline compounds could be isolated after several weeks, albeit of poor quality for single crystal X-ray diffraction. Carrying out the same layering experiments using more concentrated solutions (*ca.* 1.0 mM) afforded the same crystalline materials, albeit of somewhat poorer quality than before.

Attempting again the complexation of ligand **2MTS** with copper(II), in acetone, but adding distilled water to the final solution, resulted in instantaneous formation of a green precipitate, which was filtrated. Recrystallization of the precipitate by slow evaporation of a multi-solvent system afforded green crystals suitable for X-ray diffraction, which revealed the 2:1-type nature of these **2MTS**-Cu(II) complexes (as will be presented in chapter 5).

Our experiments indicated that the presence of perchlorate counterion (ClO_4^-) in the crystallization process could hinder crystal formation. Addition of water to the final solution seems to stimulate the precipitation of the complex, leaving the perchlorate ion solubilized in the aqueous layer. After filtration, the precipitate was then solubilized in a mixture of acetone and water (*ca.* 5% water in 95% acetone). The compound is more soluble in the volatile acetone, becoming increasingly less soluble in the remaining mixture. Through a slow evaporation of acetone, at room temperature, we could obtain the crystalline complex in few weeks. Using this same method we could produce other crystalline complexes of **TS**-Cu(II), **TS**-Co(II) and **TSMT**-Cu(II), although of poor quality for single crystal X-ray diffraction.

2.2. Detailed synthetic procedures

2.2.1. Solvents and reagents

All chemicals were used as purchased (from Sigma-Aldrich, Merck or Fluka; analytical grade). When required, solvents (technical grade) were freshly distilled from appropriate drying agents before use: THF was distilled from metallic sodium, using benzophenone as indicator, under a constant flow of dry nitrogen, and kept over molecular sieves, (4 Å); dichloromethane and trichloromethane was distilled from calcium chloride, under a constant flow of dry nitrogen, and kept over molecular sieves, (4 Å). Appropriate deuterated solvents (D_6-DMSO; D_1-chloroform; D_4-methanol) were supplied by Sigma-Aldrich and were used without additional purification.

Once isolated, the compounds prepared were characterised by the usual techniques. Melting points were recorded on a Stuart Scientific SMP3 melting point apparatus and are uncorrected. NMR spectra were recorded at 400 and 101 MHz, for ^{1}H and ^{13}C, respectively, obtained on a Bruker Avance III 400 spectrometer; chemical shifts (δ) are described in parts per million (ppm) relative to tetramethylsilane as internal standard (TMS; δ = 0.0 ppm). High-resolution mass spectra were obtained by electron ionization (EI) on a TOFMS (*Time of Flight – Mass Spectrometer*) Micromass GCT mass spectrometer. Elemental analyses (CHNS) were performed using a Fisons Instruments EA 1108 CHNS-O elemental analyser. Electronic absorption spectra (190-1100 nm wavelength range) were recorded on a Varian CARY 50 Bio UV-visible spectrophotometer, using quartz cells (1x1 cm); absorbance changes at selected UV lengths were measured using a 96-well microplate and a Biotek Synergy 4 Microplate Reader. Additionally, specific techniques and tools were used for detailed structural and photochemical studies. These are described below, in this chapter.

2.2.2. Preparation of the saccharyl building block: pseudo-saccharyl chloride (1)

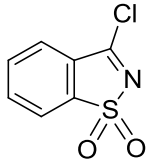

Saccharin (10.2 g; 56 mmol) and phosphorus pentachloride (14.0 g; 68 mmol) were heated at 220 ºC for 3 hours. Phosphorus oxychloride was then distilled off the reaction medium, under vacuum, at 180 ºC, and the residue crystallised on cooling to room temperature. The crystals were filtered, dried and re-crystallised with toluene and chloroform (1:1) until

colourless needles of pure *pseudo*-saccharyl chloride **1** were obtained (7.0 g; 63% yield); m.p. 143-145 ºC (lit.[1] 144-145 ºC); ^{1}H NMR (400 MHz, $CDCl_3$): δ 7.95-7.93 (d, 2H), 7.89-7.82 (m, 2H); ^{13}C NMR (101 MHz, $CDCl_3$): δ 166.08 (CCl), 140.63 (CSO_2), 134.93, 134.41, 129.94, 125.07, 122.49; MS (EI): m/z 201 $[M]^+$.

2.2.3. Preparation of the tetrazolyl building blocks (2)

2.2.3.1. 1-Methyl-(1*H*)-tetrazole-5-amine (1MT; 11)

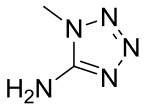

A 5M solution of sodium hydroxide was added dropwise to a stirred suspension of 5-aminotetrazole monohydrate **8** (10.3 g; 0.1 mol) in water (30 mL), until complete dissolution of the suspended material. Dimethyl sulfate (10 mL; 0.11 mol) was then added in small portions, keeping an alkaline medium through addition of aqueous sodium hydroxide. The final mixture was refluxed for 1 h, then cooled, and finally left in an ice bath, for 2 days, allowing for the precipitation of 1MT as colourless needles (5.0 g; 51% yield), m.p. 220-221 ºC, ^{1}H NMR (400MHz, DMSO): δ 6.62 (s, NH_2), 3.69 (s, CH_3); ^{13}C NMR (101 MHz, DMSO) δ 156.29 (CNH_2), 31.93 (CH_3); MS (EI): m/z calc. for $C_2H_2N_5$ 99.0545, found 99.0529 $[M]^+$ (57.0442, fragment N_3CH_3).

2.2.3.2. 2-Methyl-(2*H*)-tetrazole-5-amine (2MT; 12)

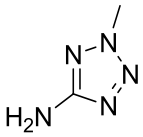

The filtrate collected was evaporated under reduced pressure to afford a solid residue. Water (50 mL) was added, and the mixture was then extracted with DCM (3 x 50 mL). The organic extract was dried and the solvent removed under reduced pressure to afford a white solid residue. Recrystallization from DCM gave 2MTS as colourless needles (2.5 g, 25% yield); m.p. 104-105 ºC; ^{1}H NMR (400 MHz, DMSO): δ 5.94 (s, NH_2) 4.06 (s, CH_3); ^{13}C NMR (101 MHz, DMSO) δ 167.63 (CNH_2), 39.26 (CH_3); MS (EI): m/z calc. for $C_2H_2N_5$ 99.0545, found 99.0534 $[M]^+$ (71.0475, fragment $NH_2CN_2CH_3$).

2.2.4. Synthesis of the ligands

2.2.4.1. General procedure for the preparation of ligands

A mixture of the tetrazolyl derivative **2** (1 eq.) and *pseudo*-saccharyl chloride **1** (1.30 g, 6.45 mmol) in dry THF was stirred at 60 ºC for 24 h under a nitrogen atmosphere. The solvent was then evaporated under reduced pressure and the remaining solid was washed with acetone, dried under vacuum at room temperature and recrystallized to give the required product.

*This general procedure was applied to the synthesis of ligands **TS**, **1MTS**, **2MTS** and **TSMT**.*

2.2.4.2. Preparation of *N*-(1*H*-tetrazol-5-yl)-1,2-benzisothiazol-3-amine 1,1-dioxide (tetrazole-saccharinate; TS)

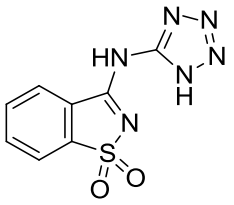

Obtained as white powder from 5-aminotetrazole monohydrate **8** (0.66 g; 6.45 mmol) and *pseudo*-saccharyl chloride **1** in dry THF (50 ml). Recrystallization from a mixture of acetone/ethanol (1:1) gave the required product as colourless crystals (1.21 g; 75% yield); m.p. 270–271 ºC; ^{1}H NMR (400 MHz, DMSO): δ 8.59-8.47 (m, 1H), 8.22-8.09 (m, 1H), 7.96-7.91 (m, 2H); MS (EI): m/z calc. for $C_8H_6N_6O_2S$ 250.0273, found 250.0249 $[M]^+$.

2.2.4.3. Preparation of *N*-(1-methyl-1*H*-tetrazol-5-yl)-2,3-dihydro-1,2-benzisothiazol-3-imine 1,1-dioxide (1-methyltetrazole-saccharinate; 1MTS)

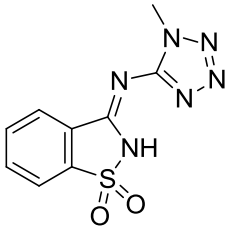

Obtained as white powder from 1-methyl-(1*H*)-tetrazole-5-amine **11** (0.64 g; 6.45 mmol) and *pseudo*-saccharyl chloride **1** in dry THF (160 ml). Recrystallization from a mixture of acetone/ethanol (1:1) gave the required product as colourless crystals (1.09 g; 64% yield); m.p. 243-245 ºC; ^{1}H NMR (400 MHz, DMSO): δ 12.46 (s, NH) 8.55-8.47 (m, 1H), 8.13-8.11 (m, 1H), 7.97-7.88 (m, 2H), 4.43 (s, CH_3); ^{13}C NMR (101 MHz, DMSO): δ 159.11 (C_{sac}S), 157.60

(SC_{tet}), 141.39, 134.20, 133.80, 127.23, 124.05, 121.82, 40.13 (CH_3); MS (EI): m/z calc. for $C_9H_8N_6O_2S$ 264.0429, found 264.0420 $[M]^+$.

2.2.4.4. Preparation of *N*-(2-methyl-2*H*-tetrazol-5-yl)-1,2-benzisothiazol-3-amine 1,1-dioxide (2-methyltetrazole-saccharinate; 2MTS)

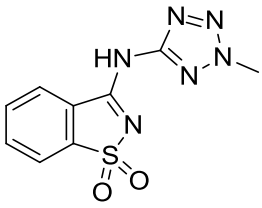

Obtained as white powder from 2-methyl-(2*H*)-tetrazole-5-amine **12** (0.64 g; 6.45 mmol) and *pseudo*-saccharyl chloride **1**, in dry THF (50 ml). Recrystallization from a mixture of acetone/ethanol (1:1) yielded the required product as colourless crystals (1.19 g; 70% yield); m.p. 285-286 ºC; ^{1}H NMR (400 MHz, DMSO): δ (n.o., NH) 8.36-8.30 (m, 1H), 8.14-8.09 (m, 1H), 7.97-7.91 (m, 2H), 4.04 (s, CH_3); ^{13}C NMR (101 MHz, DMSO): δ 159.86 ($C_{sac}S$), 149.97 (SC_{tet}), 141.51, 134.34, 133.80, 127.45, 124.28, 121.73, 34.40 (CH_3) MS (EI): m/z calc. for $C_9H_8N_6O_2S$ 264.0429, found 264.0420 $[M]^+$.

2.2.4.5. Preparation of *N*-deuterated 1- and 2-methyltetrazole-saccharinates (Nd-1MTS and Nd-2MTS)

N_d-1MTS and **N_d-2MTS** were obtained from the parent compounds by direct H→D exchange in deuterated methanol, under vigorous stirring conditions and refluxing (48 h, under nitrogen atmosphere). The solvent was evaporated under reduced pressure. Deuteriation yields could be estimated from the IR spectra of the obtained crystals to be within the 50–70% range.

2.2.4.6. Preparation of the 3-((1-methyl-1*H*-tetrazol-5-yl)thio)-1,2-benzisothiazol 1,1-dioxide (1-methyltetrazole-5-thiosaccharinate; TSMT)

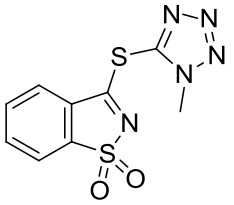

Obtained as white powder from 5-mercapto-1-methyltetrazole (0.75 g; 6.45 mmol) and *pseudo*-saccharyl chloride **1**, in dry THF (50 ml). Recrystallization from a mixture of chloroform/THF (2:1) gave the required product as colourless crystals (1.49g; 82% yield); m.p. 222-224 °C. ^{1}H NMR (400 MHz, $CDCl_3$): δ 7.98-7.96 (m, 1H), 7.91-7.79 (m, 3H), 4.22 (s, CH_3); ^{13}C NMR (101 MHz, $CDCl_3$): δ 170.35 ($C_{sac}S$), 165.77 (SC_{tet}), 139.44, 135.13, 134.35, 128.84, 123.34, 122.94, 35.26 (CH_3). MS (EI): m/z calc. for $C_9H_7N_5O_2S_2$ 281.0041, found 281.0060 $[M]^+$.

2.2.5. Synthesis of Cu(II) complexes comprising tetrazole-saccharinates as ligands

Cu(II) complexes were prepared from reaction of the corresponding ligands, **TS** and **2MTS**, with $Cu(ClO_4)_2{\cdot}6H_2O$, in acetone and water.

Caution! *Perchlorate salts of metal complexes with organic ligands are potentially explosive. Only a small amount of material should be prepared, and it must be handled with care.*

2.2.5.1. [Cu(TS)(H_2O)$_2$(OH)] (CuTS)

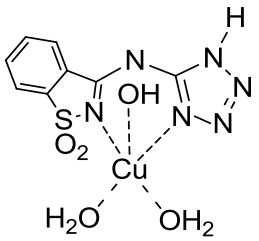

A solution of **TS** (0.050 g, 0.20 mmol) in acetone (20 mL) was added slowly to a stirring solution of $Cu(ClO_4)_2{\cdot}6H_2O$ (0.074 g, 0.20 mmol) in acetone (5 mL). After addition, the colour changed to green and the final solution was stirred for 30 min at room temperature. Distilled water (10 mL) was then added, resulting in instantaneous formation of a green precipitate, which was filtered. The filtrate was solubilized in acetone, then a few drops of H_2O were added and the resulting mixture was left for slow evaporation, affording a turquoise crystalline

material, albeit of poor quality for single crystal X-ray diffraction. Yield: (0.059 g, 81%); elemental analysis: found: C, 26.06; H, 2.72; N, 22.85; S, 8.59. Calc. for $C_8H_{10}CuN_6O_5S$: C, 26.27; H, 2.76; N, 22.97; S, 8.77%; IR (KBr pellet, cm^{-1}): 3566, 3175, 1602 (CN), 1568 (CNC), 1275, 1153 (SO_2), 981 (NS), 817, 767.

2.2.5.2. $[Cu(2MTS)_2(H_2O)]\cdot H_2O$ ($Cu2MTS_2$)

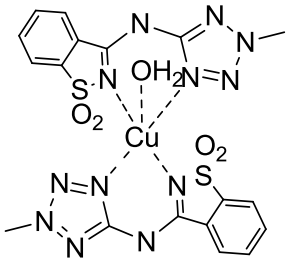

This complex was obtained as described for the previous one. From **2MTS** (0.050 g, 0.19 mmol) in acetone (20 mL), added slowly to a stirring solution of $Cu(ClO_4)_2\cdot 6H_2O$ (0.070 g, 0.19 mmol) in acetone (5 mL). Green coloured crystals were collected after 2 weeks, filtered, dried under reduced pressure, and characterized by X-ray diffraction. Yield: (0.046 g, 77%); elemental analysis: found C, 34.49; H, 2.87; N, 26.80 S, 9.94. Calc. for $C_{18}H_{18}CuN_{12}O_6S_2$: C, 34.53; H, 2.90; N, 26.85; S, 10.24%; IR (KBr pellet, cm^{-1}): 3635, 3526, 1605, 1576 (CN), 1503 (CN), 1388, 1371, 1301 (SO_2), 1262, 1161 (SO_2), 1114, 960 (CNC), 792, 765, 705.

2.3. Matrices preparation

The matrix isolation studies described in this thesis were performed at the Laboratory of Molecular Cryospectroscopy and Biospectroscopy (LMCB) integrated in the Department of Chemistry of the Faculty of Science and Technology of the University of Coimbra. The setup used during the studies is illustrated in Figure 2.1.

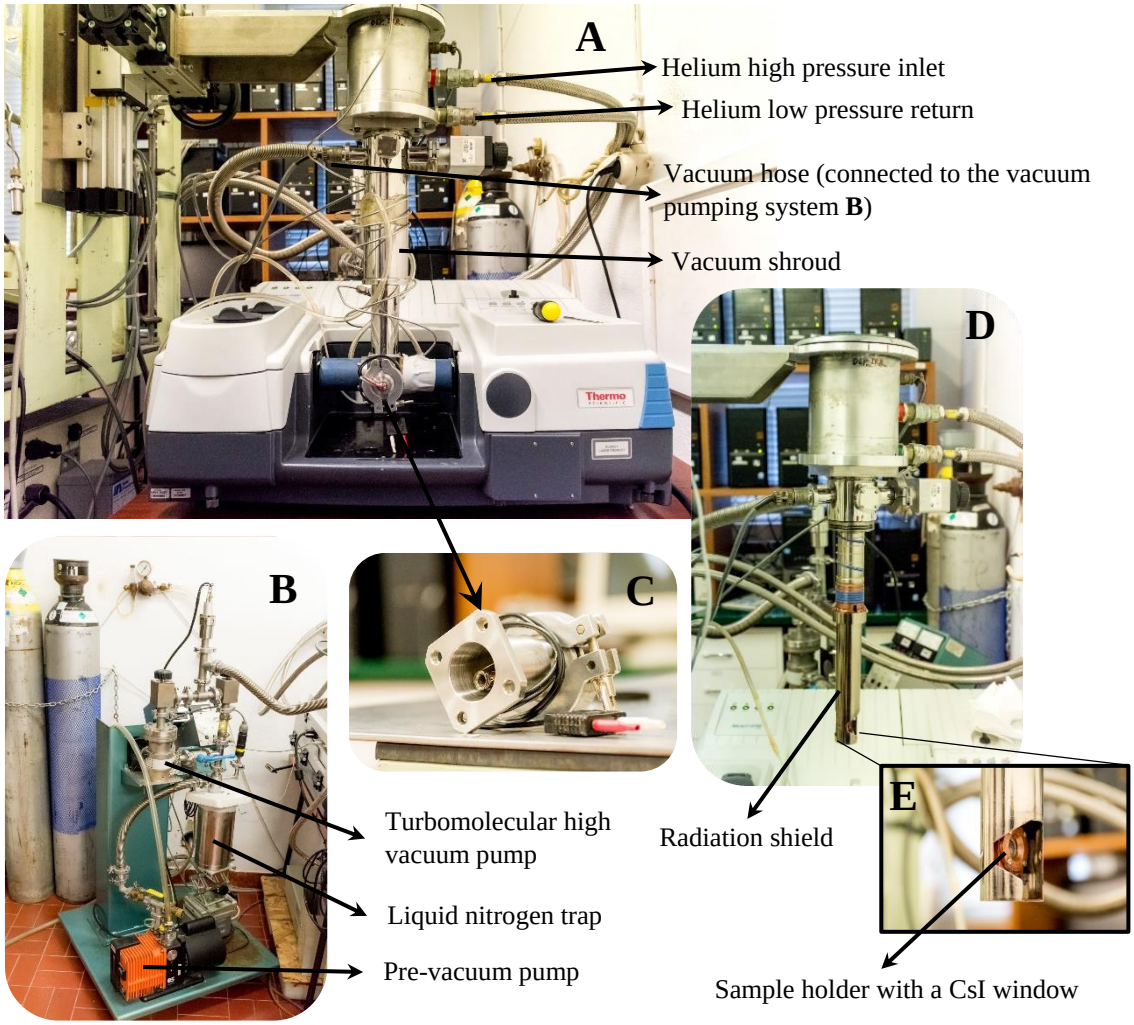

Figure 2.1 – Matrix isolation setup used in the course of the studies conducted and described in this thesis: A) Cryostat (APD Cryogenics closed-cycle helium refrigeration system) with a DE-202A expander coupled to a Nicolet 6700 Fourier transform infrared spectrometer (necessary modifications of the sample compartment of the spectrometer were done in order to accommodate the cryostat head and allow purging of the instrument by a stream of dry air, to remove water vapours and CO_2); B) vacuum pumping system; C) specially designed variable-temperature mini-oven for sublimation of solid substances; D) DE-202A expander without the vacuum shroud; E) sample holder with a CsI window.

The low-temperature matrices were prepared by codeposition of the matrix gas (argon 99.9998%, obtained from Air Liquid) and vapours of the compound under analysis, produced by sublimation in a specially designed variable-temperature mini-oven assembled inside the cryostat (Figure 2.1, C), onto the cooled CsI (Cesium Iodide) substrate of the cryostat (Figure 2.1, E). The temperature of the mini-oven used for evaporation of the compounds was *ca.* 175 ºC for **TS**, 150 °C for **2MTS**, 100 ºC for **TSMT**, 60 ºC for **1MT** and 30 ºC for **2MT**. The cryogenic system was based on a closed-cycle helium refrigeration system with a DE-202A expander (Figure 2.1, A). The temperature of the CsI substrate during deposition was *ca.* 15 K.

2.4. Infrared and Raman spectroscopies

2.4.1. Matrix isolation IR spectroscopy (isolated compounds)

The infrared spectra of matrix isolated compounds were obtained using a Nicolet 6700 Fourier transform infrared spectrometer (Figure 2.1, A) equipped with a deuterated triglycinesulphate (DTGS) detector and a Ge/KBr beamsplitter, with 0.5 cm^{-1} spectral resolution in the spectral range 4000-400 cm^{-1}. The spectra were acquired after accumulating interferograms from 256 up to 512 scans. The average matrix deposition time was two hours. During the experiments, the flux of the matrix gas was controlled by a micrometre needle valve and monitored by reading the drop pressure in the reservoir with a capacitance manometer. In a typical experiment, we deposit *ca.* 40 mbar of argon (in a rate 0.3-0.9 mbar/min) onto the substrate of the cryostat.

2.4.2. IR spectroscopy (solid polycrystalline compounds)

The room-temperature IR spectra (4000-500 cm^{-1}) of solid polycrystalline compounds in a KBr pellet were obtained using a Bomem MB104 or a Bruker FTIR-TENSOR 27 Fourier transform spectrometer equipped with a deuterated triglycinesulphate (DTGS) detector and Zn/Se optics. Data collection was performed with 4 cm^{-1} spectral resolution and 128 scans.

Temperature variation studies (within 0.1 ºC resolution) were undertaken by coupling a Mettler-Toledo FP84HT-TA cell (controlled by a Mettler-Toledo FP90 central Processor) with the IR spectrometer.

2.4.3. Raman spectroscopy (solid polycrystalline compounds)

The room-temperature Raman spectra (3380-70 cm^{-1}) were obtained for the neat polycrystalline solids as a pellet, using a dispersive Raman instrument, model DXR SmartRaman™ (Thermo Fisher Scientific, Inc.), equipped with an externally stabilized diode laser providing excitation light at 780 nm (13 mW output power). The calibration of the instrument is performed once weekly with the Thermo Fisher Scientific, Inc. patented auto-alignment and automated calibration device. Data collection was performed for an exposure time of 15 s, 10 sample exposures, and a slit aperture of 25 μm. Fluorescence correction was applied using a polynomial of fifth degree.

2.5. Crystallographic analysis

X-ray data were collected on a Bruker APEX II-CCD diffractometer, using small single crystals. The crystallographic structures were solved by direct methods using SHELXS-97.[11] Refinements were carried out with the SHELXL-97 package.[12] All refinements were made by full-matrix least-squares on F^2 with anisotropic displacement parameters for all non-hydrogen atoms. All hydrogen atoms could be located on a difference Fourier synthesis; their positions were refined as riding on parent atoms with an isotropic temperature factor using SHELXL-97 defaults that constrains these atoms to idealized positions. X-ray data collection and processing parameters for studied compounds (**TS**, **1MTS**, **2MTS**, **TSMT** and **Cu2MTS$_2$**) are presented in Table S1, in Appendix.

2.6. UV irradiations experiments

In a first approach, broadband irradiations of the matrices were carried out with light from a 500 W Hg(Xe) lamp (Newport, Oriel Instruments), with output power set to 150 W, through the quartz window of the cryostat ($\lambda > 200$ nm).

In other experiments, the matrices were irradiated using narrowband (fwhm ~0.2 cm^{-1}) with the frequency-doubled signal beam of a Quanta-Ray MOPO-SL optical parametric oscillator, pumped with a pulsed Nd:YAG laser (repetition rate = 10 Hz, pulse energy ~1-6 mJ, duration = 10 ns). The UV light used to induce the initial photochemistry of compounds was selected according to the UV/Vis spectra obtained in ethanol, at room temperature, which show absorption maxima at ~222 nm for **1MT**, ~248 nm for **2MT**, ~254 nm for **2MTS** and ~263 nm for **TSMT**.

2.7. Computational details

The quantum chemical calculations were performed using the density functional theory (DFT) and the B3LYP or O3LYP functional.[13,14] The basis set used were: the valence double-ζ polarized 6-31++G(d,p) or the extended valence triple-ζ polarized 6-311++G(3df,3pd) for the ligands (**TS**, **1MTS**, **2MTS** and **TSMT**) and the triple-ζ polarized 6-311++G(d,p) for the tertrazoles used as building blocks in the synthesis of the ligands (**1MT** and **2MT**).[15–18] Inclusion of both diffuse and polarization functions in the basis sets is required for a more accurate approximation to the calculated infrared spectra, since vibrational modes involving hypervalent S atoms, as in the case of these ligands (in particular the SO_2 stretching and bending modes), are known not to be correctly predicted at a lower level of approximation.[19,20] The use of the B3LYP or O3LYP functionals with the 6-311++G(3df,3dp) basis set was found to be appropriate to attain reliable results for these ligands, with moderate computational effort.[19–21] The transition states were located using the synchronous-transit quasi-Newton method (QST3 implementation).[22,23] The optimization of geometries was followed by harmonic vibrational calculations undertaken at the same level of theory, and the nature of the obtained stationary points was checked through analysis of the corresponding Hessian matrix. The frequencies are related to the eigenvalues of the Hessian matrix, which contains second derivatives: if the eigenvalues are all positive, then the frequencies are all real and the stationary point is a local minimum.

The calculated harmonic vibrational frequencies were used to simulate the spectra using Lorentzian functions, and to assist the analysis of the experimental spectra. Different scaled factors were used, depending on the functional and basis set used: 0.978 for the B3LYP/6-311++G(3df,3pd)[24] and 0.992 for the O3LYP/6-311++G(3df,3pd);[21] 0.98 for the B3LYP/6-31++G(d,p) and 0.968 for B3LYP/6-311++G(d,p) (obtained by least-squares linear fit of the experimental *versus* calculated frequencies; Figure S3; in Appendix). Calculations were performed with the Gaussian 03 or Gaussian 09 suite of programs.[25]

Quantum chemistry calculations for the complex (**Cu2MTS$_2$**) have been performed using the GAMESS (US) program,[26] both at the Restricted Open Shell Hartree-Fock (ROHF) and unrestricted density functional theory with the hybrid B3LYP functional (UB3LYP), with a spin multiplicity of 2 (S = 1/2). The geometry of the complex was optimized starting from the observed geometry in the crystal, determined from XRD, using the standard 6-31G(d,p) basis set for the non-metal atoms, and the LANL2DZ (Los Alamos National Laboratory 2 Double-ζ)

effective core potential (EPC) on the metal atom.[27–29] Tight conditions for convergence on both energy (SCF cycles) and energy gradient (10^{-7} atomic units) were employed.

2.8. Metal chelating activity

The ligands **TS** and **2MTS** were assayed for their Cu^{2+}, Fe^{2+} and Ca^{2+} chelating activity, at different concentrations, and these activities were compared with the chelating activity exhibited by the metal chelator EDTA (ethylenediamine tetraacetic acid)[30] or, for calcium ions, EGTA (ethylene glycol tetraacetic acid). EGTA shows a much higher affinity for Ca^{2+}, compared to other cations,[31] and is currently used when Ca^{2+} specific chelation is desired.

The Fe^{2+}, Cu^{2+} and Ca^{2+} chelating activities were separately evaluated by spectrophotometry, using selected chelating indicators that produce coloured complexes, following standard methods described in the literature.[32,33] The metal ion chelating activities were determined by measuring the colour changes due to the Fe^{2+}/ferrozine complex,[34,35] Cu^{2+}/pyrocatechol violet (PV),[36–38] and Ca^{2+}/*o*-cresolphthalein complexone,[39,40] respectively. The change in colour of the solutions was measured at selected wavelengths, using a microplate reader, and the chelating activity (%) was calculated using equation (2.1)[36], relative to a control without the ligand under study.

$$Chelating\ activity\ (\%) = \left(1 - \frac{absorbance\ of\ sample\ at\ \lambda\ (nm)}{absorbance\ of\ control\ at\ \lambda\ (nm)}\right) \times 100 \qquad (2.1)$$

Copper: Solutions of the ligand (30 μL, at 1, 5 and 10 mM) were added to a mixture comprising 100 μL of 0.2 mM $CuSO_4$ and 6 μL of 4 mM pyrocatechol violet, dissolved in 200 μL of a 50 mM sodium acetate buffer (pH 6.0), in 96-well microplates. The change in absorbance of the PV solution was measured at 632 nm.

Iron: Solutions of the ligand (30 μL, at 1, 5 and 10 mM) were added to a mixture of 100 μL of 0.5 mM $FeCl_2$ and 12.5 ml of ferrozine solution (40 mM), dissolved in 250 μL of sodium acetate buffer (pH 4.9), in 96-well microplates. The change in colour was measured at 562 nm.

Calcium: Solutions of the ligand (60 μL at 1, 5 and 10 mM) were added to a mixture of 30 μL of 0.5 mM $CaCO_3$ and 20 μL of 0.47 mM *o*-cresolphthalein complexone, dissolved in 200 μL of ammonium chloride buffer (pH 9.96), in 96-well microplates. The change in colour was measured at 575 nm.

Details on the methodology used for determination of metal chelating activity: The metal ion chelating activity was evaluated by spectrophotometry, using selected metal chelating

indicators that produce coloured complexes. The chelating activity was determined measuring the colour change that occurs when the indicator goes from its metal ion-bound form to the unbound form. This colour change takes place when the introduced metal chelator removes the metal ion bound to the indicator. For instance, the blue complex of pyrocatechol violet (PV) with Cu^{2+} turns yellow (pH 6.0) when copper ions are sequestered by the chelating agent. The change in colour of the solution was measured at 632 nm, and the chelating activity was calculated using the equation (2.1).

The complex formed between PV and Cu^{2+} absorbs at 632 nm, whereas PV dissociated from the metal results in a considerable decrease of the absorption at 632 nm. A solution containing the complex PV and Cu^{2+} was used as a control, and introduced in the equation "absorbance of control at 632 nm" to normalize the absorbance in the range [0-1]. Addition of chelating agent (EDTA, TS or 2MTS) to the mixture of PV and Cu^{2+} resulted in a reduction of absorption at 632 nm, expressed in the equation as "absorbance of sample at 632 nm". It should be noticed that these changes in absorption result from competition for a coordination position of the studied ligand and the PV molecule, promoting release of PV, so that the introduced ligand can be coordinated with Cu^{2+} to form the new complex. Therefore, the amount of PV released is responsible for the change in absorbance. The chelating activity of the ligand under study is the difference between 1 (when all the PV molecules are released) and the normalized absorbance of the PV molecules remaining coordinated with Cu^{2+}.

2.9. Toxicity evaluation *in vitro*

Cell culture: For the evaluation of cytotoxic activity, five tumour cell lines were used: hepatocellular carcinoma (HepG2), human cervical epithelioid carcinoma (HeLa), human neuroblastoma (SH-SY5Y), human histocytic lymphoma (U937) and human acute monocyclic leukaemia (THP-1); and 2 non-tumour cell lines: murine bone marrow (S17) and murine microglia (N9). All cells were maintained in Dulbecco's modified eagle medium (DMEM) supplemented with 10% heat-inactivated foetal bovine serum (FBS), 1% L-glutamine (2 mM), and 1% penicillin (50 U/mL)/streptomicin (50 μg/mL), at 37 °C in a humidified atmosphere with 5% CO_2.

Cytotoxicity assay: Exponentially growing cells were plated in 96-well tissue plates at a density of 5×10^3 cells/well. Adherent cell lines were previously incubated for 24 h to ensure adhesion to the wells. Compounds were then applied at various concentrations (0-100 μM) and control cells were treated with dimethyl sulfoxide (DMSO) at the highest concentration used in

test wells (0.5%). Cell viability was determined, after 72h of incubation, by the MTT [3-(4,5-dimethylthiazol-2-yl)-2,5-diphenyltetrazolium bromide] colorimetric assay.[41] Briefly, 2 hours prior to the end of the incubation period 20 μL of MTT (5 mg/mL in PBS (phosphate-buffer saline)) were added to each well and further incubated at 37 °C. Then, 150 μL of DMSO were added to each well in order to dissolve the formazan crystals and the absorbance was measured at 590 nm (Biotek Synergy 4). Results were expressed in terms of % of cell viability, relatively to the negative control or as IC_{50} (half maximal inhibitory concentration μM). All experiments were run in triplicate. The IC_{50} values were calculated by sigmoidal fitting of the data in the GraphPad Prism V 5.0 program (GraphPad Software, La Jolla, CA, USA). The selectivity index (SI) of the compounds was estimated using the following equation: Selectivity = IC_{50} NT/IC_{50} T, where NT and T indicate IC_{50} modulated by the compound on non-tumour and tumour cells, respectively.

2.10.References

(1) Brigas, A. F.; Fonseca, C. S. C.; Johnstone, R. A. W. *J. Chem. Res.* **2002**, No. 6, 2.
(2) Ostrovskii, V. A.; Koren, A. O. *Heterocycles* **2000**, *53* (6), 1421–1448.
(3) Henry, R. A.; Finnegan, W. G. *J. Am. Chem. Soc.* **1954**, *76* (3), 923–926.
(4) Koldobskii, G. I. *Russ. J. Org. Chem.* **2006**, *42* (4), 469–486.
(5) Roh, J.; Vávrová, K.; Hrabálek, A. *European J. Org. Chem.* **2012**, *2012* (31), 6101–6118.
(6) Herbst, R. M.; Roberts, C. W.; Harvill, E. J. *J. Org. Chem.* **1951**, *16* (1), 139–149.
(7) Frija, L. M. T. T.; Cristiano, M. L. S.; Guimarães, E. M. O.; Martins, N. C.; Loureiro, R. M. S. S.; Bickley, J. F.; Guimaraes, E. M. O. *J. Mol. Catal. A-Chemical* **2005**, *242* (1–2), 241–250.
(8) Araujo, N. C. P.; Brigas, A. F.; Cristiano, M. L. S.; Frija, L. M. T.; Guimaraes, E. M. O.; Loureiro, R. M. S. *J. Mol. Catal. A-Chemical* **2004**, *215* (1–2), 113–120.
(9) Brigas, A. F.; Goncalves, P. M.; Johnstone, R. A. W. *Acta Crystallogr. Sect. C Cryst. Struct. Commun.* **1998**, *54* (2), 251–253.
(10) Ismael, A.; Gago, D. J. P.; Cabral, L. I. L.; Fausto, R.; Cristiano, M. L. S. *Croat. Chem. Acta* **2014**, *87* (4), 363–373.
(11) Sheldrick, G. M. *SHELXS-97, Program for the Solution of Crystal Structure*; University of Göttingen: Göttingen, Germany, 1997.
(12) Sheldrick, G. M. *SHELXL-97, Program for the Refinement of Crystal Structure*; University of Göttingen: Göttingen, Germany, 1997.
(13) Gill, P. M. W.; Johnson, B. G.; Pople, J. A.; Frisch, M. J. *Chem. Phys. Lett.* **1992**, *197* (4–5), 499–505.
(14) Becke, A. D. *Phys. Rev. A* **1988**, *38* (6), 3098–3100.
(15) Frisch, M. J.; Pople, J. A.; Binkley, J. S. *J. Chem. Phys.* **1984**, *80* (7), 3265.
(16) Clark, T.; Chandrasekhar, J.; Spitznagel, G. W.; Schleyer, P. V. R. *J. Comput. Chem.* **1983**, *4* (3), 294–301.
(17) McLean, A. D.; Chandler, G. S. *J. Chem. Phys.* **1980**, *72* (10), 5639–5648.
(18) Krishnan, R.; Binkley, J. S.; Seeger, R.; Pople, J. A. *J. Chem. Phys.* **1980**, *72* (1), 650.
(19) Almeida, R.; Gómez-Zavaglia, A.; Kaczor, A.; Ismael, A.; Cristiano, M. L. S.; Fausto, R. *J. Mol. Struct.* **2009**, *938* (1–3), 198–206.

(20) Kaczor, A.; Almeida, R.; Gómez-Zavaglia, A.; Cristiano, M. D. S.; Fausto, R. *J. Mol. Struct.* **2008**, *876* (1–3), 77–85.
(21) Duarte, L.; Reva, I.; Cristiano, M. de L. S.; Fausto, R. *J. Org. Chem.* **2013**, *78* (7), 3271–3275.
(22) Peng, C.; Bernhard Schlegel, H. *Isr. J. Chem.* **1993**, *33* (4), 449–454.
(23) Peng, C.; Ayala, P. Y.; Schlegel, H. B.; Frisch, M. J. *J. Comput. Chem.* **1996**, *17* (1), 49–56.
(24) Andrzejewska, A.; Lapinski, L.; Reva, I.; Fausto, R. *Phys. Chem. Chem. Phys.* **2002**, *4* (14), 3289–3296.
(25) Frisch, M. J.; Trucks, G. W.; Schlegel, H. B.; Scuseria, G. E.; Robb, M. A.; Cheeseman, J. R.; Scalmani, G.; Barone, V.; Mennucci, B.; Petersson, G. A.; Nakatsuji, H.; Caricato, M.; Li, X.; Hratchian, H. P.; Izmaylov, A. F.; Bloino, J.; Zheng, G.; Sonnenberg, J. L.; Hada, M.; Ehara, M.; Toyota, K.; Fukuda, R.; Hasegawa, J.; Ishida, M.; Nakajima, T.; Honda, Y.; Kitao, O.; Nakai, H.; Vreven, T.; Montgomery, J. A.; Jr.; Peralta, J. E.; Ogliaro, F.; Bearpark, M.; Heyd, J. J.; Brothers, E.; Kudin, K. N.; Staroverov, V. N.; Kobayashi, R.; Normand, J.; Raghavachari, K.; Rendell, A.; Burant, J. C.; Iyengar, S. S.; Tomasi, J.; Cossi, M.; Rega, N.; Millam, J. M.; Klene, M.; Knox, J. E.; Cross, J. B.; Bakken, V.; Adamo, C.; Jaramillo, J.; Gomperts, R.; Stratmann, R. E.; Yazyev, O.; Austin, A. J.; Cammi, R.; Pomelli, C.; Ochterski, J. W.; Martin, R. L.; Morokuma, K.; Zakrzewski, V. G.; Voth, G. A.; Salvador, P.; Dannenberg, J. J.; Dapprich, S.; Daniels, A. D.; Farkas, O.; Foresman, J. B.; Ortiz, J. V.; Cioslowski, J.; Fox, D. J. *Gaussian 09, Revision A.02*; Gaussian, Inc.: Wallingford, CT, 2009.
(26) Schmidt, M. W.; Baldridge, K. K.; Boatz, J. A.; Elbert, S. T.; Gordon, M. S.; Jensen, J. H.; Koseki, S.; Matsunaga, N.; Nguyen, K. A.; Su, S.; Windus, T. L.; Dupuis, M.; Montgomery, J. A. *J. Comput. Chem.* **1993**, *14* (11), 1347–1363.
(27) Hay, P. J.; Wadt, W. R. *J. Chem. Phys.* **1985**, *82* (1), 270–283.
(28) Hay, P. J.; Wadt, W. R. *J. Chem. Phys.* **1985**, *82* (1), 299–310.
(29) Wadt, W. R.; Hay, P. J. *J. Chem. Phys.* **1985**, *82* (1), 284–298.
(30) Wiberg, E.; Holleman, A. F.; Wiberg, N. *Inorganic Chemistry*; Academic Press: San Diego, 2001.
(31) Schmid, R. W.; Reilley, C. N. *Anal. Chem.* **1957**, *29* (2), 264–268.
(32) Megías, C.; Pastor-Cavada, E.; Torres-Fuentes, C.; Girón-Calle, J.; Alaiz, M.; Juan, R.; Pastor, J.; Vioque, J. *Eur. Food Res. Technol.* **2009**, *230* (2), 353–359.
(33) Hidaka, S.; Nishimura, H.; Nakajima, K.; Liu, S. Y. *J. Periodontal Res.* **1996**, *31* (6), 408–413.
(34) Carter, P. *Anal. Biochem.* **1971**, *40* (2), 450–458.
(35) Stookey, L. L. *Anal. Chem.* **1970**, *42* (7), 779–781.
(36) Egusa Saiga, A.; Nishimura, T. *Biosci. Biotechnol. Biochem.* **2013**, *77* (11), 2201–2204.
(37) Taylor, P.; Irving, H. M. N. H.; Iwantscheff, G.; Germany, W. *CRC Crit. Rev. Anal. Chem.* **2008**, No. January 2013, 37–41.
(38) Su, J.; Sun, Y.-Q.; Huo, F.-J.; Yang, Y.-T.; Yin, C.-X. *Analyst* **2010**, *135* (11), 2918–2923.
(39) Stavropoulos, W. S.; Thiegs, B. J.; Mack, R. F. Determination of calcium. US3938954 A, 1973.
(40) Pollard, F. H.; Martin, J. V. *Analyst* **1956**, *81* (963), 348.
(41) Mosmann, T. *J. Immunol. Methods* **1983**, *65* (1–2), 55–63.

Chapter 3. Structure of tetrazole-saccharinates

The work described in this chapter was included in the following publications:

Gómez-Zavaglia, A.; Ismael, A.; Cabral, L. I. L.; Kaczor, A.; Paixão, J. A.; Fausto, R.; Cristiano, M. L. S.; "Structural investigation of nitrogen-linked saccharinate-tetrazole." *J. Mol. Struct*. 2011; 1003; 103-110.

Ismael, A.; Paixão, J. A.; Fausto, R.; Cristiano, M. L. S.; "Molecular structure of nitrogen-linked methyltetrazole-saccharinates."; *J. Mol. Struct*. 2012; 1023; 128-142.

Ismael, A.; Gómez-Zavaglia, A.; Borba, A.; Cristiano, M. de L. S.; Fausto, R.; "Amino→Imino Tautomerization upon *in Vacuo* Sublimation of 2-Methyltetrazole-Saccharinate as Probed by Matrix Isolation Infrared Spectroscopy." *J. Phys. Chem. A* 2013; 117 (15); 3190-3197.

Ismael, A.; Borba, A.; Henriques, M. S. C.; Paixão, J. A.; Fausto, R.; Cristiano, M. L. S.; "Structure and Photochemistry of a Saccharyl Thiotetrazole." *J. Org. Chem*. 2015; 80(1); 392-400.

As such, the contents of these publications are partially reproduced below.

3.1. Summary

This chapter presents a general overview of the results obtained from our investigations on the structure of a series of tetrazole-saccharinates, in both the crystalline phase and in the isolated molecule situation. Among the conjugates investigated, *N*-linked saccharinate tetrazoles proved especially challenging because of the possibility of tautomerism involving the saccharyl system. Moreover, it was found that the amino-linked conjugates may exhibit different structures in the crystalline and gaseous phases.

In **section 3.3**, the molecular structure of *N*-(1*H*-tetrazol-5-yl)-1,2-benzisothiazol-3-amine 1,1-dioxide, abbreviated as (**TS**), is discussed. The results presented comprise data obtained from analysis of **TS** in the crystalline state, using X-ray crystallography and infrared and Raman spectroscopies, and also as isolated molecule in an argon matrix, by infrared spectroscopy. Interpretation of the experimental results was supported by quantum chemical calculations. The main objective of this study was to attain a deep understanding of the conformational and tautomeric preferences of the compound in both the isolated molecule

situation and in crystalline phase. Very interestingly, it was shown that, while the isolated molecule of the compound exists preferentially as the (1*H*)-tetrazole iminosaccharin tautomer, in the crystal **TS** units exist in the (1*H*)-tetrazole aminosaccharin tautomeric form.

The results obtained for **TS** stimulated us to investigate the effect of quenching tautomerism in the tetrazole ring on the relative intrinsic stabilities of the amino and iminosaccharin tautomeric species, which determine the preferential linkage between the two heterocycles. As such, analogues of **TS** bearing a methyl substituent at positions 1 and 2 of the tetrazole ring (1- and 2-methyltetrazole-saccharinates; **1MTS** and **2MTS** respectively, were prepared and their structures were studied in detail, as isolated molecules and in the crystal phase, following the approach described for **TS**.

Section 3.4 describes our investigations on the structures of *N*-(1-methyl-1*H*-tetrazol-5-yl)-2,3-dihydro-1,2-benzisothiazol-3-imine 1,1-dioxide, **1MTS**, and N-(2-methyl-2H-tetrazol-5-yl)-1,2-benzisothiazol-3-amine 1,1-dioxide, **2MTS**. In the neat crystalline solid, **1MTS** units were found to exist in the predicted most stable iminosaccharin tautomeric form. On the other hand, as observed for the parent **TS**, **2MTS** units assume the predicted less stable aminosaccharin tautomeric form in the crystal. The observed difference in the crystallographic basic units of the compounds revealed the prevalence of H-bonding networks in determining the structural preferences of the tetrazole-saccharyl conjugates in the solid state.

Since the presence of the methyl substituent in the tetrazole ring of **2MTS** reduces the number of possible tautomers relatively to the unsubstituted compound, the methyl derivative appeared as an adequate target to explore in a deeper detail the tautomerism in this type of conjugates. Hence, as presented in **section 3.5**, we have undertaken a detailed theoretical structural characterization of **2MTS** and, subsequently, identified its structure in the gas phase by analysis of the infrared spectrum of the matrix-isolated compound. It could be doubtlessly demonstrated that, in the gas phase, **2MTS** exists as the theoretically predicted most stable imino-bridged form. Also a mechanism for the conversion of the tautomeric form existing in the crystal into that present in the gas phase was proposed.

Since the preferred tautomeric species of the *N*-linked conjugates are very much determined by the chemical environment, we decided to investigate an *S*-linked saccharyl-tetrazole, 3-((1-methyl-1*H*-tetrazol-5-yl)thio)-1,2-benzisothiazol 1,1-dioxide, **TSMT** presented in **section 3.6**. The structure of **TSMT** simplifies because no tautomerism involving the saccharyl system is observed. In addition, the possibility of tautomerism involving the tetrazole ring may be quenched through the introduction of a suitable substituent. The molecular structure of **TSMT** was studied in the monomeric state, by means of matrix-isolation FTIR spectroscopy and

theoretical calculations, and in the crystal phase, by X-ray crystallography. The results have shown that, in the crystal, **TSMT** molecules assume the same conformation as for the isolated molecule, with each molecule forming four weak hydrogen bonds with three neighbouring molecules, leading to a network of **TSMT** oligomers.

3.2. Introduction

In recent years, the design of bridging ligands for controlling the molecular architectures required for defining specific physical properties in resulting coordination compounds has been a topic for many research groups, in major fields such as supramolecular chemistry[1] and molecular magnetism.[2] As referred in chapter 1, tetrazoles and benzisothiazoles find wide applications in coordination chemistry, as ligands.[3,4] It has been demonstrated that the heterocycle tetrazole is able to participate in at least seven distinct types of coordination modes with metal ions, in the construction of novel metal-organic frameworks. Numerous tetrazolyl ligands, coordinated with different metal centres, such as nickel, ruthenium, palladium or platinum, have been tested in catalyzed reactions.[5–9] Furthermore, the coordination ability of the tetrazolyl ligand through four nitrogen electron-donating atoms allows it to serve as a multidentate or as a bridging building block in supramolecular assemblies.[3]

Similarly, the diversity of bonding modes adopted by the 1,2-benzisothiazole-3-one 1,1-dioxide anion (deprotonated saccharin) and the crystalline nature of the resulting complexes are excellent reasons to explore this system. The saccharinate anion interacts with metal centres in various ways, and as a polyfunctional ligand, can co-exist simultaneously as ionic and coordinated species in the same structure. It can be engaged in *N*, *O* (C=O) or *O* (SO_2)-coordination, forming saccharinate–metal complexes,[4] and may also act as a bidentate amidate-like bridging agent.[10–13]

Although several tetrazole derivatives and the saccharinate anion have demonstrated the ability to bind cations of transition metals individually, they have scarcely been investigated together as ligands. As presented in chapter 2, we have devised synthetic routes to tetrazole-saccharinates with the final aim of investigating their application as nitrogen ligands for coordination with transition metals.

In chemical systems the structure determines reactivity and function. Understanding the relevance of different tautomeric forms and preferred conformations of chemical systems is instrumental in predicting and exploring their properties. As such, the structure of selected saccharyl-tetrazole conjugates was investigated in detail, both in the isolated molecule situation,

by matrix-isolation infrared spectroscopy supported by quantum chemical calculations, and in the neat crystalline phase, by X-ray crystallography and infrared and Raman spectroscopies. Results of these studies are presented in this chapter.

3.3. Structural investigation of *N*-(1*H*-tetrazol-5-yl)-1,2-benzisothiazol-3-amine 1,1-dioxide, a nitrogen-linked tetrazole-saccharinate (TS)

The nitrogen-linked tetrazole-saccharinate *N*-(1*H*-tetrazol-5-yl)-1,2-benzisothiazol-3-amine 1,1-dioxide (**TS**) was subjected to a detailed structural investigation. The main objective of this study was to attain a deep understanding of the conformational and tautomeric preferences of the compound, in both the isolated molecule situation and crystalline phase. Matrix isolation, infrared and Raman spectroscopies and X-ray crystallography were selected as experimental techniques. Interpretation of the experimental results was supported by quantum chemical calculations undertaken at the DFT(B3LYP)/6-311++G(3df,3pd) level of theory.

3.3.1. Results and discussion

3.3.1.1. Geometries and energies: the potential energy landscape of a nitrogen-linked tetrazole-saccharinate (TS)

The tetrazole-saccharinate **TS** may exist in four different tautomeric forms (Scheme 3.1). In tautomers A and B, the saccharinate and tetrazole rings have a NH group as spacer. These tautomers differ only in the position of the hydrogen substituent in the tetrazole ring. On the other hand, in tautomers C and D the NH group is part of the saccharyl system, and an imino bond, conjugated with the tetrazolyl system, serves as linkage between the two heterocycles. As for the pair of tautomers (A, B), tautomers C and D differ in the position of the hydrogen substituent in the tetrazole ring. All tautomers may have different conformers resulting from internal rotation about the $N–C_{(tetrazole)}$ bond. In A and B, internal rotation around the $N–C_{(saccharin)}$ bond may also lead to different conformers, while isomeric forms with *E* and *Z* orientation around the $N=C_{(saccharin)}$ bond exist in case of tautomers C and D.

Along this work, structures will be referred to by a letter (A, B, C or D) indicating the tautomeric species, followed by the values of the $NC_{(saccharin)}NC_{(tetrazole)}$ (ψ_1) and $C_{(saccharin)}NC_{(tetrazole)}H_{(tetrazole)}$ (ψ_2) dihedrals, which define the specific geometric isomers (for C and D) and conformers. For instance, $A_{\_0\_0}$ denotes the conformer of tautomer A having (ψ_1) and (ψ_2) equal to 0º (as shown in Scheme 3.1).

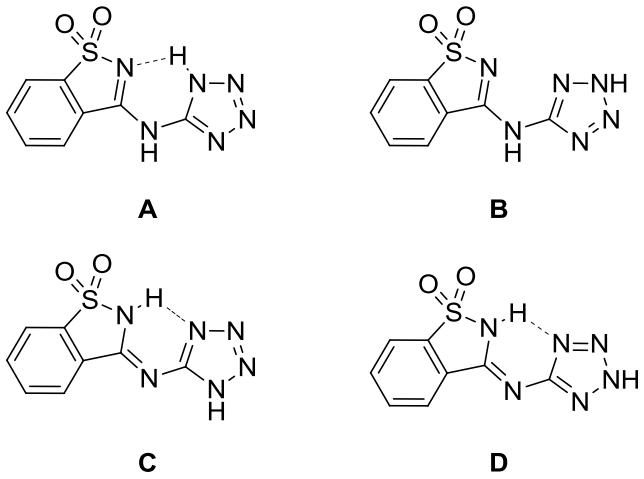

Scheme 3.1 - Tautomeric forms of **TS**: (A) *N*-(1*H*-tetrazol-5-yl)-1,2-benzisothiazol-3-amine 1,1-dioxide; (B) *N*-(2*H*-tetrazol-5-yl)-1,2-benzisothiazol-3-amine 1,1-dioxide; (C) *N*-(1*H*-tetrazol-5-yl)-2,3-dihydro-1,2-benzisothiazol-3(*Z*)-imine 1,1-dioxide; (D) *N*-(2*H*-tetrazol-5-yl)-2,3-dihydro-1,2-benzisothiazol-3(*Z*)-imine 1,1-dioxide. For each tautomer, the most stable structure is represented.

A search on the DFT(B3LYP)/6-311++G(3df,3pd) potential energy surface of the four tautomers of **TS** revealed the existence of 11 different minimum energy structures. The most stable species for each tautomer are represented in Scheme 3.1. The complete set of obtained minimum energy structures is shown in Figure 3.1. The relative energies, dipole moments and symmetry point group of all structures, are presented in Table 3.1, while their geometric parameters are provided in Table S6, in Appendix.

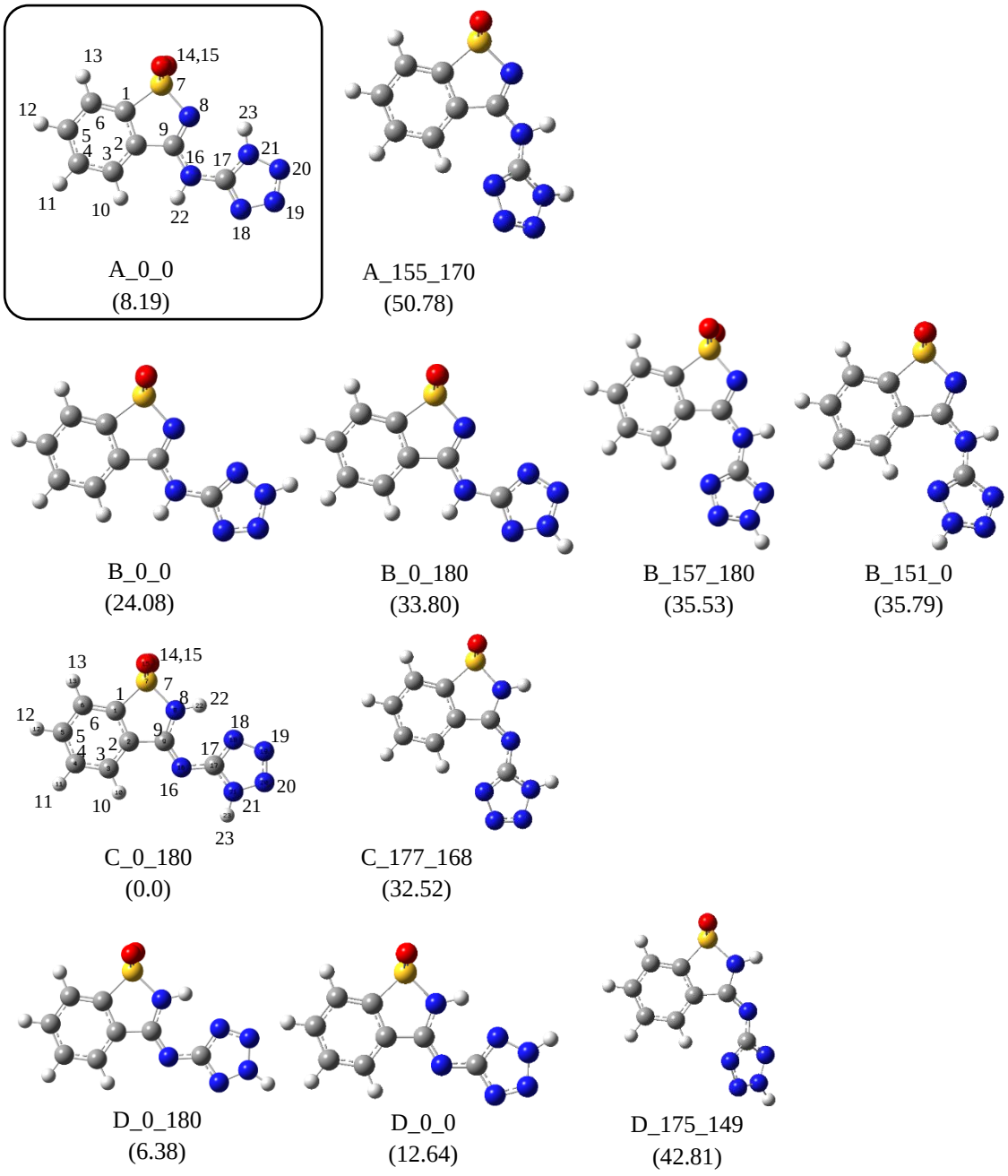

Figure 3.1 - Optimized [B3LYP/6-311++G(3df,3pd)] minimum energy structures of **TS**. Values in parentheses denote zero-point corrected energy (in kJ mol^{-1}) relative to the most stable form. First and second numbers in the name of the conformer indicate value of the N_8-C_9-N_{16}-C_{17} and C_9-N_{16}-C_{17}-H_{23} angle, respectively. The black frame indicate the structure acting as the basic unit found in the **TS** crystal.

Table 3.1 - Relative energies, including zero point vibrational contributions (ΔE_{ZPE}, kJ mol^{-1}), dipole moments (μ, Debye) and symmetry point group (PG) of the various minimum energy structures of TS.[a]

	DFT(B3LYP)/6-311++G(3df,3pd)		
	ΔE_{ZPE}	μ	PG
$C_{\_0\_180}$	0.00[b]	8.17	C_S
$D_{\_0\_180}$	6.38	4.43	C_S
$A_{\_0\_0}$	8.19	8.46	C_S
$D_{\_0\_0}$	12.64	1.45	C_S
$B_{\_0\_0}$	24.08	5.53	C_S
$B_{\_0\_180}$	33.80	9.50	C_S
$C_{\_177\_168}$	35.52	1.55	C_1
$B_{\_157\_180}$	35.53	7.70	C_1
$B_{\_151\_0}$	35.79	8.37	C_1
$D_{\_175\_149}$	42.81	4.53	C_1
$A_{\_155\_170}$	50.78	4.41	C_1

[a] Energies in kJ mol-1; structures are depicted in Figure 3.1. [b] Total energy with zero point vibrational energy contribution of C_0_180 form amounts to -1185.687639 Hartree. All relative energies were calculated relatively to the global minimum, C_0_180.

According to the calculations, all minimum energy structures having (ψ_1) equal to 0º (*i.e.*, all forms having the tetrazolyl fragment pointing to the nitrogen atom of the saccharyl moiety) belong to the C_S symmetry point group, and correspond to the lowest energy forms of all tautomers. The global minimum is form $C_{\_0\_180}$, bearing an intramolecular hydrogen bond between the NH group of the saccharyl moiety and the nitrogen in position 4 of the tetrazole ring (N_{18} in Figure 3.1). In this form, additional stabilizing interactions occur between both the C_3–H_{10} and N_{21}–H_{23} groups and the nitrogen inter-ring spacer atom (N_{16}). The second more stable minimum energy form is $D_{\_0\_180}$, whose structure is very similar to that of the most stable form, but where the N_{21}–$H_{23}\cdots N_{16}$ interaction is absent. The energy of this form lies 6.38 kJ mol^{-1} above that of the global minimum, about half of that of the $D_{\_0\_0}$ form, which differs from $D_{\_0\_180}$ by a 180º rotation about the (ψ_2) dihedral. The third form in the increasing energy scale is $A_{\_0\_0}$ (relative energy: 8.19 kJ mol^{-1}). This form has an intramolecular H-bond between the tetrazole NH group and the saccharyl nitrogen atom. Among all minimum energy structures of **TS**, these four forms are those bearing intramolecular H-bonds, which can then be considered the most important stabilizing factor in the molecule. Forms $B_{\_0\_0}$ and $B_{\_0\_180}$ belong also to the C_S point group but, in absence of any intramolecular H-bond interaction, have relative energies above 24 kJ mol^{-1}.

All minima where the tetrazolyl fragment points to the phenyl group of the saccharyl ring have large relative energies and are strongly non-planar, due to steric hindrance resulting from

the proximity of the two rings. For tautomers A and B, the planes of the saccharyl and aminotetrazole fragments make an angle (ψ_1) of *ca.* 150º. On the other hand, for tautomers C and D, while (ψ_1) is close to 180º, the tetrazole ring is considerably rotated in relation to the main plane of the molecule (*i.e.*, (ψ_2) is equal to 168º and 149º respectively; (see Figure 3.1). Non-planar geometries of the two rings (saccharyl and tetrazolyl) do not benefit from increased stabilization due to conjugation, which is an additional factor to increase the energy of these forms.

3.3.1.2. Crystal structure of TS

The X-ray structure of crystalline **TS** is presented in Figure 3.2. Atomic coordinates, bond lengths, valence angles, dihedral angles, and other crystallographic data were deposited at the Cambridge Crystallographic Data Centre CCDC No. 827883.

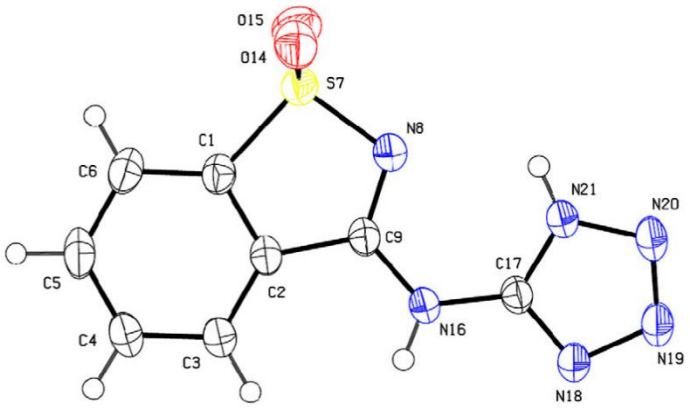

Figure 3.2 – ORTEPII plot of the **TS** molecule (from single crystal RD data). Displacement ellipsoids are drawn at the 50% probability level.

In the crystal, **TS** exists in a single tautomeric form, $A_{\_0\_0}$. The prevalence of this form in the crystalline phase results from the more favourable intermolecular interactions, in particular hydrogen bonds, that it can establish compared to forms $C_{\_0\_180}$ and $D_{\_0\_180}$, which are predicted to be more stable than $A_{\_0\_0}$ for the isolated molecule situation (see Table 3.1). The following hydrogen bonds were observed in the crystal (atom symbols followed by the symbol ′ or ″ designate atoms belonging to two different neighbouring molecules): $N_{16}H_{22}\cdots N_{18}'$; $N_{18}\cdots H_{22}'N_{16}'$; $N_8\cdots H_{23}N_{21}$ (intramolecular); $N_{21}H_{23}\cdots O_{14}''{=}S''$; $S{=}O_{14}\cdots H_{23}''N_{21}''$. This indicates that each **TS** molecule is involved in four hydrogen bonds (one being bifurcated) in the crystalline phase. The hydrogen bond network is shown in Figure 3.3.

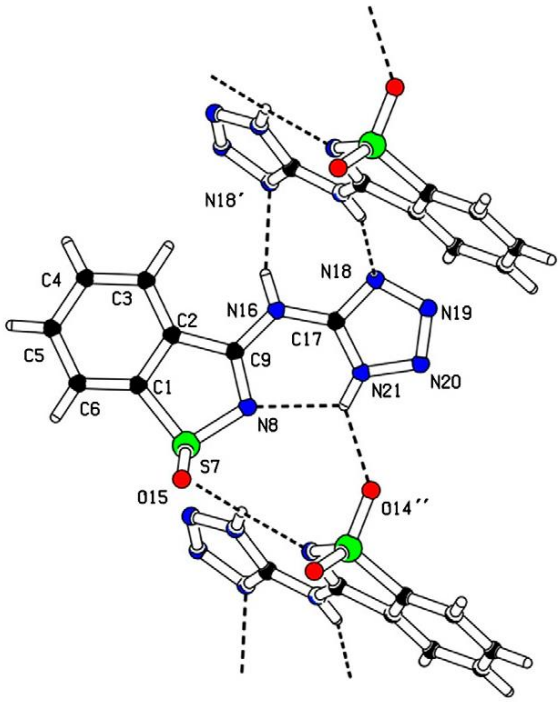

Figure 3.3 - Hydrogen bond network in **TS** crystal.

The comparison between the geometrical parameters of the $A_{\_0\_0}$ monomer, obtained at the B3LYP/6-311++G(3df,3pd) level of theory, and those determined for the compound in the crystal (see Table S7 in Appendix), reveals an excellent correlation between the two sets of data, though in the gas phase $A_{\_0\_0}$ is predicted to be strictly C_S symmetry while in the crystal it appears slightly distorted as a result of intermolecular interactions.

3.3.1.3. Infrared and Raman spectra of crystalline TS

Figure 3.4 shows the infrared and Raman spectra of neat crystalline **TS**. Since the crystal unit cell is centrosymmetric, the observed IR and Raman spectra do not exhibit common bands. The proposed band assignments are given in Table 3.2. These assignments were greatly helped by comparison of the experimental spectra with the corresponding B3LYP/6-311++G(3df,3pd) calculated spectra for the isolated $A_{\_0\_0}$ form (which are also presented in Figure 3.4 for comparison). The good general description of the experimental spectra of the crystal by the calculated spectra for the isolated monomer is an indication that the intermolecular interactions present in the solid do not substantially perturb the intramolecular vibrations. The observed Davidov splittings (DS), taken as the absolute value of the difference between the frequencies of the Raman and infrared corresponding bands, are in general smaller than 7 cm^{-1}, the largest values appearing almost exclusively for modes involving predominantly the N–H_{22} and N–H_{23} groups, which are directly involved in H-bonding in the crystal (νNH_{22} (DS = 40), νNH_{23} (13);

γNH_{22} (17) δNH_{23} (25 and 16; there are two modes with significant contribution of this coordinate; Table 3.2).

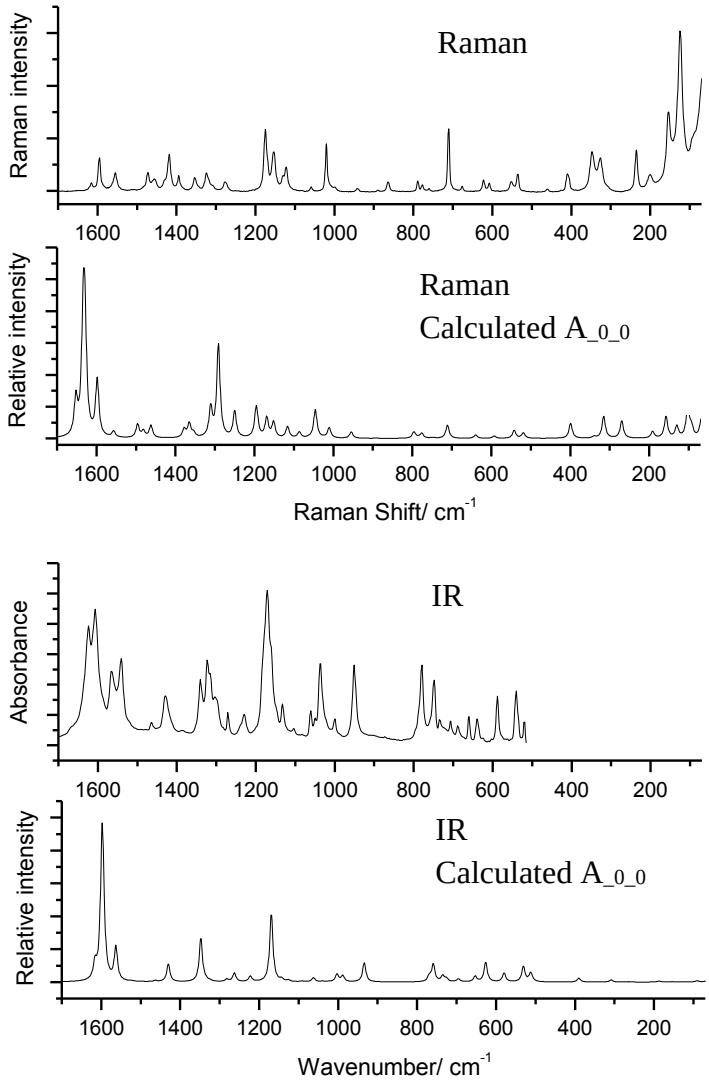

Figure 3.4 - Room temperature Raman and infrared spectra of crystalline **TS** and B3LYP/6–311++G(3df,3pd) calculated Raman and infrared spectra for form $A_{\_0\_0}$ monomer. The calculated spectra were simulated by Lorentzian functions centred at the calculated (scaled by 0.978) wavenumber/Raman shift with FWHM = 10 cm^{-1}.

Table 3.2 - Proposed band assignments for infrared and Raman spectra of crystalline **TS**.[a]

Observed		Calculated			
Infrared	Raman	Wavenumber	I_{IR}	I_R	Approximate Description[b]
3264/3220/3177	3180	3546.3	66.9	86.1	νNH_{22}
3106/3090/3066	3094/3077/3053	3521.4	121.4	51.6	νNH_{23}
3014	2991	3139.0	3.7	260.2	νCH ph
n.o.	2953	3131.1	2.5	122.2	
2912	2920	3118.1	3.0	79.1	
2861	2888	3106.1	3.2	42.8	
1623	1616	1616.1	72.7	94.5	νCC ph/ νCN_8
1603	1597	1597.8	711.8	269.8	νCN_{16}C as
		1593.5	82.5	239.0	νCC ph
1565/1541	1556	1563.2	160.6	139.3	νCN_8/νCC ph
1520	1516	1522.6	2.1	14.2	δNH_{22}
1464	1474	1463.6	5.3	29.6	δCH ph
1448	1457	1449.8	0.3	14.4	δCH ph
1429	1431/1420	1430.1	83.8	26.7	νCN_{18}
1341	1355	1347.8	205.9	16.6	νSO as
1303	1319	1335.2	5.8	27.2	δNH_{23}/νNN t
1296	1311	1324.3	3.7	8.4	νCC ph
1271	1277	1282.5	11.5	52.3	νCC ph
1323/1315	1326	1262.8	42.4	165.5	δCH ph
1240/1229	1210	1222.5	25.8	44.2	νNN t/δNH_{23}
1180/1171/1162	1175	1169.3	310.1	41.9	νSO s
		1167.1	13.1	10.1	δCH ph
1148	1155	1143.2	11.5	30.5	νC_2C_9 ph
1132	1131	1126.4	7.1	23.5	νCC ph
1103	1123	1091.5	3.2	16.1	νNN t/δNNN t
1061	1060	1062.6	19.9	8.1	νNN t
1049	n.o.	1040.0	3.3	0.6	νCS
n.o.	1021	1022.7	2.1	37.9	νCC ph
1036/1023	n.o.	1002.7	36.0	0.8	νNN t
n.o.	n.o.	995.4	0.0	0.0	γCH ph
999	999	988.4	29.3	13.1	νNN t
n.o.	n.o.	955.3	0.4	0.1	γCH ph
951	944	933.8	91.5	7.5	νNS
n.o.	865	873.8	0.0	0.2	γCH ph
n.o.	791	778.6	0.1	5.9	δ skeletal
795	779	772.4	20.4	0.7	γCH ph
779	761	759.0	82.1	4.5	δCSN/δCC ph
748	n.o.	738.8	31.3	0.3	τCC ph
n.o.	n.o.	731.3	0.2	0.4	γCN t
734/724	n.o.	725.7	16.4	0.1	γCN t/γNH_{23}
706	711	695.5	13.8	10.7	δCC ph/νCS
660	677	654.7	24.7	0.1	τCC ph
639/625	623	626.8	48.3	0.1	γNH_{23}/γCN t
		625.6	46.0	2.3	δ skeletal
603/588	610	579.7	42.1	1.5	δCC ph/νSN
540	553	531.1	41.1	0.2	γSO (rocking)
		530.1	32.3	4.5	δSO (wagging)
520	537	512.6	41.2	0.2	γNH_{22}
		507.2	4.2	2.8	δCC_9
	462	436.9	0.6	0.1	γCN_{16}
	425	419.2	0.3	0.1	τCC ph
	410	390.3	18.5	6.1	δSO (scissors)
	348	332.0	0.0	0.6	γNC_{17}
	328	308.3	10.2	6.9	$\delta NC_{17}N$
	n.o.	284.4	0.0	0.0	γSO (twisting)
	237	263.6	1.7	4.6	$\delta CN_{16}C$
	202	187.1	5.1	1.2	δ skeletal
	155	154.1	1.7	3.2	τ skeletal
	124	127.3	1.2	1.4	τ skeletal

Table 3.2 (Continued) [a]

Observed		Calculated			
Infrared	Raman	Wavenumber	I_{IR}	I_R	Approximate Description[b]
		100.1	0.5	3.0	τ skeletal
	94	90.6	6.2	0.8	$\delta NC_{17}N/\delta CN_{16}C$
	75	66.5	7.1	1.2	$\tau N_{16}C_{17}$
		44.9	0.6	0.3	δ butterfly

[a] Wavenumbers/Raman shifts in cm^{-1}; calculated infrared intensities (I_{IR}) in km mol^{-1}; calculated Raman activities (I_R) in $Å^4$/a.m.u.; calculated wavenumbers/Raman shifts scaled by 0.978. The infrared region below 515 cm^{-1} was not investigated. [b] ν, Stretching; δ, bending; γ, rocking/out-of-plane bending; τ, torsion; s, symmetric; as, asymmetric; ph, phenyl ring; t, tetrazole ring. Extensively delocalized modes are designated generally as skeletal bending (δ) or out-of-plane bending (γ; τ); in the ''butterfly'' mode the saccharin and tetrazole rings flap in relation to each other. Calculated data, for form $A_{\_0\_0}$.

3.3.1.4. Matrix isolation experiments

Figure 3.5 shows the spectrum of **TS** isolated in argon matrix at 15 K. As described in chapter 2 (section 2.3), the matrix was prepared by sublimation (at ~175 ºC) of the compound under high vacuum and codeposition with large excess of argon (*ca.* 1:1000 molar ratio) on the cooled (15 K) CsI substrate of the cryostat. Since, according to the calculations, the tautomeric form existing in the crystalline **TS** ($A_{\_0\_0}$) does not correspond to the most stable species in the gas phase, the composition of the vapour resulting from the sublimation cannot be predicted *a priori*. Indeed, the tautomerization barriers in the gas phase can be expected to be large enough to prevent conversion between **TS** tautomers under the used experimental conditions (for instance, in tetrazole tautomerization between 1*H* and 2*H* tautomers was found to be *ca.* 230 kJ mol^{-1})[14], but mechanisms involving participation of H-bonded aggregates are known that allow for tautomerization processes to take place during sublimation.[15,16] For example, cytosine exists in crystals as the amino-oxo tautomer,[17] but in gas phase and in cryogenic matrices it assumes at least three different tautomeric forms.[18] The mechanism of cytosine tautomerization has been addressed by Yang and Rodgers.[15] These authors explained the coexistence in the gas phase of several cytosine tautomers, in spite of very high energy barriers between them, by bimolecular tautomerization rising from the hydrogen bonded cytosine dimers in the crystal. Such hydrogen bonding interactions result in a significant lowering of the barriers to tautomerization that allows for the dimer dissociation in the gas phase with the production of new tautomers. The relevant case of 1-(tetrazolyl-5-yl)ethanol has been recently studied by Ismael *et al.*,[16] where a considerably different relative population of the two tautomers of the molecule was found for the compound trapped in cryogenic matrices, compared to the theoretical predictions for the gas phase equilibrium situation at the thermodynamic reference temperature. In that case, the population found in the matrices of the tautomer existing in the crystal was *ca.* twice as predicted for a hypothetical gas phase equilibrium at the reference temperature.[16]

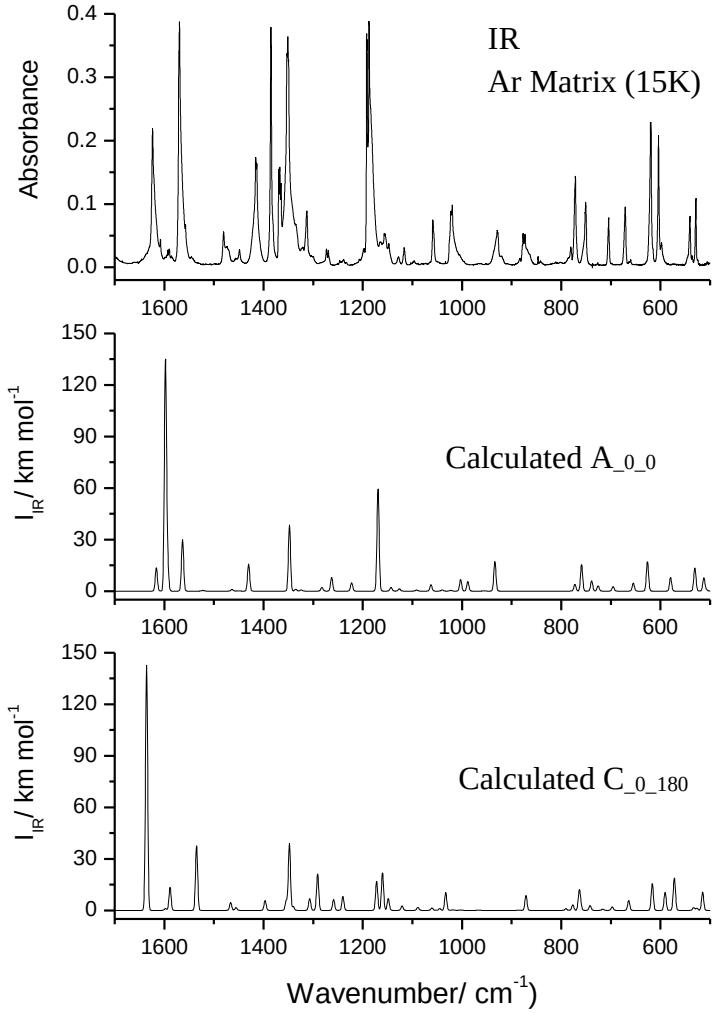

Figure 3.5 - Infrared spectra of matrix isolated **TS** (Ar matrix; 15 K) and B3LYP/6– 311++G(3df,3pd) calculated infrared spectra for forms $A_{\_0\_0}$ and $C_{\_0\_180}$. The calculated spectra were simulated by Gaussian functions cantered at the calculated (scaled by 0.978) wavenumber with FWHM= 5 cm^{-1}.

Detailed analysis of the matrix-isolation infrared spectrum obtained for **TS** (see Figure 3.5, for the proposed band assignments see Table 3.3) and comparison of this spectrum with those predicted for the different minimum energy **TS** structures allowed us to conclude that the spectrum contains the spectral signatures of both forms $A_{\_0\_0}$ (the one present in the crystal before deposition) and $C_{\_0\_180}$. The latter corresponds to the most stable species in the gas phase, as predicted by the theoretical calculations. A fairly good simulation of the observed spectrum of the matrix-isolated **TS** could be achieved by summing the predicted spectra of $A_{\_0\_0}$ and $C_{\_0\_180}$ in a ~2:1 proportion, pointing to a population of the $A_{\_0\_0}$ tautomer in the deposited vapour of about two times that of $C_{\_0\_180}$ (*i.e.*, quite interestingly, a situation similar to the one found previously for 1-(tetrazolyl-5-yl)ethanol).[16]

Table 3.3 - Proposed band assignments for infrared spectrum of matrix-isolated **TS**.[a]

Approximate Description[b]	$A_{\_0\_0}$			$C_{\_0\_180}$		
	Calculated		Observed	Calculated		Observed
	ν	I_R		ν	I_R	
νNH_{22}	3546.3	66.9	3564	3573.6	119.6	2552
νNH_{23}	3521.4	121.4	3537	3320.7	307.9	3436
νCH ph	3139.0	3.7	2995	3143.3	3.0	3003
	3131.1	2.5	2953	3138.1	2.0	
	3118.1	3.0	2914	3126.5	3.6	2941
	3106.1	3.2	2880	3113.9	1.1	2899
νCC ph/ νCN_8	1616.1	72.7	1620	1635.8	763.1	1623
$\nu CN_{16}C$ as	1597.8	711.8		1597.7	5.6	
νCC ph	1593.5	82.5		1588.5	71.3	1608
νCN_8/νCC ph	1563.2	160.6	1593/1590	1535.0	199.6	1570/1569
δNH_{22}	1522.6	2.1	n.o.	1466.4	24.4	1480/1470
δCH ph	1463.6	5.3	1470	1455.6	8.7	1449
δCH ph	1449.8	0.3	n.o.	1396.9	30.1	1385
νCN_{18}	1430.1	83.8	1415/1414	1354.3	29.7	1369/1367/1365
νSO as	1347.8	205.9	1352/1351/1350	1347.9	208.0	1352/1351/1350
δNH_{23}/νNN t	1335.2	5.8	1335	1340.2	11.4	1342
νCC ph	1324.3	3.7	1331	1307.0	36.3	1324/1320
νCC ph	1282.5	11.5	1300	1291.0	112.5	1313
δCH ph	1262.8	42.4	1273	1258.8	33.5	1269
νNN t/δNH_{23}	1222.5	25.8	1239/1234	1240.1	42.7	1246/1243
νSO s	1169.3	310.1	1192/1191	1172.1	89.5	1200/1199/1197
δCH ph	1167.1	13.1	1189/1187/1184	1160.2	116.2	1165/1163/1160/1158
νC_2C_9 ph	1143.2	11.5	1147	1148.6	36.7	1157/1155
νCC ph	1126.4	7.1	1129	1120.9	13.6	1118/1116
νNN t/δNNN t	1091.5	3.2	1103	1089.0	9.5	1098/1096
νNN t	1062.6	19.9	1059	1060.6	7.7	1057
νCS	1040.0	3.3	n.o.	1045.0	5.5	1033
νCC ph	1022.7	2.1	1025	1032.9	55.4	1022/1019
νNN t	1002.7	36.0	1009/1004	1018.0	1.8	n.o.
γCH ph	995.4	0.0	n.o.	1002.8	1.1	n.o.
νNN t	988.4	29.3	1002	998.6	0.0	n.o.
γCH ph	955.3	0.4	952	966.9	0.6	967
νNS	933.8	91.5	936/931/929/928/920	885.5	0.2	884/883
γCH ph	873.8	0.0	n.o.	871.1	45.7	878/877/873/868/864
δ skeletal	778.6	0.1	n.o.	790.6	5.2	786
γCH ph	772.4	20.4	780/779	776.7	17.3	783
δCSN/δCC ph	759.0	82.1	771	763.9	55.1	773
τCC ph	738.8	31.3	752/751	761.1	19.0	
γCN t	731.3	0.2	n.o.	741.9	14.7	754
γCN t/γNH_{23}	725.7	16.4	729/726	716.1	3.7	n.o.
δCC ph/νCS	695.5	13.8	704	697.2	10.8	706
τCC ph	654.7	24.7	671	664.0	30.3	662/660
γNH_{23}/γCN t	626.8	48.3	623/620/619/615	616.6	82.6	623/620/619/615
δ skeletal	625.6	46.0		590.7	56.1	604/598/597
δCC ph/νSN	579.7	42.1	604/598/597	573.0	35.6	
γSO (rocking)	531.1	41.1	540	571.6	69.4	
δSO (wagging)	530.1	32.3		533.1	8.5	545
γNH_{22}	512.6	41.2	530	526.6	6.6	536
δCC_9	507.2	4.2		515.1	56.3	529
γCN_{16}	436.9	0.6		449.9	9.4	453

[a] Wavenumbers (ν, cm^{-1}) were scaled by 0.978; calculated infrared intensities (I_{IR}) in km mol^{-1}. The infrared region below 450 cm^{-1} was not investigated. [b] ν, stretching; δ, bending; γ, rocking/out-of-plane bending; τ, torsion; s, symmetric; as, asymmetric; ph, phenyl ring; t, tetrazol ring; n.o., band not observed; extensively delocalized modes are designated generally as skeletal bending (δ skeletal). See Figure 3.1 for atom numbering.

Taking into account the structure of **TS** in the crystal, a general mechanism for conversion between $A_{\_0\_0}$ and $C_{\_0\_180}$ can be proposed, involving an intramolecular H-shift from the N-H tetrazole fragment to the saccharyl nitrogen atom, together with crossed intermolecular H-shifts involving the N-H separators and the tetrazole nitrogen atoms in position 4 of the considered molecule and of a neighbour molecule (Figure 3.6).

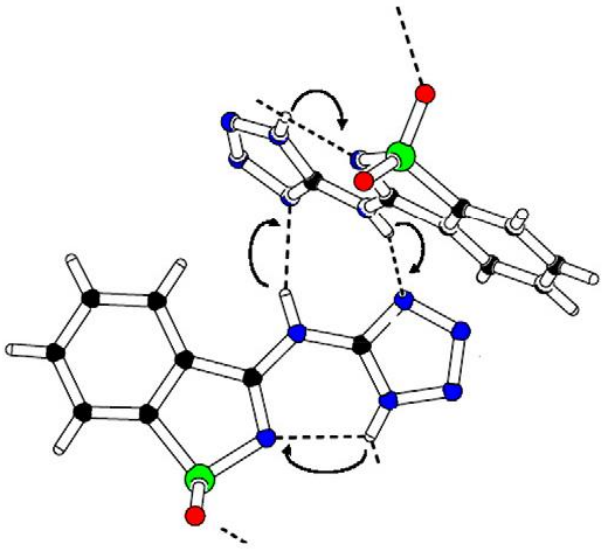

Figure 3.6 - Schematic representation of the proposed hydrogen shifts converting $A_{\_0\_0}$ into $C_{\_0\_180}$. The atom coordinates were taken from the X-ray structure of the compound. Arrows indicate the H-shifts.

Note also that formation of other species than $C_{\_0\_180}$ looks very improbable: B and D type tautomeric forms would imply H-migration to the nitrogen tetrazole atoms placed more far away from the possible donor group, and the $A_{\_155\_170}$ and $C_{\_177\_168}$ forms would require an extensive reorganization of the molecule heavy atom backbone (besides being high energy forms; see Table 3.1 and Figure 3.1).

3.3.2. Conclusions

The conformational and tautomeric preferences of the **TS** molecule in both the matrix isolated situation and in the crystalline phase have been investigated. According to calculations at the DFT(B3LYP)/6-311++G(3df,3pd) level of theory, **TS** may exist in four tautomeric forms, two of them (A and B) having a NH group as spacer and the other two (C and D) having the NH group as part of the saccharyl system and an imino bond, conjugated with the tetrazolyl and sacharyl systems, as linker. The position of the hydrogen substituent in the tetrazole ring makes the differences between tautomers belonging to groups A and B and tautomers belonging to groups C and D. The rotational axes of each group of tautomers lead to different conformers

within each group. A search on the DFT(B3LYP)/6-311++G(3df,3pd) potential energy surface of the four groups of tautomers revealed the existence of 11 different minimum energy structures. In the most stable form, $C_{\_0\_180}$, the intramolecular hydrogen bond between the NH group of the saccharyl moiety and the nitrogen in position 4 of the tetrazole ring and the interactions between both the C_3–H_{10} and N_{21}–H_{23} groups and the nitrogen inter-ring spacer atom (N_{16}) are relevant stabilizing factors. The tautomeric form found in the crystal was $A_{\_0\_0}$. The prevalence of this form in the crystalline phase results from the more favourable intermolecular interactions it can establish, in comparison to the forms of lower energies in the gaseous phase. Both FTIR and Raman spectra of the crystalline phase agree with the occurrence of form $A_{\_0\_0}$ in the crystal. The good general description of the experimental spectra of the crystal by the calculated spectra for the isolated monomer is an indication that the intermolecular interactions present in the solid do not substantially perturb the intramolecular vibrations. In the matrix isolated experiments, the obtained spectra revealed the presence in the matrix of two tautomeric forms: $A_{\_0\_0}$, the one present in the crystal before deposition, and $C_{\_0\_180}$, the most stable form predicted by the calculations in the gas phase. Taking into account the crystalline structure of **TS**, a general mechanism for the conversion between $A_{\_0\_0}$ and $C_{\_0\_180}$ has been proposed, which follows the general ideas of previously reported tautomerization processes upon sublimation in other H-bonded systems. This mechanism involves an intramolecular H-shift from the N-H tetrazole fragment to the saccharyl nitrogen atom, together with crossed intermolecular H-shifts involving the N-H separators and the tetrazole nitrogen atoms in position 4 of the considered molecule and of a neighbour molecule.

3.4. Molecular structure of nitrogen-linked methyltetrazole-saccharinates (1MTS and 2MTS)

The results obtained for **TS** stimulated us to investigate the effect of quenching tautomerism in tetrazole on the structure of the methyltetrazole-saccharinate ligands, specially concerning the relative intrinsic stabilities of the amino and iminosaccharin tautomeric species (which determine the preferential linkage between the two heterocycles), and on the structure selection upon crystallization. As such, we have prepared and characterized structurally the analogues of **TS** bearing a methyl substituent at positions 1 and 2 of the tetrazole ring (1- and 2-methyltetrazole-saccharinates). Structural analysis of these methyltetrazole-saccharinates was carried out in the crystal phase, using X-ray crystallography, infrared and Raman spectroscopies, and quantum chemical calculations.

3.4.1. Results and discussion

3.4.1.1. Relative stability of monomeric 1- and 2-methyltetrazole-saccharinates

Isomeric methyltetrazole-saccharinates, **1MTS** and **2MTS**, may exist in two different tautomeric forms (imino- and amino- forms, Figure 3.7). In one of these forms, the saccharinate and tetrazole rings have an amino group as spacer, with the saccharyl nitrogen atom being deprotonated (labelled as **1MTAS** and **2MTAS** for 1- and 2-methyltetrazole-aminosaccharinate, respectively). This tautomeric form may have different conformers resulting from internal rotation about the N-$C_{(tetrazole)}$ and N-$C_{(saccharin)}$ bonds. Conformations where the tetrazole ring is directed to the phenyl group of the saccharinate moiety can be expected to correspond to high energy structures due to steric hindrance. The relevant low energy forms differ from each other by internal rotation about the N-$C_{(tetrazole)}$ bond and correspond to the structures labelled as **1MTAS-A/B** and **2MTAS-A/B**, shown in Figure 3.7. For the latter molecule, both structures **2MTAS-A** and **2MTAS-B** were found to be energy minima, belonging to point group Cs, *i.e.*, bearing a planar amino spacer group. On the other hand, for 1-methyltetrazole-aminosaccharinate, only structure **1MTAS-B** corresponds to a minimum energy conformation, while structure **1MTAS-A** is destabilized by steric repulsions between the closely located NH and CH_3 groups and converged upon geometry optimization to **1MTAS-B**. According to the calculations, the **1MTAS-B** conformer has the amine spacer pyramidalized (the calculated C-N(-H)-C dihedral is 154.2º) and the N=C-N-C, N=C-N-H and C-N-C-N(CH_3) dihedrals are equal to 7.8º, 161.0º and -54.8º, respectively.

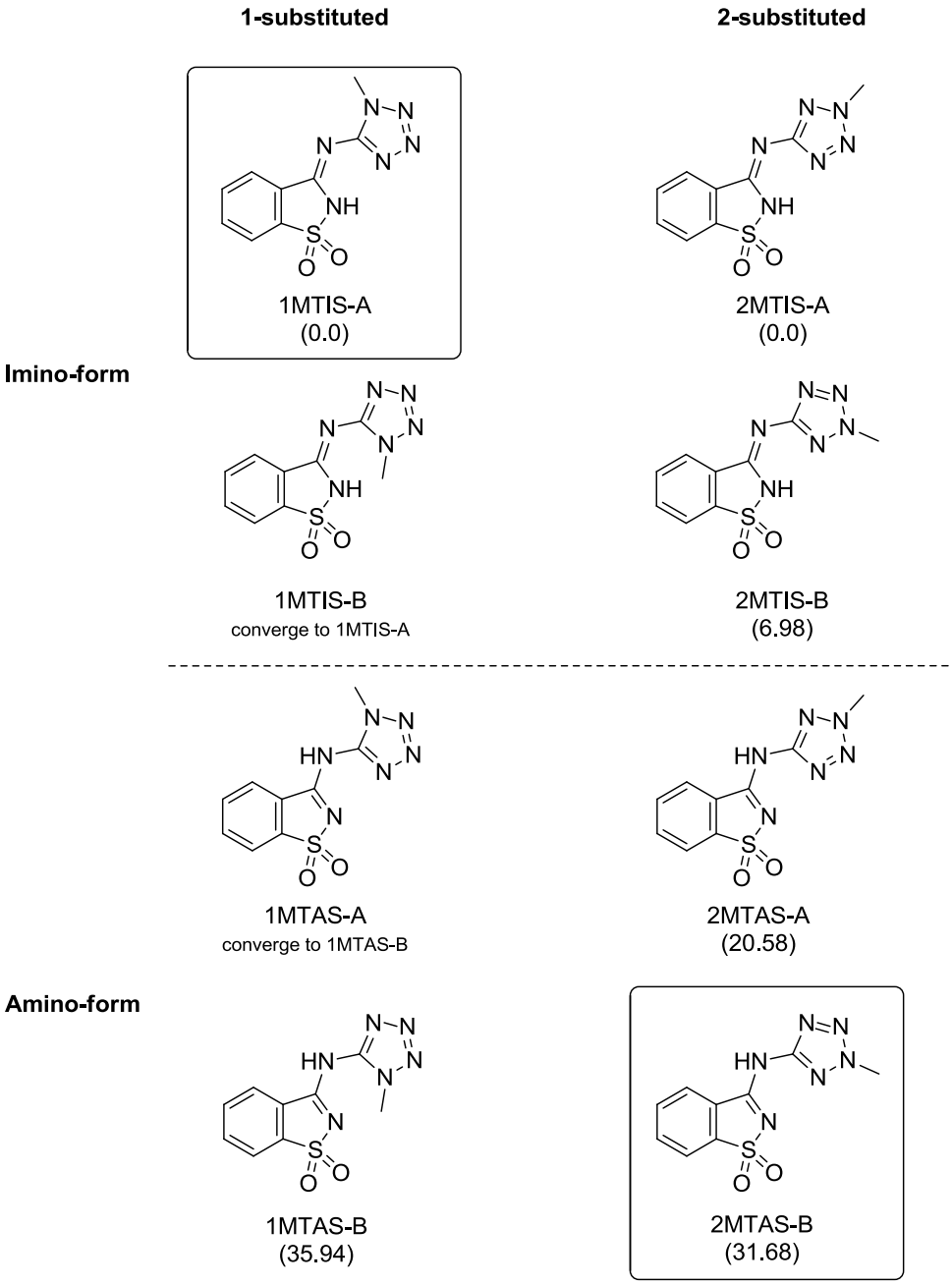

Figure 3.7 - Relevant structures of 1- and 2-metyltetrazole-saccharinates. Relative energies and dipole moments of these structures are provided in Table 3.4. Structures **1MTIS-B** and **1MTAS-A** were found not to be minima on the potential energy surface of the compound. Values in parentheses denote zero-point corrected energy (in kJ mol^{-1}) relative to the respective most stable form (**1MTIS-A** or **2MTIS-A**). The black frames indicate the structures acting as the basic units found in the studied crystals.

In the second tautomeric form of the compounds, the saccharinate and tetrazole rings are linked by an imino functionality and the NH group is part of the saccharyl system (labelled as **1MTIS** and **2MTIS** for 1- and 2-methyltetrazole-iminosaccharinate, respectively). Isomeric forms with *E* and *Z* orientation around the $N{=}C_{(saccharin)}$ bond may exist. The *E*-type structures have the tetrazole ring directed to the phenyl group of the saccharinate moiety, corresponding to high energy structures destabilized by steric hindrance. Two low energy conformers of *Z*-type were found for 2-methyltetrazole iminosacharinate (**2MTIS**), (**2MTIS-A/B**; see Figure 3.7), while only one conformer was found in the case of the 1-methyl-substituted compound, **1MTIS-A**, since the structure **1MTIS-B** is destabilized sterically due to the close proximity of the NH and CH_3 groups and was found to converge to structure **1MTIS-A** upon optimization.

According to the calculations, for both compounds studied, form **MTIS-A** is the most stable structure in gas phase. The energetic data are presented in Table 3.4. As seen in this table, for 1-methyltetrazole-saccharinate the form **1MTIS-A** is more stable than the form **1MTAS-B** by ~36 kJ mol^{-1} (zero-point corrected energy difference), while in the 2-methyl-substituted compound **2MTIS-A** is *ca.* 7 kJ mol^{-1} lower in energy than **2MTIS-B** and more stable by *ca.* 20 and 32 kJ mol^{-1} than the two forms containing the amino spacer (**2MTAS-A/B**). The greater stability of **1MTIS-A** and **2MTIS-A** results mainly from the presence in these forms of the strongly stabilizing N-H···N intramolecular hydrogen bond, between the NH saccharinate group and the nitrogen atom in position 4 of the tetrazole group. These forms are identical to the most stable form of the parent tetrazole-saccharine molecule (**TS**), whose prevalence in the gas phase was confirmed experimentally, thus appearing to be a general trend for this family of compounds.

Table 3.4 - Relative energies (ΔE/kJ mol^{-1}), relative energies with zero-point correction (ΔE_0/kJ mol^{-1}), dipole moments ($|\mu|$/Debye) and symmetry point group of selected lowest energy structures of 1- and 2-methyltetrazole-saccharinates as calculated at the B3LYP/6-31++G(d,p) level of theory.[a]

Form	Point group	ΔE	ΔE_0	$\|\mu\|$	Obs.
1-Methyltetrazole-Saccharinate					
1MTIS-A	C_S	0.00	0.00	9.04	Basic-unit in the crystal
1MTIS-B					Converged to 1MTIS-A
1MTAS-A					Converged to 1MTAS-B
1MTAS-B	C_1	33.94	35.94	8.63	
2-Methyltetrazole-Saccharinate					
2MTIS-A	C_S	0.00	0.00	5.15	
2MTIS-B	C_S	7.83	6.98	0.55	
2MTAS-A	C_S	19.11	20.58	10.43	
2MTAS-B	C_S	30.72	31.68	5.33	Basic-unit in the crystal

[a] Energies and zero-point corrected energies are relative to the most stable form of each molecule. The total electronic energies for **1MTIS-A** and **2MTIS-A** are -1224.853777 and -1224.854641 E_h, respectively; the total zero-point corrected energies for the same species are -1224.670838 and -1224.671349 E_h. See Figure 3.7 for schematic drawings of the structures. 1 E_h = 2625.5001 kJ mol^{-1}; 1 Debye ≈ 3.33564 x 10^{-30} C m.

3.4.1.2. Crystal structures of 1- and 2-methyltetrazole-saccharinates

The X-ray structure of crystalline 1-methyltetrazole-saccharinate is presented in Figure 3.8 and Figure 3.9. Atomic coordinates, bond lengths, valence angles, dihedral angles, and other crystallographic data were deposited at the Cambridge Crystallographic Data Centre CCDC No. 866734.

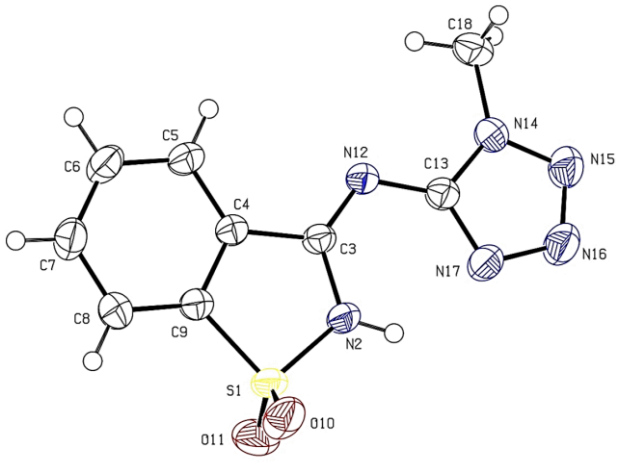

Figure 3.8 – ORTEPII plot of the **1MTIS** molecule (from single crystal RD data). Displacement ellipsoids are drawn at the 50% probability level.

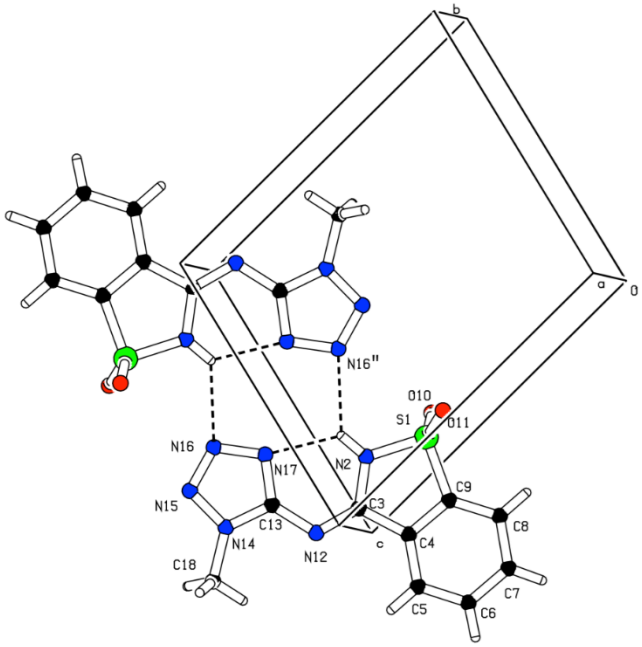

Figure 3.9 - Hydrogen bond network in crystalline 1-metyltetrazole-saccharinate (**1MTIS**).

In the crystal, 1-methyltetrazole-saccharinate units assume the most stable configuration predicted for the isolated molecule, the (1*H*)-1-methytetrazole iminosaccharin tautomeric form (**1MTIS**). In the solid, the proton of the NH group of the saccharyl system is shared in a bifurcated hydrogen bonding scheme (N_2-H_2···N_{17} and N_2-H_2-N_{16}''; where $''$ denotes an atom of a neighbour molecule) involving an intramolecular bond with the nitrogen atom in position 4 of the tetrazole ring (N_{17}) as acceptor and an intermolecular bond with the nitrogen (N_{16}) in position 3 of the tetrazole ring of a neighbouring molecule, as acceptor. Details of the hydrogen bonds are given in Table 3.5 (see also Figure 3.9).

Contrary to what happens for 1-methyltetrazole-saccharinate, the existing species in the crystal of the 2-methyl substituted compound is different from the most stable structure in gas phase. The X-ray structural data for this compound are presented in Figure 3.10 and Figure 3.11 and Table 3.5. Atomic coordinates, bond lengths, valence angles, dihedral angles, and other relevant crystallographic results were deposited at the Cambridge Crystallographic Data Centre CCDC No. 866735. In the crystal, 2-methyltetrazole-saccharinate exists in the (2*H*)-2-methytetrazole aminosaccharin tautomeric form (**2MTAS-B**). Pairs of molecules are linked in dimers through an intermolecular hydrogen bond involving the NH spacer group as proton donor and the nitrogen in position 4 of the tetrazole ring as acceptor: N_{12}-H_{12}···N_{17}' (the symbol $'$ after the atom symbol designates an atom belonging to a neighbouring molecule). Details of the hydrogen bonds are given in Table 3.5 (see also Figure 3.11).

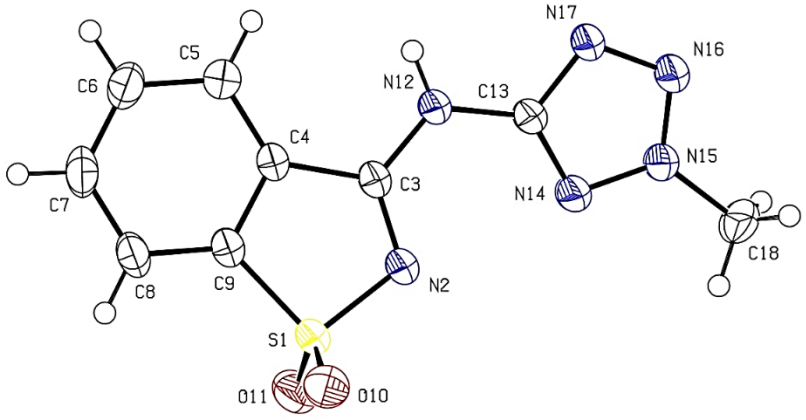

Figure 3.10 - ORTEPII plot of the **2MTAS** molecule (from single crystal XRD data). Displacement ellipsoids are drawn at the 50% probability level.

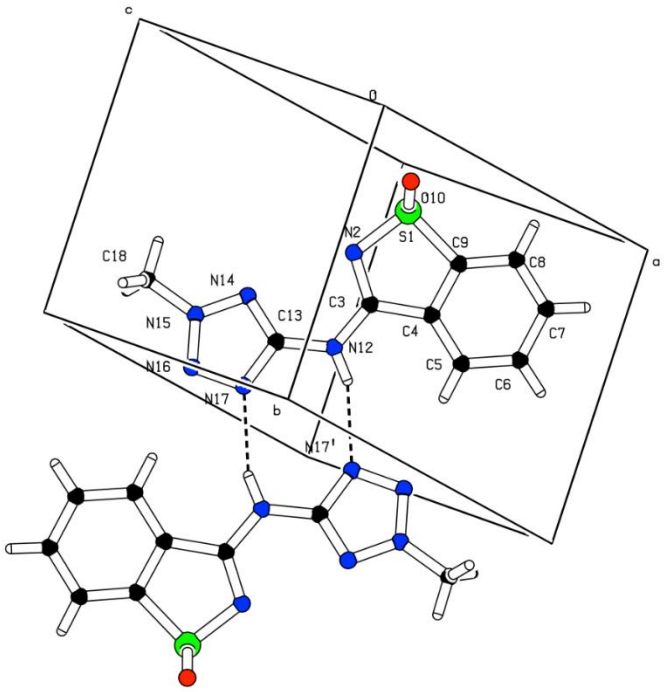

Figure 3.11 - Hydrogen bond network in crystalline 2-metyltetrazole-saccharinate (**2MTAS**).

Table 3.5 – Details of the hydrogen bonding patterns in the crystal structures of 1- and 2-methyltetrazole-saccharinates (**1MTIS**, **1MTAS**).[a]

r(D-H···A)	*r*(D-H)	*r*(H···A)	*r*(D···A)	∠(D-H···A)
1MTIS				
N_2-H_{12}···N_{17}	0.86	2.06	2.649(2)	124.7
N_2-H_2···N_{16}″	0.86	2.49	3.126(2)	131.7
2MTAS:				
N_2–H_{12}···N_{17}′	0.86	2.17	2.990(2)	160.1

[a] Distances (*r*) in Å; angles (∠) in degrees. See Figure 3.8 and Figure 3.10 for structures and atom numbering. Values assumed during the X-ray structure refinement procedure and correspond to the hydrogen atom riding idealized distance on the donor (D) (SHELXL-97 default).

It is interesting to note that the prevalent intermolecular interaction in the crystal of 2-methyltetrazole-saccharinate is identical to that found in the crystal of the parent compound, **TS**. This indicates that the preference for the tautomeric amino form in both crystals (**2MTAS** and **TS**) is strongly determined by this intermolecular interaction, which, on the other hand, cannot operate efficiently in the case of 1-methyltetrazole-saccharinate. In fact, in this latter compound the presence of the methyl substituent directly hinders the possibility of formation of the dimeric structure based on **1MTAS-A** form (see Figure 3.7), because the $NH_{(bridge)}$···N_{14} bonds cannot be formed, since N_{14} bears the methyl substituent. On the other hand, as described above, structure **1MTAS-B** should have its rings considerably deviated from a single plane and its amine spacer substantially piramidalized. These structural features would strongly difficult the establishment of the required intermolecular $NH_{(bridge)}$···N_{17} H-bonds. Under these circumstances, in the crystal 1-methyltetrazole-saccharinate molecules keep their intrinsically most stable form (the one prevalent in the gas phase), with the intermolecular H-bonding scheme adopted resembling the second type of intermolecular H-bonding previously observed in crystalline **TS**. Indeed, in the crystal of **TS** each molecule has as main interaction the one identical to that observed for 2-methyl-tetrazole-saccharinate, and a secondary one consisting in a bifurcated H-bond from the NH tetrazole moiety to one of the oxygen atoms of the SO_2 group of a third molecule and to the nitrogen atom of its own saccharin ring; in 1-methyltetrazole-saccharinate, the bifurcated H-bond interaction occurs between the NH group of the saccharin and both the N_{16} atom of a neighbour molecule and the nitrogen atom in position 4 of its own tetrazole moiety.

3.4.1.3. Infrared and Raman spectra of crystalline 1MTS and 2MTS: assignments, structural implications and analysis of H-bond networks

Figure 3.12 shows the infrared spectrum of neat crystalline 1-methyl-tetrazole-saccharinate at room temperature. The calculated spectrum for the basic constituent unit of the crystal, **1MTIS-A** monomer, is also given in this figure, for comparison. The Raman spectrum of the crystal is depicted in Figure 3.13. Proposed assignments for the spectra are given in Table 3.6. Since the crystal unit cell is centrosymmetric, the observed infrared and Raman spectra do not exhibit common bands. The observed Davidov splittings, taken as the absolute value of the difference between the frequencies of the Raman and infrared corresponding bands, are, in general smaller than 10 cm^{-1} (see Table 3.6), indicating that the intermolecular interactions do not substantially perturb most of the intramolecular modes and justifying the use of a monomeric model to help in the interpretation of the observed spectra of the crystal. Identical data for 2-methyltetrazole-saccharinate is provided in Figure 3.14, Figure 3.15 and Table 3.7. For this molecule, the observed Davidov splittings were also found to be in general small.

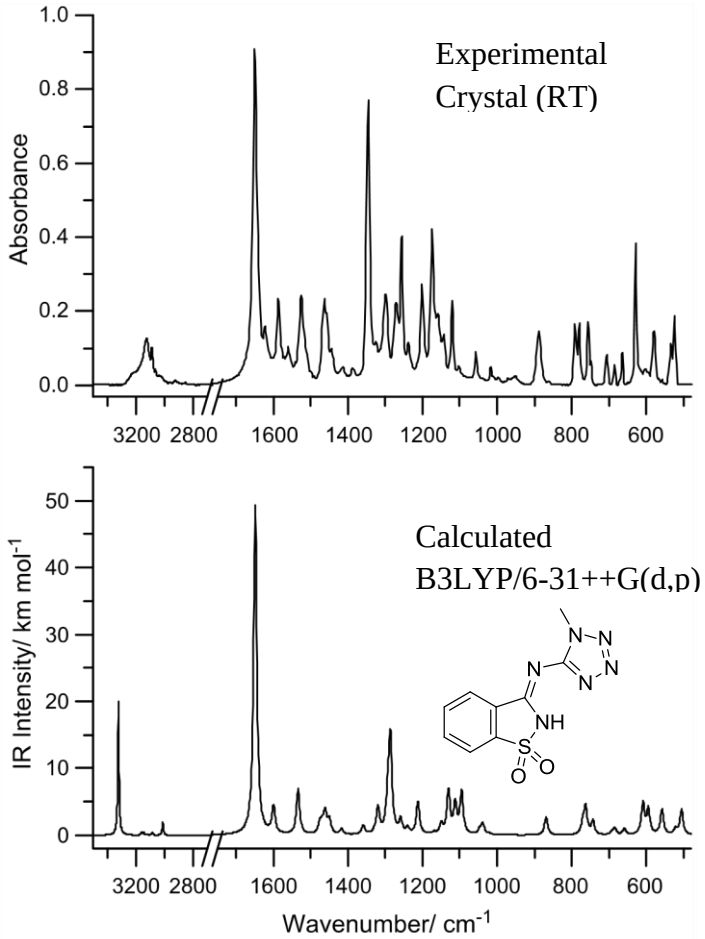

Figure 3.12 – Room temperature infrared spectrum of crystalline 1-methyltetrazole-saccharinate and B3LYP/6-31++G(d,p) calculated infrared spectra for **1MTIS-A**. The calculated spectra were simulated by Lorentzian functions centred at the calculated (scaled by 0.98) wavenumber with full width at half maximum (FWHM) of 10 cm^{-1}; calculated intensities correspond to the area below the Lorentzians.

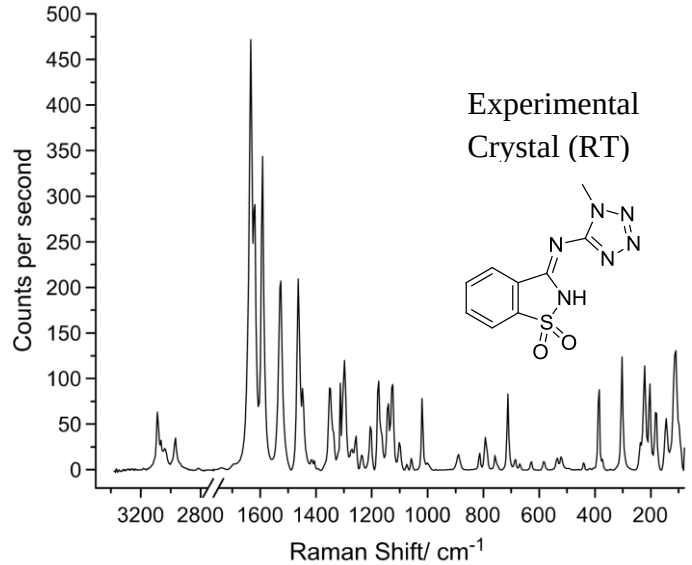

Figure 3.13 - Room temperature Raman spectrum of crystalline 1-methyltetrazole- saccharinate.

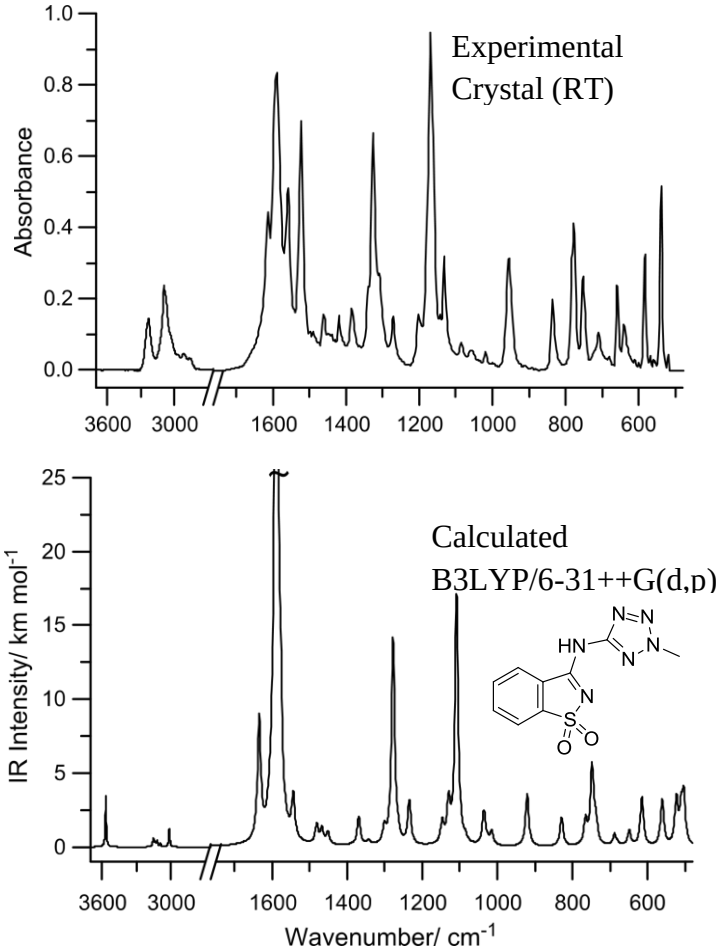

Figure 3.14 - Room temperature infrared spectrum of crystalline 2-methyltetrazole-saccharinate and B3LYP/6-31++G(d,p) calculated infrared spectra for **2MTAS-B**. The calculated spectra were simulated by Lorentzian functions centred at the calculated (scaled by 0.98) wavenumber with full width at half maximum (FWHM) of 10 cm^{-1}; calculated intensities correspond to the area below the Lorentzians.

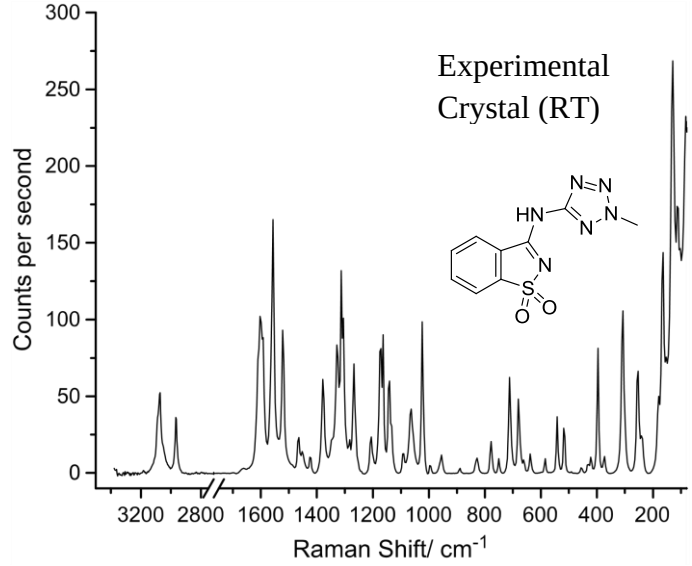

Figure 3.15 - Room temperature Raman spectrum of crystalline 2-methyltetrazole-saccharinate.

In the interpretation of the experimental spectra of the crystals, based on the calculated spectra of the corresponding prevalent monomers (**1MTIS-A** and **2MTAS-B**), attention has to be paid to effects of the intermolecular interactions on some of the vibrations. These effects can be expected to reflect predominantly on the vibrations localized in the interacting groups, *i.e.*, the NH moiety from the saccharin group and the N_{16}-N_{17} fragment of the tetrazole ring for **1MTIS**, and the bridging NH group and N_{17} for **2MTAS**. As usually, the NH stretching (νNH) and out-of-plane bending (γNH) modes of the H-bond donor groups could be anticipated to be the vibrations experiencing the largest frequency shifts in going from the isolated monomer to the crystal. Also, the position of the SO_2 stretching bands (νSO_2 sym. and νSO_2 asym. modes) have to be established taking into account that the level of theory used in the performed calculations is known to underestimate the calculated frequencies for these vibrations.[19–21]

In the present study, the infrared spectra of N-deuterated **1MTIS** and **2MTAS** samples were also used to help band assignments. This proved to be especially useful in case of **2MTAS**, since the observed changes upon deuteration were found to be more important for this compound. Such observation is in agreement with the theoretical predictions of the infrared spectra of the two compounds, which revealed that the calculated spectrum of N-deuterated **1MTIS** (**N_d-1MTIS-A**) does not differ much from that of the parent compound, while the calculated spectrum of N-deuterated **2-MTAS** (**N_d-2MTAS-B**) is substantially different from the one of the non-deuterated species (Figure 3.16). The calculated vibrational data obtained for the two studied N-deuterated tetrazole-saccharinates are shown in Table 3.8 and Table 3.9, together with the proposed assignments for the experimental spectra.

Assignment of the νSO_2 sym. and νSO_2 asym. modes was facilitated by the fact that these vibrations give rise to quite intense bands in infrared (calculated infrared intensities are 102 and 216 km mol^{-1}, for **1MTIS** and 267 and 218 km mol^{-1}, for **2MTAS** (see Table 3.6 and Table 3.7). For **1MTIS**, these modes were then assigned to the intense infrared bands observed at 1174/1163 cm^{-1} (νSO_2 sym.) and 1346 cm^{-1} (νSO_2 asym.) (with Raman counterparts at 1174 and 1350 cm^{-1}), while for **2MTAS** they were ascribed to the infrared bands at 1169/1164 and 1326 cm^{-1}, respectively, which have Raman counterparts at 1172 and 1328 cm^{-1}. The νSO_2 sym. and νSO_2 asym. vibrations were predicted at nearly the same frequency values in the deuterated and non-deuterated compounds and, in consonance with the theoretical predictions, were observed at 1185/1161 and 1346 cm^{-1} in the spectrum of crystalline **N_d-1MTIS** and at 1175/1160 and 1325 cm^{-1} in case of **N_d-2MTAS** (see Table 3.8 and Table 3.9).

Table 3.6 - Assignments for vibrational spectra of crystalline 1-methyltetrazole-saccharinate.[a]

Infrared		Raman	Calculated (1MTIS-A)		
ν	$\Delta\nu_T$[b]	Δν(Raman shift)	ν	I_{IR}	Approximate description
3218	**+10**	3122	3323.2	314.5	NH
3126[FR]	**+15**				
3089	—	3089	3163.1	3.5	νCH Ph
3063	—	3064	3156.9	3.3	νCH Ph
3038	+3	3039	3146.0	4.5	νCH Ph
3027	—	3039	3133.9	1.4	νCH Ph
2961	—	2970	3117.4	0.8	νCH_3 as
			3086.2	6.0	νCH_3 as
2925	–2	n. obs.	3012.1	30.0	νCH_3 s
2873[FR]					
2856[FR]					
1650	–2	1634	1648.9	774.4	νC=N (bridge), δNH
1623	–7	1620	1610.9	1.0	νCC Ph
1586	–3	1592	1600.0	63.5	νCC Ph
1526	**–5**	1527	1534.1	107.0	νC-N (bridge), δN14CN17 t
1463	–2	1463	1475.9	23.0	δCH_3 as
			1469.4	21.1	δCH Ph
1457	—		1461.4	9.1	δCH_3 as
			1461.1	40.5	δCH Ph
1445	**–3**	1449	1450.0	33.6	νCN17 t
1414	—	1416	1417.5	13.0	δCH_3 s
1388	—	1406	1359.2	21.1	νCC Ph
1326	+1	1338	1328.2	4.2	νN15N16 t, δNH
		1313	1319.8	61.7	νCN (saccharine), νNN t, δNH
1299	—	1298	1293.3	82.8	δNH, νNN t
1346	—	1350	1286.4	216.0	νSO_2 as
1271	—	1272	1258.9	33.9	δCH Ph
1256[FR]	—	1257			
1238	–2	1235	1240.3	14.4	$\nu NC(H_3)$
1201	—	1204	1212.4	76.1	νN14N15 t, γCH_3
1159	—	1166	1168.8	4.8	δCH Ph
			1149.5	22.9	δCH Ph
1174	—	1176	1130.5	101.6	δCH Ph, νCS, νSO_2 s
1163[FR]			1130.0	0.04	γCH_3
1143	–2	1142	1112.3	71.0	νNN t, νSO_2 s
1120	–1	1126	1095.2	99.4	νSO_2 s, νNN t, δNH
1102	**–7**	1100	1046.8	10.8	γCH_3, δN15N16N17 t
1057	–2	1058	1038.5	25.8	δCCC Ph
1017	–3	1020	1020.6	3.4	νCC Ph
998	—	1001	990.7	0.01	γCH Ph
970	+3	971	990.0	0.6	νN14N15 t, γCH_3
951	—	950	955.5	0.4	γCH Ph
888	**–4**	890	876.3	0.4	γCH Ph
			868.7	41.7	νNS, δNH
816	—	813	810.6	1.4	δ skeletal
790	–3	792	769.9	27.0	γCH Ph
780	–4		762.4	63.1	νCS, δCCC Ph
755	–2	757	742.9	31.6	puckering t, γCH Ph
748	—	748	738.8	0.03	γ skeletal
705	–2	712	692.4	1.2	δCCC Ph
685	–3	686	691.4	4.6	τNN t
			684.5	14.7	δ skeletal
664	–3	665	658.7	14.7	τCC Ph
629	–3	629	608.8	73.9	δ skeletal
672	–4	669	594.4	58.7	γNH
579	–4	583	557.8	58.7	δSO_2
533	—	534	522.0	11.6	τCC Ph
			520.1	1.8	δ skeletal
524	—	521	505.3	59.5	wSO_2
458	—	440	450.6	8.2	τ skeletal
438	—	419	429.2	15.9	$wN(CH_3)$
		385	389.6	1.7	γSO_2
		373	359.6	3.9	τ skeletal
			359.3	11.0	δ skeletal
		303	281.1	15.9	δ skeletal

Table 3.6 (Continued) [a]

Infrared		Raman	Calculated (1MTIS-A)		
ν	$\Delta\nu_T$[b]	Δν(Raman shift)	ν	I_{IR}	Approximate description
		246	268.5	1.7	tw SO_2
		222	208.2	1.7	γN(CH_3)
n.i.		204	204.4	7.0	δ skeletal
		182	187.8	0.3	δ skeletal
		145	160.9	0.9	τ skeletal
		111	106.2	0.1	τ skeletal
		98	89.4	2.1	δCNC (bridge)
		n.i.	81.0	0.8	τ skeletal
		n.i.	45.7	1.4	τ skeletal
		n.i.	40.7	0.03	τ skeletal
		n.i.	32.6	0.6	τCH_3

[b] $\Delta\nu_T$ are the wavenumber shifts observed upon increasing the temperature from room temperature to 170 ºC; –, means that no shifts were observed or it was not possible to measure them; values indicated in bold type correspond to the largest shifts, which are associated with bands originated in the NH group or vibrations involving N_{16} or N_{17}, that are directly involved in the H-bonding (see Figure 3.9). [a] Wavenumbers and Raman shifts in cm^{-1}.ν, stretching, δ, bending, w, wagging, tw, twisting, γ, rocking, τ, torsion, s, symmetric, as., asymmetric, n. obs., not observed, n. i., not investigated, Ph, phenyl, t, tetrazole, FR, Fermi resonance. See Figure 3.8 for atom numbering.

Table 3.7 - Assignments for vibrational spectra of crystalline 2-methyltetrazole-saccharinate.[a]

Infrared		Raman	Calculated (2MTAS-B)		
ν	$\Delta\nu_T$[b]	Δν(Raman shift)	ν	I_{IR}	Approximate description
3231	**+14**	n.obs.	3567.0	54.2	νNH
3081[FR]	**+12**				
3094	–4	3094	3156.1	7.0	νCH Ph
n. obs	—	3073	3147.9	5.6	νCH Ph
3028	—	3051	3134.8	4.1	νCH Ph
n. obs.	—		3125.4	0.3	νCH_3 as
2965	—	2966	3119.5	6.0	νCH Ph
			3092.3	3.5	νCH_3 as
2923	—	n. obs.	3015.5	19.9	νCH_3 s
2869[FR]					
2852[FR]					
1613	–3	1609	1634.5	130.3	νC=N (saccharine)
1594	—	1661	1606.9	15.1	νCC Ph
1590	**–9**	1593	1589.3	947.7	νCN (bridge), δNH
1559	–3	1557	1577.6	96.9	νCN (bridge), νC=N (saccharine)
1523	**–5**	1521	1543.8	45.8	νCN17 t, δNH
1463	–4	1465	1481.0	20.5	δCH_3 as
1447	—	1452	1467.3	16.3	δCH Ph
			1453.5	0.4	δCH Ph
1419	–2	1425	1451.6	12.6	δCH_3 as
		1422	1425.9	0.5	δCH_3 s
1384	**–6**	1378	1388.0	0.9	ν$NC(H_3)$, δNNN t
			1369.4	30.3	νCN14 t, δN(bridge)CN17
1339	—	1346	1342.9	5.2	νCC Ph
1310	**–5**	1312	1301.2	16.9	νNN t, γCH_3, δNH
n. obs.	—	1306	1278.4	1.7	δCH Ph
1326	–2	1328	1277.9	217.9	νSO_2 as
1272	**–4**	1268	1267.3	8.9	δNH, νNN t
1203	–2	1207	1234.6	46.4	νNN t, νCN t
n. obs.	—	1164	1169.7	0.1	δCH Ph
1143	—	1142	1146.9	22.9	δCH Ph
1132	–3	1134	1129.9	43.3	δCH Ph, νCS
			1125.8	0.002	γCH_3
1169	–4	1172	1108.6	267.0	νSO_2 s
1164[FR]					
1085	**–6**	1092	1085.1	5.2	δNCN t, δCN17N t
1059	**–8**	1064	1036.6	16.0	γCH_3, νNN t
		1058	1035.1	21.0	δCCC Ph
			1026.2	3.3	νCC Ph
1019	–2	1023	1015.2	14.0	νNN t, γCH_3

Table 3.7 (Continued) [a]

Infrared		Raman	Calculated (2MTAS-B)		
ν	$\Delta\nu_T$ [b]	Δν(Raman shift)	ν	I_{IR}	Approximate description
998	—	996	985.3	0.002	γCH Ph
n. obs.	—		940.4	0.2	γCH Ph
956	–4	956	920.7	56.2	νNS, δCNC (bridge)
892	—	890	862.9	0.02	γCH Ph
834	–2	829	828.9	30.2	δ skeletal
781	—	777	765.2	25.9	γCH Ph
777	–1		748.3	77.4	νCS, δCCC Ph
752	–3	750	744.4	10.5	puckering t, γCH_3
			737.2	22.2	γ skeletal
710	–3	711	688.1	12.0	δCCC Ph
680		680	679.4	2.6	δ skeletal
668			663.7	0.6	τNN t
658	–2	661	648.8	16.0	τCC Ph
640	—	638	615.0	51.5	δ skeletal
583	+1	585	561.0	49.1	δSO_2
538	–3	542	523.2	47.7	τCC Ph
518		518	510.7	32.8	wSO_2
			504.0	8.2	δ skeletal
720	**–6**	711	503.5	42.5	γNH
456		421	433.0	0.3	γSO_2
421		396	409.4	1.6	τ skeletal
402			403.3	5.9	$wN(CH_3)$
		372	368.5	15.8	δ skeletal
			360.0	0.01	τ skeletal
		308	286.3	4.8	δCNC (bridge)
		301	276.6	0.04	tw SO_2
		254	231.2	3.2	δ skeletal
		238	201.3	3.0	$\gamma N(CH_3)$
n.i.		166	169.1	1.2	δ skeletal
		130	139.9	0.9	τ skeletal
		111	117.2	0.04	τ skeletal
		102	98.7	0.004	τCH_3
		83	96.7	0.3	τ skeletal
		73	66.7	4.0	δ skeletal
		n.i.	41.6	0.01	τ skeletal
		n.i.	28.2	5.6	τ skeletal

[b] $\Delta\nu_T$ are the wavenumber shifts observed upon increasing the temperature from room temperature to 270 ºC; –, means that no shifts were observed or it was not possible to measure them; values indicated in bold type correspond to the largest shifts, which are associated with bands originated in the NH group or vibrations involving N_{17}, that are directly involved in the H-bonding (see Figure 3.11). [a] Wavenumbers and Raman shifts in cm^{-1}.ν, stretching, δ, bending, w, wagging, tw, twisting, γ, rocking, τ, torsion, s, symmetric, as., asymmetric, n. obs., not observed, n. i., not investigated, Ph, phenyl, t, tetrazole, FR, Fermi resonance. See Figure 3.10 for atom numbering.

Table 3.8 - Assignments for vibrational spectra of crystalline N-deuterated 1-methyltetrazole-saccharinate.[a]

Infrared	Calculated (N_d-1MTIS-A)		
ν	ν	I_{IR}	Approximate description
3089	3163.1	3.3	νCH Ph
3063	3157.0	3.0	νCH Ph
3038	3146.0	4.6	νCH Ph
3027	3133.9	1.4	νCH Ph
2961	3117.5	0.8	νCH_3 as
	3086.2	6.0	νCH_3 as
2925,2873[FR],2856[FR]	3012.2	29.9	νCH_3 s
2346	2440.3	187.2	νND
1640	1639.1	704.1	νC=N (bridge), δND
1621	1610.8	1.4	νCC Ph
1586	1599.3	86.9	νCC Ph
1526	1533.3	97.7	νC-N (bridge), δN14CN17 t
1463	1475.8	23.1	δCH_3 as
	1468.9	19.9	δCH Ph
1457	1461.4	9.1	δCH_3 as
	1460.7	39.2	δCH Ph
1445	1449.9	34.2	νCN17 t
1411	1417.3	14.3	δCH_3 s
1388	1358.3	19.4	νCC Ph
1322	1321.3	40.1	νN15N16 t
	1314.9	26.5	νCN (saccharine), νNN t
1346	1286.4	214.0	νSO_2 as
1299	1261.5	4.9	δCH Ph
1271, 1242[FR]	1249.7	16.8	$\nu NC(H_3)$
1201	1216.6	16.1	νN14N15 t, γCH_3
1159	1168.5	3.9	δCH Ph
	1149.7	138.9	δCH Ph, νCN (saccharine)
1185, 1161[FR]	1136.6	252.1	δCH Ph, νCS, νSO_2 s
	1130.0	0.04	γCH_3
1143	1121.2	77.7	νNN t, νSO_2 s, δND
1120	1111.5	21.7	νNN t, νSO_2 s
1101	1048.9	10.5	νSO_2 s, νNN t, δND
	1045.6	19.8	γCH_3, δN15N16N17 t, δND
1044	1033.1	38.9	δCCC Ph, δND
1017	1019.9	3.8	νCC Ph
996	990.7	0.01	γCH Ph
970	989.7	0.9	νN14N15 t, γCH_3
951	955.5	0.4	γCH Ph
888	876.2	0.3	γCH Ph
813	816.4	0.4	$\nu N(CH_3)$, δCNC (bridge), δND
n. obs.	781.0	2.5	νNS, δND
787	769.8	25.4	γCH Ph
755	742.8	30.0	puckering t, γCH Ph
	739.7	58.7	νCS, δCCC Ph, δND
747	737.8	0.1	γ skeletal
701	691.2	3.6	τNN t
684	685.6	3.5	δ skeletal
	681.5	16.9	δCCC Ph
664	658.7	14.4	τCC Ph
627	607.9	80.6	δ skeletal
577	554.5	57.9	δSO_2
534	522.5	16.9	τCC Ph
	515.3	6.2	δ skeletal
520	496.6	47.0	wSO_2
457	454.5	0.1	τ skeletal
437	429.1	15.9	$wN(CH_3)$
[b]	429.0	36.6	γND
	388.6	0.3	γSO_2
	359.2	3.0	τ skeletal
	358.5	10.9	δ skeletal
	280.7	16.0	δ skeletal
	265.1	2.4	tw SO_2
	207.5	2.0	$\gamma N(CH_3)$

Table 3.8 (Continued) [a]

Infrared	Calculated (N_d-1MTIS-A)		
ν	ν	I_{IR}	Approximate description
	204.4	7.0	δ skeletal
n.i.	187.7	0.3	δ skeletal
	160.8	0.9	τ skeletal
	106.2	0.1	τ skeletal
	89.1	2.1	δCNC (bridge)
	81.0	0.8	τ skeletal
	45.7	1.4	τ skeletal
	40.5	0.03	τ skeletal
	32.4	0.5	τCH_3

[b] Most probably overlapped with the band at 520 cm^{-1}, due to wSO_2. [a] Wavenumbers and Raman shifts in cm^{-1}.ν, stretching, δ, bending, w, wagging, tw, twisting, γ, rocking, τ, torsion, s, symmetric, as., asymmetric, n. obs., not observed, n. i., not investigated, Ph, phenyl, t, tetrazole, FR, Fermi resonance. See Figure 3.8 for atom numbering.

Table 3.9 - Assignments for vibrational spectra of crystalline N-deuterated 2-methyltetrazole-saccharinate.[a]

Infrared	Calculated (N_d-2MTAS-B)		
ν	ν	I_{IR}	Approximate description
3094	3156.1	7.0	νCH Ph
3077	3147.9	5.6	νCH Ph
3028	3134.8	4.2	νCH Ph
3004	3125.4	0.3	νCH_3 as
2958	3119.5	6.1	νCH Ph
	3092.3	3.5	νCH_3 as
2924,2869,2853[FR]	3015.5	19.9	νCH_3 s
2353	2613.4	34.9	νND
1610	1632.3	172.3	νC=N (saccharine)
1590	1606.8	24.3	νCC Ph
1561	1581.2	440.3	νCN (bridge)
1543	1568.4	509.0	νCN (bridge), νNN t
1465	1485.4	2.8	δCH_3 as
1452	1470.3	3.6	δCH Ph
1442	1456.8	96.8	νCN17 t
	1452.6	19.5	δCH Ph
	1451.6	12.6	δCH_3 as
1422	1425.9	0.2	δCH_3 s
1397	1386.7	1.0	ν$NC(H_3)$, δNNN t
1386	1368.0	41.8	νCN14 t, δN(bridge)CN17
1340	1340.1	11.2	νCC Ph
n. obs.	1287.8	0.9	νNN t, γCH_3
1325	1277.9	217.1	νSO_2 as
1278	1277.3	0.6	δCH Ph
1205	1243.3	29.1	νNN t, νCN t
n. obs [b]	1174.2	4.4	δCH Ph
n. obs	1163.2	8.9	δCH Ph
1135	1136.3	61.8	δCH Ph, νCS
1117	1125.8	0.002	γCH_3
1175,1160[FR]	1108.6	267.6	νSO_2 s
1087	1084.2	6.3	δNCN t, δCN17N t
1061	1040.0	12.2	γCH_3, νNN t
	1036.1	24.8	δCCC Ph, νNN t
1021	1026.5	1.7	νCC Ph
1011	1015.5	12.7	νNN t, γCH_3
1046	988.1	3.6	δND
n. obs.	985.2	0.007	γCH Ph
n. obs.	940.3	0.1	γCH Ph
946	911.1	61.7	νNS, δCNC (bridge)
n. obs.	862.7	0.005	γCH Ph
819	810.2	29.5	δ skeletal
783	764.9	23.7	γCH Ph
775	748.2	77.2	νCS, δCCC Ph
752	744.4	10.8	puckering t, γCH_3
	737.2	21.2	γ skeletal
709	688.0	11.4	δCCC Ph
675	671.6	3.1	δ skeletal
670	662.8	0.2	τNN t
660	648.2	19.6	τCC Ph

Table 3.9 (Continued) [a]

Infrared	Calculated (N_d-2MTAS-B)		
ν	ν	I_{IR}	Approximate description
631	605.2	46.9	δ skeletal
584	560.7	50.3	δSO_2
538	521.2	20.6	τCC Ph
527	510.1	35.1	wSO_2
n. obs.	500.3	4.4	δ skeletal
455	436.0	6.6	γSO_2
419	414.7	1.8	τ skeletal
402	402.1	6.0	$wN(CH_3)$
514	386.0	19.3	γND
|	367.8	15.6	δ skeletal
|	339.6	8.8	τ skeletal, γND
|	286.3	4.7	δCNC (bridge)
|	276.3	0.1	tw SO_2
|	231.1	3.2	δ skeletal
|	198.0	4.0	$\gamma N(CH_3)$
n. i.	168.7	1.2	δ skeletal
|	139.9	0.9	τ skeletal
|	116.5	0.002	τ skeletal
|	98.7	0.003	τCH_3
|	96.7	0.3	τ skeletal
|	66.6	4.0	δ skeletal
|	41.5	0.01	τ skeletal
|	28.1	5.6	τ skeletal

[b] Superimposed with the intense band due to νSO_2 s. [a] Wavenumbers in cm^{-1}.ν, stretching, δ, bending, w, wagging, tw, twisting, γ, rocking, τ, torsion, s, symmetric, as., asymmetric, n. obs., not observed, n. i., not investigated, Ph, phenyl, t, tetrazole, FR, Fermi resonance. See Figure 3.10 for atom numbering.

Assignment of the νNH mode in the two crystals could also be easily undertaken, because this vibration gives rise to a band in a quite characteristic frequency range. When the NH group is involved in H-bonding, the νNH stretching gives rise to considerably intense and broad infrared bands, appearing in the ~3300-3050 cm^{-1} region, while the corresponding Raman features can be expected to be very weak. For both studied compounds, two main bands ascribable to the νNH stretching vibration were observed: at 3218/3126 cm^{-1} for **1MTIS**, and at 3231/3081 cm^{-1} for **2MTAS**. The doublets result from Fermi resonances with overtones of bands in the 1600-1500 cm^{-1} region with significant contribution from the δNH bending coordinate. Compared to the predicted values for the monomer (3323 and 3537 cm^{-1}, respectively for **1MTIS** and **2MTAS**; see Table 3.6 and Table 3.7), the νNH bands show the expected shift to lower frequencies.

In the deuterated compounds, νND is not affected by Fermi resonance interactions and these vibrations give rise to single bands at 2346 cm^{-1} (**N_d-1MTIS**) and 2353 cm^{-1} (**N_d-2MTAS**). The observed vibrational changes upon deuteration of **2MTAS** is presented in Figure 3.16.

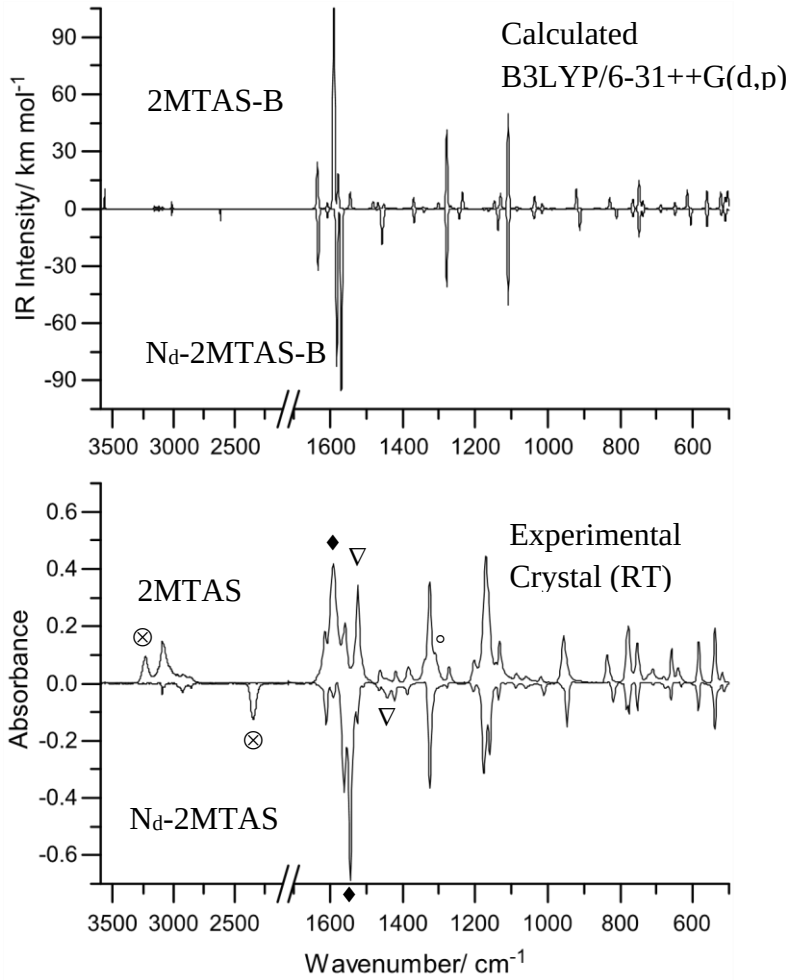

Figure 3.16 - (Bottom) room temperature infrared spectra of crystalline 2-methyltetrazole-saccharinate and its N-deuterated analogue and (top) B3LYP/6-31++G(d,p) calculated infrared spectra for **2MTAS-B** and **N_d-2MTAS-B**. The experimental spectrum of **N_d-2MTAS-B** was obtained from the recorded spectrum, after nullification of the bands due to the non-deuterated species. The calculated spectra were simulated by Lorentzian functions centred at the calculated (scaled by 0.98) wavenumber with full width at half maximum (FWHM) of 10 cm^{-1}; calculated intensities corresponds to the area below the Lorentzians. The spectra of the N-deuterated compound were multiplied by -1. Symbols ⊗, ♦ and ∇ indicate the most significant frequency shifts observed for the νNH stretching and δNH bending modes upon deuteration, as described in the text.

Identification of the bands due to the δNH and γNH modes was not so straightforward. In case of δNH, calculations predicted a considerable mixing with other coordinates. For **1MTIS**, δNH contributes in some extent for several modes, giving rise to bands in both the 1650-1500 cm^{-1} and 1350-1300 cm^{-1} regions (see Table 3.6). Consequently, deuteration was found to affect only in a minor degree these bands. On the other hand, in **2MTAS**, δNH contributes mainly to the bands observed at 1590, 1523 and 1310 cm^{-1}, and these bands can then be expected to experience large frequency shifts upon deuteration. Accordingly, the two first bands have

equivalent counterparts in the spectrum of N_d-2MTAS at 1543 and 1442 cm^{-1} (corresponding to shifts of -47 and -81 cm^{-1}; see Figure 3.16). The last band corresponds to a vibration that, in absence of coupling with the δNH coordinate (in the deuterated compound), reduces very much its intensity (according to the theoretical predictions, from *ca.* 17 to less than 1 km mol^{-1}; see Table 3.7 and Table 3.9), and no counterpart band could then be observed in the spectrum of **N_d-2MTAS**. The band due to γNH is predicted by the calculations to occur in the **1MTIS** and **2MTAS** monomers, at *ca.* 594 and 504 cm^{-1}, respectively (Table 3.6 and Table 3.7), but this mode can indeed be expected to increase considerably its frequency in the crystals upon hydrogen bonding establishment. Comparison of the experimental IR spectra for the deuterated and non-deuterated crystalline samples indicated as best candidates for assignment γNH the bands observed at 672 (**1MTIS**) and 720 cm^{-1} (**2MTAS**), which are absent from the spectra of the deuterated compounds.

Temperature variation studies gave further support to the proposed assignments. Table 3.6 and Table 3.7 show the frequency shifts accompanying the increase of the temperature in the two samples. As it can be seen, the largest shifts are associated with vibrations of the interacting groups and reflect the weakening of the H-bonds upon temperature increase (the increase of the disorder in the crystal can also be noticed in the observed general broadening of the bands). Then, for example, the bands associated with the νNH mode shift considerably (by *ca.* 10-15 cm^{-1}) to larger frequency (blue-shift), and those associated with the γNH mode and most of the modes localized predominantly in the acceptor fragments shift to lower frequency (red-shift), as expected. Figure 3.17 and Figure 3.18 show selected spectral regions showing this effect. Figure 3.17 concerns 1-methyltetrazole-saccarinate and illustrates the shift of the νNH bands, which vary distinctively while the remaining bands shown in the figure, due to CH stretching vibrations of the phenyl and methyl groups, practically do not change their position with temperature. Figure 3.18, for 2-methyltetrazole-saccarinate, shows the behaviour upon temperature increase of the bands due to νNH (top panel) and of the bands observed in the 1700–1450 cm^{-1} region. For these latter, the largest shifts are observed for the bands at *ca.* 1590 and 1523 cm^{-1}, ascribed to modes with significant contributions of δNH and νCN_{17} coordinates (see Table 3.7).

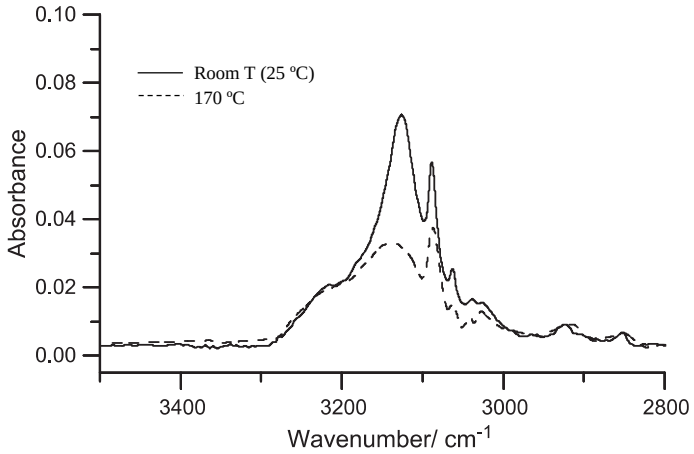

Figure 3.17 - νNH/νCH region of the infrared spectrum of crystalline 1-methyltetrazole-saccharinate as a function of temperature.

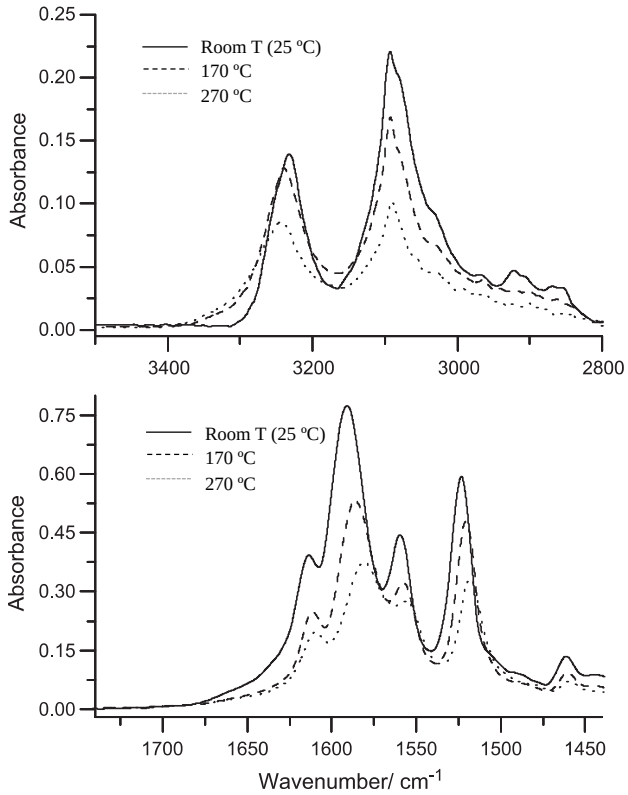

Figure 3.18 - Selected regions [top: νNH/νCH; bottom: νC=N (saccharine)/νC=C phenyl/δNH/νCN (bridge)] of the infrared spectrum of crystalline 2-methyltetrazole-saccharinate as a function of temperature.

3.4.2. Conclusions

In this investigation, the molecular structures of nitrogen-linked 1- and 2-methyltetrazole-saccharinates were studied in the crystalline phase, using X-ray crystallography and infrared and Raman spectroscopies. The studies were complemented by quantum chemical calculations

performed at the DFT(B3LYP)/6-31++G(d,p) level of theory for the isolated molecules. In the neat crystalline solids, 1-methyltetrazole-saccharinate units assume the most stable configuration for the isolated molecule, **1MTIS-A**, with the N=C spacer linking the two heterocycles, while 2-methyltetrazole-saccharinate units exist in the **2MTAS-B** form, with the two heterocycles connected by an NH spacer. The **2MTAS-B** species does not correspond to the intrinsically most stable form of 2-methyltetrazole-saccharinate and is selected upon crystallization due to its better ability to for intermolecular hydrogen bonds, compared to the most stable structure of the compound in the gas phase (**2MTIS-A**). In both crystals, the structure consists of a packing of dimeric units, the dimers formed via hydrogen bonding involving either the NH group of the saccharyl system (**1MTIS**) or the spacer amine group (**2MTAS**). In the former, the hydrogen bond is bifurcated and the NH group acts as a donor both towards a neighbour molecule and an N atom of the tetrazole ring, forming an intramolecular hydrogen bond. In **2MTAS**, pairs of molecules are linked in dimers through an intermolecular hydrogen bond involving the NH spacer group as proton donor and the nitrogen in position 4 of the tetrazole ring as acceptor. The observed difference in the crystallographic basic units of the two compounds reveals the prevalence of the H-bond networks in determining the structural preferences of the tetrazole-saccharinates in the solid state. Such structural flexibility appears also to be of potential interest in the design of new ligands based on the tetrazole-saccharinate framework. The infrared and Raman spectra of the crystals of the two compounds (including the infrared spectra of the N-deuterated isotopologues) were assigned and interpreted.

3.5. Amino→imino tautomerization upon *in vacuo* sublimation of 2-methyltetrazole-saccharinate (2MTS) as probed by matrix isolation infrared spectroscopy

It was shown in the previous section that, in the neat crystalline solid, 1-methyltetrazole-saccharinate (**1MTS**) units assume the most stable configuration for the isolated molecule, the imino-bridged tautomeric form, with the N=C spacer linking the two heterocycles, while in the case of its isomer, 2-methyltetrazole-saccharinate (**2MTS**), the amino-bridged tautomer was found to be present in the crystalline phase. However DFT(B3LYP)/6-31++G(d,p) calculations performed on 2-methyltetrazole-saccharinate (**2MTS**) predicted the imino-bridged tautomer as the most stable species for the isolated molecule. It could then be expected that **2MTS** should also exist in this tautomeric form in the gas phase.

Since the presence of the methyl substituent in the tetrazole ring of **2MTS** reduces the number of possible tautomers relatively to the unsubstituted compound, the methyl derivative appeared as an adequate target to explore in a deeper detail the tautomerism in this type of conjugates. Hence, in this study we have undertaken a detailed theoretical structural characterization of **2MTS** and, subsequently, identified its structure in the gas phase by analysis of the infrared spectrum of the matrix-isolated compound. As shown in detail below, it could be doubtlessly demonstrated that, in the gas phase, **2MTS** exists as the theoretically predicted most stable imino-bridged form. A mechanism for the conversion of the tautomeric form existing in the crystal into that present in the gas phase is proposed.

3.5.1. Results and discussion

3.5.1.1. Tautomerism and isomerism (structural and conformational) in 2MTS: structural characterization of the compound

2MTS has five possible tautomeric forms (Figure 3.19), each one exhibiting four different isomeric structures (either structural or conformational). According to the calculations, in the most stable tautomer of the compound (**I** in Figure 3.19), the labile hydrogen atom is attached to the saccharyl nitrogen. In this form, the two heterocyclic fragments are linked by an imino moiety in which the double-bond is established with the carbon atom of the saccharyl fragment. In the lowest energy isomeric form of this tautomer, the two rings assume a *zusammen* (*Z*) arrangement around the C=N bond of the bridging group. Depending on the orientation of the tetrazole ring, two different conformers of this species may exist (**Ia** and **Ib**; see Figure 3.19),

which correspond to the two lowest energy structures of **2MTS**. Both Ia and Ib exhibit an intramolecular NH···N hydrogen bond, which largely contributes to their stabilization. Two conformers analogous to these low-energy forms, but where the arrangement about the C=N imino linkage is *entgengen* (*E*), also exist (**Ic**, **Id**). However, their energies are much higher (*ca.* 40 kJ mol^{-1}; see Table 3.10), mainly because of the steric hindrance resulting from the close proximity of the tetrazole ring and the phenyl group of the saccharyl moiety.

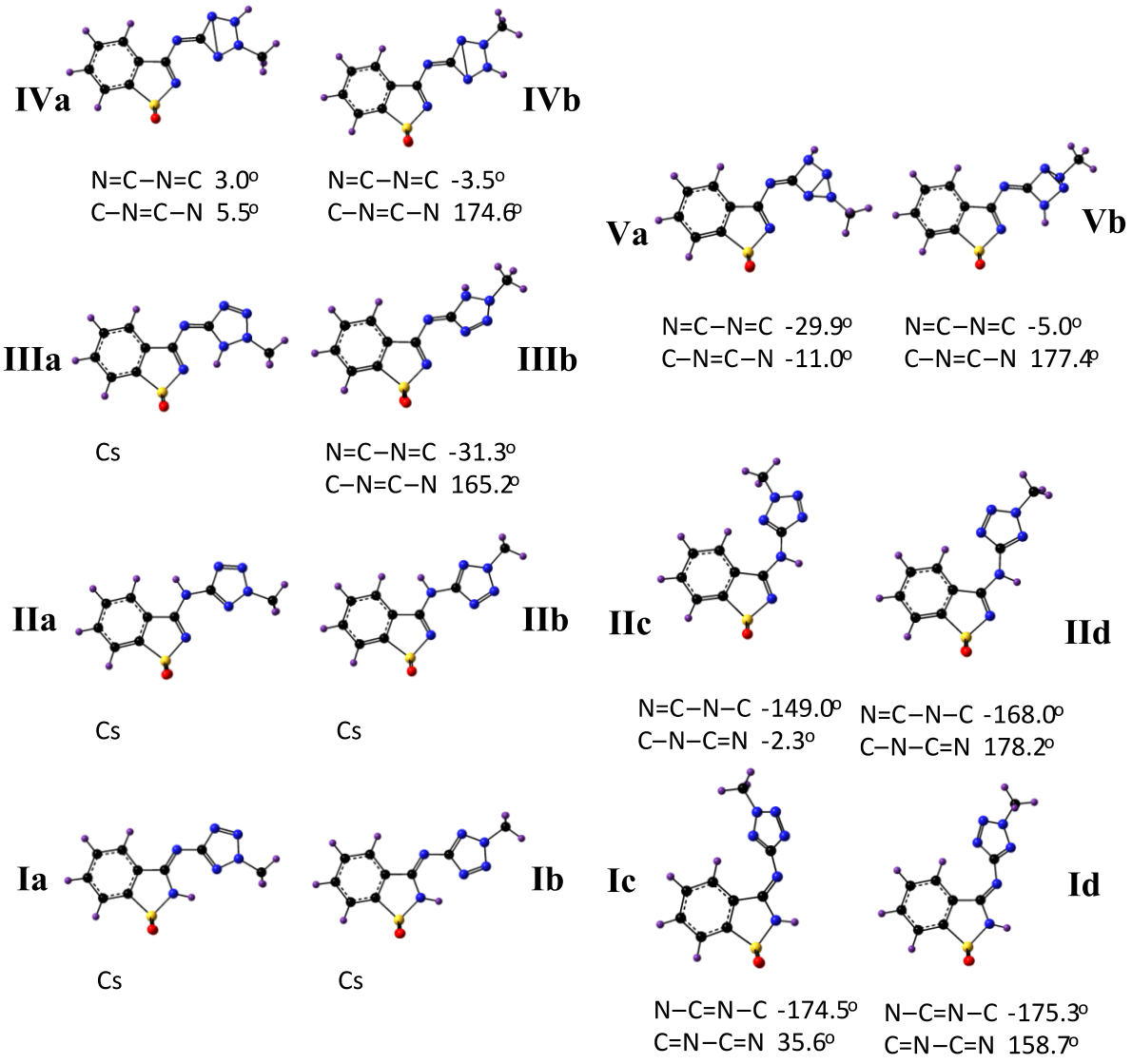

Figure 3.19 - Possible tautomers of **2MTS** (**I**–**V**) with the corresponding isomeric (structural or conformational) forms (**a-d**). The *entgengen* (**c**,**d**) forms of **III**, **IV**, and **V** correspond to high-energy forms (see text) and are not represented. The indicated dihedral angles about the bridge bonds were calculated at the B3LYP/6-31G++(d,p) level of theory. The angles are not given for forms with a planar molecular skeleton (Cs point group). For relative energies of the different forms, see Figure 3.19.

Table 3.10 - Relative energies (ΔE), zero-point corrected relative energies (ΔE_{ZPE}), and relative Gibbs energies at T = 150 °C ($\Delta G_{(150)}{}^{o}$) for the various tautomers of 2MTS [a]

	ΔE	ΔE^{o}	$\Delta G_{(150)}{}^{o}$
Ia	7.7 (7.4)	7.1 (6.9)	2.3 (6.1)
Ib	0.0 (0.0)	0.0 (0.0)	0.0 (0.0)
IIa	18.9 (15.7)	20.3 (17.1)	19.8 (14.6)
IIb	30.7 (26.7)	31.6 (27.7)	29.2 (18.2)
IIIa	81.8	78.0	79.0
IIIb	141.3	138.7	138.4
IVa	197.1	194.6	191.8
IVb	198.8	196.2	192.3
Va	405.2	397.4	399.2
Vb	388.4	381.1	384.8
Ic	46.9	46.3	45.6
Id	39.0	38.8	38.8
IIc	29.9	31.7	30.7
IId	27.8	30.2	27.2

[a] All values are in kJ mol^{-1}. B3LYP/6-31++G(d,p) calculations. Values in parentheses were obtained at the B3LYP/6-311++G(3df,3pd) level of theory. The B3LYP/6-31++G(d,p) calculated absolute values of E, E^{o} and $G_{(150)}{}^{o}$ for the most stable form, **Ib**, are -1224.854632, -1224.671350, and -1224.742365 hartree, respectively; at the B3LYP/6-311++G(3df,3pd), these values are -1225.171291, -1224.987660, and -1225.057712 hartree. 1 hartree = 2625.5001 kJ mol^{-1}.

Other imino-bridged tautomers of the compound do also exist, where the labile hydrogen atom occupies the different available positions at the tetrazole ring (**III**, **IV**, **V**; see Figure 3.19). In all these forms, the C=N bond of the imino bridge is established with the carbon atom of the tetrazole moiety. When the hydrogen is in positions 3 or 4, the resulting tautomeric forms (**IV**, **V**) have highly strained Dewar-tetrazole bicyclic structures, thus corresponding to high-energy species with relative energies larger than *ca.* 200 kJ mol^{-1} or 400 kJ mol^{-1}, respectively. However, when the hydrogen atom occupies the position 1 of the tetrazole ring (**III**; Figure 3.19), the situation is different, and the resulting isomer exhibiting an intramolecular NH···N hydrogen bond (where the saccharyl nitrogen atom acts as acceptor; **IIIa** in Figure 3.19) has a comparatively lower relative energy (~80 kJ mol^{-1}). Note that, on the other hand, form **IIIb** has no intramolecular H-bond and has a much higher relative energy (~140 kJ mol^{-1}), with the two heterocyclic rings considerably deviated from planarity. For tautomers **III**, **IV**, and **V**, isomeric structures with the *entgengen* arrangement about the N=C bridge bond (of types **c** and **d**, according to the notation used in Figure 3.19) do also exist, but their relative energies are expectably very high (over *ca.* 200 kJ mol^{-1}). The labile hydrogen atom can also be attached to the bridging nitrogen atom (**II**, Figure 3.19). In this case, the spacer between the saccharyl and tetrazole rings is an amino group. Internal rotations around the two C-N bridging bonds lead to the existence of four different conformers, with predicted energies ranging from *ca.* 20 to 30 kJ

mol^{-1}. As shown in the previous section, in the crystalline phase of the compound **2MTS** molecules were found to exist in the amino-bridged form **IIa**, which allows for a more efficient packing. In the crystal, the structure consists of a packing of dimeric centrosymmetric units, the dimers being formed via hydrogen bonding involving the NH group of the spacer of one of the units of the dimer and the nitrogen 4 of the tetrazole ring of the second unit (and vice versa), see Figure 3.11. According to the calculations, for the isolated molecule, the most stable form is **Ib**. The second most stable species is form **Ia**, which differs from the most stable form by a 180° internal rotation around the bridging N-C bond. Both forms have a planar heavy atom skeleton and bear an intramolecular N-H···N hydrogen bond. The potential energy profile for the interconversion between these two forms is depicted in Figure 3.20. As shown in this figure, the B3LYP/6-31++G(d,p) barrier for the **Ib→Ia** conformational isomerization amounts to 35.7 kJ mol^{-1} (28.0 kJ mol^{-1} in the reverse direction).

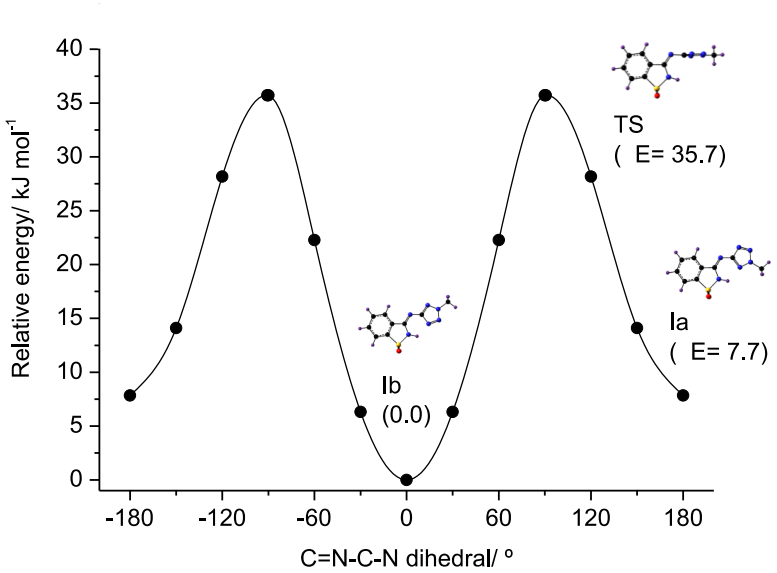

Figure 3.20 - B3LYP/6-31++G(d,p) calculated potential energy profile for the **Ia-Ib** conformational isomerization in 2MTS.

Table 3.11 shows some relevant molecular parameters for characterization of the intramolecular H-bonds in forms **Ia** and **Ib**, as well as for forms **IIIa** and **Vb** that also have geometric arrangements compatible with the existence of such type of interaction (see Figure 3.19). As it could be expected, all parameters indicate that the H-bond is stronger in the most stable form **Ib** than in **Ia**: in form **Ib** the N-H and H···N distances are longer and shorter than in **Ia**, respectively, while the ∠N-H···N angle is larger and the charge on the H atom is more positive. In addition, the charge on the donor N atom is more negative in form **Ib**, evidencing the greater localization of the charge on this atom at expenses of the N-H bond. Furthermore,

the charge on the N atom acceptor is less negative, indicating the migration of electron charge from this atom toward the H···N hydrogen bond. Very interestingly, the data shown in Table 3.11 also indicate that, among all the forms of **2MTS** bearing an intramolecular H-bond, form **IIIa** is the one where this interaction is stronger. In this case, the charges on the N atoms are not directly comparable with those of **Ia** and **Ib** because the donor and acceptor atoms are different. However, both the values of the charge on the H atom and the bond distances are quite illustrative of the greater strength of the H-bond in **IIIa** compared to **Ia** and **Ib**. The results also show that, if it exists, the H-bond in form **Vb** will be very weak.

Table 3.11 - B3LYP/6-31++G(d,p) calculated intramolecular hydrogen bond parameters for the 2MTS forms **Ia**, **Ib**, **IIIa** and **Vb**. [a]

	Ia	**Ib**	**IIIa**	**Vb**
N-H	1.018 (1.014)	1.022 (1.017)	1.037	1.016
H···N	2.075 (2.067)	2.027 (2.022)	1.832	2.466
∠N-H···N	120.3 (121.1)	122.0 (122.7)	120.7	95.4
$q_{(N)}$ donor	–0.717 (–0.955)	–0.759 (–0.992)	–0.683	–0.282
$q_{(H)}$···	+0.432 (+0.592)	+0.435 (+0.603)	+0.483	+0.375
$q_{(N)}$ acceptor	–0.720 (–0.862)	–0.614 (–0.579)	–0.558	–0.574

[a] Distances in Å; angles in degrees; Mulliken charges on the atoms in units of electron (1e = 1.60217646 × 10^{-19} C). For **Ia** and **Ib**, the values in parentheses were obtained at the B3LYP/6-311++G(3df,3pd) level of theory.

3.5.1.2. Preferred structure of 2MTS in the gas phase: matrix isolation infrared spectroscopy experiments

As mentioned in the previous section, in the room temperature crystalline phase **2MTS** exists in the amino-bridged form **IIa**. Since the theoretical calculations performed on the compound predicted that the lowest energy tautomer of the compound in gas phase should correspond to imino-bridged tautomer **I**, a sample of crystalline **2MTS** was sublimated *in vacuo* (at ~150 ºC), and the obtained vapours of the compound were deposited together with argon (in a *ca.* 1:1000 molar ratio) onto a substrate kept at 15 K (see details in Chapter 2; section 2.3), and the corresponding matrix was investigated spectroscopically to structurally characterize the sublimate. The infrared spectrum of the argon matrix of **2MTS** is presented in Figure 3.21a.

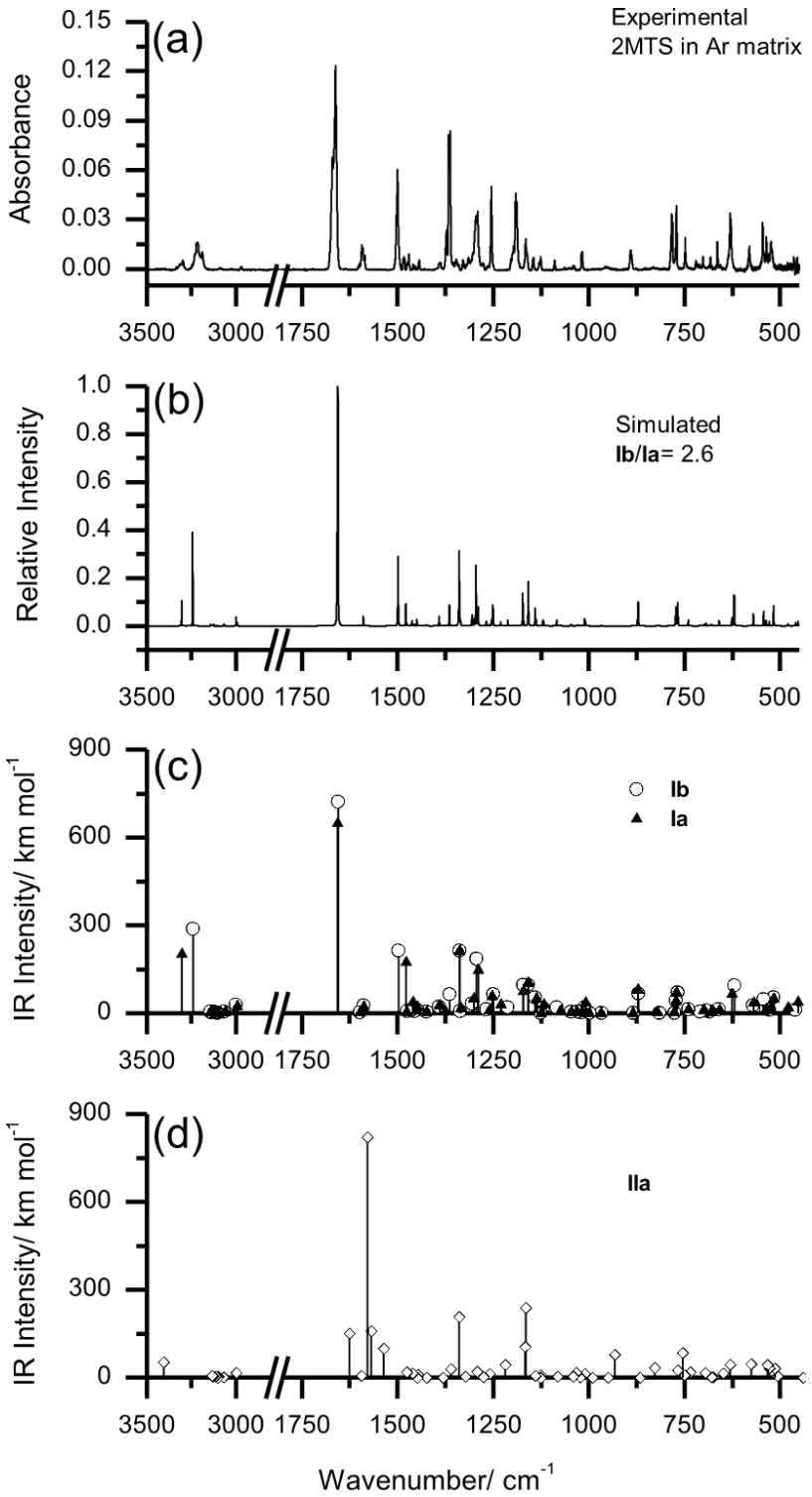

Figure 3.21 - (a) Infrared spectrum of the as-deposited argon matrix (15 K) of **2MTS**. (b) Normalized to unit simulated infrared spectrum built from the B3LYP/6-311++G(3df,3pd) calculated IR spectra of forms **Ia** and **Ib** (shown in panel (c) as stick spectra), with intensities scaled by the ratio **Ib**/**Ia** = 2.6 (see text). (d) B3LYP/6-311++G(3df,3pd) calculated IR spectrum of form **IIa**. In the simulated spectrum, bands were simulated by Lorentzian functions with full bandwidth at half maximum equal to 1 cm^{-1}, cantered at the calculated wavenumbers (scaled by 0.978 except in the νN-H stretching region where the scale factor used was 0.938)

The comparison of the spectrum of the matrix with those theoretically obtained for the different forms of **2MTS** revealed that the experimental spectrum corresponds to a mixture of the two lowest energy conformers of the imino-bridged tautomer **I** (**Ia** and **Ib**). The B3LYP/6-311++G(3df,3pd) calculated infrared spectra of forms **Ia** and **Ib** are drawn as stick spectra in Figure 3.21c. A simulated spectrum, built by adding the calculated spectra of these two forms with intensities weighted assuming an **Ib**/**Ia** population ratio of 0.72/0.28, is presented in Figure 3.21b. The population ratio was obtained from the observed relative intensities of the νN-H bands ascribed to each conformer (which appear well separated in the experimental spectrum), normalized by the corresponding theoretical infrared intensities calculated at the B3LYP/6-311++G(3df,3pd) level. This population ratio agrees fairly well with that predicted (according to Boltzman statistics) for the gas phase equilibrium between the two conformers (**Ia**, **Ib**) at the temperature of sublimation of the compound, using the B3LYP/6-31G++(d,p) calculated $\Delta G_{(150)}^{o}$ values: 0.66/0.34 (the larger 6-311++G(3df,3pd) basis set predicted a somewhat larger relative population of **Ib**, with **Ib**/**Ia** = 0.86/0.14). It is clear from Figure 3.21 that the simulated spectrum fits the experimentally observed one very well. Though the spectral signatures of forms **Ia** and **Ib** are very similar, there are a few spectral regions that can be used to doubtlessly establish the presence of the two conformers in the matrix (see Table 3.12 for calculated vibrational data for forms **Ia** and **Ib** and detailed assignment of the observed spectrum).

In the νNH stretching region, the two conformers give rise to well-separated features (structured bands resulting from matrix-site splitting). In agreement with the stronger N-H···N intramolecular hydrogen bond in conformer **Ib**, the νNH stretching mode of this form appears at a considerably lower frequency (~3210 cm^{-1}) than in form **Ia** (~3300 cm^{-1}). Moreover, the bridge νC=N stretching mode in both conformers is shown by the vibrational calculations to be coupled in some extent with the in-plane bending of the H-bonded N-H group. Because of that, this vibration appears at experimentally discernible frequencies in the two conformers. In agreement with the calculations, form **Ia** absorbs at a slightly higher frequency (1670 cm^{-1}), while the higher intensity band at (1662 cm^{-1}) is ascribed to the most abundant form **Ib**. Other bands assigned exclusively to the less abundant form **Ia** are observed in the 1480-1470 cm^{-1} region (mostly bridge νN-C stretching), and at 1362 (νSO_2 antisymmetric stretching), 1303 (with an important contribution of the saccharyl νC-N stretching), 1291 (H-bonded δN-H in-plane bending), 1188 (νSO_2 symmetric stretching), 1017/1016 (predominantly tetrazole νN-N and νC-N stretchings mixed with a γCH_3 rocking mode), 711 (principally νS-C stretching), 678 (νN-C(H3) stretching), 636 (νN-S stretching), 480 (H-bonded γN-H out-of-plane bending), and

456 (delocalized mode, also with a significant contribution from the γN-H out-of-plane bending coordinate) cm^{-1}. All these bands are observed at positions fitting well their predicted positions (1478, 1337, 1300, 1288, 1171, 1008, 698, 678, 626, 477, and 451 cm^{-1}, respectively), see Table 3.12 and Figure 3.22 for atom numbering.

Note that the calculated spectrum for the **2MTS** crystalline phase, relevant form **IIa** (and also those predicted for the other amino-bridged higher-energy conformers, **IIb**, **IIc**, and **IId**), are markedly different from the experimentally observed spectrum (see Figure 3.21d). This is particularly noticeable in the νN-H stretching region and the 1630-1500 cm^{-1} range. In the first case, **IIa** is predicted by the calculations to give rise to a band at *ca.* 3400 cm^{-1} (typical for a non-hydrogen bonded N−H group) where no corresponding absorptions were found in the experimental spectrum. In the second case, according to the calculations **IIa** should give rise to four intense bands in the 1630-1500 cm^{-1} region (at 1626, 1579, 1569, and 1537 cm^{-1}), while in the experimental spectrum only one band was observed (which is ascribable to a phenyl ν*C*C stretching mode of tautomer **I** forms).

In conclusion, the experimental results doubtlessly demonstrate that, upon *in vacuo* sublimation of **2MTS** in an effusive-type cell, tautomerization takes place, transforming the crystal phase **IIa** into tautomer **I**. Under the experimental conditions used, the two lowest energy conformers of **I** (**Ia** and **Ib**) approach their relative populations of thermodynamic equilibrium in the gas phase at the temperature of sublimation, suggesting a high collision rate in the gaseous beam seeding region. The observed tautomerization follows the previously reported (amino-bridged)→(imino-bridged) tautomerization upon sublimation of the parent tetrazole-saccharinate (**TS**), and seems then to be a relatively general phenomenon in this type of conjugates.

Table 3.12 - Assignments for the observed infrared spectrum of **2MTS** isolated in an argon matrix.[a]

Infrared	Calculated B3LYP/6-311++G(3df,3pd)		
ν	ν	I_{IR}	Approximate description [b]
3334/ 3310/ 3299/ 3295	3305	201.4	νNH (**Ia**)
3230/ 3221/, 3214/ 3201/ 3189	3243	286.0	νNH
3093	3143	3.1	νCH ph
3093	3137	2.8	
3087	3125	5.3	
n.o.	3112	1.4	
n.o.	3102	0.3	νCH_3 as'
3032	3067	4.0	νCH_3 as''
3021	3060	5.0	νCH_3 as'' (**Ia**)
2970	2999	27.1	νCH_3 s
1670	1658	649.5	νC=N (**Ia**)
1662	1655	720.5	νC=N
1602/ 1599	1600	2.5	νCC ph
1593/ 1590	1589	26.9	νCC ph
1589/ 1580	1588	21.5	νCC ph (**Ia**)
1502/ 1500	1498	212.9	νN=C, νN–C
1486/ 1484/ 1482/ 1472/ 1470	1478	178.1	νN–C, δCH ph (**Ia**)
1474	1475	5.8	δCH_3 as'
1459	1463	10.0	νCC ph
1456/ 1455	1462	37.9	νCC ph, δCH ph (**Ia**)
1454	1456	4.7	νCC ph, δCH ph
1444	1449	11.3	δCH_3 as'' (**Ia**)
1444	1449	19.8	νCC ph, δCH ph (**Ia**)
1443	1448	11.2	δCH_3 as''
1429	1424	3.6	δCH_3 s
1391/ 1387	1391	21.0	$\nu N–C(H_3)$, νN=N
1374/ 1373/ 1371	1364	64.6	$\nu N_{20}–N_{21}$, $\nu C_{17}–N_{18}$
1366/ 1365/ 1364	1338	212.3	νSO_2 as
1362	1337	211.8	νSO_2 as (**Ia**)
1349/ 1346/ 1344	1337	6.7	νCC ph
1340	1334	16.7	νCC ph (**Ia**)
1320/ 1314	1305	32.4	νCC ph
1303	1300	48.8	δCH ph, $\nu C_9–N_8$ (**Ia**)
1297/ 1296/ 1295/ 1293	1295	182.9	δN–H
1291	1288	148.0	δN–H (**Ia**)
1277/ 1276	1268	14.0	$\nu N_{19}–N_{20}$
1265	1260	12.0	$\nu N_{19}–N_{20}$, γCH_3' (**Ia**)
1262/ 1258	1252	58.5	δCH ph, $\nu C_9–N_8$ (**Ia**)
1254	1251	65.3	δCH ph
1204	1230	30.0	νN=N (**Ia**)
1199/ 1197	1211	18.6	νN=N, δ t
1191/ 1190	1172	94.7	νSO_2 s
1188	1171	73.3	νSO_2 s, δCH ph (**Ia**)
1168/ 1165/ 1162	1158	95.6	δ(CH ph
1145	1140	54.4	$\nu C_9–N_8$, δCH ph
n.o.	1126	0.0	γCH_3''
1129/ 1125	1120	18.0	νCC ph
1089	1084	19.0	νN=C, δ t, $\nu N_{20}–N_{21}$
1064	1046	4.4	δ ph
1044	1046	5.0	δ ph (**Ia**)
1041/ 1039	1029	3.3	γCH_3'
1038/ 1035	1018	2.6	νCC ph
1019/ 1018	1011	20.1	$\nu C_{17}–N_{18}$, $\nu N_{19}–N_{20}$
1017/ 1016	1008	35.2	$\nu N_{19}–N_{20}$, γCH_3' (**Ia**)
n.o.	999	0.0	γCH ph
956	967	0.6	γCH ph, γCH ph
n.o.	885	0.3	γCH ph, γCH ph
891	871	80.1	νN–S, $\nu C_9–N_8$ (**Ia**)
890	871	66.3	νN–S, $\nu C_9–N_8$
n.o.	815	1.0	δ t
n.o.	777	0.3	τ t, γC=N
786/ 785	773	38.7	γ(CH ring 3) (**Ia**)
783/ 781	773	40.6	τ t, γCH ph
772/ 771/ 770	767	70.6	δ ph, νN–S
749/ 748/ 746	742	14.1	τCC ph, γCH ph

Table 3.12 (Continued) [a]

Infrared	Calculated B3LYP/6-311++G(3df,3pd)		
ν	ν	I_{IR}	Approximate description [b]
720/ 719	709	3.8	νN–C(H_3), δ ph
711	698	10.7	δ ph, νS–C (**Ia**)
702	694	8.4	δ ph
682	684	3.4	τ t
678	679	4.2	τ t (**Ia**)
664	660	12.9	γC=N
636	626	65.5	νN–S (**Ia**)
632/ 630/ 629/ 628	620	93.4	νN–S, δ ph
581	570	24.7	δSO_2
546/ 545	539	44.6	γN–H
536	537	15.5	wSO_2
530	528	11.9	γSO_2, τCC ph
525/ 524	517	53.2	wSO_2
480	477	16.2	γN–H (**Ia**)
464	460	10.4	τ CC ph
456	451	40.8	γN–H, τ CC ph, τC=N (**Ia**)

[a] Wavenumbers in cm^{-1}; calculated infrared intensities in km mol^{-1}; calculated wavenumbers were scaled by 0.978, except in the N-H stretching region where the scale factor used was 0.938. Whenever the bands due to both **Ia** and **Ib** are superimposed, in the Table they are ascribed to form **Ib**. The spectrum was not investigated below 450 cm^{-1}. [b] ν, bond stretching; δ, bending; γ, rocking; τ, torsion; w, wagging; tw, twisting; as, anti-symmetric; s, symmetric; ph, phenyl ring; t, tetrazole ring. See Figure 3.22 for atom numbering.

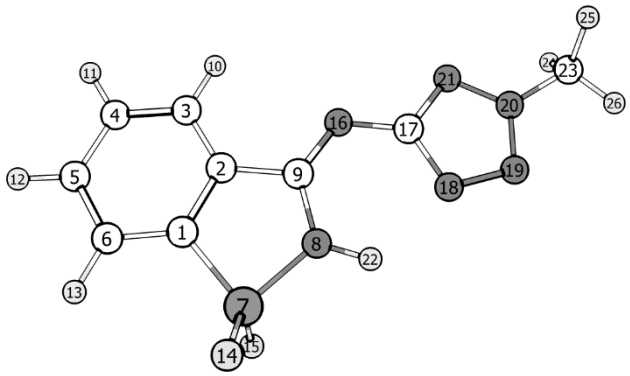

Figure 3.22 - Optimized structure of the theoretically predicted form **Ib** of **2MTS**. The atom numbering adopted is shown.

To establish a mechanism for the observed tautomerization is a difficult task, in particular because one can expect that it takes place (at least partially) in the condensed phase or at the solid-gas interface. In any case, for the specific system under study it was possible to obtain enough structural and energetic information that can be used to propose a possible route for the observed conversion of **IIa** into **Ia** and **Ib**.

The first point to notice is that no evidence of the presence in the gas phase of tautomer **II** (either of its conformer **IIa** or any other conformer of this tautomeric form, *i.e.*, **IIb**, **IIc**, **IId**) was obtained. This fact suggests that tautomer **II** is not released from the crystal into the gas phase, at least as a monomer. The second point to note is that the location of the labile hydrogen atom in the form existing in the crystal of **2MTS** (**IIa**) is not appropriate for its direct migration

to the saccharyl nitrogen atom, where it is attached in tautomer **I**. For a direct migration of the hydrogen, one has to assume that **IIa** should first convert into **IIc** by internal rotation around the bridge C(saccharyl)-N bond. The calculated barrier for such rotamerization amounts to 49.3 kJ mol^{-1} (B3LYP/6-31++G(d,p) results), which is low enough to be overcome in the gas phase at the temperature used to sublimate the compound in the present experiments. However, starting from **IIc** (or from **IId**, assuming the conversion of **IIc** into **IId**, whose associated calculated barrier is only 7.0 kJ mol^{-1}), the resulting tautomer **I** formed after the required migration of the hydrogen atom from the bridging group to the saccharyl nitrogen atom would be **Ic** (or **Id**). The calculated H-transfer barrier (converting **IIc** into **Ic**) amounts to 186 kJ mol^{-1}. In addition, conversion of **Ic** (or **Id**), with an *E* configuration about the C=N bridge moiety, into the observed **Ia** (or **Ib**) forms, with the *Z* configuration, is a highly improbable thermal process, with a high energy barrier (over 250 kJ mol^{-1}).[22,23] Under these conditions, an alternative route resulting in the observed tautomeric conversion must exist.

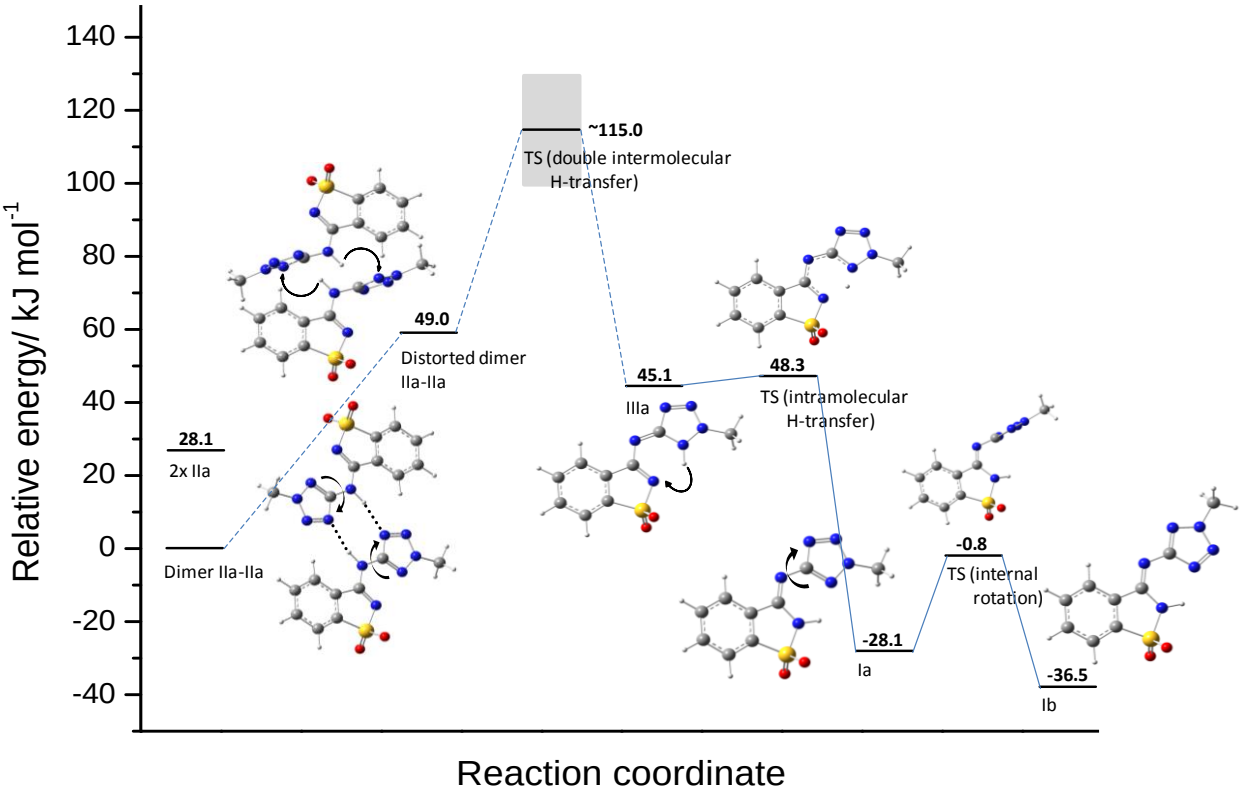

Figure 3.23 - Proposed mechanism for conversion of tautomer **IIa**, existing in crystalline **2MTS**, into the experimentally observed forms **Ia** and **Ib**, existing in the gas phase. A barrier for double proton transfer in the range 50-80 kJ mol^{-1} is assumed in the scheme (see text).

In the mechanism here proposed, schematically depicted in Figure 3.23, the fact that the main constituting unit of the **2MTS** crystal is a **IIa** dimer is of fundamental importance. As

shown in Figure 3.11, in this dimer the molecules are linked through intermolecular hydrogen bonds involving the amine N-H spacer group of each monomeric unit as proton donor and the nitrogen at position 4 of the tetrazole ring of the second molecule as acceptor. Besides, the saccharyl and tetrazole rings are not coplanar, but distorted through internal rotation around the most flexible N-C(tetrazole) bond of the bridge by about 15º. We calculated the rise of energy in the dimer upon further increase of the angle of internal rotation about the flexible N-$C_{(tetrazole)}$ bond until a nearly perpendicular orientation of the two rings. The obtained value, 49 kJ mol^{-1}, is well within the range of energies surpassable during sublimation.[24] At this geometry, a double proton-transfer can take place within the dimeric unit, from the amino spacer-group of each molecule to the tetrazole nitrogen atom in position 1 of the second molecule, instead of to that in position 4. The transfer to the nitrogen in position 4 would in fact be the result of the direct intra-dimer double proton-transfer for the dimeric structure existing in the crystal (see Figure 3.11). However, the species resulting from that process would be the high-energy tautomer **V** (see Table 3.10), and such process is certainly not energetically accessible. On the other hand, the tautomer produced upon proton transfer to the nitrogen in position 1 of the tetrazole is form **IIIa**, which has a much lower energy. Assuming that the double proton-transfer process has an energy barrier between 50 and 80 kJ mol^{-1}, as found for other nitrogen containing heterocyclic dimers,[25–27] one can roughly estimate the energetic demand for production of a **IIIa** unit of **2MTS** in the gas phase from a **IIa** unit in the crystal as being within 100-130 kJ mol^{-1} (see Figure 3.23). This appears as a meaningful accessible energy value for the considered process.[28,29] Once produced, **IIIa** can then be promptly converted into **Ia** by intramolecular H-transfer in the gas phase. The calculated potential energy profile for this reaction is shown in Figure 3.24, and shows a **IIIa→Ia** barrier of only 3.2 kJ mol^{-1}. Finally, once **Ia** is obtained, equilibrium between **Ia** and **Ib** can be established, as discussed above, leading to the sole observation of these two forms.

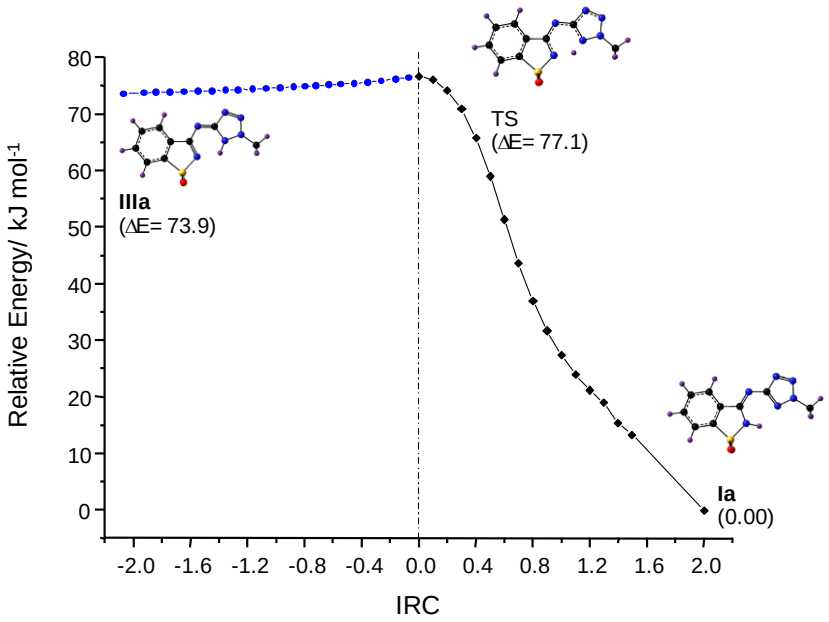

Figure 3.24 - Potential energy profile for the intramolecular proton transfer converting **2MTS** form **IIIa** into form **Ia**, obtained in the performed B3LYP/6-31++G(d,p) IRC calculations.

It is important to note that the low barrier associated with the considerably exothermic **IIIa→Ia** conversion implies that this step is a fast process obeying the Hammond-Leffler postulate,[30,31] *i.e.*, the associated transition state corresponds to an early transition state structurally resembling more the higher-energy reactant (**IIIa**) than the product (**Ia**).

It shall also be pointed out that the involvement of dimeric units in tautomerization processes associated with sublimation has received both experimental and computational support in the last years, including for tetrazole-based compounds.[16,29,32] Furthermore, it has also been suggested that double H-transfer type processes in hydrogen bonded complexes, like the one herein proposed to take place during sublimation of **2MTS**, shall play an especially important role in the aggregated phase.[29] This is also in agreement with the absence of tautomer **II** of **2MTS** in the gas phase, as doubtlessly shown in the present matrix-isolation experiments.

3.5.2. Conclusions

2MTS was found to undergo complete amino→imino tautomerization upon sublimation, where the amino-bridged tautomeric form **IIa** existing in the crystalline phase of the compound is converted into a mixture of two conformers of the theoretically predicted most stable imino-bridged tautomer (**Ia**, **Ib**). In this tautomer, the labile hydrogen atom is connected to the saccharyl nitrogen, and the two heterocyclic fragments are linked by an imino moiety in which the double-bond is established with the carbon atom belonging to the saccharyl fragment. The

observed isomeric forms of this tautomer are characterized by a *zusammen* (*Z*) arrangement of the two rings around the C=N bond of the bridging group and an intramolecular NH···N hydrogen bond. A simplified mechanism for the observed tautomeric conversion was proposed, which implies a partial internal rotation about the flexible bridging $N-C_{(tetrazole)}$ bond of the two molecules in the dimer, followed by a concerted double H-transfer in the deformed dimeric structure, leading to the formation of two units of tautomer **IIIa**, in a process whose energetic demand for production of a **IIIa** unit of **2MTS** in the gas phase from a **IIa** unit in the crystal could be roughly estimated to be within 100-130 kJ mol^{-1}. The produced tautomer **IIIa** can then promptly convert into tautomeric form **Ia** in the gas phase in a low-barrier (3.2 kJ mol^{-1}) intramolecular H-transfer. Once **Ia** is obtained from **IIIa**, an equilibrium between **Ia** and **Ib** can be established by internal rotation about the $N\text{-}C_{(tetrazole)}$ bond in a process with an estimated energy barrier of ∼28 kJ mol^{-1} (in the **Ia**→**Ib** direction). The proposed mechanism assumes involvement of the dimer of the compound in the tautomerization accompanying the sublimation and is consistent with recent experimental and computational evidence for similar processes in other compounds, including other tetrazole-based substances.[16,29,32] Finally, the experimental IR spectrum of the matrix-isolated **2MTS** has been fully assigned based on the B3LYP/6-311++G(3df,3pd) calculated spectra for the relevant forms of the compound (**Ia**, **Ib**).

3.6. Molecular structure of 5-thiosaccharyl-1-methyltetrazole (TSMT)

In the previous sections, the investigation of nitrogen-linked tetrazole-saccharinates proved to be especially challenging because of the possibility of tautomerism involving the saccharyl system. For these compounds, two forms are possible: the iminosaccharin and aminosaccharin tautomers. If, additionally, the tetrazole ring is unsubstituted, as is the case for the parent compound **TS**, then four tautomers become possible, two belonging to the iminosaccharin group and the other two to the aminosaccharin group. We found that the amino-linked conjugates may exhibit different structures in the crystalline and gaseous phases. On the contrary, for a thio-linked saccharyl tetrazole the structure simplifies, because of the absence of tautomerism involving the saccharyl system. In addition, the possibility of tautomerism involving the tetrazole ring may be quenched through the introduction of a suitable substituent, further restricting complexity. Here we describe the structure of 3-((1-methyl-1*H*-tetrazol-5-yl)thio)-1,2-benzisothiazole 1,1-dioxide (5-thiosaccharyl-1-methyltetrazole, **TSMT**) (Figure 3.25) in the crystalline state and in solid argon.

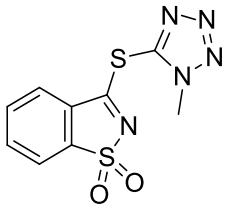

Figure 3.25 – Representation of the structure of 5-thiosaccharyl-1-methyltetrazole (**TSMT**)

3.6.1. Results and discussion

3.6.1.1. Geometries and energies of TSMT

TSMT has two intramolecular rotational degrees of freedom, represented by arrows in Figure 3.26, which may result in different conformers. These are related to the orientations of the saccharyl and tetrazolyl rings relative to the C-S-C plane (dihedral angles A and B, respectively).

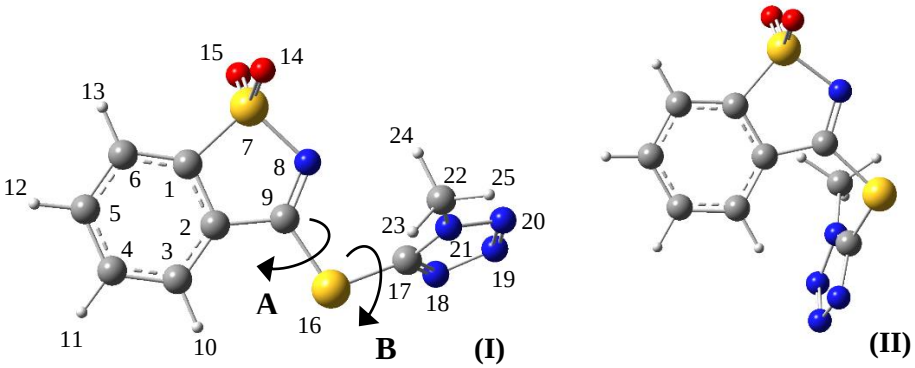

Figure 3.26 - Optimized structures of the conformers of 5-thiosaccharyl-1-methyltetrazole (**TSMT**) investigated. The atom numbering adopted is shown. Arrows A and B relate to conformationally relevant degrees of freedom.

To identify the minimum-energy conformations of **TSMT**, a systematic investigation of the potential energy surface (PES) of the molecule was undertaken using the B3LYP/6-31++G(d,p) method. The locations of the minima on the bidimensional PES map obtained by performing relaxed scans on the PES are shown in Figure 3.27. In building this map, dihedral angles A (N_8-C_9-S_{16}-C_{17}) and B (C_9-S_{16}-C_{17}-N_{18}) were varied in increments of 30°, while all of the other geometric parameters were let free during the geometry optimization. According to the calculations, **TSMT** may exist in two different conformers (**I** and **II**; Figure 3.26). The full geometry optimization of the two conformers was carried out at the O3LYP/6-311++G(3df,dpd) level of theory. The O3LYP hybrid functional was selected for these calculations because it has been shown to constitute an improvement over the B3LYP one,[33] particularly in the prediction of geometries and infrared spectra of derivatives of saccharin.[34]

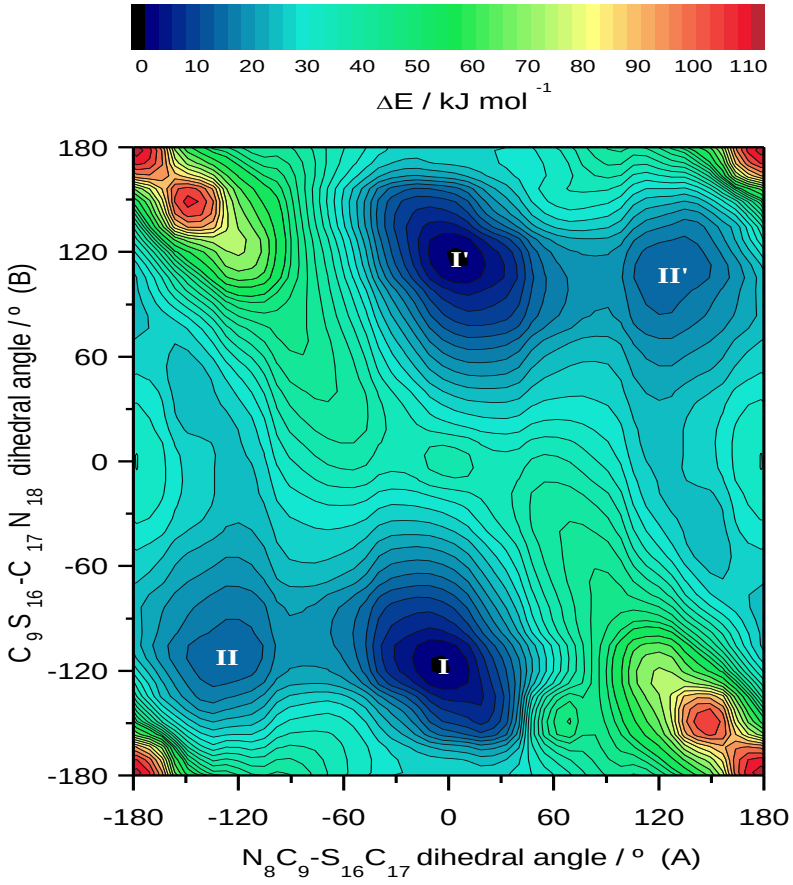

Figure 3.27 - Potential energy surface map of **TSMT** calculated at the B3LYP/6-31++G(d,p) level of theory, as function of the dihedral angles $C_9S_{16}C_{17}N_{18}$ and $N_8C_9S_{16}C_{17}$. These two dihedral angles were incrementally fixed with a step of 30 degrees while the remaining parameters were let free during geometry optimization. The position of both conformers are shown in the graph by their numbers, **I** and **II**. Each of these minima belongs to the C_1 symmetry point group and has a symmetry equivalent counterpart, also represented in the graph with quotes, **I'** and **II'**. The electronic energy of form **I** is chosen as relative zero. See Figure 3.26 for structures and atom numbering.

In the more stable conformer, **I**, the tetrazole ring is considerably rotated in relation to the C-S-C plane (*i.e.*, B = ±115° in the two symmetry-equivalent minima corresponding to this conformer; see Figure 3.27), while the dihedral angle A is close to 0° (*i.e.*, the plane of the saccharyl moiety is nearly aligned with the C-S-C plane, with the C=N bond eclipsing the S_{16}–C_{17} bond). It should be noted that the structures with Cs symmetry, in which the tetrazolyl and saccharyl groups are coplanar (A = 0°, B= 0° and A = 0°, B = 180°), are destabilized by steric repulsions between the closely located N_{18} and N_8 lone-electron pairs and the CH_3 group and N_8 lone pair, respectively. In conformer **I**, a stabilizing interaction occurs between the nitrogen atom of the saccharyl moiety and the hydrogen of the methyl group because in the minimum-energy geometry the distance between these atoms and their relative orientation fits

well the requirements for an attractive interaction (weak C-H···N hydrogen-bond-like interaction). In addition, electronic delocalization involving the lone pairs of electrons on the sulfur atom and the π systems of the rings also contribute to determine this conformational preference.

The energy of conformer **II** was predicted to be 15 kJ mol^{-1} higher than that of conformer **I**. Conformer **II** differs from conformer **I** by internal rotation about the C_9-S_{16} bond (*i.e.*, A = ±137°). In this conformer, a weak stabilizing intramolecular interaction of the C-H···N type is present between nitrogen atom N_{18} of the tetrazole ring and hydrogen atom H_{13} of the phenyl ring (see Figure 3.26). The calculated barrier for isomerization of the higher-energy conformer **II** into the more stable conformer **I** is 6.1 kJ mol^{-1} (19.4 kJ mol^{-1} in the reverse direction; for coordinates of the transition-state structure). According to the calculated energy difference between **II** and **I**, the population of conformer **II** in the gas phase at room temperature (25 °C) is only 0.2%; at the temperature used to prepare the matrices of the compound in the present investigation (100 °C), it is still below 1%. One can then anticipate that only conformer **I** might be trapped from the gas phase into the deposited cryogenic matrices.

3.6.1.2. Crystal structure of TSMT and IR spectrum of the crystal

The structure of crystalline **TSMT**, determined by X-ray analysis, is provided in Figure 3.28 (structure of the monomeric unit in the crystal) and Figure 3.29 (packing diagram). Atomic coordinates, bond lengths, valence angles, dihedral angles, and other crystallographic data were deposited at the Cambridge Crystallographic Data Centre with the reference CCDC 1025233.

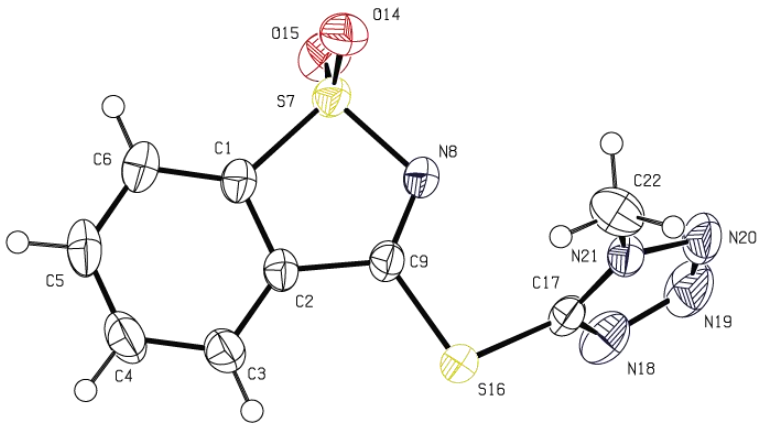

Figure 3.28 - ORTEPII plot of the **TSMT** molecule in the crystal of the compound (from single crystal XRD data). Displacement ellipsoids are drawn at the 50% probability level.

In the crystal, **TSMT** exists in the more stable conformation predicted for the isolated molecule (compare Figure 3.26 and Figure 3.28). Each molecule is involved in four weak hydrogen bonds with three neighbouring molecules. The methyl substituent on the tetrazolyl ring establishes two intermolecular hydrogen bonds with two neighbouring molecules, one with a nitrogen atom at position 4 of the tetrazole ring (N_{18}) in the first molecule and another with an oxygen atom of the SO_2 group of the saccharyl system (O_{14}) in the second molecule as acceptors. This same molecule establishes a third intermolecular hydrogen bond through O_{14} of the SO_2 group with the methyl substituent of the previous "second" neighbour and a fourth hydrogen bond with a third neighbour molecule in which N_{18} acts as the acceptor. In addition to these four intermolecular hydrogen bonds, a weak intramolecular interaction can also be considered between the third H atom of the methyl group and the S atom.

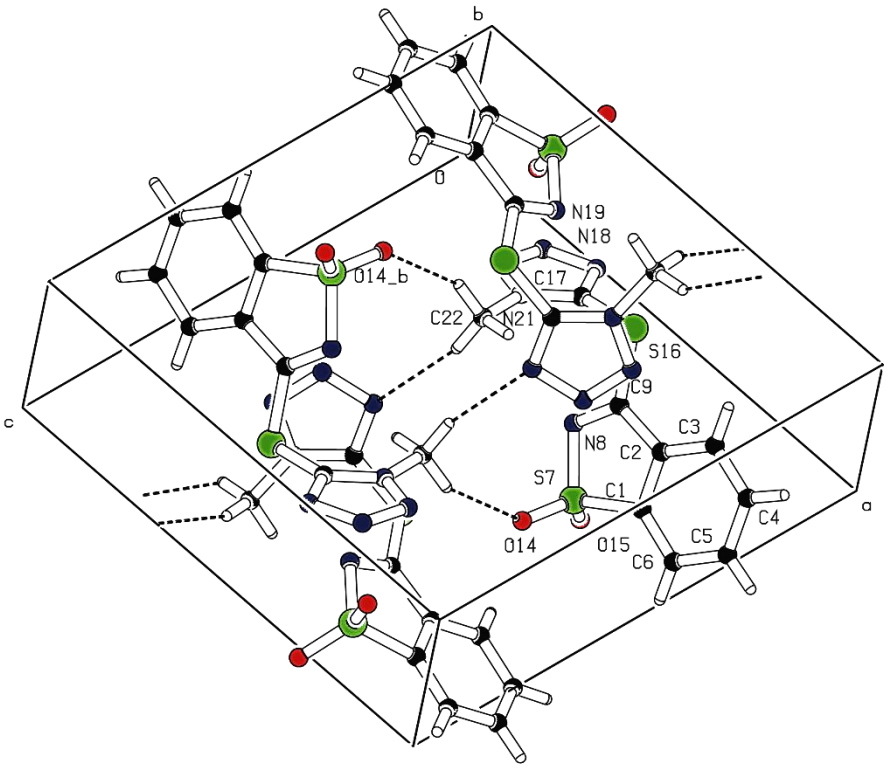

Figure 3.29 - Hydrogen-bonding network in the crystal of **TSMT**.

The hydrogen-bonding scheme is shown in Figure 3.29, and the symmetry-unique short contacts are $C_{22}H_{24}\cdots N_{18}^{a}$ (3.486(2) Å), $C_{22}H_{25}\cdots O_{14}^{b}$ (3.345(2) Å), and $C_{22}H_{23}\cdots S_{16}$ (3.323(2) Å), where the superscripts "a" and "b" designate atoms belonging to neighbouring molecules. This hydrogen-bonding pattern leads to the formation of **TSMT** oligomers. The oligomeric structure is formed from dimers of **TSMT**. In each dimer, the two molecules of **TSMT** are disposed in a head-to-tail arrangement, with the tetrazole moiety of one molecule

overlapping the thioimino moiety of the other at the inner part of the dimer while the carbocyclic aromatic rings are directed to the extremities. The oligomeric structure results from an intricate network of weak hydrogen bonds formed between consecutive dimers (with involvement of both molecules of the dimer) and adjacent dimers. Weak π-π interactions between tetrazole rings and thioimino moieties as well as S-O···π interactions (short contacts of 4.65 and 3.01 Å, respectively) may also play a role in the stabilization of the observed supramolecular structure.

A comparison between the geometrical parameters of **TSMT** monomer **I**, calculated at the O3LYP/6-311++G(3df,3pd) level of theory, and those determined for the compound in the crystal (Table S8 in Appendix) reveals an excellent correlation between the two sets of data, although in the crystal the dihedral angles A and B (see Figure 3.26) appear slightly rotated (*i.e.*, A = -10.5° and B = -108.8°) relative to those theoretically obtained for the isolated molecule (A = -3.3° and B = -115.3°), as a result of the intermolecular interactions.

The infrared spectrum of neat crystalline **TSMT** at room temperature is provided in Figure 3.30. The calculated spectrum of conformer **I** is also shown in this figure for comparison. Proposed assignments of the spectra are given in Table 3.13. The good general description of the experimental spectrum of the crystal by the calculated spectrum of the isolated monomer is an indication that the intermolecular interactions present in the solid do not substantially perturb the intramolecular potential.

Table 3.13 - Proposed band assignments for the infrared spectrum of crystalline and matrix isolated **TSMT**.[a, b]

Observed Crystalline	Observed Matrix isolated	Calculated (**I**)		Approximate description
ν	ν	ν	I_{IR}	
3091	3083	3182	4.9	νCH Ph
3079	3021	3176	1.8	
3060	2994	3165	4.3	
3027	2962	3154	0.5	
2961	2941	3150	1.0	νCH_3 as
	2871	3127	1.5	νCH_3 as
	2859	3045	8.4	νCH_3 s
1601	1607	1620	20.0	νCC Ph
1575	1589	1607	1.1	νCC Ph
1571	1541/1539/1538	1557	121.4	νC=N (saccharinate)
1484	1474	1488	21.3	δCH_3 as
n.o.	n.o.	1467	0.5	δCH Ph
1455	1455.1454	1464	10.9	δCH_3 as
1416	1445. 1444	1457	3.8	δCH Ph
1398	1441	1453	22.5	δCH_3 as
n.o.	n.o.	1412	0.4	δCH_3 s
1385	1397	1411	20.0	δCH_3 s, νNN t
1343	1380/1378/1375	1376	179.1	νSO_2 as
	1354	1365	5.3	νCC Ph
	1327	1297	3.0	$\nu N_{19}N_{20}$, γCH_3
	n.o.	1281	0.0	δCH Ph
1229	1240/1237/1235	1229	78.5	νC_2C_9, γCH_3
1207	1226	1225	78.2	νC_2C_9, γCH_3, νNN t
1175	1194/1190/1187	1189	254.6	νSO_2 s
	1175	1178	73.4	νNN t
	1164	1172	9.9	δCH Ph
1130	1135	1139	16.5	δCH Ph
	1132	1134	3.5	γCH_3
n.o.	n.o.	1107	1.1	$\nu N_{18}N_{19}$, γCH_3
1086	1082	1055	10.1	νCC Ph
1015	1017	1036	5.6	νNN t, γCH_3
n.o.	n.o.	1033	0.8	νCC Ph
n.o.	n.o.	996	0.1	γCH Ph
n.o.	n.o.	996	1.5	νNN t, γCH_3
983	990	972	127.4	νC_9S,
954	987	960	0.4	tw CH Ph
	n.o.	879	0.0	γCH Ph
766	767	770	47.3	γCH Ph
	766	769	67.3	γCH Ph, νS_7N_8
756	758.757.755	750	28.5	δCC Ph
733	740	733	6.7	γCH Ph
724	721	729	3.0	twNN t
698	701	707	4.9	$wN(CH_3)$
	697	695	14.2	δ skeletal
	686	689	3.0	δ skeletal
622	622	622	10.0	τ skeletal
584	587	581	36.2	δ skeletal
567	569	562	44.2	δSO_2 s
531	535	529	13.6	τ skeletal
	529	523	12.5	wSO_2
502		503	5.9	δ skeletal
431		429	5.7	δ skeletal
414		422	2.5	γCH Ph
		407	2.2	τ skeletal
		399	7.7	τ skeletal
		365	2.8	δSO_2 s
		290	0.2	tw SO_2
		286	3.1	wSO_2
		253	2.9	wSO_2, $wN(CH_3)$
		226	3.2	δCH3
		203	0.1	δ skeletal
		145	1.0	δ skeletal
		139	0.4	τ skeletal

Table 3.13 (Continued)[a, b]

Observed Crystalline	Observed Matrix isolated	Calculated (**I**)		Approximate description
ν	ν	ν	I_{IR}	
		112	0.6	τSO_2
		100	0.7	τ skeletal
		82	0.0	τ CH_3
		58	2.2	δ skeletal
		41	6.2	τ (tetrazole)
		32	1.4	τ skeletal

[a] Wavenumbers (ν, cm^{-1}) were scaled by 0.992; calculated infrared intensities (*I*) in km mol^{-1}.
[b] ν, stretching; δ, bending; γ, rocking; w, wagging; tw, twisting; τ, torsion; s, symmetric; as, anti-symmetric; n.o., not observed.

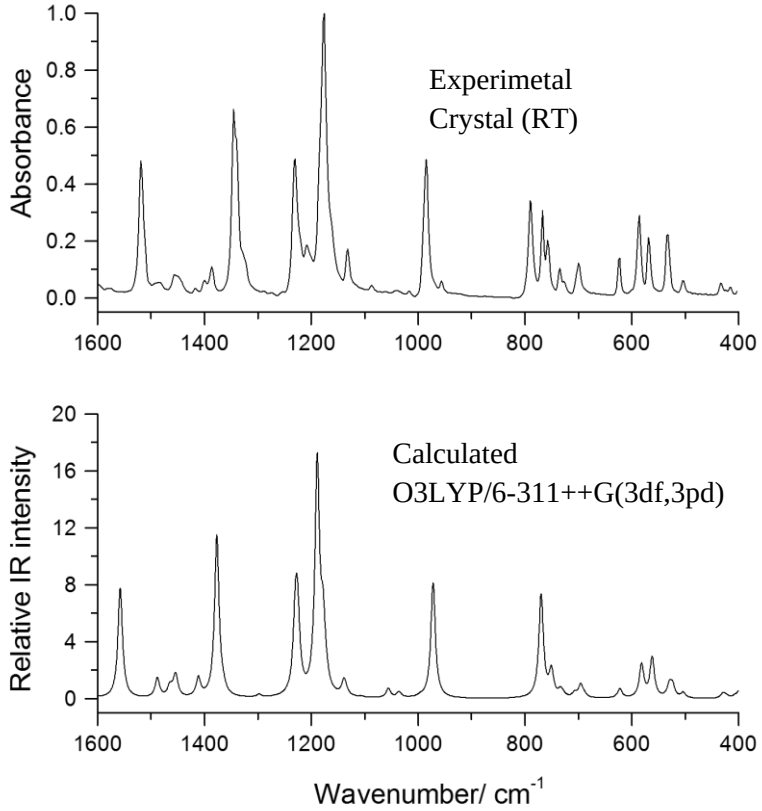

Figure 3.30 - Room temperature IR spectrum of crystalline **TSMT** and O3LYP/6-311++G(3df,3pd) calculated infrared spectrum for the most stable conformer. The calculated spectra were simulated by Lorentzian functions centred at the calculated frequency scaled by 0.992 and with FWHM (full width at half maximum) equal to 10 cm^{-1}. Please note also that the peak intensities in the calculated spectrum differ from the calculated intensity values; in the figure the calculated intensities correspond to the areas of the peaks.

3.6.1.3. Infrared spectra of matrix-isolated TSMT

As described in the chapter 2 (section 2.3), a sample of crystalline **TSMT** was sublimed *in vacuo* (at ~100 °C), the vapours of the compound were mixed with argon (*ca.* 1:1000 molar ratio) and the mixture was deposited onto a substrate kept at 15 K. Figure 3.31 shows the infrared spectrum of **TSMT** isolated in an argon matrix prepared in this way. The detailed analysis of the spectrum of matrix-isolated **TSMT** doubtlessly shows that only conformer **I** is present in the matrix, as anticipated taking into account the predicted relative energies of the two conformers and their estimated populations in the gas-phase equilibrium before deposition. This is particularly noticeable in the low-frequency region where, according to the calculations, the spectra of the two conformers are clearly differentiable (Figure 3.32). Proposed assignments of the spectra are given in Table 3.13.

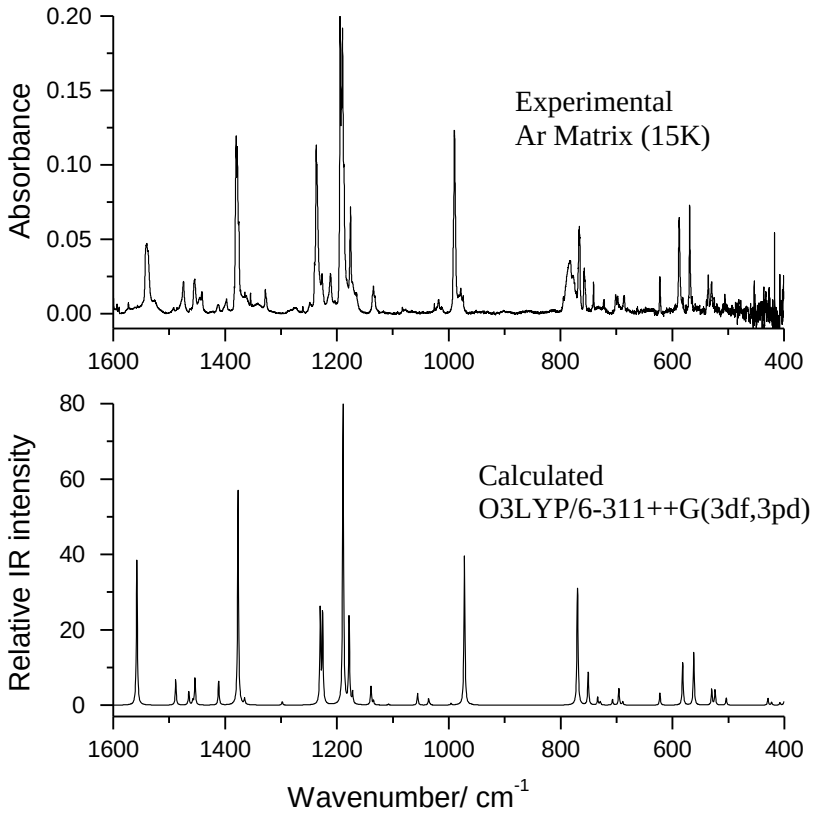

Figure 3.31 - Infrared spectrum of matrix isolated **TSMT** (Ar matrix; 15 K) and O3LYP/6-311++G(3df,3pd) calculated infrared spectrum for the most stable conformer. The calculated spectra were simulated by Lorentzian functions centred at the calculated frequency, scaled by 0.992 and with FWHM (full width at half maximum) equal to 2 cm^{-1}. Please note also that the peak intensities in the calculated spectrum differ from the calculated intensity values; in the figure the calculated intensities correspond to the areas of the peaks.

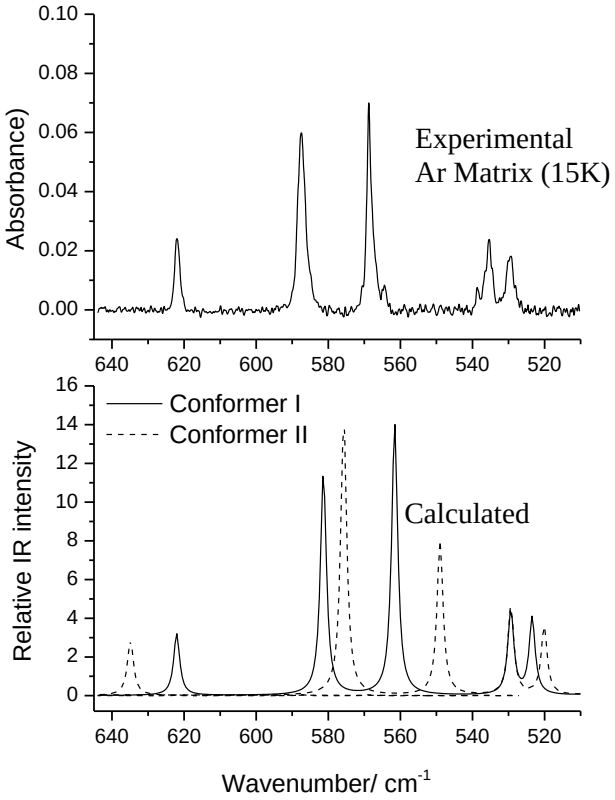

Figure 3.32 - Low-frequency region of the infrared spectrum of matrix isolated **TSMT** (Ar matrix; 15 K) and O3LYP/6-311++G(3df,3pd) calculated infrared spectra for the two conformers of the compound in the same spectral range. The calculated spectra were simulated by Lorentzian functions centred at the calculated frequency scaled by 0.992 and with FWHM (full width at half maximum) equal to 2 cm^{-1}. Please note also that the peak intensities in the calculated spectrum differ from the calculated intensity values; in the figure, the calculated intensities correspond to the areas of the peaks.

3.6.2. Conclusions

A combined matrix-isolation FTIR and theoretical study of the molecular structure and photochemistry of 5-thiosaccharyl-1-methyltetrazole was performed. The conformational preferences of **TSMT** in both the matrix-isolated situation and the crystalline phase were also investigated.

According to the performed DFT calculations, **TSMT** has two conformers, **I** and **II**. However, the higher-energy form, **II**, has a relative energy of *ca.* 15 kJ mol^{-1}, and only conformer **I** is significantly populated in the gas phase. As could be expected, this conformer was found to be the only one detectable in the cryomatrices (15 K) prepared from the vapour of the compound at 100 °C. The infrared spectrum of matrix-isolated **TSMT** was fully assigned on the basis of the O3LYP/6-311++G(3df,3pd) spectra calculated for conformer **I**.

In the crystal, **TSMT** was also found to exist in form **I**. In the crystalline phase, each molecule of **TSMT** forms four hydrogen bonds with three neighbouring molecules, and a network of **TSMT** dimers is clearly observed. In the dimers, the two molecules of **TSMT** are disposed in a head-to-tail arrangement, with the tetrazole moiety of one molecule overlapping the thioimino moiety of the other (and vice versa) at the inner part of the dimer while the aromatic rings are directed to the extremities. The formation of dimers is possibly due to π-π interactions between complementary tetrazole ring and thioimino moieties. The oligomeric structure results from an intricate network of weak hydrogen bonds formed between consecutive dimers (with involvement of both molecules of the dimer) and adjacent dimers.

3.7. References

(1) Lehn, J.-M. *Supramolecular Chemistry*; Verlag Wiley-VCH, Weinheim: Germany, 1995.
(2) Kahn, O. E. *Magnetism: A Supramolecular Function*; Kluwer Academic Publishers: Dordrecht, The Netherlands, 1996.
(3) Zhao, H.; Qu, Z.-R. R.; Ye, H.-Y. Y.; Xiong, R.-G. G. *Chem. Soc. Rev.* **2008**, *37* (1), 84–100.
(4) Baran, E. J.; Yilmaz, V. T. *Coord. Chem. Rev.* **2006**, *250* (15–16), 1980–1999.
(5) Abu-Youssef, M. A. M.; Mautner, F. A.; Massoud, A. A.; Öhrström, L. *Polyhedron* **2007**, *26* (7), 1531–1540.
(6) Gupta, A. K.; Song, C. H.; Oh, C. H. *Tetrahedron Lett.* **2004**, *45* (21), 4113–4116.
(7) Gupta, A. K.; Rim, C. Y.; Oh, C. H. *Synlett* **2004**, No. 12, 2227–2229.
(8) Kim, Y. J.; Han, J. T.; Han, W. S.; Lee, S. W. *J. Chem. Soc. Trans.* **2002**, No. 18, 3611–3618.
(9) Xiong, R.-G.; Xue, X.; Zhao, H.; You, X.-Z.; Abrahams, B. F.; Xue, Z. *Angew. Chem. Int. Ed. Engl.* **2002**, *41* (20), 3800–3803.
(10) Naumov, P.; Jovanovski, G. *Struct. Chem.* **2000**, *11* (1), 19–33.
(11) Jovanovski, G.; Hergold-Brundić, A.; Grupče, O.; Matković-Čalogović, D. *J. Chem. Crystallogr.* **1999**, *29* (2), 233–237.
(12) Cotton, F. A.; Falvello, L. R.; Schwotzer, W.; Murillo, C. A.; Valle-Bourrouet, G. *Inorganica Chim. Acta* **1991**, *190* (1), 89–95.
(13) Jovanovski, G.; Šoptrajanov, B. *J. Mol. Struct.* **1988**, *174*, 467–472.
(14) Balabin, R. M. *J. Chem. Phys.* **2009**, *131* (15), 154307.
(15) Yang, Z.; Rodgers, M. T. *Phys. Chem. Chem. Phys.* **2004**, *6* (10), 2749.
(16) Ismael, A.; Cristiano, M. L. S.; Fausto, R.; Gómez-Zavaglia, A. *J. Phys. Chem. A* **2010**, *114* (50), 13076–13085.
(17) Barker, D. L.; Marsh, R. E. *Acta Crystallogr.* **1964**, *17* (12), 1581–1587.
(18) Lapinski, L.; Reva, I.; Nowak, M. J.; Fausto, R. *Phys. Chem. Chem. Phys.* **2011**, *13* (20), 9676.
(19) Zeng, A.; Yu, L.; Wang, Y.; Kong, Q.; Xu, Q.; Mingfei, Z. **2004**.
(20) Borba, A.; Gómez-Zavaglia, A.; Simões, P. N. N. L.; Fausto, R. *Spectrochim. Acta Part A Mol. Biomol. Spectrosc.* **2005**, *61* (7), 1461–1470.
(21) Borba, A.; Gómez-Zavaglia, A.; Simões, P. N. N. L.; Fausto, R. *J. Phys. Chem. A* **2005**, *109* (16), 3578–3586.
(22) Chattopadhyay, N.; Reva, I.; Lapinski, L.; Fausto, R.; Arnaut, L. G.; Formosinho, S. J. *J.*

Phys. Chem. A **2002**, *106* (15), 3722–3726.
(23) Wang, Y.; Poirier, R. A. *J. Comput. Chem.* **1996**, *17* (3), 313–325.
(24) Jeevan, T. S. A.; Nagaraja, K. S. *J. Chem.* **2013**, *2013*, 1–5.
(25) Lin, Y.; Wang, H.; Gao, S.; Li, R.; Schaefer, H. F. *J. Phys. Chem. B* **2012**, *116* (30), 8908–8915.
(26) Hargis, J. C.; Vöhringer-Martinez, E.; Woodcock, H. L.; Toro-Labbé, A.; Schaefer, H. F. *J. Phys. Chem. A* **2011**, *115* (12), 2650–2657.
(27) Lopez, J. M.; Männle, F.; Wawer, I.; Buntkowsky, G.; Limbach, H.-H. *Phys. Chem. Chem. Phys.* **2007**, *9* (32), 4498.
(28) Long, G. T.; Brems, B. A.; Wight, C. A. *J. Phys. Chem. B* **2002**, *106* (15), 4022–4026.
(29) Kiselev, V. G.; Cheblakov, P. B.; Gritsan, N. P. *J. Phys. Chem. A* **2011**, *115* (9), 1743–1753.
(30) Hammond, G. S. *J. Am. Chem. Soc.* **1955**, *77* (2), 334–338.
(31) Leffler, J. E. *Science (80-.).* **1953**, *117* (3039).
(32) Pagacz-Kostrzewa, M.; Reva, I. D.; Bronisz, R.; Giuliano, B. M.; Fausto, R.; Wierzejewska, M. *J. Phys. Chem. A* **2011**, *115* (22), 5693–5707.
(33) Belaidi, O.; Bouchaour, T.; Maschke, U. *J. Struct.* **2013**, *2013*, 1–9.
(34) Duarte, L.; Reva, I.; Cristiano, M. de L. S.; Fausto, R. *J. Org. Chem.* **2013**, *78* (7), 3271–3275.

Chapter 4. Photochemistry of selected tetrazole-saccharinates and tetrazole precursors

Part of the work described in this chapter was included in the following publications:

Ismael, A.; Borba, A.; Henriques, M. S. C.; Paixão, J. A.; Fausto, R.; Cristiano, M. L. S.; "Structure and Photochemistry of a Saccharyl Thiotetrazole." *J. Org. Chem*. 2015; 80 (1); 392-400.

Ismael, A.; Fausto, R.; Cristiano, M. L. S.; "Photochemistry of 1- and 2-Methyl-5-aminotetrazoles: Structural Effects on Reaction Pathways."; *J. Org. Chem.* 2016, *81* (23), 11656–11663.

As such, contents of these publications are partly reproduced below.

4.1. Summary

In this chapter we report the UV-induced photochemistry of two tetrazole-saccharyl conjugates, **TSMT** and **2MTS**, and of two building blocks used for the preparation of the *N*-linked tetrazole-saccharinates, **1MT** and **2MT**, isolated in solid argon.

In **section 4.3** we describe and discuss results of our studies on the photolysis of **TSMT** in solid argon, using matrix-isolation FTIR spectroscopy. This conjugate appears to be a excellent candidate to study, since, as mentioned in section 3.6 of chapter 3, in the 5-thiosaccharyl-1-methyltetrazole (**TSMT**) conjugate the methyl substituent on the tetrazole ring quenches the possibility of tautomerism involving the tetrazole and the thioether linkage restricts tautomerism involving the saccharyl system, thus reducing the number of structures present in the matrix and simplifying the interpretation of the photochemical reactions.

Upon UV (λ = 265 nm) irradiation of the matrix-isolated **TSMT**, two photodegradation pathways were observed, both arising from cleavage of the tetrazolyl ring. Pathway *a* involved cleavage of the N_1-N_2 and N_3-N_4 bonds with extrusion of molecular nitrogen, leading to photostable diazirine and thiocarbodiimide derivatives. The photostability of the photoproduced diazirine under the conditions used precluded its rearrangement to the nitrile imine, as reported for 5-phenyltetrazole by Bégué *et al.*[1] Pathway *b* involved cleavage of the C_5-N_1 and N_3-N_4 bonds, leading to thiocyanate and methyl azide, the latter undergoing subsequent fragmentation to give CNH.

In **section 4.4**, the results of our investigations on the photolysis of 2-methyltetrazole-saccharinate (**2MTS**), isolated in solid argon, are disclosed and discussed. The conjugate **2MTS** has assumed an important role in our investigation due to the good results demonstrated as a

selective copper chelator, affording copper complexes with effective cytotoxic properties against cancer cell lines, as will be presented in chapter 5.[2] These promising results stimulated us to explore the photoreactivity of this conjugate. Moreover it could be expected that substitution in position 2 (N_2) of the tetrazolyl ring would give different photofragmentation pathways and species formed, compared to the (N_1) substituted counterpart.

Upon tunable UV-laser irradiation of the matrix-isolated **2MTS** at $\lambda = 250$ nm selective photoinduced cleavage of the C_5-N_4 and N_2-N_3 bonds of the tetrazolyl ring was observed, leading to extrusion of molecular nitrogen and formation of nitrile imine that can then isomerize to diazirine, which undergoes subsequent photoconversion into carbodiimide. A second pathway was observed, involving concomitant decomposition of the diazirine and leading to nitrile and CNH as photoproducts. Upon irradiation at $\lambda = 290$ nm, the same selective cleavage of the tetrazole ring with extrusion of molecular nitrogen was observed, however leading to the diazirine derivative as the sole photoproduct.

Although the main objective of these studies was to attain a deep understanding on the UV-induced photochemical reactions of both conjugates, the interpretation of the photochemical products revealed to be quite difficult since most of the vibrational modes are related with the benzisothiazole ring, which is unaffected by irradiation under the experimental conditions used. This resulted in extensive overlap of the bands due to the conjugate with those due to the photoproducts, complicating the interpretation of the data. Nevertheless the obtained results on the photochemistry of both conjugates **TSMT** and **2MTS** showed further evidence that the photochemistry of 1*H* and 2*H* tetrazoles is different, as suggested by Bégué *et al*,[1] and also that the production of nitrile imine might be exclusively generated upon photolysis of 2-substituited tetrazoles.

Since the photolysis of both conjugates **TSMT** and **2MTS**, led only to fragmentation of the tetrazole ring, and to better understand the effects of the ring substitution pattern on the photofragmentation pathways and species formed, from 1- and 2-substituted tetrazoles, we decided to study the photochemistry of 1- and 2-methyl-5-aminotetrazole (**1MT** and **2MT**) used as the tetrazolyl building blocks for preparation of the *N*-linked saccharyl-tetrazole conjugates. Moreover we could expect with these smaller molecules to simplify the interpretation and assignment of the IR absorptions due to the photoproducts formed, and corroborate our proposed reaction pathways resulting from irradiation of the studied tetrazole-saccharyl conjugates, **TSMT** and **2MTS**.

Besides, as presented in chapter 1 (see section 1.1.7.7), in the last few years photolysis of several 2,5-disubstituted tetrazoles served for *in situ* generation of highly reactive nitrile imine

dipolar species, which undergo 1,3-dipolar cycloaddition with alkenes present in a biological system. This powerful reaction method has been applied for proteome profiling in living cells. Therefore, a comparison of the photochemistry of both isomers, 1,5 and 2,5-disubstituted tetrazoles (**1MT** and **2MT**), using similar experimental conditions, could provide valuable information regarding the effects of the ring substitution pattern on the photofragmentation pathways of disubstituted tetrazoles. Indeed, we were able to report, for the first time, the intermediates generated from photolysis of a 1,5-disubstituted tetrazole in solid argon.

In **section 4.5** it is shown that the photochemistries of the two isomers, **1MT** and **2MT**, although resulting in the common intermediate diazirine, which undergoes subsequent photoconversion into an *N*-aminocarbodiimide, showed marked differences: formation of an amino cyanamide was only obtained from the photocleavage of the isomer **1MT**, whereas formation of a nitrile imine was only observed from photolysis **2MT**. The exclusive formation of nitrile imine from the isomer **2MT**, confirms the possibility that only the 2*H*-tetrazoles forms can give a direct access to nitrile imines, while observation of the amino cyanamide represents a novel reaction pathway in the photochemistry of tetrazoles and seems to be characteristic of 1*H*-tetrazoles.

Also, and as result of these studies, we could conclude two important points: i) the photochemistry of **2MTS** and the parent tetrazolyl moiety **2MT** is quite similar (the reaction pathways and obtained photoproducts are equivalent on both compounds). However, the saccharyl system was found to increase substantially the photostability of the tetrazole ring and of the nitrilimine intermediate, in the **2MTS** conjugate, by more than 20 times, compared to the parent tetrazole **2MT**. When using bis-tetrazole molecules or conjugates where the tetrazole ring is linked to other heterocycles in coordination chemistry, the quite low photostability of tetrazoles may narrow the range of applications. As such, when considering the applications of these conjugates, this remarkable increase of photostability introduced by the saccharyl system, reveals to be a quite promising characteristic of these novel conjugates.

For **TSMT** and for the tetrazolyl building block **1MT**, although in the conjugate **TSMT** we have a thio-saccharyl-, and in **1MT** we have an amino-substituent in C5 of the tetrazole ring, in both situations we are in presence of 1,5-disubstituted tetrazoles. Although the results are not exactly similar, we can easily conclude from them that 1,5-disubstituted tetrazoles do not give direct access to nitrile imines.

4.2. Introduction

Considering the putative applications of saccharyl-tetrazole conjugates, assessment of their photostability may be a relevant aspect. As shown in chapter 1, the benzisothiazole moiety (section 1.2.3) is known to be rather photostable compared with the tetrazole moiety (section 1.1.7). A search in the literature revealed some data regarding the photochemistry of benzisothiazoles, isolated in cryogenic matrices and in solution.[3–10] The photocleavage of the benzisothiazole ring of a monomeric saccharyl derivative, trapped in a rigid environment of solid argon, was observed for the first time for one of our tetrazole-saccharyl conjugates (compound **93**, section 1.1.7.6; ii).[11] More recently, the photochemistry of monomeric saccharin was also studied in solid argon (see section 1.2.3).[12] In solution, the photoreactivity of benzisothiazoles seems to be determined by the structure of the saccharyl ring, the nature of substituents and the reaction medium (see section 1.2.3).

By their turn, tetrazoles are known for their rich photochemistry, both in solution and when isolated in cryogenic matrices (section 1.1.7).[1,11,13–48] Generally, the photochemistry of tetrazole derivatives leads to cleavage of tetrazole ring and was shown to be influenced by the chemical nature and conformational flexibility of substituents. It was also observed that tautomer selective photochemistry may take place, if the molecule exhibits tautomerism.

The fact that tetrazole-saccharyl conjugates combine heterocyclic moieties with dissimilar intrinsic photoreactivities is challenging, providing yet another reason to explore the photoreactivity of these compunds by matrix-isolation FTIR spectroscopy. As explained in chapter 1 (section 1.1.6), this method offers several advantages for studying the photochemistry of monomeric compounds (*i.e.*, molecular diffusion is inhibited, leading in principle only to the observation of unimolecular reactions and enabling the stabilization, detection, and characterization of products and, in some cases, of highly reactive intermediates). As such, the saccharyl-tetrazole conjugates selected and the corresponding tetrazolyl building blocks were isolated in solid argon (15 K) and the matrices were subjected to *in situ* narrowband UV irradiation at different wavelengths. The progress of the reactions was followed by infrared spectroscopy and analysis of the results was supported by quantum chemical calculations. A structural and vibrational characterization of both reactants and photoproducts has been undertaken, supporting our proposals for the reaction pathways resulting from irradiation of the matrix-isolated compounds under study. All data, for each compound, is presented and discussed below.

4.3. Photochemistry of 5-thiosaccharyl-1-methyltetrazole (TSMT)

As mentioned above, in the saccharyl-tetrazole conjugate **TSMT** the methyl substituent on the tetrazole ring quenches the possibility of tautomerism involving the tetrazole, and the thioether linkage restricts tautomerism involving the saccharyl system, thus reducing the number of structures present in the matrix and simplifying the interpretation of the photochemical reactions. This section presents results of our investigations on the UV-induced photochemistry of **TSMT** in solid argon. Interpretation of the experimental results was assisted by quantum-chemical calculations, undertaken at different levels of approximation (calculated vibrational frequencies for all relevant photoproducts are provided in Table S9 in Appendix).

4.3.1. UV-induced photodegradation pathways of matrix-isolated TSMT

In order to investigate the photochemistry of **TSMT**, the deposited matrix was irradiated with UV light, as described in chapter 2 (section 2.6). The sample was monitored after each irradiation by recording its infrared spectrum. The wavelengths used for irradiation were chosen according to the UV/Vis spectrum of **TSMT** in ethanol, at room temperature, which shows an absorption maximum at 263 nm.

Upon irradiation at 265 nm, the bands due to **TSMT** decreased in intensity, indicating that the compound was being consumed, and, simultaneously, new bands due to photoproduced species appeared in the spectrum. The changes are particularly noticeable in the 2300-1700 cm^{-1} spectral region, presented in Figure 4.1, where the results of irradiation at $\lambda = 265$ nm, for 1 h, are shown. In this figure, the calculated spectra of the proposed photoproducts (see Scheme 4.1) in the same spectral range are also shown, for comparison. The observation that the changes in the intensities of the various new bands in the 2300-1700 cm^{-1} spectral range follow different patterns with time of irradiation indicates that these bands originate from different products.

It must be noticed that **TSMT** is a molecule composed of 25 atoms, 15 of them belonging to the rigid benzisothiazole ring. Thus, of the 69 vibrational modes, 39 are related to the benzisothiazole ring, which is unaffected by irradiation under the experimental conditions used. Therefore, the presence of bands due to the benzisothiazole ring of **TSMT** results in extensive overlap with those of the photoproducts, complicating interpretation of the data. The strong overlap of the spectra of some of the proposed photoproducts, with each other and with the spectrum of **TSMT,** can be clearly noticed in Figure 4.2, where the calculated infrared spectra for the relevant species are shown. As can be perceived in this figure, such superposition is particularly noticeable in the case of the most intense bands appearing in the low-frequency

spectral range (below 1700 cm^{-1}), where most of the bands due to the benzisothiazole moiety appear. However, the most characteristic bands of the photoproducts are observed in the 2300-1700 cm^{-1} spectral region, which is a clean spectroscopic window; this allowed us to doubtlessly identify these species, as described in detail below.

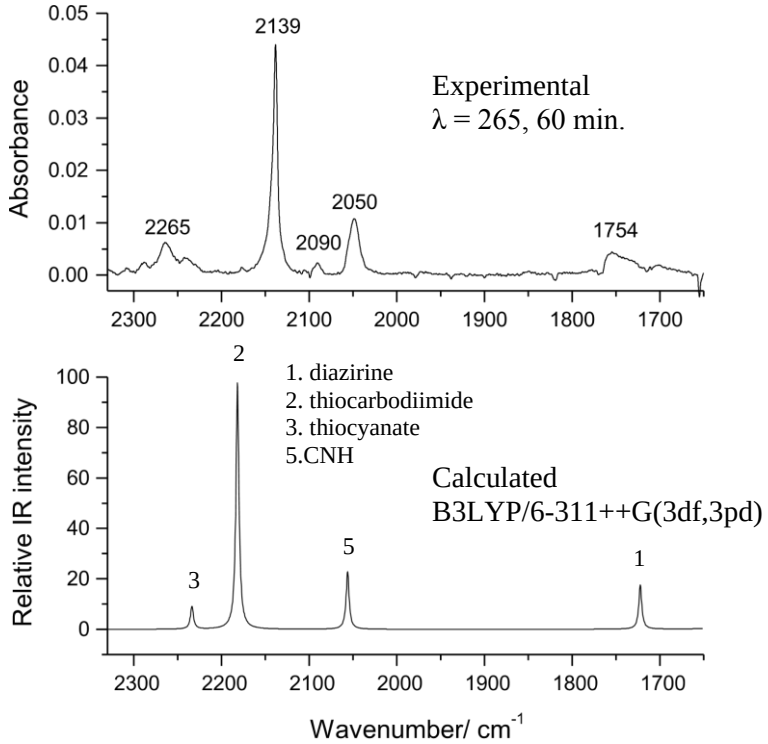

Figure 4.1 - Figure 7. (top) IR spectrum in the 2300-1700 cm^{-1} spectral region for **TSMT**, after irradiation of the matrix with UV light (λ = 265 nm) for 1 h, showing peaks due to the photolysis products. The peak at 1754 cm^{-1} is assigned to the N=C stretching vibration in diazirine **1**, the peak at 2139 cm^{-1} to the N=C=N antisymmetric stretching of thiocarbodiimide **2**, the peak at 2090 cm^{-1} to the N=N=N antisymmetric stretching of methyl azide **4**, the peak at 2050 cm^{-1} to the CN stretching of CNH **5**, and the peak at 2265 cm^{-1} to the C≡N stretching of thiocyanate **3**. (bottom) Theoretical spectra obtained for the observed photoproducts. The intensities of the individual spectra were multiplied by different factors to obtain a better simulation of the experimental spectrum. Theoretical wavenumbers were scaled by a factor of 0.978, and bands were broadened using Lorentzian functions with fwhm equal to 4 cm^{-1}.

The band appearing at 2139 cm^{-1} (Figure 4.1) nicely fits the predicted frequency for the NCN antisymmetric stretching vibration of thiocarbodiimide **2** (Scheme 4.1). The observation of carbodiimides resulting from photolysis of matrix-isolated tetrazole derivatives has been reported previously.[1,20,21] Additionally, the bands appearing around 1754 cm^{-1} fit well the predicted frequencies for the νC=N stretching vibration of diazirine **1**. The formation of

diazirines (including 1,3-substituted diazirines) from photochemically induced cleavage of the tetrazole ring has also been reported.[19,20]

The identification of bands assigned to thiocarbodiimide **2** and diazirine **1** suggests photocleavage of the N_1-N_2 and N_3−N_4 bonds with extrusion of molecular nitrogen. It should be noticed that the broad profile of the band around 1754 cm^{-1} may be due to the presence in the matrix of different conformers of diazirine **1**, which has two rotational axes, S-$C_{(saccharin)}$ and S-$C_{(diazirine)}$. Calculations predicted the existence of two conformers of **1**, with relative energies differing by only 2.9 kJ mol^{-1}. The two conformers have similar IR spectra, but the calculated frequencies for the νC=N mode are different enough (1722 and 1740 cm^{-1}) to result in the observed broad band.

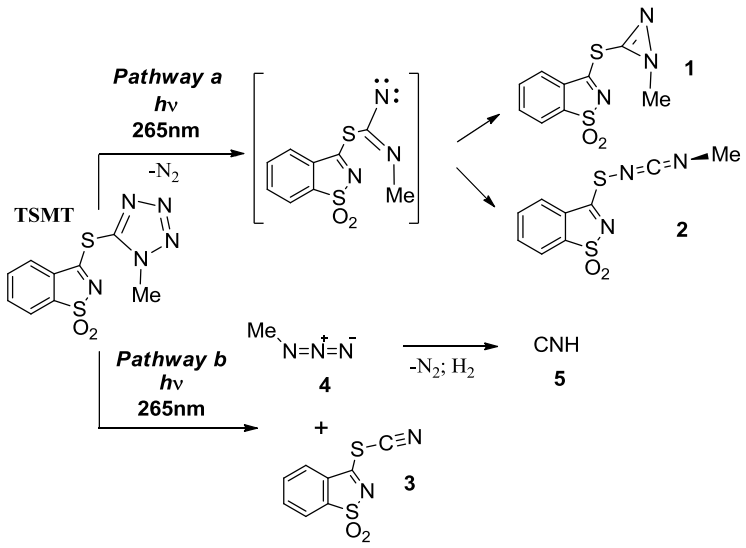

Scheme 4.1 - Proposed reaction pathways resulting from irradiation of the **TSMT** monomer isolated in solid argon.

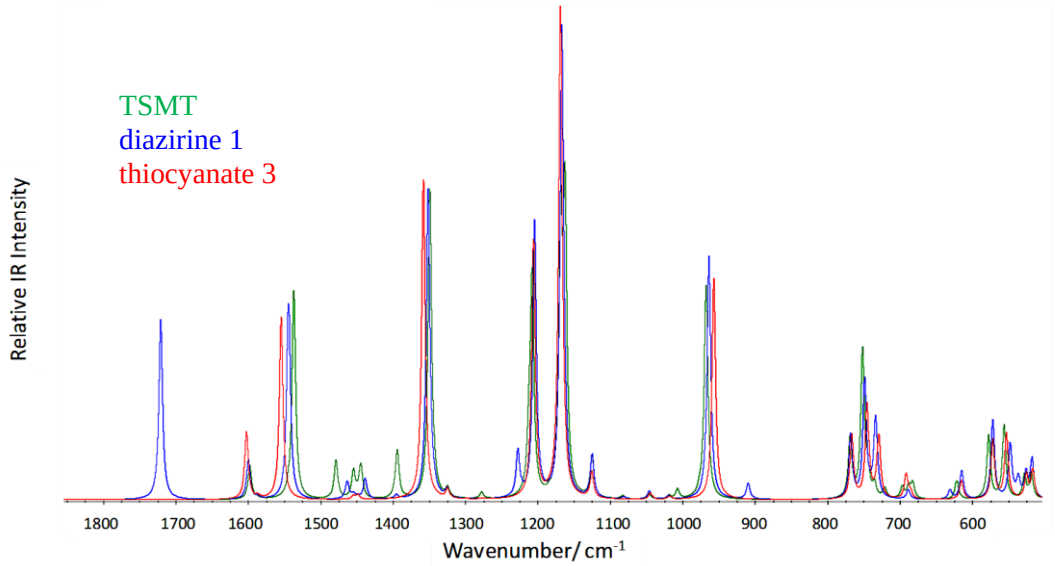

Figure 4.2 - DFT(B3LYP)/6-311++G(d,p) calculated infrared spectra of **TSMT** (green), diazirine **1** (blue) and thiocyanate **3** (red) in the low-frequency region (below 1800 cm^{-1}). Wavenumbers were scaled by 0.978 and bands were broadened by Lorentzian functions with FWHM equal to 6 cm^{-1}.

It should also be noticed that in the case of carbodiimide **2** the calculated spectrum does not coincide so much with those of the reactant molecule and other photoproducts. As shown in Figure 4.3, several bands observed in the low-frequency range in the spectrum of the photolyzed matrix doubtlessly confirm this species as one of the dominant photoproducts of **TSMT**. Moreover, it should also be noticed that both carbodiimide **2** and diazirine **1** were formed from the very beginning of the irradiation, as they were already present in significant amounts after only 30 s of irradiation (see Figure 4.3).

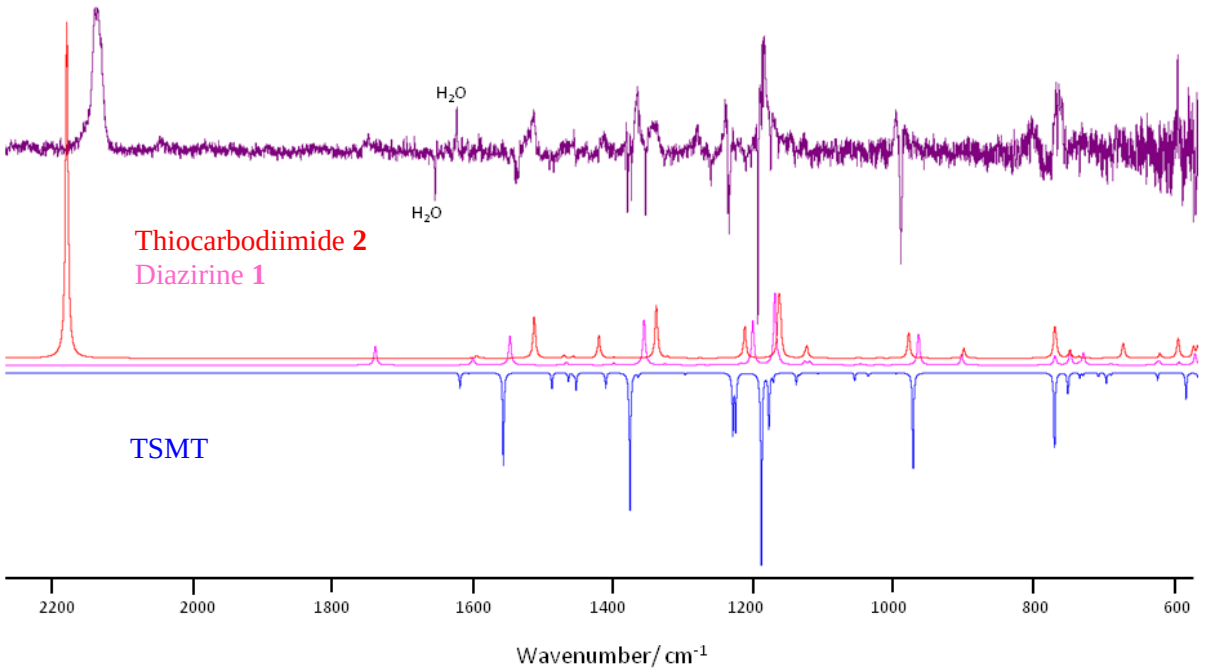

Figure 4.3 - (top): Infrared difference spectrum (violet) obtained by subtracting the spectrum of the deposited **TSMT** matrix from that resulting from irradiation of the matrix (λ = 265 nm) during 30 s; (bottom): DFT-calculated (wavenumbers scaled) spectra for **TSMT** (blue trace, bands pointing down), thiocarboidiimide **2** (red trace) and diazirine **1** (magenta trace).

The band observed at around 2100 cm^{-1} is likely due to methyl azide **4** νNNN antisymmetric stretching, which can be formed, concomitant with thiocyanate **3**, by photocleavage of the C_5-N_1 and N_3-N_4 bonds of the tetrazole ring of **TSMT** upon irradiation. Under the irradiation conditions used, **4** has been found to partially react, yielding CNH **5** as the final main product (together with H_2 and N_2) in a process involving methylenimine (CH_2=NH) as intermediate.[49–52] Indeed, the photochemistry of **4** in an argon matrix has been studied in the past and, according to the available knowledge, one can then expect that the formation of this compound from photolysis of **TSMT** should essentially result in the accumulation of CNH. In consonance with such expectations, a product band was observed around 2050 cm^{-1}, corresponding to the νCN stretching mode of CNH observed by Milligan and Jacox[51] upon photolysis of matrix-isolated **4**, at nearly this frequency (2032 cm^{-1}). In the present study, CNH is formed together with other products and with all probability interacts in the matrix cage with other species. Because of that, the frequencies may shift slightly. Nevertheless, the assignment of the band at 2050 cm^{-1} to CNH seems to be doubtless. It is unfortunate that the other two additional bands due to CNH, reported by Milligan and Jacox (at *ca.* 535 and 3583 cm^{-1})[51], could not be ascribed with certainty in the present study, though a product band at 536 cm^{-1} (almost coincident with a band of **TSMT**) seems also to be present in

the spectrum of the photolyzed matrix. However, the large spectral noise below *ca.* 600 cm^{-1}, in the spectrum of the photolyzed matrix, makes this observation uncertain. On the other hand, the band observed by Milligan and Jacox[51] at 3583 cm^{-1} is due to the NH stretching mode of CNH and can be expected to be extensively broadened due to intermolecular interactions (hydrogen bonding) between CNH and other species present in the matrix cage (several bumps in the baseline are present in the spectrum of the photolyzed **TSMT** matrix in the high-frequency region; however, no band could be safely assigned to this mode). It should also be noticed that no spectroscopic evidence for the presence of methylenimine in the photolyzed matrix could be found, specifically in the CH and C=N stretching spectral regions, where putative bands due to this compound appearing in a spectral region relatively less congested with bands due to other species should be observed. However, in the present experiments this species can be expected to be present only in very low amounts, as a result of its expected prompt fragmentation into CNH and H_2.[49–52] Furthermore, since its infrared spectrum is characterized by bands of very low intensity,[52] successful observation would be very improbable.

The bands observed at around 2265 cm^{-1} correspond to typical frequencies of C≡N stretching modes[53,54] and can be assigned to the νC≡N vibrational mode of thiocyanate **3**, which is the photoproduct that can be expected to be formed together with **4** (see Scheme 4.1). The calculated intensity of this band for the thiocyanate in the gas phase is small, but it is possible that it intensifies to some extent in the matrix as a result of polarization effects induced by the medium. Very unfortunately, most of the other thiocyanate bands with significant predicted intensity are expected to be superimposed with bands due to diazirine **1** and **TSMT** (see Figure 4.2). Since the direct evidence for the identification of thiocyanate **3** resides mainly in the observation of the feature in the ~2265 cm^{-1} region, it must be considered as tentative. However, this assignment is strongly suggested from the mechanistic point of view, since, as already mentioned, the thiocyanate is the product that can be expected to be formed simultaneously with methyl azide **4**.

A schematic drawing that summarizes the proposed photochemical pathways of matrix-isolated **TSMT** is presented in Scheme 4.1. As mentioned above, according to the identified photoproducts, two photodegradation pathways can be postulated, both arising from cleavage of the tetrazolyl ring: the dominant pathway *a* involves photoinduced cleavage of the N_1-N_2 and N_3-N_4 bonds with extrusion of molecular nitrogen, leading to the production of diazirine **1** and thiocarbodiimide **2**. A nitrene-type intermediate can be postulated to be involved in this process,[1,20] though we could not experimentally observe it. The concentrations of both

thiocarbodiimide **2** and diazirine **1** increased continuously with time, with no apparent sign of their further chemical transformations. The minor pathway *b* involves photoinduced cleavage of the C_5-N_1 and N_3-N_4 bonds of the tetrazole ring, leading to the formation of thiocyanate **3** and methyl azide **4**; the thiocyanate **3** remains photostable, while methyl azide undergoes subsequent decomposition into CNH **5**.

An additional note shall here be made in relation to the observed photostability of diazirine **1**. Recent studies on the photolysis of matrix-isolated 2,5-disubstituted tetrazoles demonstrated that elimination of molecular nitrogen leads to the initial production of a nitrile imine after a few seconds of irradiation, which can then isomerize to a 1*H*-diazirine that undergoes subsequent photoconversion into a carbodiimide (see chapter 1, section 1.1.7.7; see also the study presented below in section 4.5).[13,15,20,55]

In the present work, no evidence for the formation of a nitrile imine was found, while the photoproduced diazirine revealed to be photostable even after 1 h of irradiation (λ = 265 nm). This indicates that the photochemistries of the 1*H* and 2*H* tautomers of substituted tetrazoles might be different, as postulated by Begué *et al* following analysis of the photolysis of 5-phenyltetrazole.[1] The suggested route for the production of the nitrile imine from the 1*H* tautomer of 5-phenyltetrazole, considered by Begué *et al.,* implies the initial production of a diazirine intermediate, despite the fact that they were not able to observe this species (see Scheme 4.2).[1] Indeed, the present results on **TSMT** should be compared more directly with those proposed by these authors for 5-phenyl-1*H*-tetrazole, since **TSMT** is also a 1-substituted tetrazole derivative.

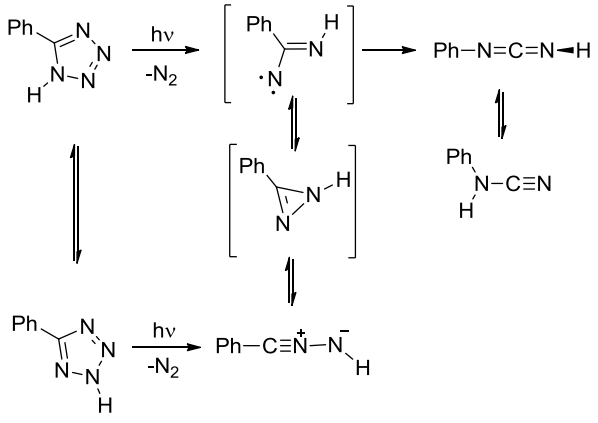

Scheme 4.2 - Photolysis of matrix-isolated 5-phenyltetrazole (λ= 254 nm), as proposed by Bégué *et al.* (adapted from *J. Am. Chem. Soc.* 2012, 134, 5339–5350)[1]

The absence of evidence for the formation of nitrile imine and the observation of diazirine **1** as a stable photoproduct seems to confirm the proposal of Begué *et al.*[1] The photostability of

1 is probably due to both the stabilizing effect of the thio-saccharyl and methyl substituents on the diazirine ring, precluding the photoinduced rearrangement of **1** under the experimental conditions used.

4.3.2. Conclusions

Upon irradiation of the matrix-isolated **TSMT** with UV light (λ = 265 nm) two photodegradation pathways were observed, both arising from cleavage of the tetrazolyl ring: Pathway *a* involves photoinduced cleavage of the $N_1{-}N_2$ and $N_3{-}N_4$ bonds, with extrusion of molecular nitrogen, leading to the production of diazirine **1** and thiocarbodiimide **2**. The concentrations of these two photoproducts increased with time, and there was no apparent sign of their photodegradation even after almost complete consumption of the reagent (**TSMT**). The observed photostability of the photoproduct diazirine **1** under the conditions used is possibly ascribable to a stabilizing effect of the thiosaccharyl and methyl substituents. Pathway *b* involves photoinduced cleavage of the $C_5{-}N_1$ and $N_4{-}N_3$ bonds, leading to thiocyanate **3** and methyl azide **4** as primary photoproducts. Thiocyanate **3** remains photostable while **4** forms CNH **5** in a secondary photoreaction.

4.4. Photochemistry of *N*-linked 2-methyl-tetrazole saccharinate (2MTS)

As mentioned above, the promising cytotoxic properties of copper complexes based on 2-methyl-tetrazole saccharinate[2] stimulated us to explore the photoreactivity of **2MTS**. Moreover it could be expected that substitution in a different position of the tetrazolyl ring (N_2), when compared with the previous studied conjugate **TSMT**, would give different photofragmentation pathways and lead to formation of different species. Here we report on the UV-induced photochemistry of 2-methyl-tetrazole saccharinate (**2MTS**) isolated in solid argon.

4.4.1. UV-induced photochemistry of matrix-isolated 2MTS

In order to investigate the photochemical reactions of **2MTS**, the deposited matrix was irradiated with UV light, as described in chapter 2 (section 2.6). The investigation of the photochemistry of **2MTS** involved irradiation experiments varying the wavelength of the tunable UV-laser source, from λ = 330 nm and gradually decreasing until λ = 222 nm (the lowest wavenumber available in our OPO system).

Irradiations at λ = 290 nm resulted in a decrease in the intensity of the bands due to **2MTS**, indicating that the compound was being consumed and, simultaneously, a distinctive absorption band at around 1680 cm^{-1} increased, ascribed to photoproduct **7** (Scheme 4.3). After 100 min of irradiations at λ = 290 nm, the bands due to photoproduct **7** kept increasing, with no evidence of other photoproducts. Further irradiations of this same matrix at λ = 250 nm resulted in several new bands, due to formation of photoproducts **6-11**, with complete consumption of the reagent **2MTS** after 10 min of irradiation.

Figure 4.4 presents the spectral changes in the range 2300-1700 cm^{-1}: (i) after 100 min of irradiation at λ = 290 nm, when around 60% of **2MTS** was consumed and photoproduct **7** (1680 cm^{-1}) was produced; (ii) after 5 and 10 min of irradiation at λ = 250 nm, showing bands due to the different photolysis products (**6-11**) obtained at this wavelength. As explained in the previous study of conjugate **TSMT**, the presence of the benzisothiazole ring, unaffected by irradiation under the experimental conditions used, results in an extensive overlap of the bands of **2MTS** with those of the photoproducts, especially in the low-frequency spectral range (below 1700 cm^{-1}). However, the most characteristic bands of the photoproducts are expected to appear in the clean spectroscopic window (2300-1700 cm^{-1}).

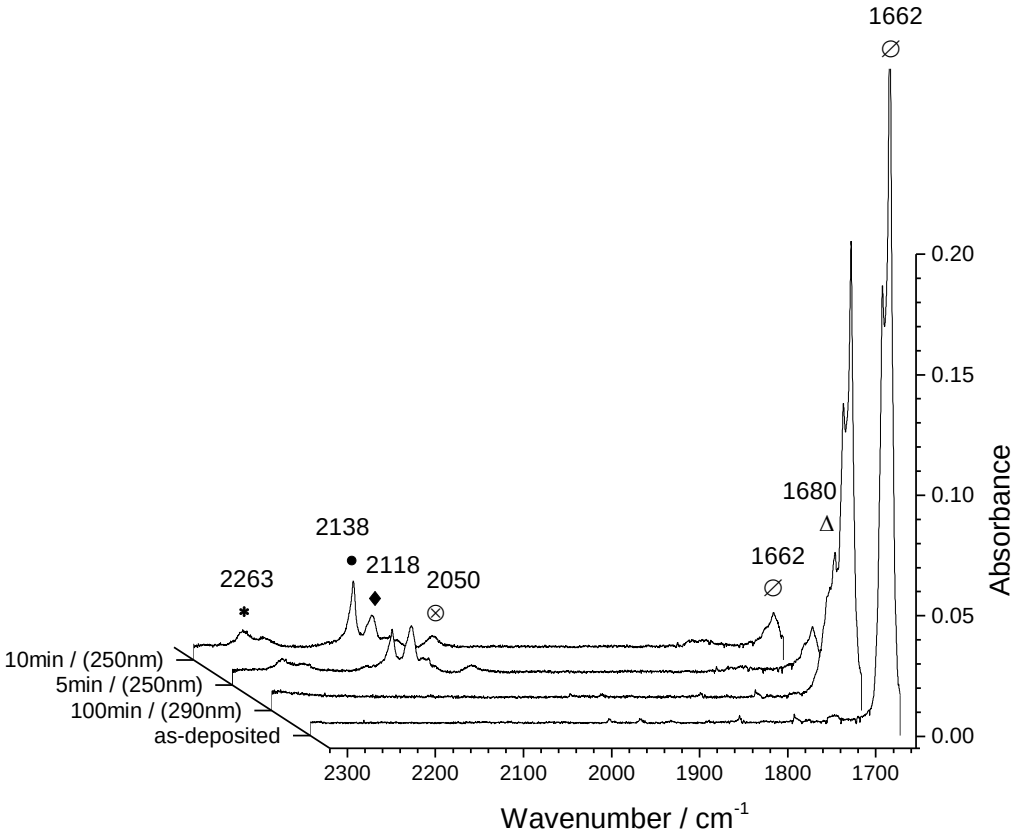

Figure 4.4 - Partial experimental IR spectra of **2MTS**: for the freshly deposited matrix; after 100 min of irradiation at λ = 290 nm, showing a sole peak at 1680 cm^{-1}, assigned to the νNC stretching vibration in diazirine **7**; after 5 and 10 min of irradiation at λ = 250 nm, subsequent to the irradiation at λ = 290 nm, showing bands due to the different photolysis products. The band at 2138 cm^{-1} is assigned to the νNCN antisymmetric stretching of carbodiimide **8**, the band at 2118 cm^{-1} is due to the νCN stretching mode of nitrile imine **6**, the band at 2050 cm^{-1} is due to the νCN stretching of CNH **11**, and the band at 2263 cm^{-1} is due to the CN stretching of nitrile **9**. Note that the band at 1662 cm^{-1}, due to **2MTS**, is also presented, showing the consumption of the reagent.

As can be seen in Figure 4.4, it is clear that in the 2300-1700 cm^{-1} spectral range no other bands increased, besides the distinctive 1680 cm^{-1} absorption, after 100 min of irradiation at λ = 290 nm. Also, irradiation of the same matrix at λ = 250 nm resulted in a fast consumption of the matrix-isolated **2MTS** (1662 cm^{-1}) while, simultaneously, several new bands, due to photoproduced species, appeared in the spectrum (2263, 2138, 2118, 2050 cm^{-1}), common to those observed from photocleavage of **TSMT** (section 4.3): a band at 2138 cm^{-1}, due to the νNCN antisymmetric stretching of cabodiimide **8**; a band at 2263 cm^{-1}, due to the νC≡N stretching of nitrile **9**; and a band at 2050 cm^{-1}, ascribed to the νCN stretching of CNH **11**. The identification of these photoproducts could be easily achieved by comparison with previous results obtained for the photolysis of the thio-linked tetrazole-saccharinate (**TSMT**).[16]

However, photolysis of **2MTS** at λ = 250 nm resulted in formation of a new intermediate with a distinctive absorption band at 2118 cm^{-1}, which increased during the first 5 min. of irradiation and then started decreasing with further irradiations at λ = 250 nm. The spectral changes observed in the range 2300-2000 cm^{-1}, after 5 and 10 min of irradiation at λ = 250 nm, are shown in Figure 4.5. The calculated IR spectra for the proposed photoproducts are also shown for comparison.

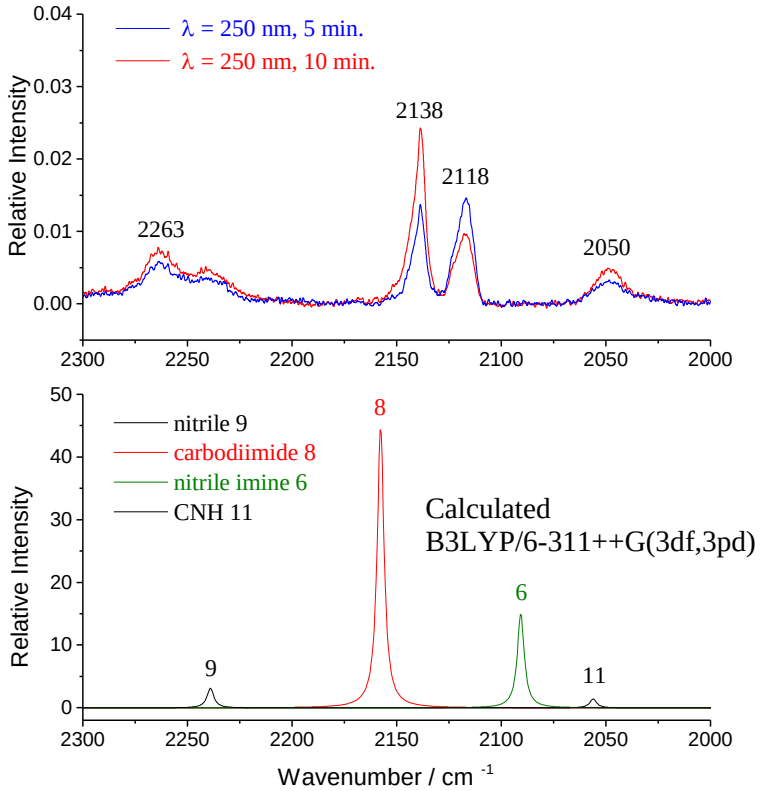

Figure 4.5 – (top) IR spectrum in the 2300-2000 cm^{-1} spectral region for **2MTS**, after irradiation of the matrix at λ = 250 nm for 5 min (red) and 10 min (blue), showing spectral changes upon irradiation; (bottom) theoretical spectra obtained for the observed photoproducts. Theoretical wavenumbers were scaled by a factor of 0.978, and bands were broadened using Lorentzian functions with fwhm equal to 4 cm^{-1}.

This characteristic absorption at 2118 cm^{-1} can be assigned to the νC=N stretching mode of the nitrile imine **6**, calculated at 2091 cm^{-1} (bottom; Figure 4.5). As briefly explained in previous section 4.3 (and as will be detailed in the section 4.5) this photoproduct is expected to result from photolysis of the 2*H* tautomeric form of the substituted tetrazole, as is the case of **2MTS**.[13,15,20,55] Indeed, nitrile imine **6**, produced from the photocleavage of the tetrazole ring of **2MTS**, which reached its maximum amount after the first 5 min. of irradiation at λ = 250 nm, is expected to be gradually consumed with increased irradiation times (see band 2218 cm^{-1} in

Figure 4.5; blue and red lines represent 5 min and 10 min of irradiation at λ = 250 nm, respectively), generating the isomer diazirine **7**, which can then follow two different photochemical pathways, as will be presented below.

Photoproduct **7**, initially formed at λ = 290 nm and with a distinctive band observed at 1680 cm^{-1}, was also consumed when irradiated at λ = 250 nm (see Figure 4.4). To investigate which bands could be generated from the consumption of photoproduct **7** when irradiated at λ = 250 nm, we irradiated an as-deposited matrix containing isolated **2MTS** at λ = 250 nm and compared the corresponding spectra, with previous results obtained when the matrix was irradiated at λ = 290 nm and subsequently irradiated at λ = 250 nm. A comparison between the results obtained in both experiments showed that the spectra resemble each other, this suggesting that diazirine **7**, produced initially at longer wavelength (λ = 290 nm), when photolysed at λ = 250 nm generates one or more of the same photoproducts formed from photolysis of **2MTS** at λ = 250 nm. From a mechanistic point of view, the absorption band at 1680 cm^{-1} can be assigned to the νC=N stretching mode of the diazirine, since this photoproduct could be expected from photochemically induced cleavage of the tetrazole ring, as reported for a diverse range of tetrazole derivatives[13,15,19,20,55] and also observed in the previous thio-linked tetrazole saccharinate (**TSMT**).[16]

Indeed, as described in the previous section, photolysis of the **TSMT** conjugate led to a stable diazirine, among other photoproducts. However, in the present work the concentration of diazirine **7** increased continuously with time, with no evidence of other photoproducts, when the matrix containing **2MTS** was irradiated at λ = 290 nm. This observation suggests that irradiation of **2MTS** at λ = 290 nm results in selective photoinduced cleavage of the C_5-N_4 and N_2-N_3 bonds of the tetrazole ring, with extrusion of molecular nitrogen, leading to diazirine **7** as the sole photoproduct. Although, diazirine **7** remains photostable at λ = 290 nm, it should be noticed that more than 40% of **2MTS** remained after 100 min of irradiation, suggesting that the efficiency of the reaction is rather low at this wavelength.

A schematic representation summarizing the proposed photodegradation pathways for matrix-isolated **2MTS** is presented in Scheme 4.3.

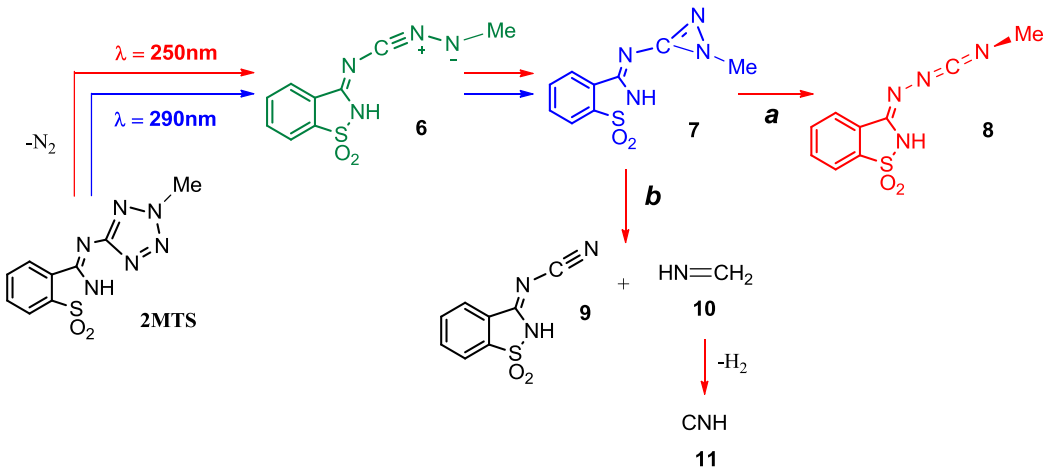

Scheme 4.3 - Proposed reaction pathways resulting from irradiation of monomeric **2MTS** isolated in solid argon, at λ = 290 nm (blue) and at λ = 250 nm (red).

In summary, irradiation of matrix-isolated **2MTS** at λ = 250 nm resulted in selective photoinduced cleavage of the C_5-N_4 and N_2-N_3 bonds of the tetrazole ring, with extrusion of molecular nitrogen, leading to nitrile imine **6** that can isomerize to diazirine **7** (although not observed when irradiated at this wavelength), which undergoes subsequent photoconversion into carbodiimide **8** (pathway *a*). A second pathway was also perceived, pathway *b*, involving concomitant decomposition of the diazirine **7** with formation of nitrile **9** and CNH **11**. Concerning pathway *b*, it should be noticed that the formation of nitrile **9** could in principle result from either the cleavage of the C_5-N_4 and N_1-N_2 bonds of the tetrazole ring of **2MTS**, generating the nitrile **9** and methyl azide (as observed in the photolysis of **TSMT**; see Scheme 4.1), or from cleavage of the diazirine **7**, generating nitrile **9** and methylenimine **10**. However, its formation via cleavage of the tetrazole ring can be ruled out, since no evidence of the intense νNNN antisymmetric mode of methyl azide could be found.[52] Although this mechanistic proposal is mainly based in the absence of one characteristic absorption in the ~2100 cm^{-1} region, it was later corroborated by an extensive photochemical investigation of the matrix-isolated parent tetrazole **2MT**, as will be explained in section 4.5. It should also be noticed that no spectroscopic evidence of the presence of methylenimine **10** in the photolyzed matrix could be found.[51,52] However, formation of the photoproduct **11** was observed beyond doubt[51] and, according to the available knowledge regarding the photochemistry of methylenimine **10**,[51,52] one can then expect that the formation of CNH **11** should result essentially from the presence of methylenimine **10** in the matrix.

Upon irradiation of matrix-isolated **2MTS** at λ = 290 nm we observed the same selective cleavage of the tetrazole ring, through C_5-N_4 and N_2-N_3 bonds, with extrusion of molecular

nitrogen, although leading to the diazirine **7** as the sole photoproduct. This exclusive formation of diazirine **7**, with no evidence of any intermediate, specially the nitrile imine **6**, may be ascribed to the wavelength of excitation (λ = 290 nm) that may be closer to the absorbance maximum of the expected preceding nitrile imine **6**, increasing even more its photoconversion into diazirine **7**. In this same way, the performed excitation at λ = 290 nm, may be in the low energy wing of the absorbance band of the produced diazirine **7**, resulting in the observed photostability for this product, under the experimental conditions used.

4.4.2. Conclusions

Irradiation of the matrix-isolated **2MTS**, using a tunable UV-laser, resulted in selective photoinduced cleavage of the C_5-N_4 and N_2-N_3 bonds of the tetrazole ring, with extrusion of molecular nitrogen. Irradiation at λ = 250 nm generated nitrile imine **6**, that can then isomerize to diazirine **7**, which undergoes subsequent photoconversion into carbodiimide **8** (pathway *a*), or photodegradation leading to nitrile **9** and CNH **11** (pathway *b*).

The same selective cleavage of the tetrazole ring, involving extrusion of molecular nitrogen, was observed upon irradiation at λ = 290 nm, although in this case diazirine **7** was obtained as the sole photoproduct. The exclusive observation of diazirine **7**, with no evidence of any intermediate, (notably the expected nitrile imine **6**), may be ascribed to the wavelength of excitation (λ = 290 nm) that may be closer to the absorbance maximum of the expected nitrile imine, boosting its photoconversion into diazirine **7**. Also, the performed excitation (λ = 290 nm) may be in the low energy wing of the absorbance band of the produced diazirine **7**, accounting for the observed photostability for this photoproduct, under the used experimental conditions.

Subsequent irradiation at λ = 250 nm of the matrix that had been subjected to irradiation at λ = 290 nm resulted, as expected, in photolysis of the produced diazirine **7**, following (concomitantly) photochemical pathways *a* and *b*.

4.5. Photochemistry of 1- and 2-methyl-5-aminotetrazoles: evaluation of structural effects on reaction pathways

In this section we present and discuss results of our investigation on the photochemistry of isomeric 1-methyl-5-aminotetrazole (**1MT**) and 2-methyl-5-aminotetrazole (**2MT**), induced using narrowband tunable UV-laser irradiation.

As mentioned above, photolysis of conjugates **TSMT** and **2MTS** led only to fragmentation of the tetrazole ring. To better understand the effects of the ring substitution pattern on the photofragmentation pathways and species formed, we decided to study the photochemistry of isomeric **1MT** and **2MT**, used as the tetrazolyl building blocks for preparation of *N*-linked saccharyl-tetrazole conjugates. A comparison of the photochemistry of both isomers can provide valuable information regarding the effects of the ring substitution pattern on the photofragmentation pathways of 1,5- and 2,5-disubstituted tetrazoles.

Moreover, in chapter 1 (see section 1.1.7.7) we described a major application of tetrazoles that recently came to light, with the tetrazole-based photoclick chemistry providing a powerful tool for proteome profiling in living cells.[56–58] To this aim, several 2,5-disubstituted tetrazoles served as starting materials for *in situ* generation of nitrile imine dipolar species through UV-induced photocleavage of the tetrazole, via extrusion of N_2. The nitrile imine dipolar species then react with an alkene dipolarophile, through a 1,3-dipolar cycloaddition reaction.[59–65] Of course, these and other applications of tetrazoles involving light-induced processes rely on their photochemistry, and a deeper understanding enables the design of better systems.

However, most studies directed to the use of tetrazoles as photoprecursors of reactive intermediates and unusual molecules are based on 2,5-disubstituted tetrazoles,[1,13,15,17,20,21,39] Even in 5-substituted tetrazoles, where the tetrazole ring bears a labile hydrogen as substituent, it was observed that the 2*H*-tautomer was the predominant form isolated in the matrix,[1,15,20] in keeping with the behaviour observed for the parent tetrazole.[66] Thus, the matrix photochemistry of 1,5-disubstituted tetrazoles remains mostly unexplored, apart from the work by Begué *et al.* [1] on the photolysis of 1-methyl-5-phenyltetrazole, where the formation of carbodiimide as the final photoproduct was demonstrated but no intermediates were detected (chapter 1; section 1.1.7.7; iv).

Although it could be expected that only the 2,5-disubstituted tetrazoles would give direct access to nitrile imines, we think that an investigation of the intermediates generated during photolysis of 1,5-disubstituted tetrazoles may add relevant information regarding the reactivity of the tetrazole chemotype and may also lead to new scaffolds. To better understand the effects

of the ring substitution pattern on the photofragmentation pathways and species formed from 1,5- and 2,5-disubstituted tetrazoles, the photolysis of the isomeric **1MT** and **2MT** were investigated, using similar experimental conditions.

As presented in chapter 1 (section 1.1.7.4), earlier photochemical studies of **2MT** in solid argon[17,36] revealed the involvement of three different primary photochemical pathways: (a) nitrogen elimination, with production of 3-amino-1-methylnitrilimine, which isomerize into 1-methyl-1*H*-diazirine-3-amine; (b) ring cleavage leading to methyl azide and cyanamide; (c) tautomerization to mesoionic 3-methyl-1*H*-tetrazol-3-ium-5-aminide. Additionally, reactions of the primary photoproducts were observed, leading to methylenimine and hydrogen isocyanide.[17,36] Recent studies on the photochemistry of a small library of tetrazoles (see section 1.1.7.7),[1,13,15,17,20,21,39] have demonstrated formation of nitrile imines and these intermediates were found to isomerize, forming carbodiimides as final products. However, in previous attempts to elucidate the photochemistry of **2MT**, this isomerization was not observed. The coexistence of several possible routes, resulting in various photoproducts (some may result from more than one route), can easily lead to erroneous assignment of the IR absorptions.

We now describe results of an investigation on the photochemistry of **1MT** and **2MT**, using a narrowband tunable UV-laser irradiation. This approach allows to induce photoreactions of the isolated species selectively, providing data for further clarification of the photochemistry of these compounds. The influence of the position of the methyl substituent in 1- and 2-methyl-substituted 5-aminotetrazoles on the photochemistry of these molecules has been evaluated.

4.5.1. UV-induced photochemistry of matrix-isolated 1MT

As described in chapter 2 (section 2.3), a sample of crystalline 1-methyl-5-aminotetrazole, **1MT**, was sublimated under reduced pressure (at ~ 60 °C), and the vapours of the compound were codeposited with argon (*ca.* 1:1000 molar ratio) onto a CsI substrate kept at 15 K. Figure 4.6a shows the infrared spectrum of **1MT** isolated in solid argon in the 3600-2900 and 2500-800 cm^{-1} regions. The full mid-IR range spectrum of **1MT** and the corresponding B3LYP/6-311++G(d,p) calculated spectrum are provided in Appendix; Figure S1.

In order to investigate the photochemistry of **1MT**, the deposited matrix was irradiated with UV light, as described in chapter 2 (section 2.6). The sample was monitored after each irradiation by recording its infrared spectrum.

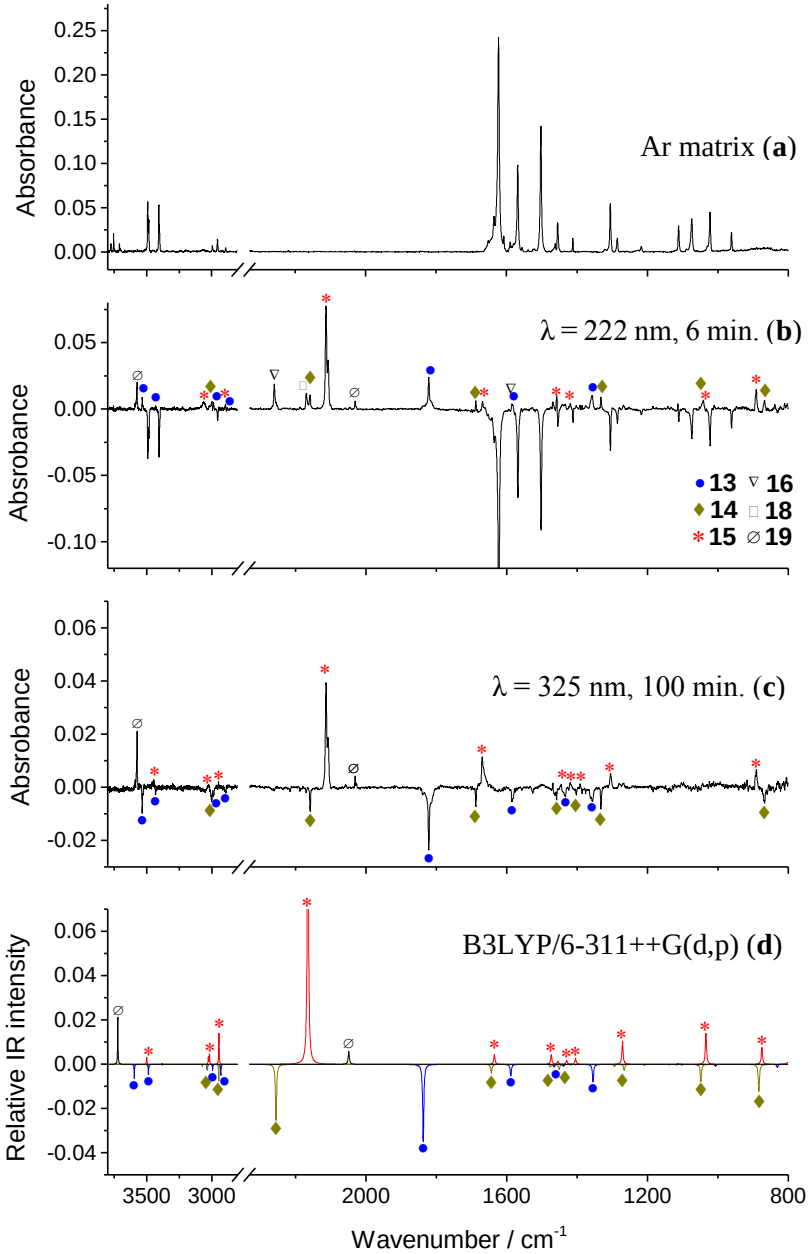

Figure 4.6 - (a) Experimental IR spectrum of 1-methyl-5-aminotetrazole **1MT**, isolated in solid argon. (b and c) Difference IR spectra, showing spectral changes upon irradiation: (b) after 6 min. of irradiation at λ = 222 nm (~17 mW) of matrix **1MT**; (c) after 100 min. of irradiation at λ = 325 nm (~22 mW), subsequent to the irradiation at λ = 222 nm for 6 min. In (c), the negative bands, blue circles and green rhombi correspond to the consumed diazirine **13** and cyanamide **14**, respectively. The bands with red stars correspond to carbodiimide **15**. (d) Theoretically calculated IR spectra of diazirine **13**, cyanamide **14**, carbodiimide **15** and CNH **19**.

Compound **1MT** was irradiated with monochromatic UV-light at λ = 222 nm. Figure 4.6b shows the matrix spectrum of **1MT** after irradiation for a total of 6 min, when around 60% of **1MT** was consumed and photoproducts **13-19** were produced (see also Scheme 4.4).

Photoproducts **13** (1822 cm^{-1}) and **14** (2159 cm^{-1}) appeared immediately after the first seconds of irradiation, followed by the increase of bands due to photoproduct **15** (2113/2107 cm^{-1}). Kinetic studies for the photolysis of **1MT** (see Figure 4.7) indicated that the maximum amount of species **13** and **14** was reached after 60 s of irradiation at λ = 222 nm, and then started decreasing gradually, while bands due to photoproduct **15** kept increasing and those due two new photoproducts appeared. These new compounds were easily identified as cyanamide **16** (2261 cm^{-1}) and hydrogen isocyanide **19** (2031 cm^{-1}), based on previously reported IR spectra of these species in argon matrix.[15,51,67–69] Upon extended photolysis, new characteristic bands evolved, due to the isomerization of cyanamide **16** into carbodiimide **18** (2169 cm^{-1}), as previously reported.[67]

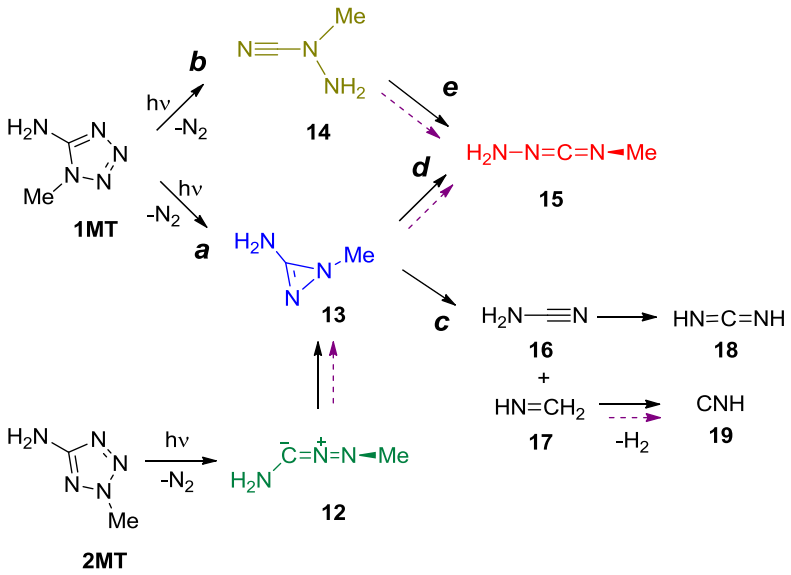

Scheme 4.4 - The photochemistry of matrix-isolated **1MT** and **2MT** was induced by using monochromatic UV light; (a) black plain arrows indicate the proposed pathways for the photolysis of tetrazoles **1MT** and **2MT**, at λ = 222 nm and λ = 250 nm, respectively, (b) violet dashed arrows indicate the proposed pathways when the matrix was irradiated at λ = 325 nm. Continuous irradiation of **1MT** at λ = 222 nm activates the primary photochemical ***pathways a*** and ***b***, then the secondary ***pathways c, d*** and ***e***. However, upon subsequent irradiation of the same matrix at λ = 325 nm, only ***pathways e*** and ***d*** were observed. Continuous irradiation of **2MT** at λ = 250 nm generates photoproduct **12**, which isomerises into **13**, then decomposes through photochemical ***pathways***, ***c*** and ***d***. However, upon subsequent irradiation of the same matrix at λ = 325 nm, only isomerization of **12** into **13**, and ***pathways d***, were observed.

Proposed assignments for the infrared absorptions of **1MT** and **2MT,** and observed photoproducts **12-19,** are included in Appendix; Table S10 - Table S19.

The characteristic bands due to photoproducts **13** and **15** were readily identified as diazirine **13** and carbodiimide **15**. As will be discussed in the next section, the same bands were observed from photolysis of isomer **2MT** in solid argon. The identification of products **13** and **15** was supported by theoretical calculations and by data from previous photochemical studies of matrix-isolated tetrazoles.[13,15,20] On the other hand, the immediate increase of distinctive absorption bands at 2159 cm^{-1} and 1688 cm^{-1} indicated the formation of an unknown primary photoproduct, **14**, obtained concomitantly with diazirine **13**. These results suggest that the formation of photoproducts **13** and **14**, occurring in the first stage of irradiation, involves two different pathways (***a*** and ***b***, respectively), both resulting from photocleavage of the tetrazole **1MT**. Then, as secondary processes, three different pathways are observed: ***pathways d*** and ***e*** correspond, respectively, to the rearrangement of primary photoproducts **13** and **14** to carbodiimide **15**; ***pathway c*** involves the decomposition of diazirine **13** into cyanamide **16** (that undergoes subsequent isomerization into carbodiimide **18**, at λ = 222 nm) and hydrogen isocyanide **19**.

It is noteworthy that the elusive diazirine **13** is one of the few observations of antiaromatic 1*H*-diazirines. The capture of such antiaromatic (*i.e.*, 4π systems) structures can be quite challenging, and has only been observed in a few cases, either upon isolation in cryogenic matrices of noble gases,[13,15,16,20,34,36] or in NMR monitored studies, at -50 ºC.[70]

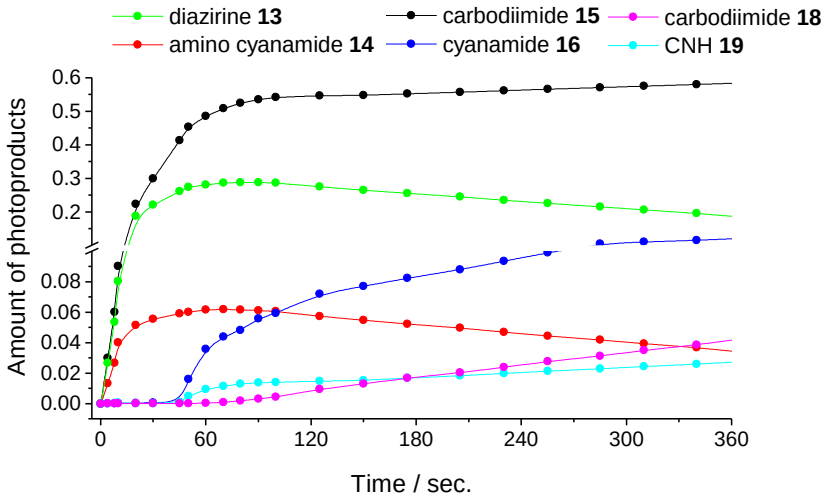

Figure 4.7 - Kinetic profiles showing changes of populations of the photoproducts **13** (1822 cm^{-1}), **14** (2159 cm^{-1}), **15** (2113/2107cm^{-1}), **16** (2261 cm^{-1}), **18** (2169 cm^{-1}) and **19** (2031 cm^{-1}) upon irradiation at λ = 222 nm of **1MT**. In these profiles, the "amount of photoproducts" corresponds to the integration of experimental band intensities, with maxima at indicated frequencies (see the kinetic measurements section for details).

To gather further evidence regarding the photocleavage pathways involved, a new experiment was designed: after irradiation of tetrazole **1MT** (at λ = 222 nm, 60 s), with generation of both photoproducts **13** and **14** in a maximal amount, we irradiated the matrix at λ = 325 nm, where the tetrazole **1MT** was observed to be photostable but its photoproducts could be transformed. These irradiation conditions resulted in photoreactions of the primary photoproducts **13** and **14**, leading to formation of carbodiimide **15**, in large amount, as sole photoproduct (see Figure 4.8, for kinetic profile). After 100 min. of irradiation at λ = 325 nm, when all **13** and **14** were consumed, the bands corresponding to carbodiimide **15** remained unaltered, even at extended irradiation times, indicating that this compound is photostable under the conditions used.

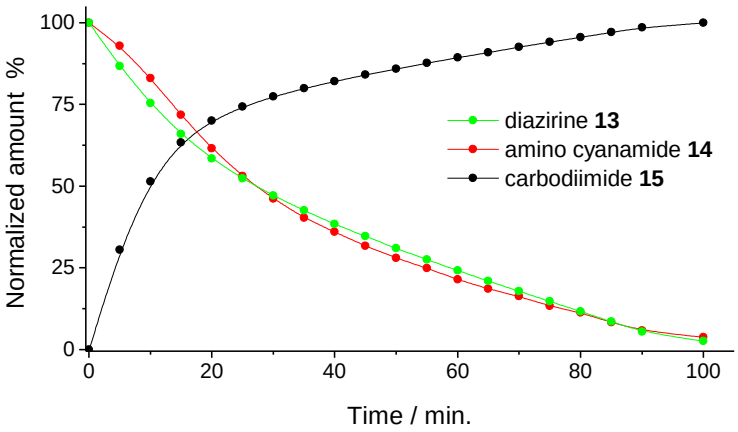

Figure 4.8 - Kinetic profiles showing consumption of matrix-isolated diazirine **13** (1822 cm^{-1}) and amino cyanamide **14** (2159 cm^{-1}) and formation of carbodiimide **15** (2113/2107 cm^{-1}), upon irradiation at λ = 325 nm (see the kinetic measurements section for details).

Altogether, the experimental evidence shows that irradiation at λ = 222 nm activates three different secondary photochemical processes of decomposition of the primary photoproducts **13** and **14**: ***pathways c***, ***d*** and ***e***. However, when a matrix containing the photoproducts **13** and **14** is irradiated at λ = 325 nm the photochemical ***pathway c*** is excluded, leading to a much cleaner spectrum (without the bands from photoproducts **16-18)**. Figure 4.6c shows the difference IR spectrum after irradiation at λ = 325 nm for 100 min., where we can observe the transformations of the primary photoproducts due to secondary photoreactions. The negative bands correspond to the consumed photoproducts **13** and **14** while the positive bands result from formation of photoproduct **15**. Thus, when irradiating at λ = 325 nm we can selectively activate ***pathways d*** and ***e***, which involve photoisomerization of photoproducts **13** and **14** into carbodiimide **15**. The spectrum in Figure 4.6c also shows the formation of some CNH **19**, which will be explained below.

The unknown species **14** could be unambiguously identified as amino cyanamide from comparison between experimental and calculated IR spectra. The absorption bands expected for **14** above 800 cm^{-1} are clearly observed in Figure 4.6c (as green rhombi; see also Figure 4.6d for theoretical IR spectra) and assigned in Table 4.1. The most characteristic band, at 2159 cm^{-1}, is assigned to the $\nu C{\equiv}N$ stretching mode, calculated at 2233 cm^{-1}. Also, a characteristic absorption at 1688 cm^{-1} fits the estimated vibration at 1627 cm^{-1}, which corresponds to the δNH_2 scissoring mode. The bands in the 1500-1400 cm^{-1} region correlate well with the calculated bands, and are assigned to the three δCH_3 bending modes. The band calculated at 1038 cm^{-1} could not be ascribed with certainty, though it seems to correspond mainly to one of the CH_3 rocking modes, appearing overlapped with the mixed $\nu NN/wNH_2$

vibration of carbodiimide **5**, observed in the experimental spectrum at 1042 cm^{-1}. As can be seen in Figure 4.6c, in the experimental difference IR spectrum resulting from the photochemistry of both **13** and **14** upon irradiation at λ = 325 nm, such superposition results in nearly cancelation of both bands (from the consumed reagent **14** and the formed product **15**). The experimental absorption bands above 2900 cm^{-1} were assigned to the anti-symmetric νNH_2 (3431 cm^{-1}) and νCH_3 (3054, 3008, and 2918 cm^{-1}) stretching vibrations, although some of the assignments shall be considered as tentative. Indeed, the bands due to the CH_3 stretching modes appearing in this spectral range are expected to have very low intensity, and the overlap of absorptions from both photoproducts (**14** and **15**) is also expectable, since they have similar predicted νNH_2 and νCH_3 stretching frequencies (see Table S14 and Table S15 in Appendix). All other bands of photoproduct **14**, observed at 1333 (νN_7C_6), 1185 (νN_7C_1; wNH_2), 1133 (γCH_3') and 868 (wNH_2) cm^{-1}, nicely fit with the calculated data (see Table 4.1).

Table 4.1 – Proposed band assignments for the observed IR bands of photoproduct amino cyanamide **14** (argon matrix; 15 K), and B3LYP/6-311++G(d,p) calculated vibrational wavenumbers (ν, cm^{-1}) and IR intensities (I, km mol^{-1}) for this molecule.[a,b]

	Ar matrix		Calculated	
Approximate description	ν	I^c	ν	I
νNH_2 as	3431	11	3445	9.2
νNH_2 s	-	-	3346	1.9
νCH_3 as''	3054	22	3044	7.2
νCH_3 as'	3008	22	3004	16.3
νCH_3 s	2918	17	2919	48.2
$\nu C{\equiv}N$	2159	67	2233	161.6
δNH_2	1688	45	1627	25.6
δCH_3 as''	1463	39	1461	8.5
δCH_3 as'	1434	22	1437	14.5
δCH_3 s	1403	11	1404	2.5
γNH_2	-	-	1281	6.2
νN_7C_6	1333	50	1254	18.1
νN_7C_1 ; wNH_2	1185	17	1197	3.2
γCH_3'	1133	17	1107	2.2
γCH_3''	1042	45	1038	49.7
wNH_2	868	62	875	80.5

[a] Calculated wavenumbers were scaled by 0.968. [b] ν, stretching; δ, bending; γ, rocking; w, wagging; s. symmetric; as, anti-symmetric. The primes in the approximate description of the methyl group vibrations refer to local symmetry of the mode, under assumption of methyl local *Cs* symmetry. [c] Experimental intensities, after 60 s of irradiation at λ = 222 nm, were obtained from the measured absorbances, by normalization to the total intensity of the observed counterparts.

Concerning ***pathway c***, it should be noted that the formation of cyanamide **16** could in principle result from either the cleavage of the tetrazole **1MT**, generating cyanamide and methyl

azide, or from cleavage of the diazirine **13**, generating cyanamide **16** and methylenimine **17**. However its formation via cleavage of the tetrazole **1MT** can be ruled out, since no evidence of methyl azide could be found in the photolyzed matrix. According to the available spectroscopic data, the νNNN anti-symmetric mode of methyl azide gives rise to an intense absorption band around 2100 cm^{-1}.[52] This expected intense band could not be observed, although we need to consider that it could be overlapped with the intense band due to carbodiimide **15**, at 2113/2107 cm^{-1}. Besides, several new bands could in principle also be assigned to methyl azide. However, after irradiations at λ = 325 nm, where **1MT** does not react and thus no formation of methyl azide from **1MT** should be observed, the bands kept increasing, providing clear indications that they belong to other photoproducts, and excluding the presence of methyl azide as putative photoproduct in the photolyzed matrix. This observation indicates that the formation of cyanamide **16** arises exclusively from photolysis of diazirine **13**, which can suffer a ring-opening photoreaction leading to cyanamide **16** and methylenimine **17**. It is well-known that the photodecomposition of matrix isolated methylenimine **17** gives rise to hydrogen isocyanide **19** by 1,1-H_2 elimination.[51,69] Also, evidence for the presence of these species (cyanamide **16**, methylenimine **17** and hydrogen isocyanide **19**) was observed only after formation of diazirine **13**. We could assign some of the observed bands to methyl imine **17**, although the assignment of bands due to this species is tentative due to the low intrinsic intensities of the bands of this species (see Table S17 in Appendix). However, formation of the photoproduct **19** was observed beyond doubt and, according to the available knowledge regarding the photochemistry of **17**, one can then expect that the formation of **19** should result essentially from the presence of methylenimine **17** in the matrix.

As previously explained, formation of cyanamide **16** was not observed upon irradiation at λ = 325 nm, suggesting that, at this wavelength, ***pathway c*** can be ruled out. However, as can be observed in Figure 4.6c, irradiation at λ = 325 nm led to formation of a small amount of hydrogen isocyanide **19**. We propose that this compound results from photodecomposition of the remaining methylenimine **17**, obtained in the first stage of irradiation, at λ = 222 nm.

The identification of the photoproducts was supported by results of earlier investigations regarding the photochemistry of the parent 5-amino tetrazole[15] and of 2-methyl-5-amino-tetrazole **2MT**[17,36], under low-temperature matrix-isolation conditions. In fact, a comparison between the observed bands in the photolysis of tetrazole **1MT** and the ones reported from earlier studies for the photolysis of the isomer **2MT**, reveals excellent correlation among several absorption bands, a clear evidence that the same photoproducts, **13** and **16-19**, were obtained in both cases. However, the previous studies on 2,5-substituted tetrazole **2MT** failed in the

correlation of one expected species, the carbodiimide **15**. In the previously investigations on the photolysis of **2MT**, several absorption bands were assigned to a methyl azide (including the distinguishable bands at 2113/2017 cm^{-1}) and different photodegradation pathways were proposed, but the carbodiimide **15** was excluded as final photoproduct.

In view of these inconsistencies, we decided to reinvestigate the photolysis of **2MT** using narrow band UV irradiation, which, as demonstrated above for **1MT**, can be expected also in this case to allow inducing selective photoconversion of the initially formed photoproducts of **2MT** without consuming this latter species. This procedure can help clarifying details of the photochemistry of the compound.

4.5.2. UV-induced photochemistry of matrix-isolated 2MT

Figure 4.9b shows the IR spectra of the matrix-isolated **2MT** after irradiation at λ = 250 nm (~ 40 mW) for a total of 4 s, when around 50% of **2MT** was consumed and bands corresponding to six different species were detected: photoproducts **12**, **13**, **15-17** and **19**. These photoproducts were readily identified as nitrile imine **12**, diazirine **13**, carbodiimide **15**, cyanamide **16**, methylenimine **17** and hydrogen isocyanide **19**, based on the previously described results for the photolysis of **1MT** and on data reported from earlier studies on the photolysis of **2MT**.[17,36] Indeed, in view of the generation of diazirine **13** as intermediate from the photolysis of both isomers **1MT** and **2MT**, it is reasonable to expect the same channels of photofragmentation of diazirine **13**, with formation of photoproducts **15-19** (***pathways c*** and ***d***) upon photolysis of both isomers. There is, however, one relevant difference: in the case of isomer **2MT**, the diazirine **13** results from photoisomerization of nitrile imine **12**, detected during our experiments. The formation of cyanamide **16** and methylenimine **17** could result from either the photofragmentation of diazirine **13**, as previously described for the photolysis of **1MT**, or directly form nitrile imine **12**, as was observed for the parent unsubstituted 5-aminotetrazole.[15] However, during photolysis of **2MT** the bands due to cyanamide **16** were only observed after formation of diazirine **13**, and kept increasing even after total consumption of nitrile imine **12** (see the kinetic profiles in Figure 4.10), in keeping with the results obtained from the photolysis of **1MT**, where we never observed any evidence of formation of nitrile imine species. It should also be noted that the formation of carbodiimide **18** was only observed in a separate experiment, when a matrix containing the photoproduct cyanamide **16** was irradiated at $\lambda < 230$ nm.

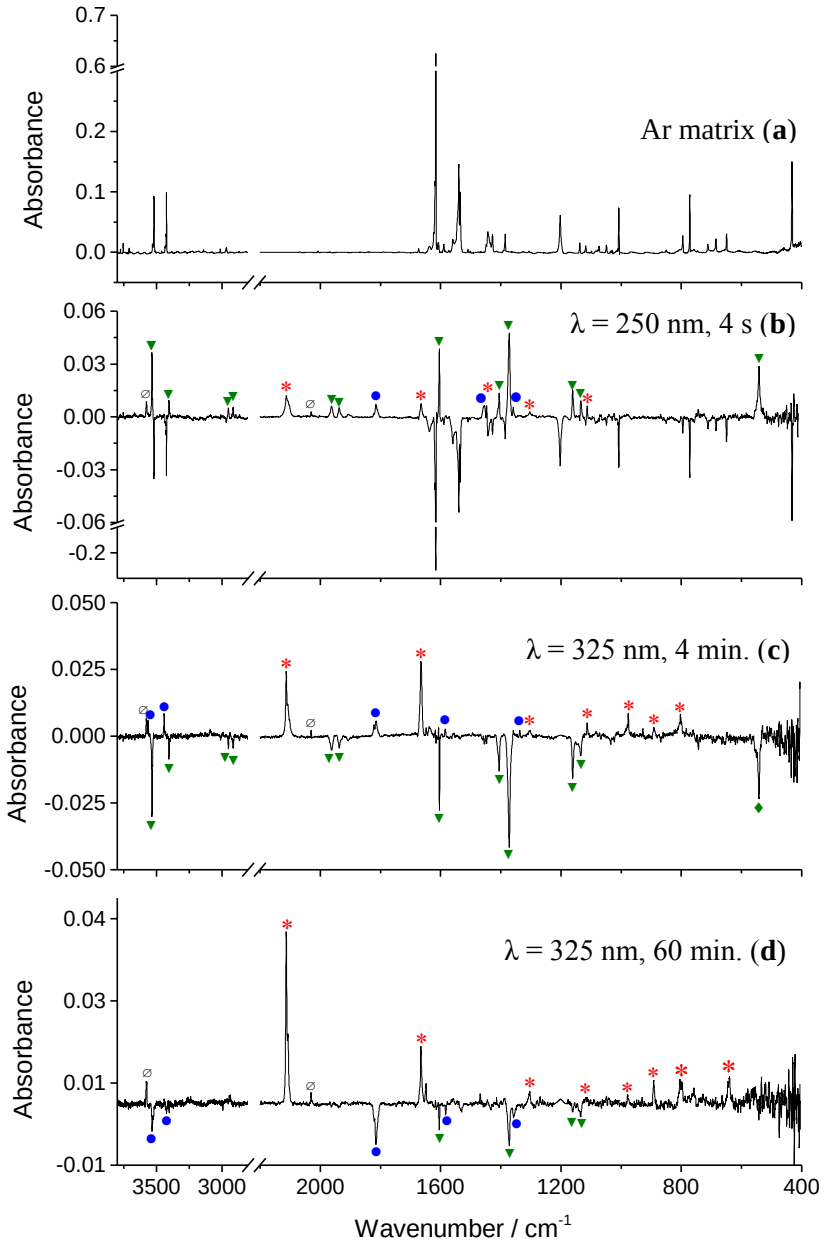

Figure 4.9 - (a) Experimental IR spectrum of 2-methyl-5-aminotetrazole **2MT**, in solid argon at 15 K. (b, c and d) Difference IR spectra in solid argon showing spectral changes: (b) after 4 s of UV irradiation at λ = 250 nm (~40 mW) of matrix isolated **2MT**; (c) after 4 min. of irradiation at λ = 325 nm (~22 mW) subsequently to the irradiation of 4 s at λ = 250 nm. In (c) the negative bands with olive triangles correspond to the consumed nitrile imine **12**. The blue circles and red stars are assigned to diazirine **13** and carbodiimide **15**, respectively; (d) after +60 min. of irradiation at λ = 325 nm, subsequently to the 4 min. of irradiation under the same conditions.

In summary the nitrile imine **12** (1963/1937 cm^{-1}) is the main species generated in the first second of irradiation, starting to be consumed after two seconds of irradiation with concomitant increase of diazirine **13** (1822 cm^{-1}), followed by photoproducts: cyanamide **16** (2261 cm^{-1}) hydrogen isocyanide **19** (2031 cm^{-1}) and carbodiimide **15** (2113/2107 cm^{-1}).

Irradiations of this same solid matrix at λ = 325 nm, where **2MT** remains photostable, resulted in two different observations (see the experimental IR in Figure 4.9 and the kinetic profiles in Figure 4.11): i) during the first 4 min of irradiation all the nitrile imine **12** is consumed, with concomitant increase of diazirine **13** and carbodiimide **15**; ii) after the first 4 min of irradiation, the bands due to diazirine **13** starts to decrease, with concomitant growth of those due to carbodiimide **15**, as sole photoproduct, until all the diazirine **13** is consumed. As observed during photolysis of the isomer **1MT**, when the matrix containing the photoproduct **13** (from isomer **1MT**) was irradiated at λ = 325 nm the photochemical ***pathway c*** was excluded.

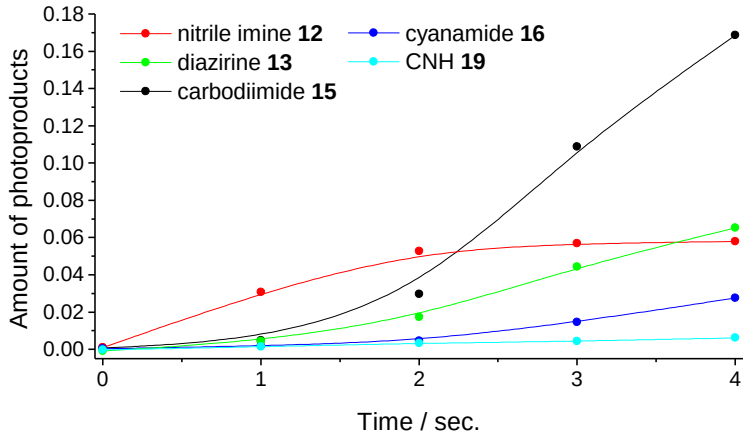

Figure 4.10 - Kinetic profiles showing changes of populations of the photoproducts **12** (1963 cm^{-1}) **13** (1822 cm^{-1}), **15** (2113/2107cm^{-1}), **16** (2261 cm^{-1}) and **19** (2031 cm^{-1}), upon irradiation at λ = 250 nm of matrix-isolated **2MT**. In these profiles, the "amount of photoproducts" corresponds to the integral of experimental band intensities, with maxima at indicated frequencies (see the kinetic measurements section for details).

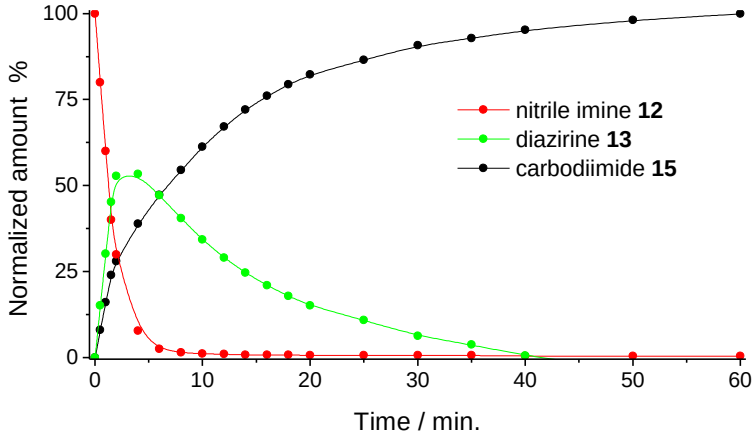

Figure 4.11 - Kinetic profiles showing changes of matrix-isolated nitrile imine **12** (1963 cm^{-1}) to carbodiimide **15** (2113/2107 cm^{-1}) via diazirine **13** (1822 cm^{-1}) upon irradiation at λ = 325 nm (see the kinetic measurements section for details).

These results unequivocally demonstrate that the 5-amino tetrazole **2MT** follows the photofragmentation patterns observed for other 2*H*-tetrazoles, with generation of nitrile imine **12** by extrusion of N_2, followed by its photoisomerization into diazirine **13** that subsequently photoisomerizes to carbodiimide **15** as final photoproduct.[1,13,15,17,20,21,39] As previously reported, the experimental IR bands at 1963 and 1937 cm^{-1} due to the νCNN anti-symmetric stretching suggests a significant carbenic character of the amino nitrile imine **12**.[17] These results are in agreement with those obtained for the parent *C*-amino nitrile imine (which was ascribed to bear a contribution of around 20% of the carbenic resonance hybrid).[15]

In contrast, during the photolysis of **1MT** we never observed any evidence of formation of a nitrile imine species, even after carefully searching for evidence during the first few seconds of irradiation (when nitrile imines are usually known to be observed). This result may mean that only 2*H*-tetrazoles could provide direct access to nitrile imines. On the other hand, the formation of amino cyanamide **14** from UV-irradiation of isomer **1MT**, was observed for the first time from photolysis of tetrazoles under low temperature matrices, and seems to be exclusively generated during photolysis of the isomeric form **1MT**, however, the mechanistic pathway for formation of species **14** upon irradiation of isomer **1MT** is not clear.

During the photochemical study of the 5-methyl-tetrazole, Nunes *et al.*[20] have shown that 1*H*-diazirines exhibit a close structural relation to imidoylnitrenes, postulated intermediates in this reaction (see chapter 1; section 1.1.7.7 iv). Indeed, geometry optimization at the B3LYP/cc-pVTZ level, of 5-methyl-1*H*-diazirine on the triplet state was found to converge to the respective imidoylnitrene structure.[20]

The $C_2H_5N_3$ isomers were calculated at the B3LYP/6-311++G(d,p) level and the structures are represented in Figure 4.12. The calculated energies indicate that 1*H*-diazirine **13** is the most energetic species in the singlet state; ∼22 and ∼11 kJ mol^{-1} below the imidoylnitrene triplet state ^{T}**N1** and ^{T}**N2**, respectively. The high energetic character of **13**, 94.1 kJ mol^{-1} above the amino cyanamide **14** (calculated as the most stable isomer) is conceivably due to both ring strain and antiaromatic destabilization. The observed trends for these isomeric species, are similar to the trends found in calculations for $H_4C_2N_2$ and H_2CN_2 isomers, which can be formed from the photolysis of 5-methyl-tetrazole and of the parent unsubstituted tetrazole, respectively.[20,39] Note that the optimized isomeric form *E* of imidoylnitrene (^{T}**N2**) is more stable than form *Z* (^{T}**N1**) by ∼ 10 kJ mol^{-1}.

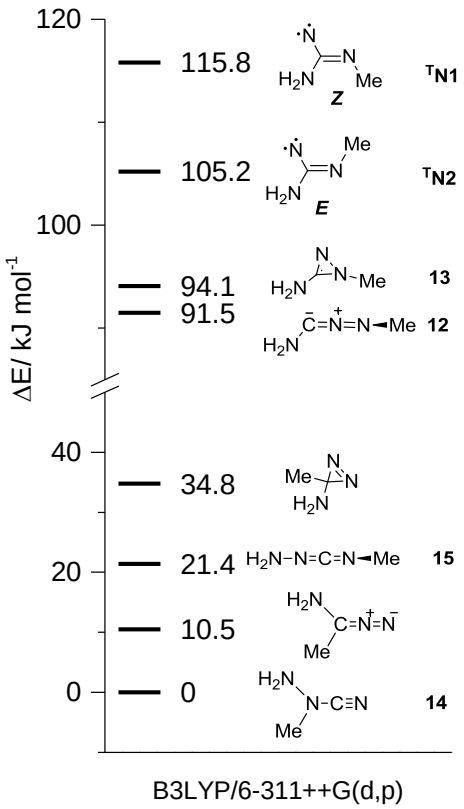

Figure 4.12 - Energies of eight $C_2H_5N_3$ isomers calculated at the B3LYP/6-311++G(d,p) level (with the ZPE correction included). The energies (in kJ mol^{-1}) are relative to the most stable isomer. For imidoylnitrene strutures **^{T}N1** and **^{T}N2** the calculated energy was based on the optimized triplet state geometries.

Accordingly to these results we postulated the formation of imidoylnitrene species, which could have different *E*/*Z* orientation, with only the one resulting from **1MT** enabling formation of amino cyanamide **14**. This could explain the different photochemical pathways observed for isomers **1MT** and **2MT**.

In Figure 4.13, a potential mechanism for the photochemical transformations of the **1MT** and **2MT** isomers is presented. As explained above, photolysis of isolated **1MT** results in cleavage of the tetrazole ring with extrusion of molecular nitrogen, generating the postulated imidoylnitrene intermediate **N1**. Under this hypothesis, it is likely that the open-shell singlet imidoylnitrene **^{S}N1** better described as a 1,3-diradical, collapses easily once formed, closing the NCN ring to give the observed 1*H*-diarzirine **13** (*pathway ii)* in Figure 4.13). Indeed, 1*H*-diazirine was shown to be a common photoproduct from photolysis of both isomers **1MT** and **2MT**. Thus, the remaining *pathway ii)* is expected to follow the same mechanism for both the **1MT** and **2MT** isomeric compounds, as will be explained below.

On the other hand, in the *Z* isomeric form of **N1**, the methyl substituent seems to preclude the 1,3-hydrogen shift from the amino group into the substituted nitrogen, instead the hydrogen is forced to migrate to the available unsubstituted nitrogen (see ^{S}**N1** in Figure 4.13).

Consistent with Hund's rule, the low energy form of nitrenes is a triplet state with one electron in each of the p orbitals and the high energy form is the singlet state with an electron pair filling one p orbital and the other one vacant. Although most of known nitrenes tend to cross to the triplet ground state,[71,72] it can be conceivably hypothesised that the high energy singlet state of imidoylnitrene ^{S}**N1**, directly obtained from cleavage of the tetrazole ring of **1MT**, is responsible for the formation of the observed amino cyanamide **14**, through various intramolecular hydrogen-atom shifts, including three member ring-closure/opening as can be observed in the postulated *pathway i)* in Figure 4.13.

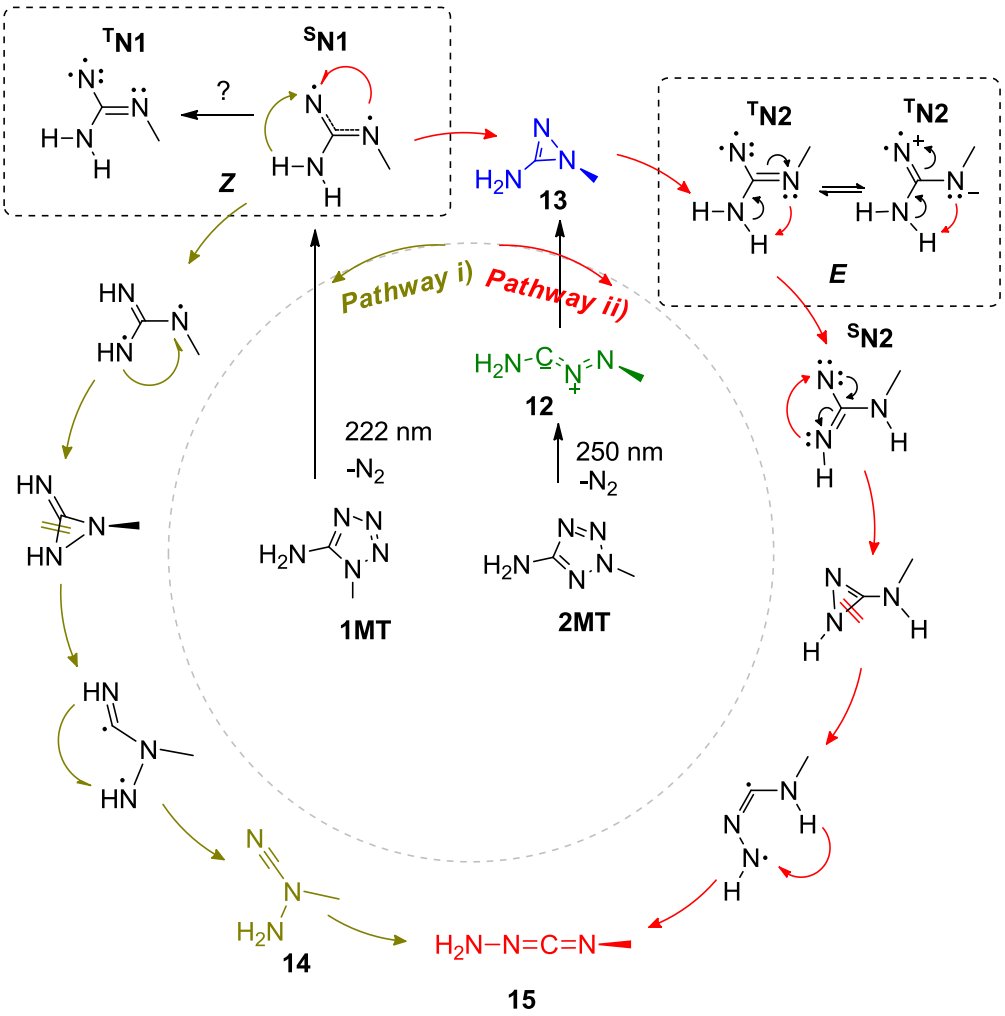

Figure 4.13 – Mechanistic proposal for the UV-induced photochemical pathways of **1MT** and **2MT** isolated in a low-temperature argon matrix.

As shown above, photolysis of **2MT** results in the cleavage of the tetrazole ring, with initial formation of nitrile imine **12** that develops to diazirine **13**. This last one is expected to generate the most stable imidoylnitrene, the *E* isomeric form **N2** (Figure 4.12 shows the relative energies of both imidoylnitrene isomers), through ring opening, precluding the *pathway i)* that would lead to formation of the amino cyanamide **14**. In fact, this seems to be the reason for the different photochemical pathways observed for the isomers **1MT** and **2MT**. Moreover, with photolysis of diazirine **13** the nitrene can be generated in the triplet state directly (**^{T}N2**, Figure 4.13), as was previously observed by McConaghy *et al*. during photolysis of ethyl azidoformate.[72,73] Structurally, the imidoylnitrene can be visualized as delocalized resonance structures **^{T}N2**.[72] It seems that in the *E* isomeric form **N2**, the methyl substituent is no longer blocking the 1,3-hydrogen shift from the amino group to the substituted nitrogen, actually the lone pair of the substituted nitrogen is now available to remove the hydrogen from the amino group, leading to the observed carbodiimide though the postulated *pathway ii)*, which involves a transition to the singlet state **^{S}N2**, leaving one vacant orbital on the unsubstituted nitrogen, allowing to the three member ring closure/opening, and a 1,4-hidrogen shift and finally generating the observed carbodiimide **15**.

One may also suppose that this reaction can occur via a direct amino group shift, from the carbon of the imidoylnitrene (**N1** and **N2**) to the nitrene moiety, in order to obtain the expected carbodiimide **15**. However, the kinetic barriers to such 1,2-amino group shifts in a rigid argon matrix can be expected to correspond to high energy transition structures, and seem to be unlikely. Indeed, the rearrangements shown in Figure 4.13 allow for a smooth conversion of the postulated imidoylnitrenes **N1** and **N2**, initially obtained, into the observed amino cyanamide **14** and carbodiimide **15**. Moreover, these rearrangements seem to explain the selective formation of amino cyanamide **14** from **1MT**, and the common pathway through diazirine **13** during photolysis of both **1MT** and **2MT** isomers.

On final note should be made in relation to the photochemical rearrangement of the amino cyanamide **14** into carbodiimide **15**. According to the calculated energies for these isomers (Figure 4.12), the amino cyanamide **14** is expected to be more stable than the carbodiimide **15**, by ~21 kJ mol^{-1}. Nevertheless, the rearrangement of **14** into **15** was shown to occur under the experimental conditions used, and can be expected to proceed though a 1,3-shift of the methyl group.

In order to provide support to our mechanistic proposals, it would be important to gather evidence for formation of nitrene species in the photodegradation of these tetrazoles, since the structure of these intermediates appears to determine the photochemical pathways. As such, to

attempt trapping and identification of these imidoylnitrene species, preliminary EPR (electron paramagnetic resonance) experiments in cryogenic conditions were performed at the laboratories of Professor Manabu Abe, in Hiroshima, where suitable equipment is available. In this preliminary EPR studies, the compounds were degassed under high vacuum, and cooled to 5 K in the EPR cavity, and then, irradiated for 60 min at 266 nm (~10 mJ), affording the EPR spectrum of triplet nitrene, at ~8200 gausses at 9.38 GHz, from the photolysis of the **2MT**, a clear evidence that the postulated imidoylnitrene species could in fact be an intermediate in this reaction (see Figure S4 in Appendix).

In similar experiments conducted with **1MT** no signal that could be ascribed to a nitrene was observed, however, we have to consider that this could be due to the low solubility of **1MT** in the solvent used. **1MT** is known to have much lower solubility than the isomer **2MT** in 2-methyl-THF (2-methyl-tetrahydrofuran), which could result in a concentration that would not be sufficient for detecting the nitrene signal. Moreover, the wavelength of the irradiation used (λ = 266 nm) is far from the maximum absorption (~222 nm) observed for **1MT**, as explained in the matrix isolation experiments.

One final note should be made in relation to the increased photostability of the tetrazole ring and the nitrile imine intermediate, introduced by the saccharyl system, in the **2MTS** conjugate, discussed in the previous section. Comparing the photochemistry of the conjugate **2MTS**, with the parent tetrazolyl moiety **2MT**, here discussed in detail, we can clearly see that the reaction pathways and obtained photoproducts are equivalent on both compounds (see Scheme 4.5 for a schematic comparison of pathways for **2MTS** and **2MT**). However photolysis of matrix-isolated **2MT** at λ = 250 nm generated nitrile imine **12** in a maximal amount after 2s of irradiation and, after 4 min of irradiation, all nitrile imine was consumed. Also, *ca.* 50% of the initial compound **2MT** was consumed after 4s of irradiation. On the other hand, the photolysis of **2MTS** at λ = 250 nm, generated nitrile imine **6** in a maximal amount after 5 min of irradiation, and only after 60 min of irradiation all nitrile imine was consumed. Moreover, *ca.* 50% of the initial **2MTS** was consumed only after 2 min of irradiation. These results suggest that the saccharyl system increases the photostability of the tetrazole ring and also of the nitrilimine intermediate by more than 20x, compared to parent tetrazole **2MT**.

As pointed out in chapter 1, section 1.1.7.6, heterocycles find wide applications in coordination chemistry as ligands and, among them, tetrazoles are known to play an important role. Indeed, when using bis-tetrazoles, or other conjugates where the tetrazole ring is linked to other heterocycles, in coordination chemistry, the quite low photochemical stability of tetrazoles has always been an issue. As such, when considering the applications of saccharyl-tetrazole conjugates, the remarkable increase of photostability induced by the saccharyl system appears as an important advantage of these novel conjugates over bis-tetrazoles.

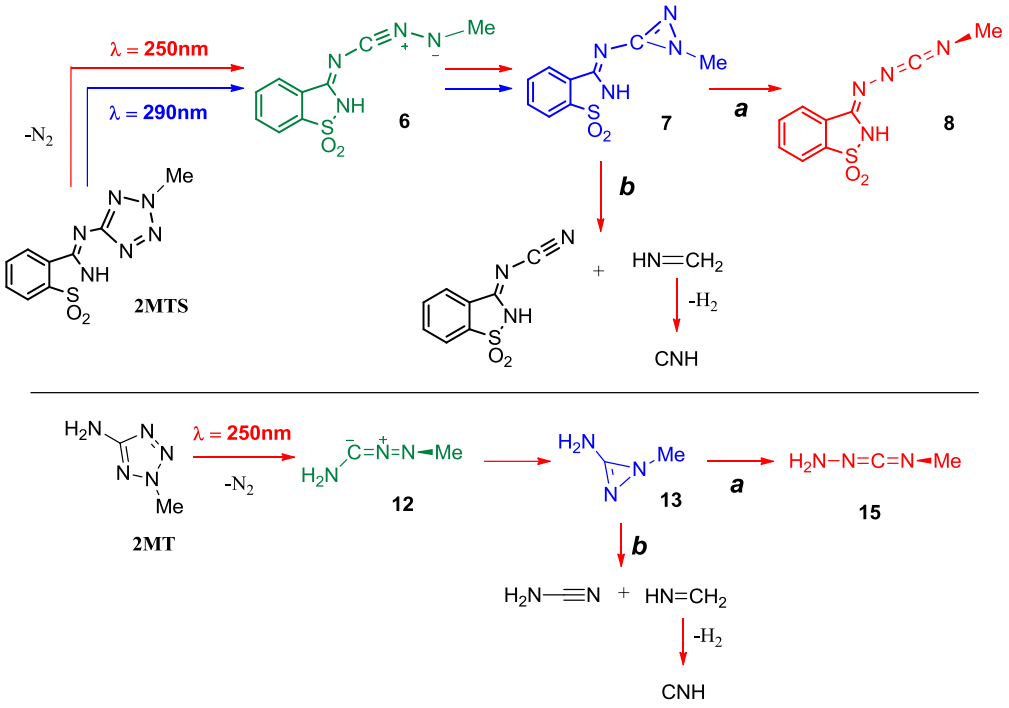

Scheme 4.5 - Proposed reaction pathways resulting from irradiation of a matrix containing monomeric **2MTS** or **2MT**, isolated in solid argon. Kinetic investigation on initial compounds, **2MTS** or **2MT**, and intermediates **6** and **12**, indicates: i) photolysis of **2MTS** at λ = 250 nm generated nitrile imine **6** in a maximal amount after 5 min and was totally consumed after 60 min; *ca.* 50% of **2MTS** was consumed after 2 min; ii) photolysis of **2MT** at λ = 250 nm generated, nitrile imine **12** in a maximal amount after 2s and was totally consumed after 4 min; *ca.* 50% of **2MT** was consumed after 4s.

4.5.3. Conclusions

We isolated compounds **1MT** and **2MT** in solid argon and studied their matrix photochemistry.

Photolysis of matrix-isolated **1MT** at λ = 222 nm results in species **13-19**, obtained in two stages. The photoproducts diazirine **13** and amino cyanamide **14** are obtained in a first stage of irradiation (primary photoproducts), through two different pathways, both resulting from the photocleavage of tetrazole **1MT**. In a second stage two different pathways are observed, involving isomerization of both diazirine **13** and amino cyanamide **14** into carbodiimide **15**. A third pathway is also observed, involving decomposition of diazirine **13** into photoproducts **16-19**. However, with subsequent irradiations of the matrix containing compounds **13** and **14** at λ = 325 nm, we could prevent decomposition of diazirine **13** and exclude this last photochemical pathway, simplifying the interpretation of the experimental spectra and rendering the interpretation of the photochemical pathways easier.

Photolysis of matrix-isolated **2MT** at λ = 250 nm results in products, **12**, **13**, **15-17** and **19**, obtained in two stages. Nitrile imine **12** is the main species generated in the first second of irradiation, isomerising readily into diazirine **13** (also obtained from photolysis of the matrix-isolated isomer **1MT**). These results unequivocally demonstrate that the amino tetrazole **2MT** follows the same photofragmentation patterns observed for other 2*H*-tetrazoles, with extrusion of N_2 and production of nitrile imine that photoisomerizes into diazirine that, subsequently, also photoisomerizes, leading to carbodiimide as final product.

Interestingly, we found that the photochemistry of the two isomers, **1MT** and **2MT**, although resulting in the same intermediate diazirine **13,** which undergo subsequent photoconversion into carbodiimide **15**, seems to follow different pathways. In fact, the amino cyanamide **14** was exclusively obtained from photocleavage of the isomer **1MT**, whereas the nitrile imine **13** was exclusively obtained during the photolysis of **2MT**. This exclusive formation of nitrile imine from the isomer **2MT** could mean that only the 2*H*-tetrazoles forms can give a direct access to nitrile imines, while observation of the amino cyanamide **14** represents a novel reaction pathway in the photochemistry of tetrazoles and seems to be characteristic of 1*H*-tetrazoles.

We could assign the vibrational absorptions of the various photoproducts and propose the different photochemical pathways. However, the mechanistic pathway for formation of the species **14**, obtained from irradiation of isomer **1MT**, is only tentative. We postulate the formation of nitrene species, which could have different structures, with only the one resulting

from **1MT** enabling formation of amino cyanamide **14**. This could explain the different photochemical pathways observed for isomers **1MT** and **2MT**. We were able to observe a signal corresponding to a triplet nitrene species arising from the photolysis of **2MT**, clearly indicating that the postulated imidoylnitrene species might be an intermediate in this reaction. However no such signals were yet observed for the case of **1MT.** The proposal of adequately supported mechanisms for these reactions still requires further investigation.

The photochemistries of **2MTS** and of the parent tetrazole **2MT** proved to be quite similar regarding reaction pathways and the nature of the photoproducts, which is equivalent on both compounds. However, the saccharyl system was found to increase substantially (by more than 20 times) the photostability of the tetrazole ring and of the nitrilimine intermediate, compared to parent **2MT**.

4.5.4. Kinetic measurements

Figure 4.7 shows one experiment where the species isolated in the matrix were irradiated for a total amount of 6 min, at λ = 222 nm, when around 60% of **1MT** was consumed and several different photoproducts (**13**-**19**) were formed. Figure 4.8 shows a different experiment where the first irradiation was performed at λ = 222 nm, to generate the maximum amount of diazirine **13** and amino cyanamide **14**. During this experiment, generation of **15** and **16** was also observed. The outset of the kinetics in Figure 4.8 corresponds to the end (60 s) of the previous irradiation (λ = 222 nm). For the second part of the experiments, with irradiation at λ = 325 nm, the relative amounts of **13**, **14**, and **15** were assumed as 100, 100, and 0%, respectively. After 100 min, **13** and **15** were completely consumed, and the produced amount of **15** was set to 100%. Figure 4.10 shows one experiment where the species isolated in the matrix were irradiated for a total amount of 4 s at λ = 250, when around 50% of **2MT** was consumed and several different photoproducts (**12**, **13**, **15**, **16**, and **19**) were formed. The aim of the experiment performed with irradiation at λ = 250 nm was to produce the maximum amount of nitrile imine **12**. Generation of species **13**, **15**, and **16** was also observed. The outset of the kinetics in Figure 4.11 corresponds to the end of the previous irradiation (λ = 250 nm). For the experiments carried out with irradiation at λ = 325 nm, the relative amounts of **12**, **13**, and **15** were assumed as 100, 0, and 0%, respectively. After 60 min of this irradiation, **12** and **13** were completely consumed, and the generated amount of **15** was set to 100%. At 4 min, the total amount of **12** and **15** was ~46.7% and achieved the bottom. The residual was parameterized to 53% as the maximal amount of **13** generated. All the amounts of species

shown in those figures correspond to the integrals of experimental band intensities, with maxima at indicated frequencies.

4.6. References

(1) Bégué, D.; Qiao, G. G.; Wentrup, C. *J. Am. Chem. Soc.* **2012**, *134* (11), 5339–5350.
(2) Ismael, A.; Henriques, M. S. da C.; Marques, C. F. S.; Rodrigues, M. J.; Barreira, L. A.; Paixão, J. A.; Fausto, R.; Cristiano, M. L. S. *RSC Adv.* **2016**, *6* (75), 71628–71637.
(3) Cho, D. W.; Oh, S. W.; Kim, D. U.; Park, H. J.; Xue, J. Y.; Yoon, U. C.; Mariano, P. S. *Bull. Korean Chem. Soc.* **2010**, *31* (9), 2453–2458.
(4) Elghamry, I.; Dopp, D.; Henkel, G. *J. Heterocycl. Chem.* **2007**, *44* (4), 849–852.
(5) Döpp, D.; Lauterfeld, P.; Schneider, M.; Schneider, D.; Henkel, G.; Abd el Sayed Issac, Y.; Elghamry, I. *Synthesis (Stuttg).* **2001**, *112* (8), 1228–1235.
(6) Elghamry, I.; Dopp, D. *Tetrahedron Lett.* **2001**, *42* (33), 5651–5653.
(7) Döpp, D. *Int. J. Photoenergy* **2001**, *3* (1), 41–48.
(8) Ono, I.; Sato, S.; Fukuda, K.; Inayoshi, T. *Bull. Chem. Soc. Jpn.* **1997**, *70* (9), 2051–2055.
(9) Yoon, U. C.; Koh, Y. S.; Him, H. J.; Jung, D. Y.; Kim, D. U.; Cho, S. J.; Lee, S. J. *Bull. Korean Chem. Soc.* **1994**, *15* (9), 743–748.
(10) Kamigata, N.; Saegusa, T.; Fujie, S.; Kobayashi, M. *Chem. Lett.* **1979**, No. 1, 9–12.
(11) Ismael, A.; Borba, A.; Duarte, L.; Giuliano, B. M.; Gómez-Zavaglia, A.; Cristiano, M. L. S. *J. Mol. Struct.* **2012**, *1025*, 105–116.
(12) Duarte, L.; Reva, I.; Cristiano, M. de L. S.; Fausto, R. *J. Org. Chem.* **2013**, *78* (7), 3271–3275.
(13) Nunes, C. M.; Reva, I.; Fausto, R.; Bégué, D.; Wentrup, C. *Chem. Commun.* **2015**, *51*, 14712–14715.
(14) Borba, A.; Cabral, L. I. L.; Fausto, R.; Cristiano, M. L. S. *Can. J. Chem.* **2015**, *10* (April), 150421143716005.
(15) Nunes, C. M.; Reva, I.; Rosado, M. T. S.; Fausto, R. *European J. Org. Chem.* **2015**, No. 34, 7484–7493.
(16) Ismael, A.; Borba, A.; Henriques, M. S. C.; Paixão, J. A.; Fausto, R.; Cristiano, M. L. S. *J. Org. Chem.* **2015**, *80* (1), 392–400.
(17) Baskir, E. G.; Platonov, D. N.; Tomilov, Y. V.; Nefedov, O. M. *Mendeleev Commun.* **2014**, *24* (4), 197–200.
(18) Pagacz-Kostrzewa, M.; Krupa, J.; Wierzejewska, M. *J. Photochem. Photobiol. A Chem.* **2014**, *277*, 37–44.
(19) Frija, L. M. T.; Cristiano, M. L. S.; Gómez-Zavaglia, A.; Reva, I.; Fausto, R. *J. Photochem. Photobiol. C Photochem. Rev.* **2014**, *18*, 71–90.
(20) Nunes, C. M.; Araujo-Andrade, C.; Fausto, R.; Reva, I. *J. Org. Chem.* **2014**, *79* (8), 3641–3646.
(21) Pagacz-Kostrzewa, M.; Mucha, M.; Weselski, M.; Wierzejewska, M. *J. Photochem. Photobiol. A Chem.* **2013**, *251*, 118–127.
(22) Ismael, A.; Serpa, C.; Cristiano, M. L. S. *Photochem. Photobiol. Sci.* **2012**, *12* (2), 272–283.
(23) Alawode, O. E.; Robinson, C.; Rayat, S. *J. Org. Chem.* **2011**, *76* (1), 216–222.
(24) Pagacz-Kostrzewa, M.; Krupa, J.; Olbert-Majkut, A.; Podruczna, M.; Bronisz, R.; Wierzejewska, M. *Tetrahedron* **2011**, *67* (44), 8572–8582.
(25) Pagacz-Kostrzewa, M.; Reva, I. D.; Bronisz, R.; Giuliano, B. M.; Fausto, R.; Wierzejewska, M. *J. Phys. Chem. A* **2011**, *115* (22), 5693–5707.
(26) Ismael, A.; Cristiano, M. L. S.; Fausto, R.; Gómez-Zavaglia, A. *J. Phys. Chem. A* **2010**,

114 (50), 13076–13085.
(27) Frija, L. M. T.; Ismael, A.; Cristiano, M. L. S. *Molecules* **2010**, *15* (5), 3757–3774.
(28) Frija, L. M. T.; Khmelinskii, I. V; Serpa, C.; Reva, I. D.; Fausto, R.; Cristiano, M. L. S. *Org. Biomol. Chem.* **2008**, *6* (6), 1046–1055.
(29) Quast, H.; Bieber, L. W. *J. Org. Chem.* **2008**, *73* (10), 3738–3744.
(30) Frija, L. M. T.; Reva, I. D.; Gómez-Zavaglia, A.; Cristiano, M. L. S.; Fausto, R. *J. Phys. Chem. A* **2007**, *111* (15), 2879–2888.
(31) Frija, L. M. T.; Reva, I. D.; Gómez-Zavaglia, A.; Cristiano, M. L. S.; Fausto, R. *Photochem. Photobiol. Sci.* **2007**, *6* (11), 1170–1176.
(32) Gómez-Zavaglia, A.; Reva, I. D.; Frija, L.; Cristiano, M. L.; Fausto, R. *J. Photochem. Photobiol. A-Chemistry* **2006**, *179* (3), 243–255.
(33) Frija, L. M. T.; Khmelinskii, I. V; Cristiano, M. L. S. *J. Org. Chem.* **2006**, *71* (9), 3583–3591.
(34) Gómez-Zavaglia, A.; Reva, I.; Frija, L.; Cristiano, M.; Fausto, R. *J. Mol. Struct.* **2006**, *786* (2–3), 182–192.
(35) Gómez-Zavaglia, A.; Reva, I. D.; Frija, L.; Cristiano, M. L. S.; Fausto, R. *J. Photochem. Photobiol. A Chem.* **2006**, *180* (1–2), 175–183.
(36) Gómez-Zavaglia, A.; Reva, I. D.; Frija, L.; Cristiano, M. L.; Fausto, R. *J. Phys. Chem. A* **2005**, *109* (35), 7967–7976.
(37) Frija, L. M. T.; Khmelinskii, I. V; Cristiano, M. L. S. *Tetrahedron Lett.* **2005**, *46* (39), 6757–6760.
(38) Awadallah, A.; Kowski, K.; Rademacher, P. *J. Heterocycl. Chem.* **1997**, *34* (1), 113–122.
(39) Maier, G. G.; Eckwert, J. J.; Bothur, A.; Reisenauer, H. P.; Schmidt, C. *Liebigs Ann.* **1996**, No. 7, 1041–1053.
(40) Bertrand, G.; Wentrup, C. *Angew. Chemie Int. Ed. English* **1994**, *33*, 527–545.
(41) Dunkin, I. R.; Shields, C. J.; Quast, H. *Tetrahedron* **1989**, *45* (1), 259–268.
(42) Quast, H.; Fuss, A.; Nahr, U. *Chem. Berichte-Recueil* **1985**, *118* (6), 2164–2185.
(43) Quast, H.; Nahr, U. *Chem. Berichte-Recueil* **1985**, *118* (2), 526–540.
(44) Quast, H.; Nahr, U. *Chem. Berichte-Recueil* **1983**, *116* (10), 3427–3437.
(45) Quast, H.; Bieber, L. *Chem. Berichte-Recueil* **1981**, *114* (10), 3253–3272.
(46) Quast, H. *Heterocycles* **1980**, *14* (10), 1677–1702.
(47) Quast, H.; Bieber, L. *Angew. Chemie-International Ed. English* **1975**, *14* (6), 428–429.
(48) Hyatt, J. A.; Swenton, J. S. *J. Org. Chem.* **1972**, *37* (21), 3216–3220.
(49) Nguyen, M. T.; Sengupta, D.; Ha, T.-K. *J. Phys. Chem.* **1996**, *100* (16), 6499–6503.
(50) Nguyen, M. T. *Chem. Phys. Lett.* **1985**, *117* (3), 290–294.
(51) Milligan, D. E.; Jacox, M. E. *J. Chem. Phys.* **1963**, *39* (3), 712.
(52) Milligan, D. E. *J. Chem. Phys.* **1961**, *35* (4), 1491.
(53) Chalmers, J. M.; Griffiths, P. R. *Handbook of vibrational spectroscopy*; J. Wiley: Chichester, U.K, 2001.
(54) Schrader, B. *Infrared and Raman Spectroscopy: Methods and Applications*, VCH.; Weinheim, Germany, 1995.
(55) Ismael, A.; Fausto, R.; Cristiano, M. L. S. *J. Org. Chem.* **2016**, *81* (23), 11656–11663.
(56) Yu, Z.; Ohulchanskyy, T. Y.; An, P.; Prasad, P. N.; Lin, Q. *J. Am. Chem. Soc.* **2013**, *135* (45), 16766–16769.
(57) Shi, H.; Zhang, C. J.; Chen, G. Y. J.; Yao, S. Q. *J. Am. Chem. Soc.* **2012**, *134* (6), 3001–3014.
(58) Lim, R. K. V; Lin, Q. *Acc. Chem. Res.* **2011**, *44* (9), 828–830.
(59) Li, Z.; Qian, L.; Li, L.; Bernhammer, J. C.; Huynh, H. V.; Lee, J. S.; Yao, S. Q. *Angew. Chemie - Int. Ed.* **2016**, *55* (6), 2002–2006.
(60) Zhao, S.; Dai, J.; Hu, M.; Liu, C.; Meng, R.; Liu, X.; Wang, C.; Luo, T. *Chem. Commun.*

2016, *4702* (52), 4702–4705.
(61) Zhu, B.; Ge, J.; Yao, S. Q. *Bioorganic Med. Chem.* **2015**, *23* (12), 2917–2927.
(62) Tasdelen, M. A.; Yagci, Y. *Angew. Chemie - Int. Ed.* **2013**, *52* (23), 5930–5938.
(63) Wang, Y.; Song, W.; Hu, W. J.; Lin, Q. *Angew. Chemie - Int. Ed.* **2009**, *48* (29), 5330–5333.
(64) Song, W.; Wang, Y.; Qu, J.; Madden, M. M.; Lin, Q. *Angew. Chemie - Int. Ed.* **2008**, *47* (15), 2832–2835.
(65) Song, W.; Wang, Y.; Qu, J.; Lin, Q. *J. Am. Chem. Soc.* **2008**, *130* (30), 9654–9655.
(66) Bugalho, S. C. S.; Maçôas, E. M. S.; Cristiano, M. L. S.; Fausto, R. *Phys. Chem. Chem. Phys.* **2001**, *3* (17), 3541–3547.
(67) Duvernay, F.; Chiavassa, T.; Borget, F.; Aycard, J.-P. *J. Phys. Chem. A* **2005**, *109* (4), 603–608.
(68) King, S. T. *J. Chem. Phys.* **1971**, *54* (3), 1289.
(69) Jacox, M. E.; Milligan, D. E. *J. Mol. Spectrosc.* **1975**, *56* (3), 333–356.
(70) Dubau-Assibat, N.; Baceiredo, A.; Bertrand, G. *J. Am. Chem. Soc.* **1996**, *118* (22), 5216–5220.
(71) Moss, R. A.; Platz, M.; Jones, M. *Reactive intermediate chemistry*; Jonh Wiley and Sons: New York, 2004.
(72) Scriven, F. V. E. *Azides and Nitrenes*; Academic Press, Inc: Indianapolis, Indiana, 1984.
(73) McConaghy, J. S.; Lwowski, W. *J. Am. Chem. Soc.* **1967**, *89* (10), 2357–2364.

Chapter 5. Tetrazole-saccharinates as selective Cu(II) ligands: structure and potential applications

The work described in this chapter was included in the following publication:

Ismael, A.; Henriques, M. S. da C.; Marques, C. F. S.; Rodrigues, M. J.; Barreira, L. A.; Paixão, J. A.; Fausto, R.; Cristiano, M. L. S.; "Exploring saccharinate-tetrazoles as selective Cu (II) ligands: structure, magnetic properties and cytotoxicity of copper (II) complexes based on 5-(3-aminosaccharyl)-tetrazoles." *RSC Adv.* 2016, 6 (75), 71628–71637.

As such, the contents of this publication are partially reproduced below.

5.1. Exploring saccharinate-tetrazoles as selective Cu(II) ligands: structure and cytotoxicity of copper (II) complexes based on 5-(3-aminosaccharyl)-tetrazoles

The role of copper in the proliferation of cancer cells is under investigation and has been explored in the context of cancer chemotherapy. The evidence gathered, indicating that the proliferation of cancer cells requires a higher abundance of Cu(II) than the proliferation of corresponding normal cells, has prompted the development of new copper chelators that can avidly capture copper ions in neoplasms, depriving them from Cu(II). Additionally the redox active Cu(II) complexes formed may exhibit cytotoxic activity, since they ultimately lead to harmful reactive oxygen species (ROS) in cancer cells. In view of the medical applications, the mandatory properties of the copper chelators are: safety (neglectable cytotoxicity), high binding affinity and selectivity towards Cu(II).

In this chapter we report the synthesis, structure and spectroscopic properties of two novel copper(II) complexes based on the tetrazole-saccharinates **TS** and **2MTS**. Quite interestingly, we found that the tetrazole-saccharinates tested exhibit strong binding selectivity to Cu(II), over Fe(II) and Ca(II). Additionally, the corresponding copper complexes have shown a huge increase in the *in vitro* cytotoxicity against cancer cells, compared to the corresponding nontoxic ligands. Thus, the new ligands may be viewed as potential precursors of selective cytotoxic agents, acting as non-cytotoxic pro-drugs that can be activated inside neoplastic cells, known to be richer in Cu(II) than the corresponding normal cells.

5.1.1. Introduction

The discovery of the antiproliferative properties of platinum complexes in the late 1960s stimulated the interest in metal-based compounds as drug candidates for cancer chemotherapy.[1,2] Further investigations led to transition-metal-based antitumor and antiviral drugs.[3–5] Cisplatin [*cis*-diamminedichloroplatinum(II)] was the first transition metal-based alkylating agent approved for cancer chemotherapy, and was rapidly followed by other platin-based drugs with optimized properties. However, these drugs show severe side effects, such as nephrotoxicity, emetogenesis or neurotoxicity, arising mostly from their indiscriminate attack on all rapidly dividing cells,[6–8] and their efficacy is compromised due to relatively fast development of resistance by cancer cells,[9,10] calling for the development of coordination compounds with antineoplastic properties and better pharmacological profile.

Copper is an essential trace element in the human body, where it is involved in a variety of vital redox processes.[11,12] However, alterations of its normal metabolism convert it into a toxic agent. The potential toxicity of copper arises from its ability to generate reactive oxygen species (ROS) that may react with biomolecules, such as lipids, proteins or nucleic acids.[11,13] Elesclomol, a drug candidate currently under clinical evaluation for cancer chemotherapy, is known to exert its potent antineoplastic activity by increasing the levels of ROS in neoplasms. The apoptotic properties evidenced by Elesclomol are ascribed to its coordination to copper (II), that ultimately leads to generation of harmful ROS.[14]

Studies focused on determining the concentrations of zinc, iron, selenium and copper have shown that, while the zinc, iron and selenium concentrations decrease significantly in serum and tumour tissues of cancer patients when compared to those observed in healthy subjects, copper concentrations generally increase significantly.[15–17] This information may support the development of selective tools for cancer chemotherapy, based on selective copper chelators.

Copper chelation is also used as a straightforward approach to mitigate impairments due to copper overload or accumulation in organisms. The typical clinical use of copper chelators focuses on reduction of the bioavailability of copper in the organ system. Some of such copper chelator-based candidates are in clinical trials for the treatment of several diseases, including the Wilson's disease.[18] In this scenario, the selectivity of a chelator for copper over other metal cations is of upmost relevance.

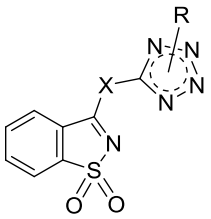

Scheme 5.1 - General representation of tetrazole-saccharyl conjugates proposed in this study.

As described in the previous chapters, we synthesized tetrazole-saccharinates with the general structure represented in Scheme 5.1 and investigated their structure and photoreactivity in detail.[19–24] Studies were then conducted to evaluate the chelation potential of a selection of the conjugates prepared towards a range of divalent cations. Quite interestingly, we found that some of the nitrogen-linked conjugates tested act readily as selective copper chelators. Furthermore, the copper complexes have shown a considerably higher *in vitro* cytotoxicity against tumour cells than the corresponding ligands. Therefore, the free ligands may be viewed as potential precursors of selective cytotoxic agents, acting as non-cytotoxic pro-drugs that can be activated inside cancer cells, where such ligands may bind intracellular copper ions (present in higher concentration, compared to normal cells), generating complexes that can lead to cell death. This possible mode of action would in fact parallel that proposed for Elesclomol, whose apoptotic properties are ascribed to its coordination with intracellular copper (II) ions, ultimately leading to formation of harmful ROS.

In this paper we report the synthesis, structural and spectroscopic (IR; UV/Vis) properties of two copper (II) complexes (**CuTS** and **Cu2MTS$_2$**; Scheme 5.2) based on tetrazole 5-aminosaccharinate (**TS**) and 2-methyltetrazole 5-aminosaccharinate (**2MTS**), as well as their *in vitro* cytotoxicity against different tumoral cell lines (HepG2, HeLa, SHSY5Y, U937 and THP1). We also show that the ligands exhibit strong binding selectivity towards Cu (II), over Fe (II) and Ca (II). Detailed information on the spectroscopic properties of the complexes is of fundamental importance to elucidate their structures and may also be extremely relevant in future biological studies aimed at unravelling their bioaccumulation, biological targets and mode of action.

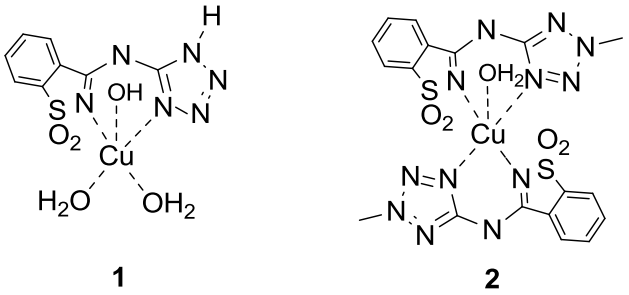

1 **2**

Scheme 5.2 – Representation of the copper (II) complexes **CuTS** and **Cu2MTS$_2$**, based on tetrazole-saccharinates **TS** and **2MTS**, respectively.

5.1.2. Analysis of the crystal structure by X-ray crystallography

As explained in chapter 2 (section 2.1.4), we were not successful in obtaining crystals of the complex **CuTS** suitable for XRD single crystal structure determination. On the other hand, proper crystals were obtained for complex **Cu2MTS$_2$**. Crystallographic data for the structure of complex **Cu2MTS$_2$** have been deposited with the Cambridge Crystallographic Data Centre as a supplementary publication, with No. CCDC 1443606.

Single-crystal XRD structure determination of **Cu2MTS$_2$** showed that the Cu(II) ion is coordinated by two bidentate **2MTS** ligands and one water molecule (Figure 5.1). In addition, the structure contains a non-coordinated extra water molecule that plays a significant role in the supramolecular arrangement of the complexes in the crystal structure *via* a network of hydrogen bonds. In the complex, the methyltetrazole moiety of the **2MTS** ligand has the methyl group oriented in the *trans* conformation with respect to the thiazole group (Figure 5.1), whereas in the crystal of the ligand it adopts the *syn* conformation[20] (see Figure 3.10 in chapter 3). As the energy of the two conformers of the ligand are quite similar,[20] steric hindrance in the complex likely determines the preference for the *trans* conformation.

The Cu^{2+} 5-coordination is intermediate between a trigonal bipyramidal (TP) and a square pyramidal (SP) geometry, and such geometry can be described by a Berry pseudo-rotation with N2' as pivot atom.[25,26] The observed coordination geometry is at 24.8% along the TP (D_{3h}) → SP (C_{4v}) pathway. The τ geometric descriptor,[27] that has a value of 1 for TP and 0 for SP coordination geometries, takes a value of 0.75 in the present case. The Cu(II)‑N distances are in the range 1.942‑2.116 Å, within typical values for such distances. The Cu(II)‑O distance to the water molecule within the coordination shell is 2.071 Å. Comparing the geometry of the anionic form of the ligand with that found in the crystal form of the neutral molecule[20] shows that deprotonation of the amine N12 atom has significantly shortened both

N12-C13/N12'-C13' and N12-C3/N12'-C3' distances, from 1.386 Å to 1.353/1.360 Å and from 1.348 Å to 1.302/1.308 Å, respectively, and decreased the angle C3-N12-C13/C3'-N12'-C13' from 124.66 to 120.35/120.08º, whereas the N2-C3/N2'-C3' distance increased from 1.299 Å to 1.364/1.357 Å. The torsion angles around the N12-C13 and N12-C3 bonds are smaller than ~6º in the complex, compared to a maximum value of ~15º in the crystal of the neutral molecule. Accordingly, the aromatic rings of benzisothiazole and tetrazole are closer to coplanarity, with angles between least-squares planes of the rings reduced from 17.2º to 1.1º /9.2º, for the two ligand molecules of the complex.

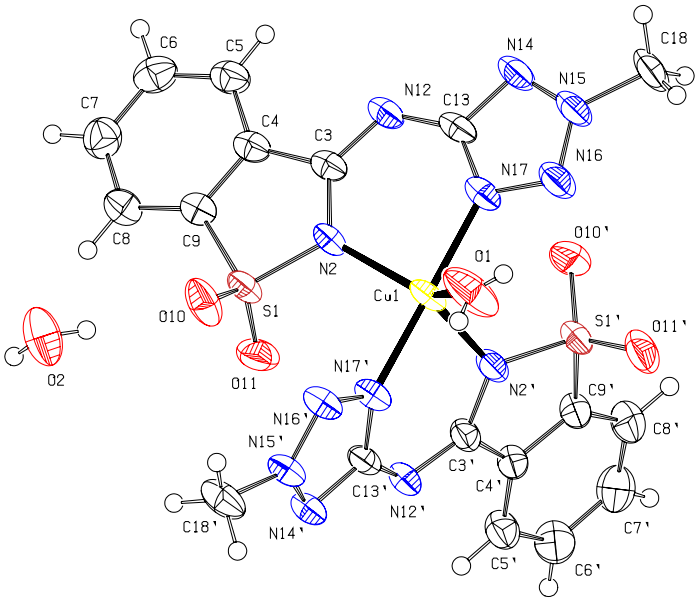

Figure 5.1 – ORTEP plot of complex **Cu2MTS$_2$**, showing the atom numbering scheme. Anisotropic displacement ellipsoids are depicted at the 50% probability level.

Stabilization of the crystal structure is mainly achieved through an extensive network of hydrogen bonds involving the two water molecules (Table 5.1). The water molecule coordinated to the metal ion is involved in an intramolecular hydrogen bond with the N16 atom, and also acts as proton donor to a neighbour uncoordinated water molecule that, itself, joins two molecules *via* hydrogen bonds to atoms O10 and N12', such pattern propagating as an infinite chain of hydrogen bonds along the *a*-axis (Figure 5.2). In addition to these hydrogen bonds involving the water molecules, other weaker C-H···O, C-H···N bonds and π-π interactions between the electron clouds of the aromatic rings are perceived, the latter occurring between stacked aromatic rings related by an inversion centre (Figure 5.3).

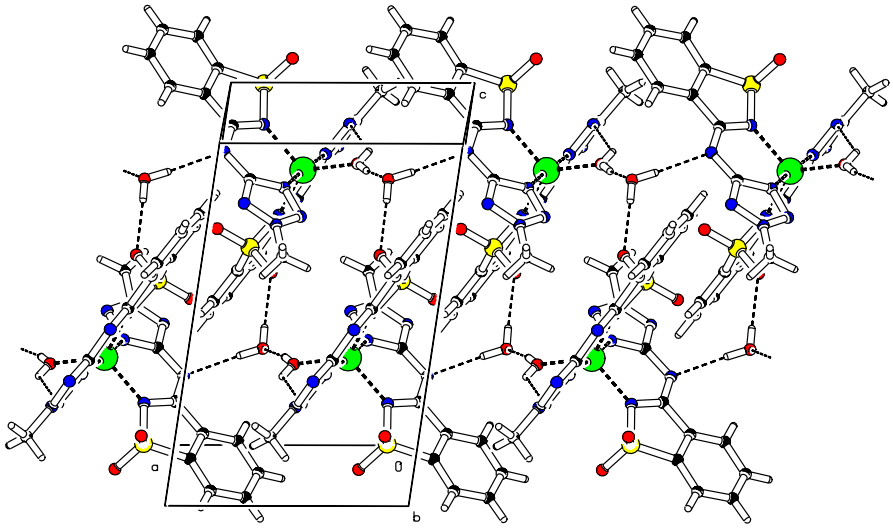

Figure 5.2 - Intermolecular hydrogen bond network involving water molecules.

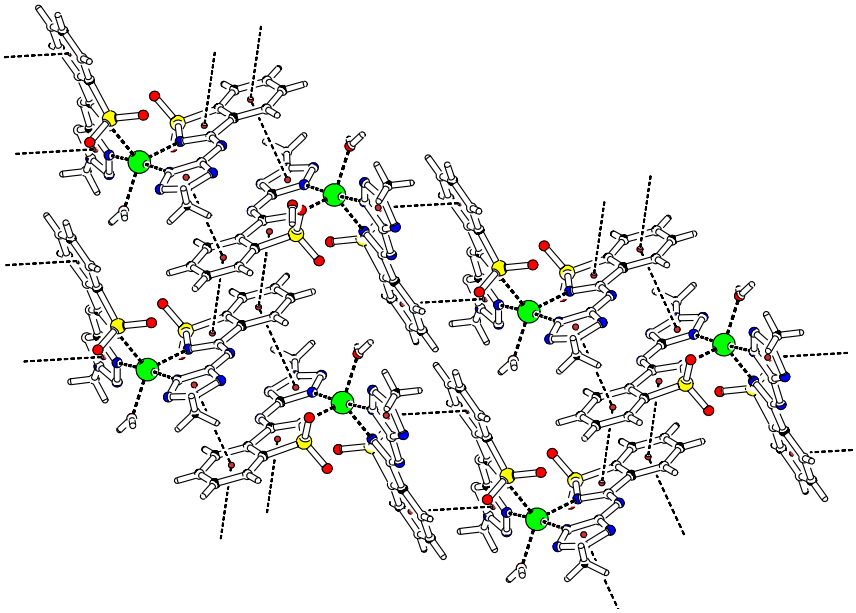

Figure 5.3 - Network of interactions between π-electron clouds of the aromatic rings.

Table 5.1 - Distances and angles of inter- and intramolecular hydrogen bonds involving the water molecules in the crystal of complex **Cu2MTS$_2$**.[a]

	D-H (Å)	H···A (Å)	D···A (Å)	D-H···A (º)
O1-H1A···O2$^{(i)}$	0.85(4)	1.78(4)	2.623(3)	172(4)
O1-H1B···N16	0.63(4)	2.60(5)	2.948(3)	117(5)
O2-H2A···N12'$^{(ii)}$	0.84(4)	2.14(4)	2.966(2)	168(3)
O2-H2B···O10	0.77(4)	2.11(4)	2.886(2)	176(4)

[a] Symmetry codes: (i) 1-*x*,-*y*,1-*z*; (ii) -*x*,-*y*,1-*z*. In addition, weaker intermolecular interactions between C-H groups as donors and N and O atoms as acceptors with D···A distances in the range 2.895 and 3.377 Å are spotted in the structure (details given in the Appendix Table S20).

An additional note should be made in relation to other forms of coordination obtained from complexation of **2MTS** with other copper(II) salts.

A recent work has been developed in collaboration with Frija *et al*,[28] in the CQE research unit at the IST (Instituto Superior Técnico de Lisboa), directed to the evaluation of the potential of tetrazole-saccharinate complexes as homogeneous catalysts for oxidation of secondary alcohols, using solvent-free and microwave assisted protocols. Very interestingly, it was observed during these studies that the reaction of tetrazole-saccharinate **2MTS** with $Cu(NO_3)_2$•$2.5H_2O$ yields blue crystals, which revealed by X-ray a complex of 1:1-type nature in relation to Cu(II) and **2MTS** (Figure 5.4). Thus, the nature of the copper(II) salt impacts on the structure of the complex formed. Indeed, in this complex the Cu(II) ion exhibits a distorted octahedral coordination geometry with a monoanionic bidentate ligand (**2MTS**), two coordinated water molecules and one bidentate nitrate ligand.

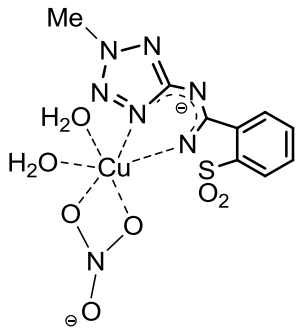

Figure 5.4 - Representation of a complex with 1:1 type-nature, formed from the reaction of **2MTS** with $Cu(NO_3)_2$•$2.5H_2O$. Adapted from Frija *et al*.[28]

5.1.3. Quantum chemistry calculations

In order to gain further insight on the stability of the new Cu(II) complexes as isolated species from the crystalline structure, we performed ROHF and DFT/UB3LYP quantum chemical calculations (see chapter 2, section 2.7 for computational details) on complex **Cu2MTS$_2$**, optimizing its geometry starting from that observed in the crystal, as given by the XRD data (Table 5.2). The isolated complex is stable at both levels of theory, although the uncoordinated water molecule, that was also included in the calculations, is only loosely bound to the complex and drifts considerably from the starting position, as it could be anticipated. Calculated coordination bond distances in the isolated complex do not differ very much from those observed in the crystal, except for the copper-water (Cu-O1) distance, that is predicted by both theoretical methods to be significantly longer for the isolated species than found in the crystal. Concerning the coordination valence angles, the calculations favour larger N2-Cu-N2' and O1-Cu-N2 at the expense of shorter O1-Cu-N2' angles. A graphical comparison of the calculated and observed geometries, where superposition of the compared structures is maximized, is provided in Figure 5.5.

Table 5.2 – Comparison of the calculated equilibrium geometry (ROHF and DFT/UB3LYP) parameters of the isolated complex **Cu2MTS$_2$** with those observed in the crystal form (XRD).[a]

	XRD	ROHF	UB3LYP
Cu−N2	2.072(2)	2.119	2.097
Cu−N2'	2.116(2)	2.153	2.153
Cu−O1	2.071(2)	2.261	2.249
Cu−N17	1.951(2)	2.047	2.000
Cu−N17'	1.942(2)	2.050	2.005
N2−Cu−N2'	112.24(7)	120.51	123.20
O1−Cu−N2'	117.11(8)	86.76	86.31
O1−Cu−N2	130.65(8)	152.10	150.11
N17−Cu−N17'	175.81(7)	171.34	175.12

[a] Distances in Å; bond angles in degrees. See Figure 1 for atom numbering.

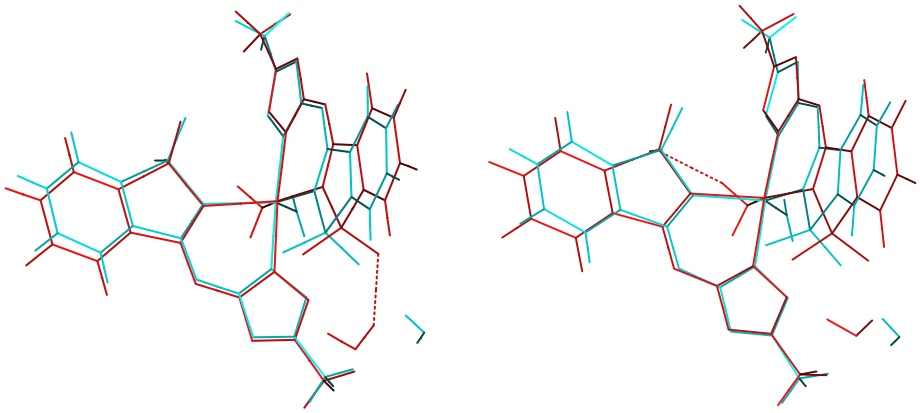

Figure 5.5 - Optimized geometry of the complex **Cu2MTS$_2$** *vs.* observed structure in the crystal. The drawing in blue is the starting geometry extracted from the XRD data and the drawing in red shows the optimized structure obtained from the quantum-chemistry calculations. *Left*: ROHF; *Right*: DFT/UB3LYP.

5.1.4. Infrared spectroscopy of the solid polycrystalline compounds

The IR spectra of the free ligands, **TS** and **2MTS**, and respective metal-ligand systems (**CuTS** and **Cu2MTS$_2$**) are shown in Figure 5.6. **TS** and **2MTS** have been studied previously by X-ray crystallography and infrared spectroscopy (see chapter 3; sections 3.3 and 3.5).[19,20] In those studies, **TS** and **2MTS** were found to exist in the amino-bridged tautomeric form, in the crystal (see chapter 3; Figure 3.2 and Figure 3.10). In the infrared spectra of the two crystals, the νNH stretching bands could be easily identified, since this vibration gives rise to bands in a very characteristic frequency range, 3300-3050 cm^{-1}. For **TS**, with a NH group as spacer and a hydrogen substituent in the tetrazole ring, two main bands were observed, at 3222 and 3090 cm^{-1}. These bands were ascribed to the νNH stretching vibrations of the bridge and on tetrazolyl ring NH groups, respectively. With the formation of complex **CuTS**, the bridged nitrogen atom deprotonates and, accordingly, the band observed at 3222 cm^{-1} in the spectrum of the free ligand has no equivalent. In turn, the band due to the νNH stretching vibration of the tetrazole NH bond is observed slightly shifted to a higher frequency, compared to its position in the spectrum of the free ligand, appearing at 3132 cm^{-1}. For **2MTS**, the νNH stretching vibration of the bridging NH group is observed as a Fermi doublet at 3230/3081 cm^{-1}. As expected, this feature disappears upon complexation, due to deprotonation. In the high-frequency spectral range, one should also notice the presence of additional bands (within the 3700-3200 cm^{-1} region) in the spectra of both complexes **CuTS** and **Cu2MTS$_2$**, due to the νOH stretching vibrations present in these species.

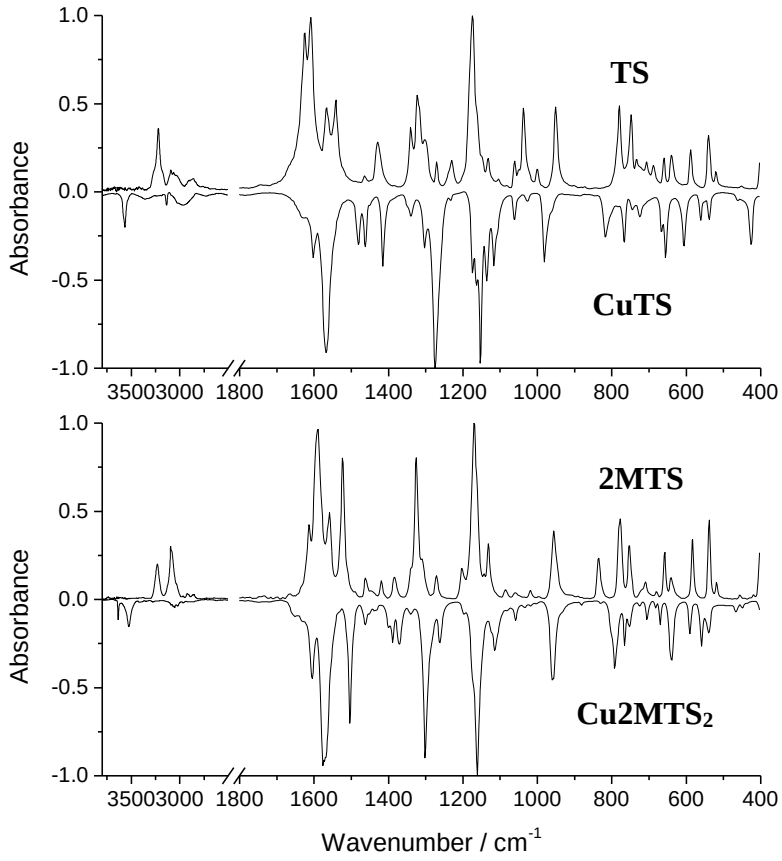

Figure 5.6 - *Top*: room temperature IR spectra of ligand **TS** (positive bands) and of complex **CuTS** (negative bands). *Bottom*: room temperature IR spectra of ligand **2MTS** (positive bands) and of complex **Cu2MTS$_2$** (negative bands). All spectra were obtained for the compounds in a KBr pellet.

In the low-frequency spectral range, the absorption profiles observed in the spectra of the free ligands were also modified upon complexation. The most pronounced changes are observed in the 1650-1540 cm^{-1} region, where characteristic vibrations due to the bridging groups absorb. This reflects the changes in the electron density of the bridging system (NCNCN) caused by deprotonation of the amine moiety and formation of a conjugated system. It is also a direct evidence for the involvement of this delocalized system in metal binding. The frequencies of the major bands in the IR spectra of the free ligands and of the complexes are provided in Appendix; Figure S5 - Figure S8.

5.1.5. UV-Vis titrations

Typical titration experiments were performed by sequential additions of 2-4 μL of a freshly made solution of the metal ion (2 mM,) to 1.5 mL of a solution of the ligand (50 μM, from 1 mM stock solution), in a quartz cuvette. The mixture was equilibrated at 25 ºC, until no further spectroscopic changes were observed (*ca.* 1 min).

UV-Vis titrations of **TS** and **2MTS** with Cu^{2+} were carried out in ethanol. With addition of Cu^{2+}, the absorption band due to free **TS** (λ_{max} = 258 nm) decreased rapidly in intensity and new absorption bands (λ_{max} = 270, 287, 304 and 314 nm), due to the complex **CuTS**, appeared and increased in intensity (Figure 5.7, *top*). The presence of clear isosbestic points at 245 and 268 nm suggests a clean formation of complex **CuTS**. The inset of Figure 5.7 (*top*) displays a plot of the absorbance of complex **CuTS**, at 314 nm, *versus* Cu^{2+} concentration, indicating that the complexation reaction occurs with formation of a 1:1 metal-ligand (M:L) complex.

The titration of **2MTS** with Cu^{2+} also revealed a decrease in intensity of the absorption band due to free **2MTS** (λ_{max} = 254 nm), concomitant with the increase in intensity of new absorption bands (λ_{max} = 265, 283, 301 and 310 nm) due to complex **Cu2MTS$_2$**. Two isosbestic points were observed, at 238 nm and 260 nm (Figure 5.7, *bottom*). The titration curve of complex **Cu2MTS$_2$** at 310 nm revealed that, unlike for complex **CuTS**, beyond ca. 0.5 mol eq. of Cu^{2+} the spectrum remained virtually unaltered, which indicates that the complexation reaction occurs with formation of a 1:2 metal-ligand (M:L) complex, in consonance with the XRD results.

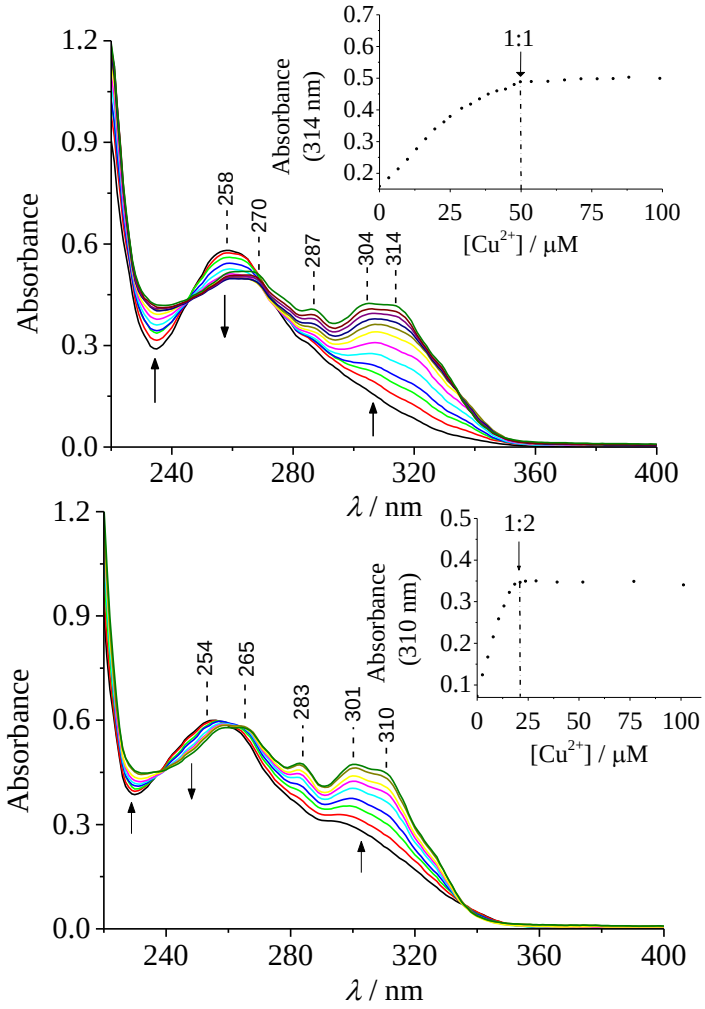

Figure 5.7 – Titration of **TS** (*top*) and **2MTS** (*bottom*) with Cu^{2+}, in ethanol, by sequential additions of 2-4 μL of Cu^{2+} solution (2 mM) to the same 1.5 mL of ligand solution (50 μM). *Insets:* titration curves: *top*, absorbance of complex **CuTS** at 314 nm *versus* Cu^{2+} concentration; *bottom*, absorbance of complex **Cu2MTS$_2$** at 310 nm *versus* Cu^{2+} concentration.

The experimental absorbance values (A) obtained were used to calculate the molar absorptivity (ε) and formation constants (K_C) of the complexes, using the Rose-Drago equation (5.1),[29,30] an extended form of the Benesi-Hildebrand equation,[31] where C_A and C_D are the initial concentrations of the Cu^{2+} and of the ligand (**TS** or **2MTS**), respectively.

$$\frac{C_A C_D}{A} = \frac{1}{K_C \varepsilon} + \frac{1}{\varepsilon}(C_A + C_D) \qquad (5.1)$$

$$\frac{C_A C_D^2}{A} = \frac{1}{K_C \varepsilon} + \frac{C_D(4C_A + C_D)}{\varepsilon} \qquad (5.2)$$

A typical Rose-Drago plot, *i.e.* the plot of $C_A C_D/A$ *vs.* (C_A+C_D) for 1:1 stoichiometry, was drawn for the reaction of **TS** with Cu^{2+} (Figure 5.7, *left*). The linearity of such plot is again in keeping with the formation of a 1:1 Cu^{2+}-**TS** complex. In the plots, the slope and intercept are equal to $1/\varepsilon$ and $1/\varepsilon K_C$, respectively. The values of both K_C and ε are given in Table 5.3. On the contrary, the scattered experimental data for the Cu^{2+}-**2MTS** complex suggest that the stoichiometry of the complex is different from 1:1. In fact, when using the equation (2.1) for the 1:2 stoichiometry,[32,33] and drawing the plot of $C_A C_D^2/A$ *vs.* $C_D(4C_A+C_D)$, a straight line was obtained (Figure 5.7, *right*).

Table 5.3 – Apparent binding constants (K_C) for Cu^{2+}-**TS** and Cu^{2+}-**2MTS** complexes in ethanol, at 25 ºC, calculated from the maximum absorbance of complexes **CuTS** and **Cu2MTS$_2$** at 314 and 310 nm, respectively.

Complex	Complex absorption (nm)	(ε) L mol^{-1} cm^{-1}	K_C
(**1**) Cu^{2+} - **TS** (1:1)	314	1.15x10^4	1.08x10^{13} (M^{-1})
(**2**) Cu^{2+} - **2MTS** (1:2)	310	2.88x10^4	1.42x10^{18} (M^{-2})

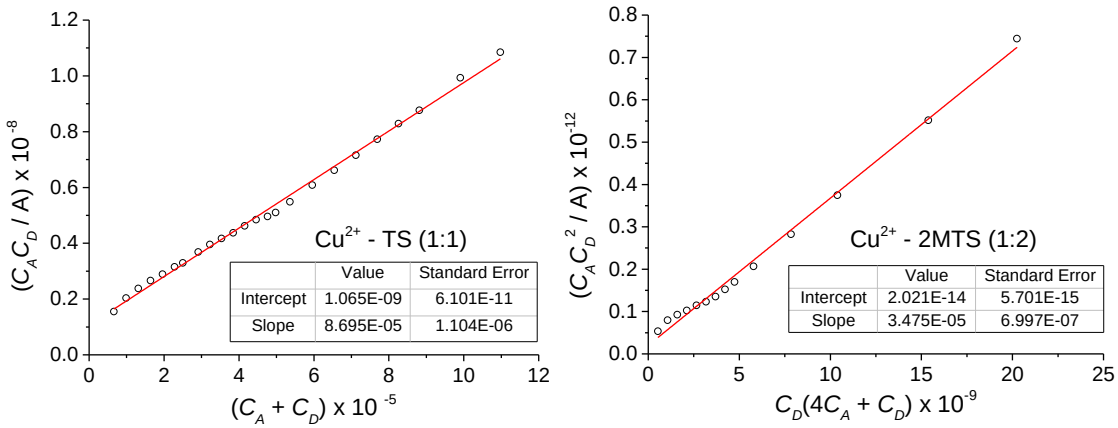

Figure 5.8 – *Left*: Rose–Drago linear plot for the titration of **TS** with Cu^{2+}, in ethanol. The plot was drawn considering the equation for the 1:1 stoichiometry (M:L). *Right*: Rose–Drago linear plot for the titration of **2MTS** with Cu^{2+}, in ethanol. The plot was drawn using the equation for the 1:2 stoichiometry (M:L). The slope and intercept are equal to $1/\varepsilon$ and $1/\varepsilon KC$, respectively.

The UV-Vis spectra of both complexes show bands below 280 nm due to π→π* and n→π* transitions from the ligands (Figure 5.7). The new bands observed at 270 nm, for complex **CuTS**, and at 265 nm, for complex **Cu2MTS$_2$**, may be ascribed to a red-shift of the 258 nm **TS** absorption band and 254 nm **2MTS** absorption band, respectively, due to the enhanced delocalization of the π electron system of the ligands upon coordination, induced by the positively charged metal centre. The new broad absorptions at 304 and 314 nm, for complex **CuTS**, and at 301 and 310 nm, for complex **Cu2MTS$_2$**, are attributed to charge transfer interactions. These new bands show extinction coefficients $\varepsilon_{314\,nm} \approx 11500\ M^{-1}\ cm^{-1}$ for complex **CuTS** and $\varepsilon_{314\,nm} \approx 28777\ M^{-1}\ cm^{-1}$ for complex **Cu2MTS$_2$**. The large values of K_C reflect the high stability of the complexes.

5.1.6. Evaluation of metal chelating activities of TS and 2MTS

The ligands **TS** and **2MTS** were assayed for their Cu^{2+}, Fe^{2+} and Ca^{2+} chelating activities, at different concentrations, and these activities were compared with the chelating activities exhibited by the metal chelator EDTA or, for calcium ions, the related EGTA chelator. EGTA shows a much higher affinity for Ca^{2+}, compared to other cations,[34] and is currently used when Ca^{2+} specific chelation is desired.

As shown in Table 5.4, both **TS** and **2MTS** ligands show good chelating activity towards Cu^{2+}, over 92% and 74%, respectively, at 5 mM concentrations. These values are high, even when compared with the value obtained for the standard chelator EDTA (88%, at 3.4 mM). Remarkably, no evidence for chelating ability of **TS** and **2MTS** towards Fe^{2+} was observed,

even at higher concentrations (10 mM), while the standard EDTA (3.4 mM) showed *ca*. 90% of chelating activity in the same conditions. Nevertheless, since this experiments were performed in competition with the strong Fe^{2+}-chelator ferrozine (K = 3.65 x 10^{15}), used as indicator,[35] we further scrutinized the ability of the studied ligands to chelate Fe^{2+}, through UV-Vis titration experiments for this metal. However, additions of Fe^{2+} to solutions of the ligands did not lead to spectral changes, confirming the absence of chelating ability of **TS** and **2MTS** to Fe^{2+}. Also, when tested for Ca^{2+} chelation, only **2MTS** shows a minor chelating ability (*ca.* 2.7%), when using the highest concentration of calcium tested (10 mM), yet a negligible value if compared with the *ca.* 81% demonstrated for the standard EGTA, at 1 mM. Thus, we conclude that **TS** and **2MTS** exhibit high efficacy and selectivity as copper chelators.

Table 5.4 - Chelating activities (%) of **TS** and **2MTS**, on Cu^{2+}, Fe^{2+} and Ca^{2+} ions.[a]

Compound	Concentration (mM)	Cu^{2+}	Fe^{2+}	Ca^{2+}
TS	1	62.2 ± 0.74	-	-
	5	92.1 ± 0.05	-	-
	10	93.1 ± 0.02	-	-
2MTS	1	24.9 ± 0.66	-	-
	5	74.3 ± 0.43	-	-
	10	86.8 ± 0.13	-	2.7 ± 1.13
EDTA[b]	3.4	88.5 ± 0.12	93.9 ± 0.32	n/a
EGTA[c]	1	n/a	n/a	80.7 ± 0.74

[a] Values are means ± SEM, n = (6); "-", without evidence of chelating activity (no change in absorbance of metal chelating indicator); n/a, not applicable. [b] EDTA was used as positive control for Cu^{2+} and Fe^{2+} chelating activity. [c] EGTA was used as positive control for Ca^{2+} chelating activity.

The investigation of cellular processes related to copper transport, storage and usage often involves strategic alterations of the bioavailability of copper ions by using metal chelating agents. When taking advantage of live cells in probing for biomolecules related to copper homeostasis, a typical approach is to change the availability of copper and search for subsequent changes in cell processes. Up-regulation or down-regulation of a specific set of genes can identify the proteins that are directly or indirectly related to copper handling. An accurate control of the ability of a chelator to limit the bioavailability of copper is thus crucial to the integrity of an experiment and to the interpretation of the results. In the studies of physiological and pathological activity of copper-dependent compounds, EDTA has often been used as a classic Cu^{2+} chelator in experiments to modulate copper concentrations in the cell, or to terminate biochemical processes of copper-containing compounds.[36–38] However, chelators such as EDTA usually lack selectivity, easily causing the loss of beneficial ions, such as iron

and calcium.[39–41] In this context, due to its high selectivity to copper ions and their excellent chelator activity to this species, **TS** and **2MTS** appear as promising chelators for investigations of copper-related processes in biological environment.

5.1.7. Evaluation of cytotoxicity of TS, 2MTS and corresponding copper complexes

Considering possible applications in medicine, the safety of **TS** and **2MTS** was evaluated by means of cytotoxicity studies. The cytotoxicity of the compounds was tested using the hepatocellular carcinoma cell line (HepG2) and the standard MTT assay. Compounds were applied at 100 μM, for 72h. Results were expressed as % of cell viability, relatively to the negative control (Table 5.5). None of the tested metal-free ligands **TS** and **2MTS** exhibited cytotoxicity against the tumour cell line (at 100 μM). However, complexes **CuTS** and **Cu2MTS$_2$** were found to exhibit potent cytotoxicity, much higher than Cu^{2+} alone, clearly evidencing that there is a significant increase in cytotoxicity when the copper is chelated by the ligands **TS** or **2MTS**.

The half maximal inhibitory concentration (IC_{50}) for complexes **CuTS** and **Cu2MTS$_2$** are 11.1 ± 0.1 μM and 18.4 ± 1.6 μM, respectively (Table 5.6). The cytotoxic activities of **CuTS** and **Cu2MTS$_2$** can be compared with that of the known anticancer drug etoposide, used as a reference in our studies. The results thus show that complexes **CuTS** and **Cu2MTS$_2$** and etoposide exhibit cytotoxic properties against the human hepatic tumoral cell line HepG2 at low micromolar concentrations, although the cytotoxicity of etoposide is somewhat higher.

Table 5.5 - Cellular viability (% of the control) of the compounds (at 100 μM), tested against the human hepatic tumour cell line HepG2.[a]

	TS	**2MTS**	**CuTS**	**Cu2MTS$_2$**	$CuSO_4$
HepG2	94.3 ± 3.6	95.1 ± 2.9	3.59 ± 0.09	3.56 ± 0.03	62.1 ± 4.0

[a] Negative control cells were treated with DMSO at the highest concentration used in test wells (0.5%).

Table 5.6 – Cytotoxicity (IC_{50} μM) of complexes **CuTS** and **Cu2MTS$_2$** and etoposide (positive control) against the human hepatic tumour cell line HepG2. [a]

	CuTS	**Cu2MTS$_2$**	etoposide
IC_{50} (μM)	11.1 ± 0.1	18.4 ± 1.6	2.34 ± 0.17

[a] Negative control cells were treated with DMSO at the highest concentration used in test wells (0.5%)

In order to evaluate the potential of these ligands as pro-cytotoxic agents that could be activated *in situ* by chelating the copper ions available in neoplasms, the cytotoxicity of compound **2MTS** was tested by previously adding 50 μM of $CuSO_4$ to the tested cells. Since the copper(II) salt $CuSO_4$ is known to exhibit some cytotoxic activity (see Table 5.5), this salt was also added to the control cells. The concentration of Cu^{2+} added to the cell lines was selected based on the standard copper levels determined in samples of serum and tumour tissues from cancer patients, as reported by Gupte *et al*.[15]

The cytotoxicity of **2MTS**, was evaluated in different tumoral cell lines, namely HepG2 (hepatocellular carcinoma), HeLa (human cervical epithelioid carcinoma), SH-SY5Y (human neuroblastoma), U937 (human leukaemic monocytic lymphoma) and THP1 (human acute monocyclic leukaemia), with previous addition of $CuSO_4$ (50μM). The **2MTS** selectivity towards tumoral cells was assessed from its cytotoxicity towards two non-tumoral derived cell lines, S17 (murine bone marrow) and N9 cells (murine microglial). Results of the half maximal concentrations (IC_{50}) are shown in Table 5.7, together with the selective indexes (SI) with respect to the non-tumoral S17 and N9 cells.

Very interestingly **2MTS** showed to be considerably cytotoxic against all adherent tumoral cell lines tested, with IC_{50} values of 3.74 in HepG2, 3.62 in HeLa and 5.28 μM in SH-SY5Y. Indeed, allowing **2MTS** to complex *in situ* with the copper(II) ions, previously added to the cell line HepG2 resulted in a dramatic increase in the anticancer activity (IC_{50} = 3.62 μM), compared with the tested complex **Cu2MTS$_2$**, which has shown a IC_{50} of 18.4 μM in HepG2 cells (see Table 5.6). In addition, **2MTS** demonstrated selectivity index values of 10.73 and 10.77 for HepG2 tumour cells, with respect to the non-tumour S17 and N9 cells. These SI values are excellent when compared with those obtained for the known anticancer drug etoposide, used as positive control, which has exhibited selectivity index values of 4.44 and 0.83 towards S17 and N9 cells, respectively (see Table 5.7).

In general, **2MTS** showed high selectivity for tumour adherent cell lines, ranging from 7.61 (SH-SY5Y) to 11.13 (HeLa). On the other hand, the significantly higher IC_{50} values, of 28.40 and 15.89 μM, obtained for tumour cell lines THP1 and U937, respectively, may indicate that the *in situ* formed complexes are somehow less effective for non-adherent cell lines.

Although deeper studies are required to further support our proposal and better define its scope, the results already obtained validate the hypothesis that these ligands may be viewed as potential tools in the development of anti-tumoral drugs, acting as non-cytotoxic pro-drugs that

can be activated *in situ*, where the ligands may bind copper ions present in tumour cells, generating cytotoxic complexes that can lead to cell death.

Table 5.7 - Cytotoxicity of compounds **2MTS** and etoposide (positive control) against several tumour and non-tumour cell lines. Results are expressed as IC_{50} (μM) values and selectivity index (SI) values were calculated in relation to the non-tumour cell lines (S17 and N9).[a]

		2MTS + $CuSO_4$ (50 μM)			**Etoposide**		
		IC_{50}	SI (S17)	SI(N9)	IC_{50}	SI(S17)	SI(N9)
Adherent cell lines	**HepG2**	3.74	10.73	10.77	2.34	4.44	0.83
	HeLa	3.62	11.10	11.13	nt.	-	-
	SH-SY5Y	5.28	7.61	7.63	nt.	-	-
	S17	40.16	-	-	10.4	-	-
	N9	40.29	-	-	1.95	-	-
Suspension cell lines	**THP1**	28.40	1.41	1.42	1.82	5.71	1.07
	U937	15.89	2.53	2.54	1.10	9.45	1.77

[a] Negative control cells were treated with DMSO at the highest concentration used in test wells (0.5%), and $CuSO_4$ at 50 μM; n.t. not tested.

5.1.8. Conclusions

In the present study, new copper (II) complexes (**CuTS**, **Cu2MTS$_2$**) based on tetrazole 5-aminosaccharinate (**TS**) and 2-methyltetrazole 5-aminosaccharinate (**2MTS**), respectively, were prepared and their structural and spectroscopic properties were investigated. The crystal structure of complex **Cu2MTS$_2$** was studied by single crystal X-ray diffraction, showing that the Cu(II) ion is coordinated by two bidentate **2MTS** ligands and one water molecule. In addition, the structure contains a non-coordinated water molecule. Stabilization of the crystal structure is mainly due to an extensive network of hydrogen bonds involving the two water molecules. The stability of the Cu(II) complex **Cu2MTS$_2$** as isolated species from the crystalline structure was investigated by ROHF and DFT calculations. The isolated complex is stable at both levels of theory, and calculated coordination bond distances in the isolated complex did not differ very much from those observed in the crystal. UV-Vis titrations of ligands **TS** and **2MTS** with Cu^{2+} were carried out in ethanol. Titration of the ligand **TS** with Cu^{2+} revealed that the complexation reaction occurs with formation of a 1:1 metal-ligand (M:L) complex. On the other hand, titration of ligand **2MTS** indicates that the complexation reaction occurs with formation of a 1:2 metal-ligand (M:L) complex, in consonance with both the XRD results.

TS and **2MTS** were assayed for their metal ion chelating activities and were found to exhibit strong binding selectivity to Cu(II), over Fe(II) and Ca(II). Moreover, when tested *in vitro* against the hepatocellular carcinoma cell line HepG2, the complexes exhibited a huge increase in cytotoxicity, compared to the corresponding ligands. The half maximal inhibitory concentrations (IC_{50}) measured were 11.1 ± 0.1 μM and 18.4 ± 1.6 μM, for complexes **CuTS** and **Cu2MTS$_2$**, respectively. Allowing **2MTS** to complex *in situ* with the copper(II) ions, previously added to the cell lines, revealed to be considerably cytotoxic against all adherent tumoral cell lines tested, with IC_{50} values of 3.74 in HepG2, 3.62 in HeLa and 5.28 μM in SH-SY5Y, and with selectivity indexes, ranging from 7.61 (SH-SY5Y) to 11.13 (HeLa). The low micromolar cytotoxic activity exhibited by complexes **CuTS** and **Cu2MTS$_2$** combined with the observed selectivity of **TS** and **2MTS** ligands to copper ions, may offer perspectives for new leads in cancer chemotherapy, especially for tumours where neoplasm cells have a higher concentration of Cu^{2+} than normal cells.

5.2. References

(1) Rosenberg, B.; Van Camp, L.; Grimley, E. B.; Thomson, A. J. *J. Bio. Chem.* **1967**, *242* (6), 1347–1352.
(2) Christie, D. A.; Tansey, E. M. In *Wellcome Witnesses to Twentieth Century Medicine*; London, 2007; Vol. 30, pp 35–36.
(3) Komeda, S.; Casini, A. *Current Topics in Medicinal Chemistry*. 2012, pp 219–235.
(4) Paterson, B. M.; Donnelly, P. S. *Chem. Soc. Rev.* **2011**, *40* (5), 3005–3018.
(5) Brabec, V.; Novakova, O. *Drug Resist. Updat.* **2006**, *9* (3), 111–122.
(6) Wang, D.; Lippard, S. J. *Nat Rev Drug Discov* **2005**, *4* (4), 307–320.
(7) Apps, M.; Choi, E.; Wheate, N. *Endocr. Relat. Cancer* **2015**, *22*, 219–233.
(8) Ruggiero, A.; Trombatore, G.; Triarico, S.; Arena, R.; Ferrara, P.; Scalzone, M.; Pierri, F.; Riccardi, R. *Anticancer. Drugs* **2013**, *24* (10), 1007–1019.
(9) Johnstone, T. C.; Park, G. Y.; Lippard, S. J. *Anticancer Res.* **2014**, *34* (1), 471–476.
(10) Brabec, V.; Kasparkova, J. *Drug Resist. Updat.* **2005**, *8* (3), 131–146.
(11) Jomova, K.; Valko, M. *Toxicology* **2011**, *283* (2–3), 65–87.
(12) Valko, M.; Morris, H.; Cronin, M. T. D. *Current Medicinal Chemistry*. 2005, pp 1161–1208.
(13) Valko, M.; Rhodes, C. J.; Moncol, J.; Izakovic, M.; Mazur, M. *Chem. Biol. Interact.* **2006**, *160* (1), 1–40.
(14) Nagai, M.; Vo, N. H.; Shin Ogawa, L.; Chimmanamada, D.; Inoue, T.; Chu, J.; Beaudette-Zlatanova, B. C.; Lu, R.; Blackman, R. K.; Barsoum, J.; Koya, K.; Wada, Y. *Free Radic. Biol. Med.* **2012**, *52* (10), 2142–2150.
(15) Gupte, A.; Mumper, R. J. *Cancer Treat. Rev.* **2009**, *35* (1), 32–46.
(16) Denoyer, D.; Clatworthy, S. A. S.; Masaldan, S.; Meggyesy, P. M.; Cater, M. A. *Prostate* **2015**, *75* (14), 1510–1517.
(17) Denoyer, D.; Masaldan, S.; Fontaine, S. La; Cater, M. a. *Metallomics* **2015**, *7* (August), 1459–1476.
(18) Ding, X.; Xie, H.; Kang, Y. J. *J. Nutr. Biochem.* **2011**, *22* (4), 301–310.

(19) Gómez-Zavaglia, A.; Ismael, A.; Cabral, L. I. L.; Kaczor, A.; Paixão, J. A.; Fausto, R.; Cristiano, M. L. S. *J. Mol. Struct.* **2011**, *1003*, 103–110.
(20) Ismael, A.; Paixão, J. A.; Fausto, R.; Cristiano, M. L. S. *J. Mol. Struct.* **2012**, *1023*, 128–142.
(21) Ismael, A.; Borba, A.; Duarte, L.; Giuliano, B. M.; Gómez-Zavaglia, A.; Cristiano, M. L. S. *J. Mol. Struct.* **2012**, *1025*, 105–116.
(22) Ismael, A.; Gómez-Zavaglia, A.; Borba, A.; Cristiano, M. de L. S.; Fausto, R. *J. Phys. Chem. A* **2013**, *117* (15), 3190–3197.
(23) Ismael, A.; Borba, A.; Henriques, M. S. C.; Paixão, J. A.; Fausto, R.; Cristiano, M. L. S. *J. Org. Chem.* **2015**, *80* (1), 392–400.
(24) Ismael, A.; Fausto, R.; Cristiano, M. L. S. *J. Org. Chem.* **2016**, *81* (23), 11656–11663.
(25) Holmes, R. R. *Progress in Inorganic Chemistry*; Lippard, S. J., Ed.; Progress in Inorganic Chemistry; John Wiley & Sons, Inc.: Hoboken, NJ, USA, 1984; Vol. 32.
(26) Muetterties, E. L.; Guggenberger, L. J. *J. Am. Chem. Soc.* **1974**, *96* (6), 1748–1756.
(27) Addison, A. W.; Rao, T. N.; Reedijk, J.; van Rijn, J.; Verschoor, G. C. *J. Chem. Soc., Dalt. Trans.* **1984**, No. 7, 1349–1356.
(28) Frija, L. M. T.; Alegria, E. C. B. A.; Sutradhar, M.; Cristiano, M. L. S.; Ismael, A.; Kopylovich, M. N.; Pombeiro, A. J. L. *J. Mol. Catal. A Chem.* **2016**, *425*, 283–290.
(29) Rose, N. J.; Drago, R. S. *J. Am. Chem. Soc.* **1959**, *81* (23), 6138–6141.
(30) Ayad, M. M. *Zeitschrift für Phys. Chemie* **1994**, *187* (Part_1), 123–133.
(31) Benesi, H. A.; Hildebrand, J. H. *J. Am. Chem. Soc.* **1949**, *71* (8), 2703–2707.
(32) Zubkov, A. V.; Ivanova, T. V. *J. Solution Chem.* **1982**, *11* (10), 699–717.
(33) Baniyaghoob, S.; Najafpour, M. M.; Boghaei, D. M. *Spectrochim. Acta - Part A Mol. Biomol. Spectrosc.* **2010**, *75* (3), 970–977.
(34) Schmid, R. W.; Reilley, C. N. *Anal. Chem.* **1957**, *29* (2), 264–268.
(35) Gibbs, C. R. *Anal. Chem.* **1976**, *48* (8), 1197–1201.
(36) Endo, N.; Nishiyama, K.; Okabe, M.; Matsumoto, M.; Kanouchi, H.; Oka, T. *Biochim. Biophys. Acta* **2007**, *1770* (4), 571–577.
(37) Habtemariam, S.; Dagne, E. *Food Chem. Toxicol.* **2009**, *47* (7), 1490–1494.
(38) Rivero-Müller, A.; De Vizcaya-Ruiz, A.; Plant, N.; Ruiz, L.; Dobrota, M. *Chem. Biol. Interact.* **2007**, *165* (3), 189–199.
(39) Oviedo, C.; Rodríguez, J. *Quim. Nova* **2003**, *26* (6), 901–905.
(40) Allain, P.; Mauras, Y.; Premel-Cabic, a; Islam, S.; Herve, J. P.; Cledes, J. *Br. J. Clin. Pharmacol.* **1991**, *31* (3), 347–349.
(41) Cheng, K. L.; Ueno, K.; Imamura, T. *CRC Handbook of Organic Analytical Reagents, Second Edition*; CRC Press, 1992.

Chapter 6. Conclusions

6.1. Conclusions and perspectives

The work described in this thesis is mostly related with the synthesis, structure and reactivity of novel molecules incorporating the tetrazole and benzisothiazole units linked by a spacer-group.

Due the intrinsic structural characteristics of both heterocycles, tetrazole and benzisothiazole, we have devised synthetic routes to the novel tetrazole-saccharyl conjugates with the final aim of investigating their application as multidentate nitrogen ligands for coordination with transition metals. The ligands were prepared using a convergent synthetic strategy whereby the two building blocks containing the heterocycles were separately synthesised and then coupled to afford the target conjugates, allowing to easily introduce chemical diversity, through different spacer-groups and substituents on the tetrazolyl ring.

A main objective of the first part of this work was to attain a deep understanding of the conformational and tautomeric preferences of the compounds, in both the isolated molecule situation and in crystalline phase. The structural investigation of the *N*-linked saccharinate tetrazoles (**TS**, **1MTS** and **2MTS**) proved especially challenging because of the possibility of tautomerism involving the saccharyl system. For these compounds, two forms are possible: the imino-bridged, and amino-bridged tautomers. If, additionally, the tetrazole ring is unsubstituted, as is the case for the parent tetrazole-saccharinate **TS**, then four tautomers become possible, two belonging to the imino-bridged group and the other two to the amino-bridged group.

In general the imino-bridged tautomeric form, with the $N{=}C_{(saccharin)}$ spacer linking the two heterocycles, seems to be the most stable configuration for the monomeric molecule. However, in the neat crystalline solid, while **1MTS** units were found to exist in the predicted most stable monomeric configuration, the imino-bridged tautomeric form, the **TS** and **2MTS** units were found to assume the less stable amino-bridged tautomeric form. The observed difference in the crystallographic basic units of the compounds revealed the prevalence of the H-bond networks in determining the structural preferences of the tetrazole-saccharyl conjugates in the solid state. Thus, the preferred tautomeric species of the *N*-linked conjugates are very much determined by the chemical environment.

It was shown that, while in the crystal **TS** and **2MTS** units exist in the amino-bridged tautomeric form, essentially due to the H-bonding network, the isolated molecules of the

compounds **TS** and **2MTS** were found to exist preferentially in the predicted most stable imino-bridged tautomer. Indeed it could be doubtless demonstrated that **2MTS** undergoes a complete amino→imino tautomerization upon sublimation, and enough structural and energetic information was obtained to propose a possible mechanism for such conversion. On the contrary, the investigation of an *S*-linked saccharyl-1-methyltetrazole (**TSMT**), in which the structure simplifies because no tautomerism involving the saccharyl system or the tetrazole ring is observed, showed that **TSMT** molecules assume the same conformation in the crystal and as isolated molecules.

During the second part of this work we focused on the assessment of the photochemical stability of tetrazole-saccharyl conjugates. Tetrazoles are known for their rich photochemistry, whereas benzisothiazoles are known to be rather photostable, as such, we decided to investigate the effect of the saccharyl system on the photostability of the tetrazole ring.

For the photochemical studies, we selected two tetrazole-saccharyl conjugates and investigated their photochemistry by matrix isolation spectroscopy. **TSMT** appeared to be a good candidate since no tautomerism involving the saccharyl system or the tetrazole ring is observed, thus reducing the number of structures present in the matrix and simplifying the interpretation of the photochemical reactions. Upon UV irradiation of the matrix-isolated **TSMT** two photodegradation channels were observed, both arising from cleavage of the tetrazolyl ring and following two general pathways: *pathway a* involving cleavage of the N_1-N_2 and N_3-N_4 bonds, with extrusion of molecular nitrogen, leading to photostable diazirine and thiocarbodiimide derivatives; *pathway b* involving cleavage of the C_5-N_1 and N_3-N_4 bonds, leading to thiocyanate and methyl azide.

The second studied conjugate, **2MTS**, has assumed an important role in our investigation due to the good results demonstrated as selective copper chelator, affording copper complexes with promising cytotoxic properties, which stimulated us to explore the photoreactivity of this conjugate. Moreover, it could be expected that substitution in a different position of the tetrazolyl ring (N_2) would give different photofragmentation pathways and species formed. Indeed, UV irradiation of the matrix-isolated **2MTS** resulted in selective photoinduced cleavage of the C_5-N_4 and N_2-N_3 bonds of the tetrazole ring, with extrusion of molecular nitrogen, leading to a nitrile imine that isomerized to diazirine and underwent subsequent photoconversion into carbodiimide.

Since the photolysis of both conjugates **TSMT** and **2MTS** led only to fragmentation of the tetrazole ring, we performed studies on the photochemistry of **1MT** and **2MT**, used as the

tetrazolyl building blocks for preparation of the *N*-linked conjugates, in order to simplify the interpretation of the respective photoproducts formed and corroborate our proposed reaction pathways for the studied tetrazole-saccharyl conjugates. Besides, in the last few years emerged, the *in situ* generation of highly reactive nitrile imine dipolar species from photolysis of tetrazoles, which revealed to be a powerful tool for proteome profiling in living cells. Therefore the results obtained from the comparison of the photochemistry of both isomers, **1MT** and **2MT**, using similar experimental conditions, enabled the clarification of important mechanistic questions regarding the effects of the ring substitution pattern on the photofragmentation pathways of disubstituted tetrazoles. It was shown that the photochemistry of the isomers **1MT** and **2MT**, although resulting in a common final photoproduct, identified as a carbodiimide, seems to follow different pathways. Indeed, through photolysis of **1MT** we were able to capture for the first time the intermediates diazirine and amino cyanamide generated photochemically from a 1,5-disubstituted tetrazole in solid argon. While the diazirine was obtained as a common intermediate from photolysis of both **1MT** and **2MT**, the amino cyanamide was exclusively obtained from photocleavage of **1MT**, whereas a nitrile imine was exclusively obtained during the photolysis of **2MT**. Observation of the amino cyanamide reveals a novel reaction pathway in the photochemistry of tetrazoles that appears to be characteristic of 1*H*-tetrazoles. On the other hand, the exclusive formation of nitrile imine from the isomer **2MT** is a clear indication that only the 2*H*-tetrazoles can give a direct access to nitrile imines.

The mechanism for direct elimination of molecular nitrogen from the tetrazole ring in solid argon was not yet fully explained. However we postulated the formation of imidoylnitrene species which could have different E/Z orientation, with only the one resulting from **1MT** enabling formation of the amino cyanamide. This could explain the different photochemical pathways observed for isomers **1MT** and **2MT**. Moreover, with photolysis of diazirine the imidoylnitrene is expected to be generated in the triplet state directly, known as the low energy form of nitrenes. Indeed, we were able to confirm, by EPR spectroscopy, the generation of a triplet nitrene species from photolysis of **2MT**, a clear evidence that the postulated triplet state imidoylnitrene species might be an intermediate of this reaction. However, the proposal of a mechanism for these reactions is only tentative, and further investigation is required to grant it adequate support.

Additionally, comparing the photochemistries of the conjugate **2MTS** and of the parent tetrazolyl moiety **2MT** we could conclude that the reaction pathways are quite similar. However, in **2MTS** the saccharyl system was found to increase substantially the photostability of the tetrazole ring and the nitrilimine intermediate (by more than 20x), compared to parent tetrazole **2MT**. When using bis-tetrazole molecules or conjugates where the tetrazole ring is linked to other

heterocycles in coordination chemistry, the quite low photostability of tetrazoles has always been an issue. As such, and considering the applications of these conjugates, this remarkable increase of photostability introduced by the saccharyl system, reveals to be a quite promising characteristic of these novel conjugates.

In the final part of this work we evaluated the ability of the conjugates to be used as multidentate nitrogen ligands for coordination with a range of divalent cations. Although the studies were primarily assessed by UV/Vis experiments, we found that some of the nitrogen-linked conjugates tested act readily as selective copper (II) chelators, over iron (II) and calcium (II). These results led to the investigation of their potential application in chelation therapy and, indeed, we came across with quite promising data regarding the potential of these copper chelators for cancer chemotherapy. Stimulated by the good results, new copper (II) complexes, **CuTS**, **Cu2MTS$_2$**, based on conjugates **TS** and **2MTS**, respectively, were prepared and their structural and spectroscopic properties were investigated. The knowledge on the spectroscopic properties of the complexes is of fundamental importance to elucidate details of their structures and may serve in future biological studies aimed at unravelling the bioaccumulation, biological targets and mode of action.

The studies on the cytotoxic activity exhibited by those complexes against different tumoral cell lines (HepG2, HeLa and SHSY5Y) revealed activity at low micromolar concentrations. These data, combined with the observed selectivity of those ligands to copper (II) ions, may offer perspectives for new leads in cancer chemotherapy, especially for tumours where neoplasm cells have a higher concentration of copper (II) than normal cells. Moreover, the copper complexes have shown a considerably higher *in vitro* cytotoxicity against tumoral cells than the corresponding ligands and therefore the free ligands may be viewed as potential precursors of selective cytotoxic agents, acting as non-cytotoxic pro-drugs that can be activated inside cancer cells, where such ligands may bind intracellular copper ions (present in higher concentration, compared to normal cells), generating complexes that can lead to cell death.

Further studies, on the cytotoxic activity of these novel tetrazole-saccharyl conjugates as copper chelators in cancer chemotherapy are being conducted. Other properties of the conjugates are also being explored, such as luminescence properties and their potential as catalysts for organic reactions.

Although not included in these thesis, a recent work developed in collaboration with researchers from IST (Instituto Superior Técnico de Lisboa) demonstrated that copper (II) and cobalt (II) tetrazole-saccharinate complexes can be used as effective catalysts for the oxidation of diverse secondary alcohols, under a solvent-free and microwave assisted protocol. Moreover, the oxidation of secondary alcohols has proceeded selectively in a short time and with very good to excellent yields, revealing that these novel conjugates can be quite promising in several different areas.

Appendix

List of Tables and Figures

Table S1 - Summary of X-ray data collection and processing parameters for tetrazole-saccharinate (**TS**) crystal.

chemical formula	$C_8H_6N_6O_2S$
colour/shape	colourless/plate
formula weight	250.25
space group	C2/c
temperature, K	293(2)
cell volume (Å ^{3})	2019.13(4)
crystal system	monoclinic
a (Å)	21.7493(3)
b (Å)	8.8594(1)
c (Å)	10.7690(1)
α (deg)	90.00
β (deg)	103.330(1)
γ (deg)	90.00
formula units/unit cell	8
D_c (Mg m^{-3})	1.646
diffractometer/scan	Bruker ApexII/ ϕ and ω scans
radiation (Å) (graph. monochromated)	0.71073
max crystal dimensions (mm)	0.29x0.21x0.09
θ range (deg)	3.29-31.73
range of *h, k,l*	–29,27; –12,12; –15;15
reflections measured/independent	15848/3082 (R_{int}= 0.0244)
reflections observed I>2σ	2441
corrections applied	Absorption (Multi-scan, SADABS)
computer programs	SHELXL-97, SHELXS-97, PLATON
structure solution	Direct Methods
No. of parameters varied	154
GOF	1.025
R1	0.0385
wR2	0.1330
function minimized	$\Sigma\, w\, (\|F_o\|^2 - S\|F_c\|^2)$
diff. density final max/min (e Å^{-3})	0.294, –0.302

Table S2 - Summary of X-ray data collection and processing parameters for 1-methyltetrazole-saccharinate (**1MTS**) crystal.

chemical formula	$C_9H_8N_6O_2S$
colour/shape	colourless/prism
formula weight	264.27
space group	$P\bar{1}$
temperature, K	293(2)
cell volume (Å ^{3})	539.77(1)
crystal system	triclinic
a (Å)	6.9763(1)
b (Å)	8.3097(1)
c (Å)	10.0737(1)
α (deg)	96.517(1)
β (deg)	107.543(1)
γ (deg)	99.989(1)
formula units/unit cell	2
D_c (Mg m^{-3})	1.626
diffractometer/scan	Bruker ApexII/ ϕ and ω scans
radiation (Å)(graph.monochromated)	0.71073
max crystal dimensions (mm)	0.44x0.17x0.14
θ range (deg)	2.15-34.74
range of *h, k,l*	-11,10;-12,12; -16;15
reflections measured/independent	14215/3915 (R_{int}= 0.0199)
reflections observed $I>2\sigma$	3077
corrections applied	Absorption (Multi-scan, SADABS)
computer programs	SHELXL-97, SHELXS-97, PLATON
structure solution	Direct Methods
No. of parameters varied	164
GOF	1.068
R1 ($I>2\sigma$)	0.0379
wR2	0.1118
function minimized	$\Sigma\, w\,(\|F_o\|^2 - S\|F_c\|^2)$
diff. density final max/min (e Å^{-3})	0.312, -0.365

Table S3 - Summary of X-ray data collection and processing parameters for 2-methyltetrazole-saccharinate (**2MTS**) crystal.

chemical formula	$C_9H_8N_6O_2S$
colour/shape	colourless/prism
formula weight	264.27
space group	$P\bar{1}$
temperature, K	293(2)
cell volume (Å ^{3})	546.59(1)
crystal system	triclinic
a (Å)	7.8010(1)
b (Å)	8.6724(1)
c (Å)	9.4984(1)
α (deg)	114.083(1)
β (deg)	107.823(1)
γ (deg)	93.080(1)
formula units/unit cell	2
D_c (Mg m^{-3})	1.606
diffractometer/scan	Bruker ApexII/ ϕ and ω scans
radiation (Å)(graph.monochromated)	0.71073
max crystal dimensions (mm)	0.38x0.33x0.28
θ range (deg)	2.52-33.83
range of *h, k,l*	-12,12;-13,12; -14;14
reflections measured/independent	14501/4208 (R_{int}= 0.0219)
reflections observed $I>2\sigma$	3183
corrections applied	Absorption (Multi-scan, SADABS)
computer programs	SHELXL-97, SHELXS-97, PLATON
structure solution	Direct Methods
No. of parameters varied	164
GOF	1.043
R1 ($I>2\sigma$)	0.0416
wR2	0.1253
function minimized	$\Sigma\, w\, (\|F_o\|^2 - S\|F_c\|^2)$
diff. density final max/min (e Å^{-3})	0.366, -0.472

Table S4 - Summary of X-ray data collection and processing parameters, for 5-thiosaccharyl-1-methyltetrazole (**TSMT**) crystal.

Chemical formula	$C_9H_7N_5O_2S_2$
Colour/shape	colourless/plate
Formula weight	281.34
Space group	$P21/c$
Temperature, K	293
Cell volume (Å ^{3})	1167.98(5)
Crystal system	monoclinic
a (Å)	11.4904(3)
b (Å)	9.2300(2)
c (Å)	11.4850(3)
α (deg)	90.00
β (deg)	106.4862(15)
γ (deg)	99.00
Formula units/unit cell	4
D_c (Mg m^{-3})	1.600
Diffractometer/scan	Bruker ApexII/ ϕ and ω scans
Radiation (Å)(graph. monochromated)	0.71073
Max crystal dimensions (mm)	0.35x0.10x0.05
θ range (deg)	1.9-32.9
Range of *h, k,l*	–17,16; –13,13; –17;17
Reflections measured/independent	18361/4127 (R_{int}= 0.027)
Reflections observed $I>2\sigma$	2994
Corrections applied	Absorption (Multi-scan, SADABS)
Computer programs	SHELXL-97, SHELXS-97, PLATON
Structure solution	Direct Methods
No. of parameters varied	164
GOF	1.02
R_1 ($I>2\sigma$)	0.0372
wR_2	0.1030
Function minimized	$\Sigma\, w\,(\|F_o\|^2 - S\|F_c\|^2)$
Diff. density final max/min (*e* Å^{-3})	0.31, –0.31

Table S5 - Summary of X-ray data collection and processing parameters, for crystal of complex **Cu2MTS$_2$**, [Cu(2MTS)$_2$(H_2O)]·H_2O.

Empirical formula	$C_{18}H_{18}CuN_{12}O_6S_2$
Formula weight (g.mol^{-1})	626.09
Temperature (K)	293(2)
Wavelength (Å)	0.71073
Crystal system	Triclinic
Space group	*P-1*
a (Å)	8.4669(3)
b (Å)	11.3079(4)
c (Å)	12.7311(4)
α (º)	97.439(2)
β (º)	98.638(2)
γ (º)	91.496(2)
Volume (Å^3)	1193.65(7)
Z	2
Calculated density (g/cm^3)	1.742
Absorption coefficient (mm^{-1})	1.155
F(000)	638
Crystal size (mm^3)	0.44×0.17×0.11
θ range for data collection (º)	4.548-56.269
Index ranges	$-10<h<10$, $-14<k<14$, $-16<l<16$
Reflections collected/unique	27450/5483 (R_{int} = 0.0278)
Completeness to 2θ=27.427º	1.00
Refinement method	Full-matrix least-squares on F^2
Data/restrains/parameters	5483/0/ 366
Goodness-of-fit on F^2	1.028
Final *R* indices [$I > 2\sigma(I)$]	R_1 = 0.0306 wR_2 = 0.0780
R indices (all data)	R_1 = 0.0408 wR_2 = 0.0838
Largest diff. peak and hole	0.425 and -0.451

Table S6 – B3LYP/6-311++G(3df,3pd) optimized geometries for the minimum energy structures of **TS**.[a]

Parameter	A_0_0	A_155_170	B_0_0	B_0_180	B_157_180	B_151_0
Bond lengths/ pm						
C_1-C_2	138.8	139.4	138.7	138.7	139.4	139.3
C_1=C_6	137.9	137.7	137.9	137.9	137.8	137.8
C_1-S_7	178.8	178.1	179.0	179.0	178.0	178.2
C_2=C_3	138.9	139.1	138.9	138.9	139.0	139.0
C_2-C_9	148.2	148.9	149.0	149.1	149.2	149.1
C_3-C_4	139.2	139.3	139.3	139.3	139.3	139.3
C_3-H_{10}	108.2	107.6	108.2	108.2	107.6	107.6
C_4=C_5	139.3	139.1	139.3	139.3	139.1	139.1
C_4-H_{11}	108.1	108.1	108.1	108.1	108.1	108.1
C_5-C_6	139.4	139.4	139.4	139.4	139.3	139.3
C_5-H_{12}	108.1	108.1	108.1	108.1	108.1	108.1
C_6-H_{13}	108.0	108.0	108.0	108.1	108.1	108.0
S_7-N_8	167.8	167.3	167.0	167.0	166.6	166.9
S_7=O_{14}	143.3	143.4	143.4	143.4	143.5	143.4
S_7=O_{15}	143.3	143.3	143.4	143.4	143.4	143.4
N_8=C_9	129.3	128.8	128.7	128.6	129.2	129.1
C_9-N_{16}	135.7	138.4	136.1	136.3	137.6	137.5
N_{16}-C_{17}	137.8	137.5	138.0	138.2	137.7	137.7
N_{16}-H_{22}	100.7	101.1	100.7	100.6	101.1	101.2
C_{17}-N_{18}	131.3	131.2	135.7	135.2	135.2	135.9
C_{17}-N_{21}	133.8	134.9	132.1	132.8	132.9	132.2
N_{18}-N_{19}	135.8	136.2	130.4	130.7	130.3	130.3
N_{19}=N_{20}	128.3	127.8	131.5	131.5	131.0	131.3
N_{20}-N_{21}	135.3	135.5	133.0	132.6	132.6	133.3
$N_{20/21}$-H_{23}	101.0	100.7	100.8	100.8	100.9	100.8
Bond Angles/ °						
C_2-C_1=C_6	122.3	123.0	122.4	122.4	123.1	123.0
C_2-C_1-S_7	108.1	108.6	107.6	107.6	108.6	108.4
C_6=C_1-S_7	129.6	128.4	130.0	130.0	128.3	128.5
C_1-C_2=C_3	120.1	119.2	120.0	120.0	119.0	119.1
C_1-C_2-C_9	109.3	108.5	109.3	109.3	108.6	108.8
C_3=C_2-C_9	130.6	132.3	130.7	130.8	132.3	132.0
C_2=C_3-C_4	118.3	118.6	118.5	118.5	118.7	118.7
C_2=C_3-H_{10}	122.0	121.3	122.1	122.1	121.2	121.2
C_4-C_3-H_{10}	119.6	120.1	119.5	119.4	120.1	120.1
C_3-C_4=C_5	120.8	121.3	120.8	120.8	121.3	121.2
C_3-C_4-H_{11}	119.5	119.1	119.6	119.6	119.1	119.2
C_5=C_4-H_{11}	119.7	119.6	119.7	119.7	119.6	119.6
C_4=C_5-C_6	120.9	120.5	120.8	120.8	120.4	120.5
C_4=C_5-H_{12}	119.6	119.8	119.6	119.6	119.9	119.8
C_6-C_5-H_{12}	119.5	119.7	119.6	119.6	117.6	119.7
C_1=C_6-C_5	117.5	117.5	117.5	117.6	117.6	117.6
C_1=C_6-H_{13}	121.3	121.1	121.2	121.2	121.1	121.1
C_5-C_6-H_{13}	121.2	121.4	121.2	121.2	121.4	121.4
C_1-S_7-N_8	94.5	94.3	94.9	94.9	94.4	94.4
C_1-S_7=O_{14}	110.6	110.4	110.2	110.2	110.2	110.1
C_1-S_7=O_{15}	110.6	111.1	110.2	110.2	111.0	111.1
N_8-S_7=O_{14}	109.2	109.2	109.5	109.6	109.6	109.7
N_8-S_7=O_{15}	109.2	109.1	109.5	109.6	109.3	109.2
C_1-S_7=O_{15}	119.8	111.1	110.2	110.2	111.0	111.1
S_7-N_8=C_9	110.5	111.1	110.5	110.5	111.4	111.3
C_2-C_9-N_8	117.6	117.5	117.7	117.7	117.0	117.1
C_2-C_9-N_{16}	120.5	126.8	118.8	118.3	127.4	126.4
N_8=C_9-N_{16}	121.9	115.5	123.5	124.1	115.5	116.3
C_9-N_{16}-C_{17}	125.8	130.6	128.7	129.1	133.5	132.3
C_9-N_{16}-H_{22}	119.6	110.7	117.9	117.2	112.4	112.4
C_{17}-N_{16}-H_{22}	114.5	115.7	113.4	113.8	111.6	112.5
N_{16}-C_{17}=N_{18}	123.8	129.5	119.2	127.1	127.6	119.1
N_{16}-C_{17}-N_{21}	126.8	122.2	127.7	119.8	119.9	128.3

N_{18}=C_{17}-N_{21}	109.4	108.3	113.1	113.1	112.5	112.6
C_{17}=N_{18}-N_{19}	105.1	105.8	105.9	105.6	106.1	106.1
N_{18}-N_{19}=N_{20}	111.5	111.6	105.7	106.3	105.9	106.0
N_{19}=N_{20}-N_{21}	106.4	106.1	115.2	114.7	114.9	114.8
C_{17}-N_{21}-N_{20}	107.6	108.2	100.1	100.4	100.6	100.5
$C_{17/}N_{21}$-$N_{21/20}$-H_{23}	128.3	131.2	122.3	122.8	122.7	122.7
$N_{19/20}$-$N_{20/21}$-H_{23}	124.1	120.6	122.5	122.5	122.4	122.6
Dihedral Angles/ °						
C_6=C_1-C_2=C_3	0.0	0.6	0.0	0.0	0.8	1.3
C_6=C_1-C_2-C_9	180.0	178.3	180.0	180.0	178.1	177.8
S_7-C_1-C_2=C_3	180.0	-177.5	180.0	180.0	-176.8	-175.7
S_7-C_1-C_2-C_9	0.0	0.2	0.0	0.0	0.4	0.8
C_2-C_1=C_6-C_5	0.0	-0.2	0.0	0.0	-0.3	-0.4
C_2-C_1=C_6-H_{13}	180.0	-179.8	180.0	180.0	-179.7	-179.6
S_7-C_1=C_6-C_5	180.0	177.4	180.0	180.0	176.9	175.9
S_7-C_1=C_6-H_{13}	0.0	-2.2	0.0	0.0	-2.6	-3.3
C_2-C_1-S_7-N_8	0.0	-0.1	0.0	0.0	-0.2	-0.3
C_2-C_1-S_7=O_{14}	112.5	112.1	112.9	112.9	112.6	112.5
C_2-C_1-S_7=O_{15}	112.5	-112.6	-112.9	-112.9	-112.8	-112.8
C_6=C_1-S_7-N_8	180.0	-178.1	180.0	180.0	-177.7	-177.0
C_6=C_1-S_7=O_{14}	67.5	-65.8	-67.1	-67.1	-64.9	-64.2
C_6=C_1-S_7=O_{15}	67.5	69.5	67.1	67.1	69.7	70.5
C_1-C_2-C_3-C_4	0.0	-0.3	0.0	0.0	-0.7	-1.1
C_1-C_2-C_3-H_{10}	180.0	-178.3	180.0	180.0	-178.9	179.9
C_9-C_2=C_3-C_4	180.0	-177.4	180.0	180.0	-177.2	-176.7
C_9-C_2=C_3-H_{10}	0.0	4.6	0.0	0.0	4.6	4.3
C_1-C_2-C_9=N_8	0.0	-0.2	0.0	0.0	-0.7	-1.3
C_1-C_2-C_9-N_{16}	180.0	-174.6	180.0	180.0	-175.5	-176.0
C_3=C_2-C_9=N_8	180.0	177.1	180.0	180.0	176.1	174.6
C_3=C_2-C_9-N_{16}	0.0	2.8	0.0	0.0	1.2	-0.1
C_2=C_3-C_4=C_5	0.0	-0.2	0.0	0.0	0.0	0.1
C_2=C_3-C_4-H_{11}	180.0	-179.7	180.0	180.0	-179.8	-179.9
H_{10}-C_3-C_4=C_5	180.0	177.8	180.0	180.0	178.2	179.1
H_{10} C_3-C_4-H_{11}	0.0	-1.7	0.0	0.0	-1.5	-0.9
C_3-C_4=C_5-C_6	0.0	0.5	0.0	0.0	0.6	0.9
C_3-C_4=C_5-H_{12}	180.0	-179.6	180.0	180.0	-179.7	-179.8
H_{11}-C_4=C_5-C_6	180.0	-180.0	180.0	180.0	-179.7	-179.2
H_{11}-C_4=C_5-H_{12}	0.0	-0.1	0.0	0.0	0.0	0.2
C_4-C_5-C_6=C_1	0.0	-0.3	0.0	0.0	-0.4	-0.7
C_4-C_5-C_6-H_{13}	180.0	179.3	180.0	180.0	179.0	178.6
H_{12}-C_5-C_6=C_1	180.0	179.9	180.0	180.0	179.9	179.9
H_{12}-C_5-C_6-H_{13}	0.0	-0.5	0.0	0.0	-0.6	-0.8
C_1-S_7-N_8=C_9	0.0	0.0	0.0	0.0	-0.2	-0.5
O_{14}=S_7-N_8=C_9	113.6	-113.3	-113.5	-113.4	-113.5	-113.6
O_{15}=S_7-N_8=C_9	113.6	114.2	113.5	113.4	113.9	113.6
S_7-N_8=C_9-C_2	0.0	0.1	0.0	0.0	0.5	1.1
S_7-N_8=C_9=N_{16}	180.0	175.1	180.0	180.0	176.0	176.3
C_2-C_9=N_{16}-C_{17}	180.0	-30.6	180.0	180.0	-28.5	-34.4
C_2-C_9=N_{16}-H_{22}	0.0	170.2	0.0	0.0	168.0	166.3
N_8=C_9=N_{16}-C_{17}	0.0	154.9	0.0	0.0	156.6	150.9
N_8=C_9 =N_{16}-H_{22}	180.0	-4.2	180.0	180.0	-7.0	-8.4
C_9-N_{16}-C_{17}=N_{18}	180.0	-11.0	180.0	0.0	-2.7	-177.7
C_9-N_{16}-C_{17}-N_{21}	0.0	170.5	0.0	180.0	179.6	0.1
H_{22}-N_{16}-C_{17}=N_{18}	0.0	147.3	0.0	180.0	160.8	-18.4
H_{22}-N_{16}-C_{17}-N_{21}	180.0	-31.3	180.0	0.0	-17.0	159.4
N_{16}-C_{17}=N_{18}-N_{19}	180.0	-179.2	180.0	180.0	-178.3	178.4
N_{21}-C_{17}=N_{18}-N_{19}	0.0	-0.5	0.0	0.0	-0.4	0.3
N_{16}-C_{17}-N_{21}=N_{20}	180.0	178.8	180.0	180.0	178.2	-178.5
$N_{16/}C_{17}$-$C_{17/}N_{21}$-$N_{21/20}$-H_{23}	0.0	-3.1	180.0	180.0	-179.6	179.9
N_{18}=C_{17}-N_{21}-N_{20}	0.0	0.0	0.0	0.0	0.1	-0.6
N_{18}=C_{17}-N_{21}-H_{23}	180.0	178.0				
C_{17}=N_{18}-N_{19}=N_{20}	0.0	0.9	0.0	0.0	0.6	0.2
N_{18}-N_{19}=N_{20}-N_{21}	0.0	-0.9	0.0	0.0	-0.5	-0.6
N_{19}=N_{20}-N_{21}-C_{17}	0.0	0.5	0.0	0.0	0.3	0.7
$N_{19/18}$=$N_{20/19}$-$N_{21/20}$-H_{23}	180.0	-177.8	180.0	180.0	179.4	-179.8

[a] See Figure S1 for atom numbering.

(continue)

(Continuation) of ***Table S6***

Parameter	C_0_180	C_177_168	D_0_180	D_0_0	D_175_149
Bond lengths/ pm					
C_1-C_2	138.9	139.8	138.9	138.9	139.6
C_1=C_6	138.2	138.0	138.3	138.3	138.1
C_1-S_7	177.2	176.3	177.0	176.9	176.4
C_2=C_3	138.8	139.3	138.8	138.8	139.3
C_2-C_9	147.3	148.8	147.4	147.4	149.0
C_3-C_4	139.0	139.2	139.0	139.0	139.1
C_3-H_{10}	108.0	107.9	108.0	108.0	107.7
C_4=C_5	139.5	139.1	139.5	139.6	139.2
C_4-H_{11}	108.1	108.1	108.1	108.1	108.1
C_5-C_6	139.2	139.2	139.1	139.1	139.1
C_5-H_{12}	108.1	108.1	108.1	108.1	108.1
C_6-H_{13}	108.0	108.0	108.0	108.0	108.0
S_7-N_8	169.5	168.4	169.0	169.2	168.1
N_8-H_{22}	102.2	100.9	101.7	101.3	101.0
S_7=O_{14}	143.2	143.5	143.4	143.4	143.6
S_7=O_{15}	143.2	143.2	143.4	143.4	143.3
N_8=C_9	136.3	138.2	137.2	137.3	139.0
C_9-N_{16}	129.3	128.3	128.5	128.4	127.5
N_{16}-C_{17}	136.2	135.8	136.6	136.6	136.3
C_{17}-N_{18}	132.8	132.5	137.1	136.5	136.6
C_{17}-N_{21}	134.8	135.3	133.4	133.9	133.5
N_{18}-N_{19}	135.4	135.3	130.2	129.8	130.4
N_{19}=N_{20}	128.6	128.8	131.8	132.1	131.8
N_{20}-N_{21}	134.6	134.0	132.0	132.4	132.1
$N_{20/21}$-H_{23}	100.7	100.6	100.8	100.8	100.8
Bond Angles/ °					
C_2-C_1=C_6	122.5	123.3	122.5	122.5	123.3
C_2-C_1-S_7	110.6	111.7	110.6	110.6	111.6
C_6=C_1-S_7	126.9	125.0	126.9	126.8	125.1
C_1-C_2=C_3	119.9	118.5	119.9	119.9	118.4
C_1-C_2-C_9	112.6	111.9	112.9	113.0	111.9
C_3=C_2-C_9	127.5	129.6	127.2	127.1	129.7
C_2=C_3-C_4	118.5	118.9	118.4	118.4	119.0
C_2=C_3-H_{10}	119.9	120.0	119.7	119.7	120.3
C_4-C_3-H_{10}	121.6	121.1	121.8	121.9	120.7
C_3-C_4=C_5	120.9	121.4	121.0	121.0	121.4
C_3-C_4-H_{11}	119.6	119.0	119.6	119.6	119.1
C_5=C_4-H_{11}	119.5	119.6	119.5	119.4	119.6
C_4=C_5-C_6	120.9	120.4	120.9	120.9	120.3
C_4=C_5-H_{12}	119.7	120.0	119.7	119.7	120.0
C_6-C_5-H_{12}	119.4	119.6	119.4	119.4	119.7
C_1=C_6-C_5	117.3	117.5	117.3	117.3	117.6
C_1=C_6-H_{13}	121.4	121.1	121.4	121.4	121.1
C_5-C_6-H_{13}	121.3	121.4	121.3	121.3	121.4
C_1-S_7-N_8	91.0	90.5	91.1	91.0	90.7
C_1-S_7=O_{14}	111.8	112.4	111.9	112.0	112.2
C_1-S_7=O_{15}	111.8	111.9	111.9	112.0	111.6
N_8-S_7=O_{14}	109.6	109.6	109.8	109.7	109.9
N_8-S_7=O_{15}	109.6	110.0	109.8	109.7	110.2
C_1-S_7=O_{15}	111.8	111.9	111.9	112.0	111.6
S_7-N_8=C_9	115.8	116.8	116.0	116.1	116.3
C_2-C_9-N_8	110.0	108.4	109.4	109.3	108.2
C_2-C_9-N_{16}	122.6	135.4	122.1	122.3	135.0
N_8=C_9-N_{16}	127.4	116.2	128.5	128.4	116.7
C_9-N_{16}-C_{17}	119.3	129.9	121.3	121.8	129.5
C_9-N_8-H_{22}	120.4	119.4	121.0	116.1	118.2
S_7-N_8-H_{22}	123.8	120.1	123.0	122.3	119.1
N_{16}-C_{17}=N_{18}	130.9	134.2	127.2	121.2	128.0
N_{16}-C_{17}-N_{21}	122.3	119.1	121.9	127.6	120.6
N_{18}=C_{17}-N_{21}	106.8	106.6	110.9	111.1	111.2
C_{17}=N_{18}-N_{19}	106.6	106.6	107.1	106.8	106.8

N_{18}-N_{19}=N_{20}	111.0	111.2	105.3	106.2	105.6
N_{19}=N_{20}-N_{21}	106.3	106.0	115.4	114.3	115.1
C_{17}-N_{21}-N_{20}	109.2	109.5	101.3	101.5	101.3
$C_{17/}N_{21}$-$N_{21/20}$-H_{23}	129.2	128.8	121.9	122.4	122.2
$N_{19/20}$-$N_{20/21}$-H_{23}	121.6	121.7	122.7	123.2	122.8
Dihedral Angless/ °					
C_6=C_1-C_2=C_3	0.0	-0.4	0.0	0.0	-0.6
C_6=C_1-C_2-C_9	180.0	179.6	180.0	180.0	178.7
S_7-C_1-C_2=C_3	180.0	179.2	180.0	180.0	179.0
S_7-C_1-C_2-C_9	0.0	-0.8	0.0	0.0	-1.7
C_2-C_1=C_6-C_5	0.0	-0.2	0.0	0.0	-0.3
C_2-C_1=C_6-H_{13}	180.0	179.7	180.0	180.0	179.6
S_7-C_1=C_6-C_5	180.0	-179.7	180.0	180.0	-179.8
S_7-C_1=C_6-H_{13}	0.0	0.2	0.0	0.0	0.1
C_2-C_1-S_7-N_8	0.0	-3.7	0.0	0.0	-4.3
C_2-C_1-S_7=O_{14}	111.7	107.8	111.9	111.8	107.6
C_2-C_1-S_7=O_{15}	-111.7	-115.5	-111.9	-111.8	-116.4
C_6=C_1-S_7-N_8	180.0	175.9	180.0	180.0	175.3
C_6=C_1-S_7=O_{14}	-68.3	-72.6	-68.1	-68.2	-72.9
C_6=C_1-S_7=O_{15}	68.3	64.1	68.1	68.2	63.1
C_1-C_2-C_3-C_4	0.0	0.7	0.0	0.0	1.0
C_1-C_2-C_3-H_{10}	180.0	-178.5	180.0	180.0	-176.9
C_9-C_2=C_3-C_4	180.0	-179.3	180.0	180.0	-178.1
C_9-C_2=C_3-H_{10}	0.0	1.6	0.0	0.0	4.0
C_1-C_2-C_9=N_8	0.0	6.2	0.0	0.0	8.5
C_1-C_2-C_9-N_{16}	180.0	-171.8	180.0	180.0	-167.7
C_3=C_2-C_9=N_8	180.0	-173.9	180.0	180.0	-172.4
C_3=C_2-C_9-N_{16}	0.0	8.2	0.0	0.0	11.4
C_2=C_3-C_4=C_5	0.0	-0.5	0.0	0.0	-0.7
C_2=C_3-C_4-H_{11}	180.0	180.0	180.0	180.0	-179.9
H_{10}-C_3-C_4=C_5	180.0	178.7	180.0	180.0	177.2
H_{10} C_3-C_4-H_{11}	0.0	-0.9	0.0	0.0	-2.0
C_3-C_4=C_5-C_6	0.0	-0.1	0.0	0.0	-0.2
C_3-C_4=C_5-H_{12}	180.0	-179.8	180.0	180.0	-179.6
H_{11}-C_4=C_5-C_6	180.0	179.5	180.0	180.0	179.1
H_{11}-C_4=C_5-H_{12}	0.0	-0.2	0.0	0.0	-0.4
C_4-C_5-C_6=C_1	0.0	0.4	0.0	0.0	0.6
C_4-C_5-C_6-H_{13}	180.0	-179.5	180.0	180.0	-179.2
H_{12}-C_5-C_6=C_1	180.0	-179.9	180.0	180.0	-179.9
H_{12}-C_5-C_6-H_{13}	0.0	0.2	0.0	0.0	0.2
C_1-S_7-N_8=C_9	0.0	7.9	0.0	0.0	10.0
O_{14}=S_7-N_8=C_9	-113.6	-106.1	-113.8	-113.9	-104.1
O_{15}=S_7-N_8=C_9	113.6	121.5	113.8	113.9	123.4
S_7-N_8=C_9-C_2	0.0	-9.5	0.0	0.0	-12.3
S_7-N_8=C_9=N_{16}	180.0	168.9	180.0	180.0	164.7
C_2-C_9=N_{16}-C_{17}	180.0	-4.9	180.0	180.0	-8.8
C_2-C_9=N_8-H_{22}	180.0	-168.0	180.0	180.0	-164.2
N_8=C_9-N_{16}-C_{17}	0.0	177.2	0.0	0.0	175.3
N_{16}=C_9 =N_8-H_{22}	0.0	10.4	0.0	0.0	12.8
C_9-N_{16}-C_{17}=N_{18}	0.0	-15.5	0.0	180.0	-37.0
C_9-N_{16}-C_{17}-N_{21}	180.0	167.8	180.0	0.0	149.3
H_{22}-N_8-S_7=C_1	180.0	166.3	180.0	180.0	161.6
H_{22}-N_8-C_9=N_{16}	0.0	10.4	0.0	0.0	12.8
N_{16}-C_{17}=N_{18}-N_{19}	180.0	-177.3	180.0	180.0	-174.8
N_{21}-C_{17}=N_{18}-N_{19}	0.0	-0.3	0.0	0.0	-0.6
N_{16}-C_{17}-N_{21}=N_{20}	180.0	178.0	180.0	180.0	175.6
$N_{16/}C_{17}$-$C_{17/}N_{21}$-$N_{21/20}$-H_{23}	0.0	-1.7	180.0	180.0	179.8
N_{18}=C_{17}-N_{21}-N_{20}	0.0	0.5	0.0	0.0	2.0
N_{18}=C_{17}-N_{21}-H_{23}	180.0	-179.2			
C_{17}=N_{18}-N_{19}=N_{20}	0.0	0.07	0.0	0.0	0.0
N_{18}-N_{19}=N_{20}-N_{21}	0.0	0.2	0.0	0.0	0.7
N_{19}=N_{20}-N_{21}-C_{17}	0.0	-0.5	0.0	0.0	-1.0
$N_{19/18}$=$N_{20/19}$-$N_{21/20}$-H_{23}	180.0	179.3	180.0	180.0	179.9

[a] See Figure 3.1 for atom numbering.

Table S7 – Experimental (X-ray; single crystal) geometrical parameters for **TS**. DFT B3LYP/6-311++G(3df,3pd) calculated geometrical parameters of the A_0_0 form are also shown for comparison. Geometrical parameters involving H atoms derived from X-ray data are given without uncertainties as the positions of the H atoms were constrained to idealized positions riding on their parent atoms; typical average values for C-H and N-H bond lengths derived from X-ray data (SHEXL-97 defaults), shorter than internuclear distances, were used.[a]

Parameter	Calculated **TS**(A_0_0)	X-ray (crystal)		Calculated **TS** (A_0_0)	X-ray (crystal)		Calculated **TS** (A_0_0)	X-ray (crystal)
Bond lengths/ pm			*Bond angles/ °*			*Dihedral angles/ °*		
C_1-C_2	138.8	138.3(2)	C_2-C_1=C_6	122.3	122.4(1)	C_6=C_1-C_2=C_3	0.0	-0.5(2)
C_1=C_6	137.9	137.8(2)	C_2-C_1-S_7	108.1	107.3(1)	C_6=C_1-C_2-C_9	180.0	-178.2(1)
C_1-S_7	178.8	176.3(2)	C_6=C_1-S_7	129.6	130.2(1)	S_7-C_1-C_2=C_3	180.0	176.9(1)
C_2=C_3	138.9	138.6(2)	C_1-C_2=C_3	120.1	120.4(1)	S_7-C_1-C_2-C_9	0.0	-0.8(2)
C_2-C_9	148.2	148.1(2)	C_1-C_2-C_9	109.3	109.3(1)	C_2-C_1=C_6-C_5	0.0	0.4(2)
C_3-C_4	139.2	138.5(2)	C_3=C_2-C_9	130.6	130.2(1)	S_7-C_1=C_6-C_5	180.0	-176.4(1)
C_3-H_{10}	108.2	93.0	C_2=C_3-C_4	118.3	117.8(2)	C_2-C_1-S_7-N_8	0.0	0.7(1)
C_4=C_5	139.3	138.3(3)	C_2=C_3-H_{10}	122.0	121.1	C_2-C_1-S_7=O_{14}	112.5	112.5(1)
C_4-H_{11}	108.1	93.0	C_4-C_3-H_{10}	119.6	121.1	C_2-C_1-S_7=O_{15}	112.5	115.4(1)
C_5-C_6	139.4	139.2(3)	C_3-C_4=C_5	120.8	121.5(2)	C_6=C_1-S_7-N_8	180.0	177.8(1)
C_5-H_{12}	108.1	93.0	C_3-C_4-H_{11}	119.5	119.3	C_6=C_1-S_7=O_{14}	67.5	64.7(2)
$_6$-H_{13}	108.0	93.0	C_5=C_4-H_{11}	119.7	119.3	C_6=C_1-S_7=O_{15}	67.5	-67.5(2)
S_7-N_8	167.8	165.4(1)	C_4=C_5-C_6	120.9	120.9(2)	C_1-C_2-C_3-C_4	0.0	0.3(2)
S_7=O_{14}	143.3	142.8(1)	C_4=C_5-H_{12}	119.6	119.5	C_9-C_2=C_3-C_4	180.0	177.5(2)
S_7=O_{15}	143.3	142.0(1)	C_6-C_5-H_{12}	119.5	119.5	C_1-C_2-C_9=N_8	0.0	0.7(2)
N_8=C_9	129.3	130.2(2)	C_1=C_6-C_5	117.5	117.1(2)	C_1-C_2-C_9-N_{16}	180.0	179.2(1)
C_9-N_{16}	135.7	134.7(2)	C_1=C_6-H_{13}	121.3	121.5	C_3=C_2-C_9=N_8	180.0	-176.7(2)
N_{16}-C_{17}	137.8	137.9(2)	C_5-C_6-H_{13}	121.2	121.5	C_3=C_2-C_9-N_{16}	0.0	1.8(2)
N_{16}-H_{22}	100.7	86.0	C_1-S_7-N_8	94.5	96.48(6)	C_2=C_3-C_4=C_5	0.0	0.0(3)
C_{17}-N_{18}	131.3	131.6(2)	C_1-S_7=O_{14}	110.6	110.01(7)	C_3-C_4=C_5-C_6	0.0	-0.2(3)
C_{17}-N_{21}	133.8	132.6(2)	C_1-S_7=O_{15}	110.6	112.31(8)	C_4-C_5-C_6=C_1	0.0	0.0(3)
N_{18}-N_{19}	135.8	136.6(2)	N_8-S_7=O_{14}	109.2	109.15(7)	C_1-S_7-N_8=C_9	0.0	-0.3(1)
N_{19}=N_{20}	128.3	128.8(2)	N_8-S_7=O_{15}	109.2	110.01(8)	O_{14}=S_7-N_8=C_9	113.6	113.6(1)
N_{20}-N_{21}	135.3	135.6(2)	S_7-N_8=C_9	110.5	109.1(1)	O_{15}=S_7-N_8=C_9	113.6	-116.9(1)
N_{21}-H_{23}	101.0	86.0	C_2-C_9-N_8	117.6	117.8(1)	S_7-N_8=C_9-C_2	0.0	-0.2(2)
			C_2-C_9-N_{16}	120.5	120.5(1)	S_7-N_8=C_9=N_{16}	180.0	-178.7(1)
			N_8=C_9-N_{16}	121.9	121.7(1)	C_2-C_9=N_{16}-C_{17}	180.0	-177.7(1)
			C_9-N_{16}-C_{17}	125.8	124.7(1)	N_8=C_9=N_{16}-C_{17}	0.0	0.8(2)
			C_9-N_{16}-H_{22}	119.6	117.7	C_9-N_{16}-C_{17}=N_{18}	180.0	-173.8(1)
			C_{17}-N_{16}-H_{22}	114.5	117.7	C_9-N_{16}-C_{17}-N_{21}	0.0	7.7(2)
			N_{16}-C_{17}=N_{18}	123.8	123.0(1)	N_{16}-C_{17}=N_{18}-N_{19}	180.0	-179.1(1)
			N_{16}-C_{17}-N_{21}	126.8	127.0(1)	N_{21}-C_{17}=N_{18}-N_{19}	0.0	-0.4(2)
			N_{18}=C_{17}-N_{21}	109.4	110.0(1)	N_{16}-C_{17}-N_{21}=N_{20}	180.0	179.5(2)
			C_{17}=N_{18}-N_{19}	105.1	104.6(1)	N_{18}=C_{17}-N_{21}-N_{20}	0.0	0.8(2)
			N_{18}-N_{19}=N_{20}	111.5	111.3(1)	C_{17}=N_{18}-N_{19}=N_{20}	0.0	-0.2(2)
			N_{19}=N_{20}-N_{21}	106.4	106.3(1)	N_{18}-N_{19}=N_{20}-N_{21}	0.0	0.7(2)
			C_{17}-N_{21}-N_{20}	107.6	107.8(1)	N_{19}=N_{20}-N_{21}-C_{17}	0.0	-0.9(2)
			C_{17}-N_{21}-H_{23}	128.3	126.1			
			N_{20}-N_{21}-H_{23}	124.1	126.1			

[a] See Figure 3.1 for atom numbering

Table S8 – Experimental (X-ray; single crystal) geometrical parameters for **TSMT**. O3LYP/6-311++G(3df,3pd) calculated geometrical parameters of the form I are also shown for comparison. Geometrical parameters involving H atoms derived from X-ray data are given without uncertainties as the positions of the H atoms were constrained to idealized positions riding on their parent atoms; typical average values for C-H bond lengths derived from X-ray data (SHEXL-97 defaults), shorter than internuclear distances, were used.[a]

Parameter	Calculated **TSMT** (I)	X-Ray (crystal)		Calculated **TSMT** (I)	X-Ray		Calculated **TSMT** (I)	X-Ray (crystal)
Bond Lengths /(Å)			*Bond Angles / º*			*Dihedral Angles / º*		
S_7-O_{14}	1.434	1.4220(13)	O_{14}-S_7-O_{15}	120.1	118.30(8)	O_{14}-S_7-N_8-C_9	112.9	112.16(12)
S_7-O_{15}	1.431	1.4246(12)	O_{14}-S_7-N_8	108.1	108.18(7)	O_{15}-S_7-N_8-C_9	-114.7	-118.03(12)
S_7-N_8	1.685	1.6750(14)	O_{14}-S_7-C_1	110.7	111.88(8)	C_1-S_7-N_8-C_9	-0.7	-3.14(12)
S_7-C_1	1.779	1.7596(15)	O_{15}-S_7-N_8	109.3	108.94(8)	O_{14}-S_7-C_1-C_6	69.3	72.96(16)
S_{16}-C_9	1.753	1.7480(15)	O_{15}-S_7-C_1	110.8	111.32(8)	O_{15}-S_7-C_1-C_6	-66.6	-61.88(17)
S_{16}-C_{17}	1.744	1.7431(15)	N_8-S_7-C_1	94.8	95.76(7)	N_8-S_7-C_1-C_6	-179.3	-174.81(15)
N_8-C_9	1.283	1.284(2)	C_9-S_{16}-C_{17}	103.0	98.99(7)	N_8-S_7-C_1-C_2	0.4	3.49(11)
N_{18}-N_{19}	1.342	1.352(2)	S_7-N_8-C_9	109.9	109.14(11)	O_{14}-S_7-C_1-C_2	-111.1	-108.75(11)
N_{18}-C_{17}	1.320	1.312(2)	N_{19}-N_{18}-C_{17}	105.6	105.18(15)	O_{15}-S_7-C_1-C_2	113.1	116.42(11)
N_{19}-N_{20}	1.293	1.294(2)	N_{18}-N_{19}-N_{20}	111.1	111.17(16)	C_{17}-S_{16}-C_9-N_8	-3.3	-10.46(14)
N_{20}-N_{21}	1.336	1.336(2)	N_{19}-N_{20}-N_{21}	107.1	106.27(15)	C_9-S_{16}-C_{17}-N_{21}	72.4	74.55(14)
N_{21}-C_{17}	1.350	1.335(2)	N_{20}-N_{21}-C_{17}	107.4	108.26(13)	C_{17}-S_{16}-C_9-C_2	177.4	168.88(11)
N_{21}-C_{22}	1.449	1.451(2)	N_{20}-N_{21}-C_{22}	121.1	121.45(15)	C_9-S_{16}-C_{17}-N_{18}	-115.3	-108.80(14)
C_1-C_2	1.390	1.382(2)	C_{17}-N_{21}-C_{22}	131.5	130.29(14)	S_7-N_8-C_9-S_{16}	-178.4	-178.65(8)
C_1-C_6	1.380	1.377(2)	S_7-C_1-C_2	107.9	107.68(11)	S_7-N_8-C_9-C_2	0.9	2.01(17)
C_2-C_3	1.390	1.383(2)	S_7-C_1-C_6	129.7	129.23(12)	N_{19}-N_{18}-C_{17}-S_{16}	-174.3	-177.38(12)
C_2-C_9	1.483	1.484(2)	C_2-C_1-C_6	122.4	123.07(14)	N_{19}-N_{18}-C_{17}-N_{21}	-0.7	-0.23(18)
C_3-C_4	1.392	1.389(3)	C_1-C_2-C_3	120.0	120.39(14)	C_{17}-N_{18}-N_{19}-N_{20}	0.0	-0.3(2)
C_4-C_5	1.394	1.379(3)	C_1-C_2-C_9	109.2	109.24(12)	N_{18}-N_{19}-N_{20}-N_{21}	0.7	0.7(2)
C_5-C_6	1.395	1.387(3)	C_3-C_2-C_9	130.8	130.27(14)	N_{19}-N_{20}-N_{21}-C_{22}	-179.1	179.00(15)
C_3-H_{10}	1.083	0.9300	C_2-C_3-C_4	118.4	117.06(15)	N_{19}-N_{20}-N_{21}-C_{17}	-1.1	-0.81(18)
C_4-H_{11}	1.083	0.9300	C_3-C_4-C_5	120.9	121.85(17)	N_{20}-N_{21}-C_{17}-S_{16}	174.3	177.73(12)
C_5-H_{12}	1.083	0.9300	C_4-C_5-C_6	120.9	121.34(17)	C_{22}-N_{21}-C_{17}-S_{16}	-8.0	-2.1(2)
C_6-H_{13}	1.082	0.9300	C_1-C_6-C_5	117.4	116.29(16)	N_{20}-N_{21}-C_{17}-N_{18}	1.1	0.65(17)
C_{22}-H_{23}	1.089	0.9600	S_{16}-C_9-N_8	123.5	122.44(12)	C_{22}-N_{21}-C_{17}-N_{18}	178.8	-179.13(16)
C_{22}-H_{24}	1.089	0.9600	S_{16}-C_9-C_2	118.3	119.51(10)	S_7-C_1-C_6-C_5	179.7	178.44(13)
C_{22}-H_{25}	1.086	0.9600	N_8-C_9-C_2	118.2	118.04(13)	C_2-C_1-C_6-C_5	0.1	0.4(2)
			S_{16}-C_{17}-N_{18}	123.3	124.33(12)	C_6-C_1-C_2-C_3	0.0	-1.0(2)
			S_{16}-C_{17}-N_{21}	127.6	126.48(11)	S_7-C_1-C_2-C_3	-179.6	-179.46(12)
			N_{18}-C_{17}-N_{21}	108.8	109.12(14)	S_7-C_1-C_2-C_9	0.0	-2.79(14)
			C_2-C_3-H_{10}	121.4	121.00	C_6-C_1-C_2-C_9	179.7	175.64(14)
			C_4-C_3-H_{10}	120.2	121.00	C_1-C_2-C_3-C_4	-0.1	1.2(2)
			C_3-C_4-H_{11}	119.5	119.00	C_3-C_2-C_9-N_8	179.0	176.87(16)
			C_5-C_4-H_{11}	119.6	119.00	C_1-C_2-C_9-S_{16}	178.7	-178.73(10)
			C_4-C_5-H_{12}	119.6	119.00	C_1-C_2-C_9-N_8	-0.6	0.63(19)
			C_6-C_5-H_{12}	119.5	119.00	C_9-C_2-C_3-C_4	-179.7	-174.71(15)
			C_1-C_6-H_{13}	121.4	122.00	C_3-C_2-C_9-S_{16}	-1.6	-2.5(2)
			C_5-C_6-H_{13}	121.2	122.00	C_2-C_3-C_4-C_5	0.1	-0.7(3)
			N_{21}-C_{22}-H_{23}	109.4	109.00	C_3-C_4-C_5-C_6	0.1	0.1(3)
			N_{21}-C_{22}-H_{24}	110.2	110.00	C_4-C_5-C_6-C_1	-0.1	0.1(3)
			N_{21}-C_{22}-H_{25}	107.7	109.00			
			H_{23}-C_{22}-H_{24}	109.6	109.00			
			H_{23}-C_{22}-H_{25}	109.9	109.00			
			H_{24}-C_{22}-H_{25}	110.1	109.00			

[a] See Figure 2 for atom numbering

Table S9 - Calculated [B3LYP/6-311++G(3df,3pd), scaled by 0.978] vibrational frequencies (ν; cm^{-1}) and calculated IR intensities (*I*, km mol^{-1}) for all relevant photoproducts of **TSMT** monomer isolated in argon matrix.[a,b]

Approximate description	Calculated	
	ν	*I*
Diazirine **1** (conformer *i)*		
νCH Ph	3137.901	4.9534
	3131.503	1.659
	3120.743	3.4348
	3112.96	0.4504
νCH_3 as	3052.52	14.101
νCH_3 as	3028.517	8.294
νCH_3 s	2952.928	24.0208
$\nu C_{17}=N_{18}$	1722.351	110.6032
νCC Ph	1601.161	24.4424
νCC Ph	1588.368	1.4076
νC=N (saccharinate)	1545.808	120.8045
δCH_3 as	1464.771	10.56
δCH Ph	1456.281	2.6894
δCH Ph	1450.46	1.5102
δCH_3 as	1439.908	12.4504
δCH_3 s	1396.774	2.4351
νSO_2 as	1352.735	191.6417
νCC Ph	1326.741	5.228
δCH Ph	1277.243	0.1882
$\nu C_{17}N_{19}(CH_3)$ as	1228.724	28.0054
νC_2C_9	1205.926	169.3808
νSO_2 s	1168.279	287.621
δCH Ph	1163.775	11.4161
Diazirine **1** (conformer *ii*)		
νCH Ph	3137.676	4.7767
	3130.728	2.4525
	3119.766	3.8669
	3111.708	0.4688
νCH_3 as	3045.93	16.9778
νCH_3 as	3005.274	13.0378
νCH_3 s	2941.561	29.0036
$\nu C_{17}=N_{18}$	1740.612	77.9013
νCC Ph	1601.163	31.2532
νCC Ph	1589.106	0.8731
νC=N (saccharinate)	1548.153	125.4778
δCH_3 as	1467.439	11.3569
δCH Ph	1456.241	2.9878
δCH Ph	1450.387	2.0217
δCH_3 as	1439.71	3.697
δCH_3 s	1399.695	8.2681
νSO_2 as	1356.222	194.4379

νCC Ph	1326.687	4.7408
δCH Ph	1276.222	0.7461
$\nu C_{17}N_{19}(CH_3)$ as	1218.036	5.8395
νC_2C_9	1200.784	192.0404
νSO_2 s	1169.193	309.971
δCH Ph	1163.226	9.0244
Nitrile imine		
νCH Ph	3137.116	5.6002
	3130.597	2.8992
	3120.646	5.9971
	3111.211	0.5336
νCH_3 as	3077.387	15.4405
νCH_3 as	3004.302	19.2048
νCH_3 s	2946.188	55.2943
νNNC as	2047.071	761.1315
νCC Ph	1601.458	34.8389
νCC Ph	1588.899	2.8633
νC=N (saccharinate)	1547.448	154.9088
δCH_3 as	1462.036	12.4088
δCH Ph	1456.719	4.0301
δCH_3 as	1453.215	11.5326
δCH Ph	1449.966	1.044
δCH_3 s	1405.043	11.4264
νSO_2 as	1349.135	200.8728
νNNC s	1346.103	222.0349
νCC Ph	1325.147	11.2214
δCH Ph	1275.269	0.0129
νC_2C_9	1207.774	202.6019
νSO_2 s	1166.516	343.2182
δCH Ph	1162.39	17.9889
δCH Ph	1125.829	26.1606
γCH_3	1122.583	19.3694
γCH_3	1066.917	2.9009
νCC Ph	1046.616	4.3711
Thiocarbodiimide **2**		
νCH Ph	3136.698	6.5209
	3129.958	2.9182
	3119.536	3.3952
	3111.012	0.4669
νCH_3 as	3065.779	16.6984
νCH_3 as	3039.646	8.2841
νCH_3 s	2974.294	31.9395
νNCN as	2181.808	1238.429
νCC Ph	1595.706	9.8293
νCC Ph	1589.004	0.6926
νC=N (saccharinate)	1513.365	148.9782
δCH_3 as	1470.535	10.9536
δCH_3 as	1461.957	1.4429
δCH Ph	1457.543	6.1178
δCH Ph	1447.32	1.2888

δCH_3 s	1420.876	82.6544
δCH_3 s, νNCN s	1399.673	3.5256
νSO_2 as	1338.717	196.3493
νCC Ph	1323.036	4.2291
δCH Ph	1276.203	0.4548
νC_2C_9	1212.327	116.2561
νSO_2 s	1163.848	178.9449
	1161.551	123.1738
δCH Ph	1126.941	9.1873
γCH_3	1123.521	43.5821
Thiocyanate **3**		
νCH Ph	3138.678	3.9631
	3132.018	1.8036
	3119.869	3.5587
	3112.437	0.649
$\nu C_{17}N_{18}$	2233.744	5.6971
νCC Ph	1603.804	41.3768
νCC Ph	1588.036	1.6934
νC=N (saccharinate)	1555.836	112.0279
δCH Ph	1456.401	2.2256
δCH Ph	1450.196	2.7601
νSO_2 as	1359.403	196.1341
νCC Ph	1326.241	5.6923
δCH Ph	1277.14	0.445
νC_2C_9	1207.391	157.7956
νSO_2 s	1170.267	301.7746
δCH Ph	1164.139	7.3589
δCH Ph	1126.846	16.0942
Methyl Azide **4**		
νCH_3 as	3080.023	8.3818
νCH_3 as	3006.212	26.2929
νCH_3 s	2949.913	45.1429
νNNN as	2190.062	559.8998
δCH_3 as’	1464.764	7.8409
δCH_3 as’	1461.131	15.967
δCH_3 s	1420.581	6.6745
νNNN s	1310.778	138.7999
γCH_3	1124.645	10.6065
γCH_3	1085.74	0.5149
Methylenimine		
νNH	3363.047	0.9108
νCH_2 as	3046.501	28.9327
νCH_2 s	2951.784	50.9714
νCN	1672.657	22.7575
δCH_2	1458.231	7.6877
δNH	1338.308	41.1177
γNH	1136.98	43.4055
γCH_2	1076.589	17.1208

ωCH$_2$	1050.076	35.9749
	CNH **5**	
νNH	3805.143	254.6716
νCN	2102.435	72.013

[a] Only the investigated bonds are shown.[b] ν, Stretching; δ, bending; γ, rocking; ω, wagging; τω, twisting; τ, torsion; s, symmetric; as, numbering.

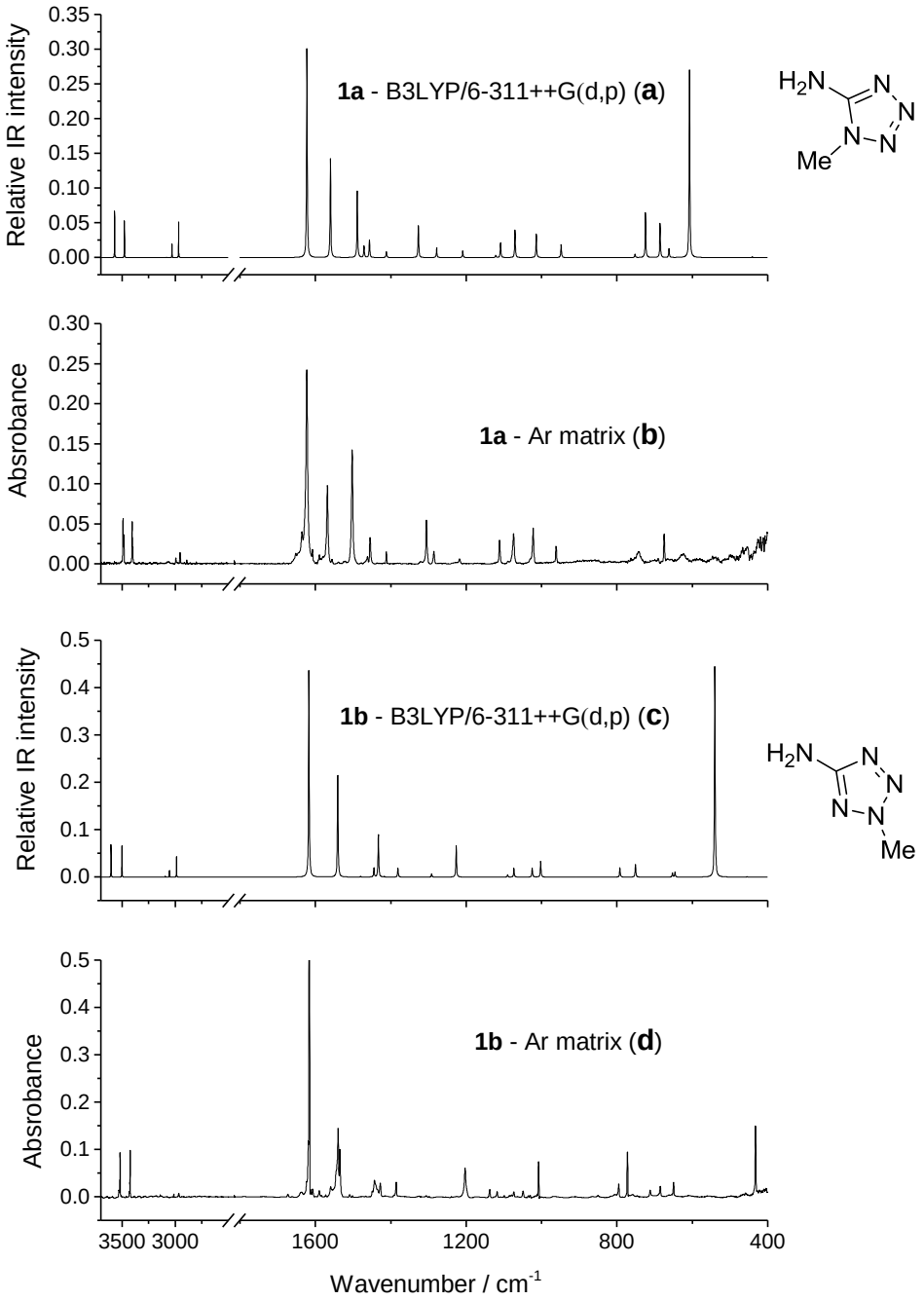

Figure S1 - (a) Experimental IR spectrum of 1-methyl-5-aminotetrazole **1MT** isolated in an argon matrix at 15 K. (b) IR spectra of **1MT** simulated at the B3LYP/6-311++G(d,p) level of theory. (c) Experimental IR spectrum of 2-methyl-5-aminotetrazole **2MT** isolated in an argon matrix at 15 K. (d) IR spectra of **2MT** simulated at the B3LYP/6-311++G(d,p) level of theory. The calculated spectra were simulated using Lorentzian functions centred at the calculated frequency scaled by 0.968 and with full width at half-maximum (fwhm) equal to 2 cm^{-1}. In relation to the observed bands corresponding to the intense wNH_2 calculated bands appearing at 602 and 535 cm^{-1} for **1MT** and **2MT**, respectively, please see the appropriate notes in Table S10 and Table S11.

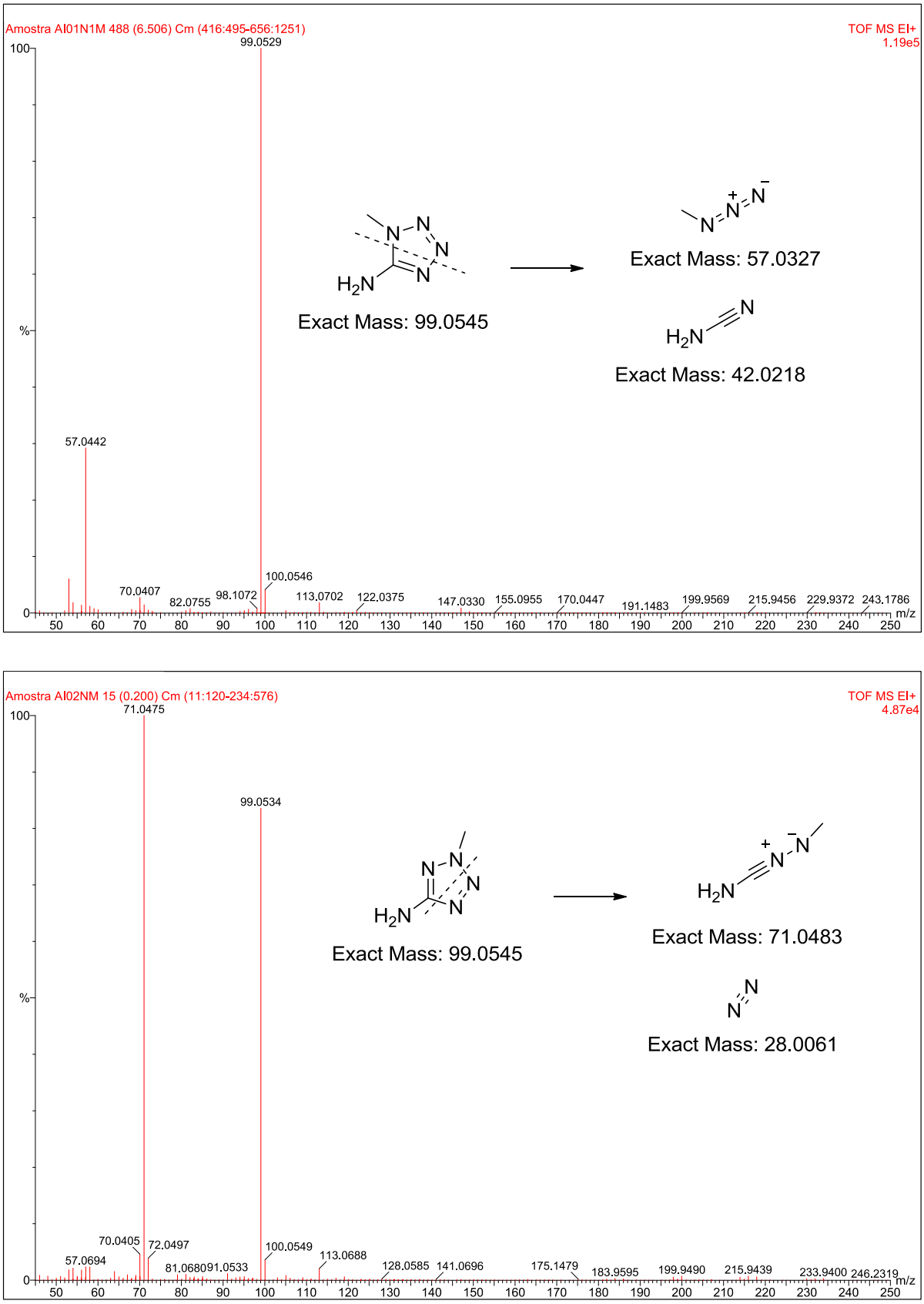

Figure S2 – *Top*: mass spectra of 1-methyl-5-aminotetrazole; *bottom*: 2-methyl-5-aminotetrazole, with a representation of the fragmentation patterns.

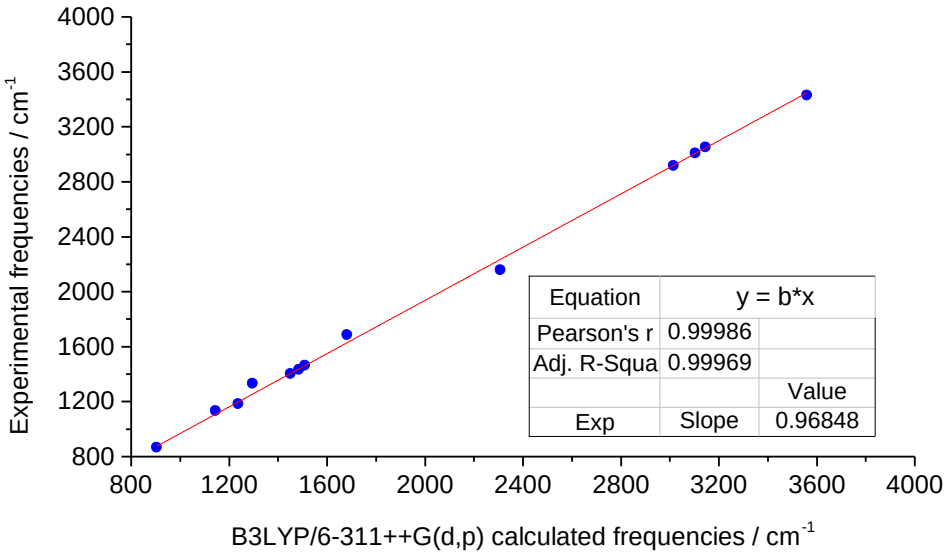

Figure S3 – Least-squares linear fit (red line) of the experimental versus calculated (B3LYP/6-311++G(d,p)) frequencies of the IR spectrum of cyanamide **14** isolated in an argon matrix.

Table S10 – Proposed band assignments for the infrared spectrum of matrix-isolated 1-methyl-5-aminotetrazole **1MT**.[a,b]

Approximate description	Ar matrix	Calculated	
	ν	ν	*I*
νNH_2 as	3494/3485	3536	40.7
νNH_2 s	3408/3402	3445	31.9
νCH_3 as'	-	3053	0.5
νCH_3 as''	2997/2915	3002	12.1
νCH_3 s	2957/2894	2940	30.8
δNH_2	1623	1606	181.0
νC_5N_6; δNH_2	1569	1545	87.1
$\nu N_4C_5N_1$ as	1503	1474	59.2
δCH_3 as'	1462	1456	10.0
δCH_3 as''	1455	1442	16.1
δCH_3 s	1412	1398	5.4
$\nu N_2{=}N_3$	1306	1314	28.3
νC_9N_2; γNH_2	1286	1266	8.5
γCH_3'	1218	1197	6.0
γCH_3''	1120	1111	1.9
νC_5N_4; γNH_2	1112	1098	12.9
γNH_2	1075	1060	23.8
$\delta N_4N_3N_2$	1023	1004	21.0
νN_1N_2	962	939	11.4
νC_5N_6	763	745	3.1
τring	741	717	39.0
τring	675	679	29.8
δring	629/623	656	8.0
wNH_2	550-450	602	170.2
δNH_2-(in-the-ring-plane)	-	437	0.7
γNH_2-(out-of-the-ring-plane)	-	294	7.0
τNH_2	-	265	27.4
δCH_3-(in-the-ring-plane)	-	250	4.6
γCH_3-(out-of-the-ring-plane)	-	170	4.7
τCH_3	-	93	0.6

[a] Calculated wavenumbers (ν, cm^{-1}) were scaled by 0.968; calculated infrared intensities (*I*) in km mol^{-1}. [b] ν, stretching; δ, bending; γ, rocking; w, wagging; τ, torsion; s. symmetric; as, anti-symmetric. The primes in the approximate description of the methyl group vibrations refer to local symmetry of the mode, under assumption of methyl local C_s symmetry. [c] The wNH_2 mode is predicted as an intense band, for the minimum energy conformation of the molecule in vacuo. As shown elsewhere,[1] this mode is extremely sensitive to change of geometry and very much influenced by steric constrains imposed on the molecule by the solid argon matrix. The observed downshift in frequency and reduction of intensity is ascribable to an increased planarity around the amine nitrogen atom upon insertion of the molecule in the matrix.[1] For the **1MT** molecule, the presence of the methyl substituent nearby the NH_2 group seems to lead to a distribution, in the matrix, of molecules exhibiting different geometries of the NH_2 group, so that instead of a single intense band (as predicted), a feature spreading between ca. 550 and 450 cm^{-1}, exhibiting several maxima, is observed experimentally.

1 A. Gómez-Zavaglia, I. D. Reva, L. Frija, M. L. Cristiano and R. Fausto, *J. Phys. Chem. A*, 2005, **109**, 7967–7976.

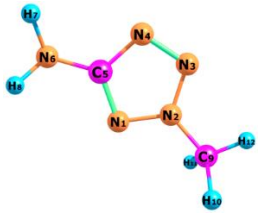

Table S11 - Proposed band assignments for the infrared spectrum of matrix-isolated 2-methyl-5-aminotetrazole **2MT**.[a,b]

Approximate description	Ar matrix	Calculated	
	ν	ν	*I*
νNH_2 as	3532/3521	3569	43.5
νNH_2 s	3429/3426	3468	39.9
νCH_3 as'	3143	3064	1.2
νCH_3 as''	3105	3026	8.5
νCH_3 s	2969	2960	27.3
δNH_2	1617	1601	262.4
νC_5N_6; δNH_2	1540/1535	1525	136.6
δCH_3 as'	-	1465	0.8
δCH_3 as''	1443	1430	12.1
$\nu N_4C_5N_1$ as	1428	1419	55.0
δCH_3 s	-	1403	0.6
νC_9N_2	1386	1367	11.5
$\nu N_3N_2N_1$ as	1306	1279	4.2
$\nu N_3{=}N_4$; γNH_2	1203	1214	40.2
γCH_3''	-	1108	0.0
γNH_2	1138	1080	2.9
$\delta C_5N_4N_3$; γNH_2	1118/1099/1074	1063	11.4
γCH_3'	1050/1035/1030	1015	11.7
νN_1N_2, νC_5N_4	1008	993	20.4
δring	796	784	12.2
τring	773	744	16.7
τring	721	647	5.2
δring	686/650	640	6.2
wNH_2	433[c]	535	267.5
δNH_2-(in-the-ring-plane)	-	451	0.6
γNH_2-(out-of-the-ring-plane)	-	337	8.4
δCH_3-(in-the-ring-plane)	-	307	2.7
τNH_2	-	276	28.1
γCH_3-(out-of-the-ring-plane)	-	172	8.5
τCH_3	-	103	0.1

[a] Calculated wavenumbers (ν, cm^{-1}) were scaled by 0.968; calculated infrared intensities (*I*) in km mol^{-1}. [b] ν, stretching; δ, bending; γ, rocking; w, wagging; τ, torsion; s. symmetric; as, anti-symmetric. The primes in the approximate description of the methyl group vibrations refer to local symmetry of the mode, under assumption of methyl local C_s symmetry. [c] The wNH_2 mode is predicted as an intense band, for the minimum energy conformation of the molecule in vacuo. As shown elsewhere,[1] this mode is extremely sensitive to change of geometry and very much influenced by steric constrains imposed on the molecule by the solid argon matrix. The observed downshift in frequency and reduction of intensity is ascribable to an increased planarity around the amine nitrogen atom upon insertion of the molecule in the matrix.[1]

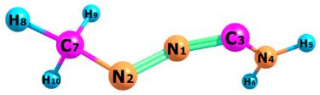

Table S12 - Proposed band assignments for the infrared spectrum of matrix-isolated nitrile imine **12**.[a,b]

Approximate description	Ar matrix	Calculated	
	ν	ν	*I*
νNH_2 as	3536	3579	89.0
νNH_2 s	3406	3402	0.2
νCH_3 as''		2992	21.2
νCH_3 as'		2975	21.3
νCH_3 s	2953/2917	2910	59.1
νCNN as	1963/1937	1828	112.3
δNH_2	1605	1601	44.6
δCH_3 as''		1451	78.5
δCH_3 as'		1425	6.8
νCNN s	1407	1412	75.2
δCH_3 s	1373	1373	45.2
γCH_3'	1161	1137	19.5
γNH_2	1134	1122	104.3
γCH_3''	1034	1060	4.9
νC_3N_4	1023	1035	16.6
νC_7N_2	869	851	4.9
τNH_2	743	618	23.7
δNCN	542	542	81.8
$\delta C_3N_1N_2$; $\delta C_7N_2N_1$		473	7.1
δNCN		368	9.9
wNH_2		299	208.5
$\delta C_7N_2N_1$		192	22.7
$\gamma C_3N_1N_2$		103	1.2
τCH_3		72	3.7

[a] Calculated wavenumbers (ν, cm^{-1}) were scaled by 0.968; calculated infrared intensities (*I*) in km mol^{-1}. [b] ν, stretching; δ, bending; γ, rocking; w, wagging; τ, torsion; s. symmetric; as, anti-symmetric. The primes in the approximate description of the methyl group vibrations refer to local symmetry of the mode, under assumption of methyl local C_s symmetry.

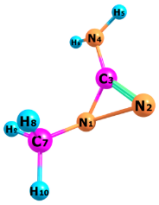

Table S13 - Proposed band assignments for the infrared spectrum of matrix-isolated diazirine **13**.[a,b]

Approximate description	Ar matrix	Calculated	
	ν	ν	*I*
νNH_2 as	3537/3566	3561	51.5
νNH_2 s	3443	3454	39.0
νCH_3 as'	3003	3007	20.0
νCH_3 as''	2990	2966	21.6
νCH_3 s	2897	2903	38.9
$\nu N_2C_3N_4$ as	1822/1816/1809	1819	279.4
δNH_2	1582	1573	42.4
δCH_3 as'	1459	1452	9.7
δCH_3 as''	1425	1424	7.1
δCH_3 s	1386	1392	1.8
νC_3N_1	1357	1342	63.7
γCH_3'	1143	1128	1.9
γCH_3''	-	1091	2.4
γNH_2	1058	1046	3.9
νC_7N_1	-	997	7.3
νC_3N_1	840	823	11.9
γC_3-(out-of-the-N_1,N_2,N_4 plane)		648	13.3
νNN		499	10.9
δNH_5[c]		463	88.4
δNH_6[c]		410	78.2
$\delta N_2C_3N_4$		395	76.3
γNH_2		344	25.4
$\delta C_3N_1C_7$		195	7.9
τCH_3		146	0.6

[a] Calculated wavenumbers (ν, cm^{-1}) were scaled by 0.968; calculated infrared intensities (*I*) in km mol^{-1}. [b] ν, stretching; δ, bending; γ, rocking; τ, torsion; s. symmetric; as, anti-symmetric. The primes in the approximate description of the methyl group vibrations refer to local symmetry of the mode, under assumption of methyl local C_s symmetry. [c] Interestingly, in this molecule the NH_2 torsion and wagging modes are replaced by single deformation modes of the individual NH bonds (NH_5 and NH_6, according to the adopted atom numbering).

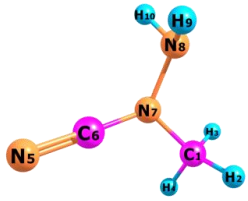

Table S14 - Proposed band assignments for the infrared spectrum of matrix-isolated amino cyanamide **14**.[a,b]

Approximate description	Ar matrix	Calculated	
	ν	ν	*I*
νNH_2 as	3431	3445	9.2
νNH_2 s		3346	1.9
νCH_3 as''	3054	3044	7.2
νCH_3 as'	3008	3004	16.3
νCH_3 s	2918	2919	48.2
νC≡N	2159	2233	161.6
δNH_2	1688	1627	25.6
δCH_3 as''	1463	1461	8.5
δCH_3 as'	1434	1437	14.5
δCH_3 s	1403	1404	2.5
γNH_2	-	1281	6.2
νN_7C_6	1333	1254	18.1
νN_7C_1; wNH_2	1185	1197	3.2
γCH_3'	1133	1107	2.2
γCH_3''	1042	1038	49.7
wNH_2	868	875	80.5
νNN		746	11.7
$\delta N_5C_6N_7$		622	5.7
$\gamma N_5C_6N_7$		531	4.1
$\delta C_1N_7N_8$		392	9.2
τNH_2		281	51.1
N-Inversion		204	8.8
$\tau C_1N_7C_6$		200	5.5
τCH_3		156	2.5

[a] Calculated wavenumbers (ν, cm^{-1}) were scaled by 0.968; calculated infrared intensities (*I*) in km mol^{-1}. [b] ν, stretching; δ, bending; γ, rocking; w, wagging; τ, torsion; s. symmetric; as, anti-symmetric. The primes in the approximate description of the methyl group vibrations refer to local symmetry of the mode, under assumption of methyl local C_s symmetry.

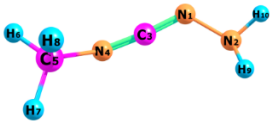

Table S15 - Proposed band assignments for the infrared spectrum of matrix-isolated carbodiimide **15**.[a,b]

Approximate description	Ar matrix	Calculated	
	ν	ν	*I*
νNH_2 as	3447	3466	14.7
νNH_2 s		3349	1.7
νCH_3 as''		2998	15.6
νCH_3 as'	3026	2990	21.8
νCH_3 s	2951	2918	67.3
νNCN as	2113/2107	2143	692.5
δNH_2	1670/1666	1619	21.5
δCH_3 as'	1469	1459	20.9
δCH_3 as''	1446	1441	6.3
νNCN s	1419	1415	8.7
δCH_3 s	1392	1391	13.0
γNH_2	1304	1259	51.1
γCH_3'	1113	1103	1.8
γCH_3''	-	1094	0.6
νNN; wNH_2	1042	1024	67.6
νC_5N_4; wNH_2	891	867	37.2
wNH_2; νNN	804	785	101.7
δNCN	640	625	37.3
γNCN,	580	557	43.5
δCNN		310	5.0
δCNC; δCNN		219	30.0
τNH_2		176	16.9
δCNC; δCNN		152	2.5
γCH_3		101	2.8

[a] Calculated wavenumbers (ν, cm^{-1}) were scaled by 0.968; calculated infrared intensities (*I*) in km mol^{-1}. [b] ν, stretching; δ, bending; γ, rocking; w, wagging; τ, torsion; s. symmetric; as, anti-symmetric. The primes in the approximate description of the methyl group vibrations refer to local symmetry of the mode, under assumption of methyl local C_s symmetry.

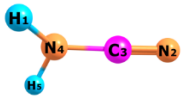

Table S16 - Proposed band assignments for the infrared spectrum of matrix-isolated cyanamide **16**.[a,b]

Approximate description	Ar matrix	Calculated		Literature data[2,3]
	ν	ν	*I*	ν
νNH_2 as	-	3533	70.4	3486
νNH_2 s	-	3443	43.3	3400
νC≡N	2261	2277	126.3	2264
δNH_2	1586	1581	48.4	1589
γNH_2	-	1151	0.4	
νC-N	1061	1062	9.9	1060
γNCN, wNH_2		529	117.7	
wNH_2		463	138.6	
δNCN		397	0.01	

[a] Calculated wavenumbers (ν, cm^{-1}) were scaled by 0.968; calculated infrared intensities (*I*) in km mol^{-1}. [b] ν, stretching; δ, bending; γ, rocking; w, wagging; s. symmetric; as, anti-symmetric.

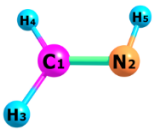

Table S17 – Proposed band assignments for the infrared spectrum of matrix-isolated methylenimine **17**.[a,b]

Approximate description	Ar matrix	Calculated		Literature data[4]
	ν	ν	*I*	ν
νNH		3324	1.5	
νCH_2 as	3034	3012	32.7	3035
νCH_2 s	2927	2914	52.8	2926
νC=N	1642	1653	25.0	1641
δCH_2	-	1445	6.9	1453
γCH_2, δNH	-	1327	35.2	1348
τNH		1125	47.4	1123
wCH_2	1062	1069	17.8	1063
γCH_2, δNH	1058	1040	34.2	1059

[a] Calculated wavenumbers (ν, cm^{-1}) were scaled by 0.968; calculated infrared intensities (*I*) in km mol^{-1}. [b] ν, stretching; δ, bending; γ, rocking; w, wagging; τ, torsion; s, symmetric; as, anti-symmetric.

2 F. Duvernay, T. Chiavassa, F. Borget and J.-P. Aycard, *J. Phys. Chem. A*, 2005, **109**, 603–8.
3 S. T. King, *J. Chem. Phys.*, 1971, **54**, 1289.
4 M. E. Jacox and D. E. Milligan, *J. Mol. Spectrosc.*, 1975, **56**, 333–356.

Table S18 - Proposed band assignments for the infrared spectrum of matrix-isolated carbodiimide **18**.[a,b]

Approximate description	Ar matrix	Calculated		Literature data[2,3]
	ν	ν	*I*	ν
νNH s		3483	29.9	
νNH as		3481	139.8	3425
νNCN as	2169	2153	712.8	2169
νNCN s		1245	0.1	
δNH as	886	871	422.3	886
δNH s		869	25.8	
τNH		695	107.8	
δNCN		524	0.2	
γNCN		523	80.0	

[a] Calculated wavenumbers (ν, cm^{-1}) were scaled by 0.968; calculated infrared intensities (*I*) in km mol^{-1}. [b] ν, stretching; δ, bending; γ, rocking; τ, torsion; s, symmetric; as, anti-symmetric.

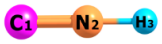

Table S19 - Proposed band assignments for the infrared spectrum of matrix-isolated CNH **19**.[a,b]

Approximate description	Ar matrix	Calculated		Literature data[5,6]
	ν	ν	*I*	ν
νNH	3576	3686	271.5	3583, 3576
νC=N	2031	2028	74.7	2032, 2031
δNH	537	478	161.5	535, 537
γNH	537	478	161.5	535, 537

[a] Calculated wavenumbers (ν, cm^{-1}) were scaled by 0.968; calculated infrared intensities (*I*) in km mol^{-1}. [b] ν, stretching; δ, bending; γ, rocking.

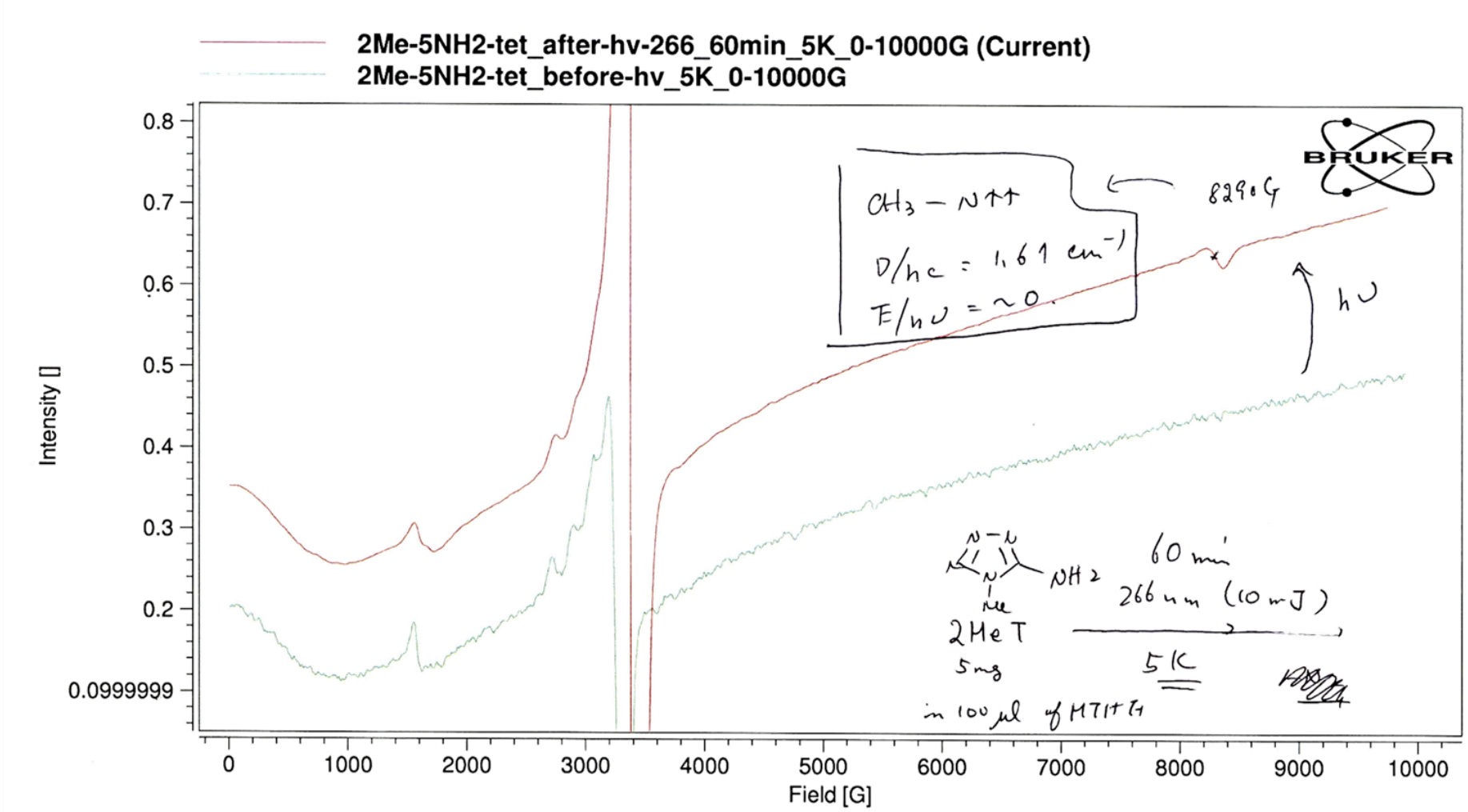

Figure S4 – EPR spectrum of nitrene ^{T}**N2** generated by irradiation of **2MT** (at λ = 266 nm, ~10 mJ; 60min) in 2-methyl-THF glass at 4K. A small XY_2 transition is observed at ~ 8200 G (gausses) at 9.38 GHz (microwave frequency). The strong signals at ~3250 G are derived from doublet impurities.

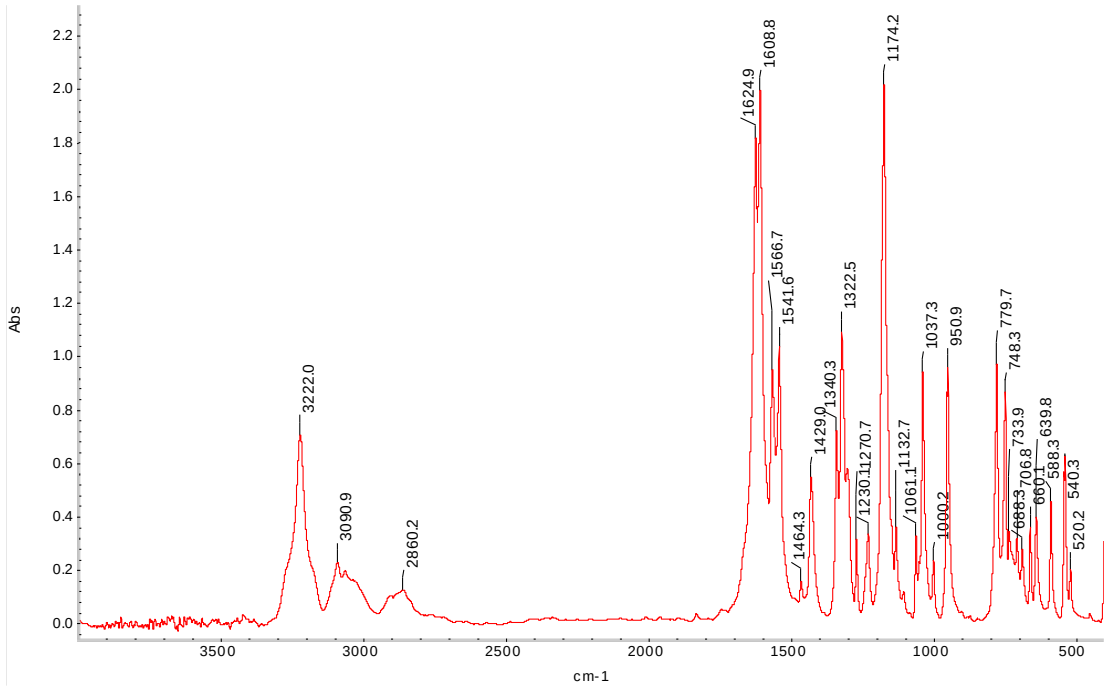

Figure S5 - Infrared spectrum of TS (KBr pellet; room temperature).

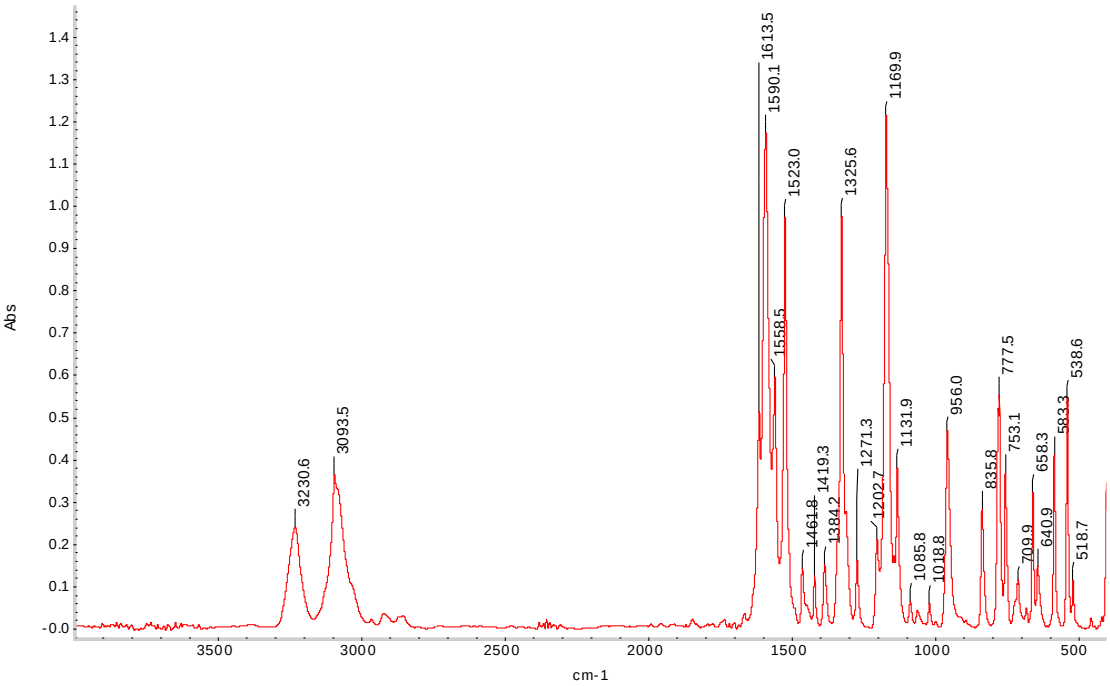

Figure S6 - Infrared spectrum of 2MTS (KBr pellet; room temperature).

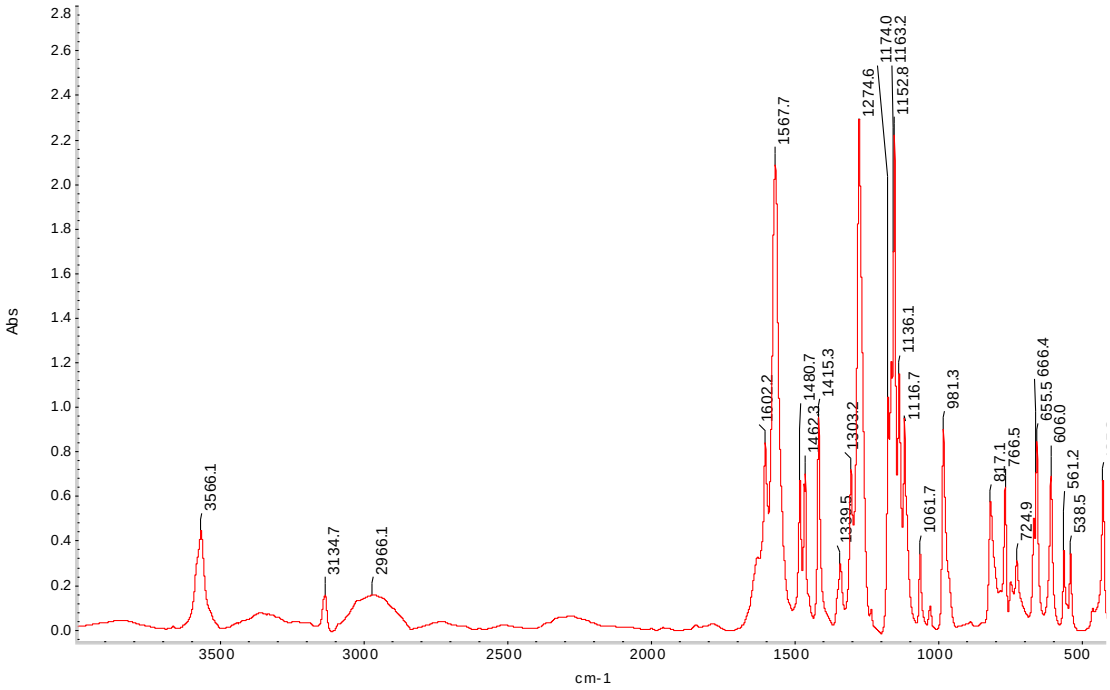

Figure S7 - Infrared spectrum of complex **CuTS** (KBr pellet; room temperature).

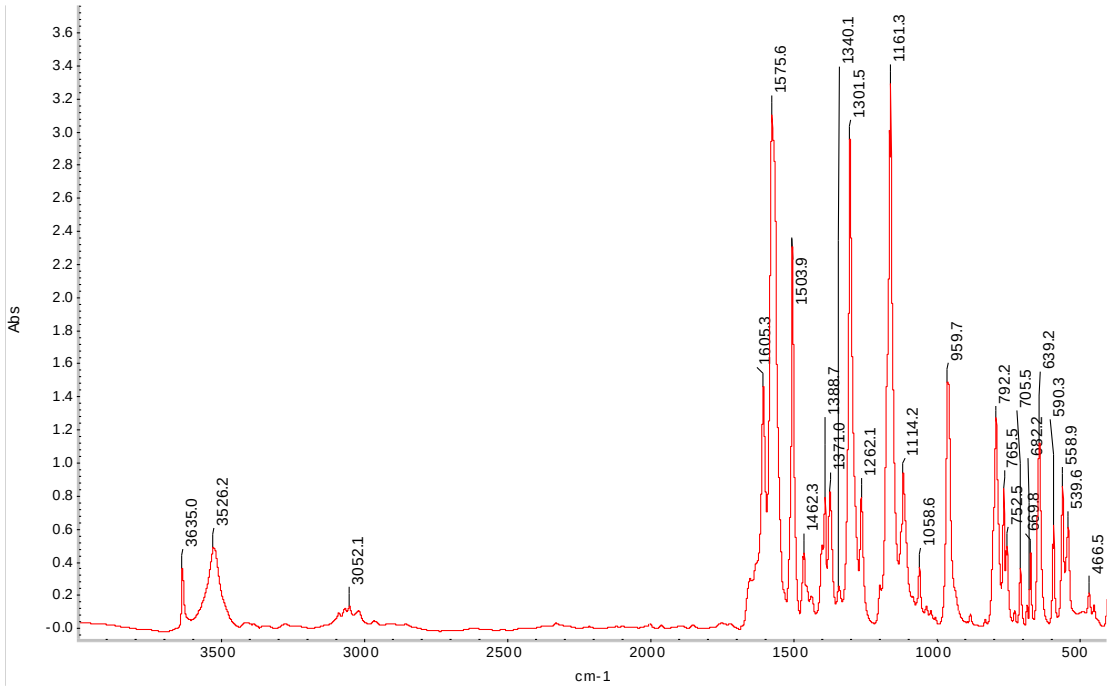

Figure S8 - Infrared spectra of complex **Cu2MTS$_2$** (KBr pellet; room temperature).

Table S20 - Structural parameters for hydrogen bonds and weaker intermolecular interactions between C-H groups as donors and N and O atoms as acceptors in the crystal of complex **Cu2MTS$_2$**.[a]

	D-H (Å)	H···A (Å)	D···A (Å)	D-H···A (º)
O1-H1A···O2$^{(i)}$	0.85(4)	1.78(4)	2.623(3)	172(4)
O1-H1B···N16	0.63(4)	2.60(5)	2.948(3)	117(5)
O2-H2A···N12'$^{(ii)}$	0.84(4)	2.14(4)	2.966(2)	168(3)
O2-H2B···O10	0.77(4)	2.11(4)	2.886(2)	176(4)
C8-H8···N14'$^{(ii)}$	0.93	2.61	3.499(3)	160.8
C18'-H18D···O10$^{(i)}$	0.96	2.57	3.377(3)	141.5
C18'-H18E···N12$^{(iii)}$	0.96	2.65	3.517(3)	150.9
C18'-H18F···O11$^{(ii)}$	0.96	2.64	3.529(3)	154.1

[a] Symmetry codes: (i) 1-*x*,-*y*,1-*z*; (ii) –*x*,-*y*,1-*z*; (iii) *x*,-1+*y*,*z*.

Table S21 - UV-vis spectroscopic evidence of the conjugate-metal complex.[a]

Salt	Metal-cation	TS	2MTS	1MTS	TSMT
$Cu(ClO_4)_2 \cdot 6H_2O$; $CuSO_4 \cdot 5H_2O$	Cu^{2+}	✓	✓	✓	✓
$PbSO_4$; $Pb(CH_3COO)_2 \cdot 3H_2O$; $Pb(NO_3)_2$	Pb^{2+}	✓	✗	✗	✓
$Ni(ClO_4)_2 \cdot 6H_2O$	Ni^{2+}	✓	✓	✓	✓
$Co(ClO_4)_2 \cdot 6H_2O$	Co^{2+}	✓	✓	✓	✓
$FeCl_2 \cdot 4H_2O$	Fe^{2+}	✗	✗	-	-
$ZnSO_4$; $ZnBr_2$; $ZnCl_2$	Zn^{2+}	✓	✗	✓	✓
$CaCl_2$; $Ca(OH)_2$; $CaCO_3$	Ca^{2+}	✗	✗	✗	✓
$Mn(CH_3COO)_2 \cdot 4H_2O$	Mn^{2+}	✓	✓	✓	✓

[a] ✓ evidence of spectroscopic changes during UV-Vis titration of the ligand with the respective salt; ✗ not observed spectroscopic changes during the UV-Vis titration. The experiment is explained e Chapter V, section 5.1.5.